8-2007

Spinning Carbon Fiber Precursors from 1-Butyl-3-Methylimidazolium Chloride Cellulose Solutions

Rhea J. Gelderloos-Sammons
University of Tennessee - Knoxville

To the Graduate Council:

I am submitting herewith a dissertation written by Rhea J. Gelderloos-Sammons entitled "Spinning Carbon Fiber Precursors from 1-Butyl-3-Methylimidazolium Chloride Cellulose Solutions." I have examined the final electronic copy of this dissertation for form and content and recommend that it be accepted in partial fulfillment of the requirements for the degree of Doctor of Philosophy, with a major in Chemical Engineering.

John R. Collier, Major Professor

We have read this dissertation and recommend its acceptance:

Billie Collier, Simioan Petrovan, Tim Rials, Joseph Spruiell

Accepted for the Council:
Dixie L. Thompson

Vice Provost and Dean of the Graduate School

(Original signatures are on file with official student records.)

To the Graduate Council:

I am submitting herewith a dissertation written by Rhea J. Gelderloos-Sammons entitled "Spinning Carbon Fiber Precursors from 1-Butyl-3-Methylimidazolium Chloride Cellulose Solutions." I have examined the final electronic copy of this dissertation for form and content and recommend that it be accepted in partial fulfillment of the requirements for the degree of Doctor of Philosophy, with a major in Chemical Engineering.

_____
John R. Collier, Major Professor

We have read this dissertation
and recommend its acceptance:

Billie Collier

Simioan Petrovan

Tim Rials

Joseph Spruiell

Accepted for the Council:

Carolyn R. Hodges

Vice Provost and Dean of the
Graduate School

(Original signatures are on file with official student records)

SPINNING CARBON FIBER PRECURSORS FROM 1-BUTYL-3-METHYLIMIDAZOLIUM CHLORIDE CELLULOSE SOLUTIONS

A Dissertation
Presented for the
Doctor of Philosophy
Degree
The University of Tennessee, Knoxville

Rhea Jessica Gelderloos-Sammons
AUGUST 2007

DEDICATION

To my parents, for always helping
me see the forest from the trees.

And to Jake, for always listening
and for your patience.

ACKNOWLEDGEMENTS

The following people have given of themselves in an effort to help me complete this project. Without them I would have not come this far and for that I am truly grateful to each one.

Dr. John Collier, my major advisor, who provided me with guidance and advice. He challenged me to examine my thoughts and ideas in a different perspective thus making them much stronger.

Dr. Simioan Petrovan, who has spent countless hours helping me with experiments and reassuring me that I "don't need to put a hole in the sky."

Dr. Joseph Spruiell, Dr. Billie Collier and Dr. Tim Rials, who directed me in different aspects of this project with their experience and expertise. Their assistance and questions further strengthen the objectives, methodology and results of this research.

Dr. Ramsis Farag, of Auburn University, who allowed me to use his tensile strength equipment.

The funding for this project was provided by the Environmental Protection Agency (EPA), Grant Number: R831658, "Cellulosic Carbon Fiber Precursors from Ionic Liquid." This research would not have been made possible without this support. Thank you.

ABSTRACT

Cellulose is an abundant natural renewable polymer that is used in the production of many materials. However, limited processibility and reduced solubility have restricted its use in fibers, films, and other products. Ionic liquids (IL) show promise as a new class of cellulose solvents.

The primary goal of this research was to spin highly oriented and highly crystalline cellulose fibers from an IL solution. These fibers, in addition to their environmentally advantageous processing, have potential as precursors for carbon fibers. The IL selected for this study was 1-butyl-3-methylimidazolium chloride, ($[C_4mim]Cl$). An elongational flow spinning technique was used to induce molecular orientation in the spinneret thus producing highly oriented, highly crystalline fibers. The effect of spinning conditions on fiber properties was determined. One prime consideration for carbon fiber precursors is the degree and size of defects. The elongational flow imposition of orientation inside the hyperbolic dies was especially effective.

TABLE OF CONTENTS

LIST OF TABLES

LIST OF FIGURES

NOMENCLATURE

	Equations
a_H	Hencky shift factor
a_T	Temperature shift value
C	Constant of the particular stream surface
d	Diameter of the fiber
D_r	Draw ratio
E^{-n} $(n=1,2,3\ldots)$	Number value times 10^{-n}
f_H	Herman's orientation factor
L	Centerline length of the die
L_T	Total die length
n	Rate constant
N_{OR}	Orientation number
$N_{OR(AG)}$	Orientation number for the air gap
$N_{OR(die)}$	Orientation number for the die
$N_{OR(Tot)}$	Total orientation number
r	Radius at a centerline distance of the die
R_e	Exit radius of the hyperbolic die
R_o	Entrance radius of the hyperbolic die
T	Solution temperature
$t_{process}$	Process time
v	Take up velocity
v_d	Velocity at the die exit
v_o	Initial velocity at the die entrance
v_t	Take-up velocity
z	Centerline distance of the die
Δ^o	Maximum birefringence of cellulose
Δn	Birefringence
ΔP	Imposed pressure drop from the die entry to the exit
$\dot{\varepsilon}$	Elongational strain rate
$\dot{\varepsilon}_{(AG)}$	Elongational strain rate for the air gap
$\dot{\varepsilon}_{(Tot)}$	Total elongational strain rate
ε_H	Hencky strain rate
$\varepsilon_{H(AG)}$	Hencky strain rate for the air gap
$\varepsilon_{H(Tot)}$	Total Hencky strain rate
Γ	Phase difference
Φ	Potential function, isobaric pressure in shear free flows
η	Complex viscosity
η_{aT}	Reduced complex viscosity
η_e	Elongational viscosity
η_o	Zero shear viscosity
η_s	Shear viscosity at an $\dot{\gamma}$ of zero

λ	Average relaxation time
ω	Angular velocity
Ψ	Flow streamlines as the stream function
$2i$	Angle of rotation

	Units
^{o}	Degrees
^{o}C	Degrees Celsius
den	Denier, grams per 9,000 meters
g_f/den	Grams force per denier
s^{-1}	Inverse seconds
J mol^{-1} K^{-1}	Joules per mole Kelvin
kCal	Kilocalories
kgf	Kilograms of force
kV	Kilovolts
m/min	Meters per minute
m/s	Meters per second
mA	Milliamps
mm	Millimeters
Pa•s	Pascal seconds
RPM	Revolutions per minute
s	Seconds

Abbreviations

$[C_4mim]Cl$	1-butyl-3-methylimidazolium chloride
CI	Crystallinity Index
ILs	Ionic Liquids
LD	Linear Density
Ld_{max}	Maximum load
NMMO	N-methyl morpholine oxide, an amine oxide
SEM	Scanning Electron Microscope
WAXS	Wide Angle X-Ray Scatter
Ten	Tenacity equals Ld_{max}/LD
TR	Trouton Ratio

Chapter 1 – Introduction

1.1 Project Summary

Cellulose is an abundant natural renewable polymer that is used in the production of many materials. However, limited processibility and reduced solubility have restricted its use in fibers, films, and other products. Many of the current processes involving cellulose also involve chemical solvents that contain sulfur and chlorine which in excessive amounts are hazardous to the environment (Seddon, 1997). A new developing area of research deals with the interactions of cellulose with environmentally benign solvents such as ionic liquids (ILs) and the amine oxide, N-methyl morpholine oxide (NMMO). Solutions of cellulose in the monohydrate, $NMMO \cdot H_2O$, have been studied rather extensively and are the basis for spinning lyocell fibers, a relatively new technology dating from the 1980s (Franks, et al., 1979). Cellulose/IL solutions however are of more recent interest and spinning fibers from these solutions is the focus of this work.

The primary goal of this research is to spin highly oriented and highly crystalline cellulose fibers from an IL solution. These fibers, in addition to their environmentally advantageous processing, should have potential as precursors for carbon fibers. Carbon fibers processed from cellulosic precursors are classified by their grade based on stiffness and use in application (Shariq, et al., 1999). Carbon fibers used for military and aircraft applications require a higher level of testing than fibers for the automotive industry and consumer goods. Although the production of cellulose derived carbon fibers has been well developed, their use has decreased due to the negative environmental impact of production, the low yield of carbon fibers that are produced from cellulose fibers, and finally the cost of cellulose-based carbon fibers (Shariq, et al., 1999). An improved source of precursor fibers should address some of these problems in processing carbon fibers for reinforcement in composites.

The IL selected for this study is 1-butyl-3-methylimidazolium chloride, ($[C_4mim]Cl$). It has been shown to be particularly effective in dissolving cellulose. Cellulose is precipitated from the solvents in both the $NMMO \cdot H_2O$ and $[C_4mim]Cl$

systems by dilution with water (Swatloski[1], et al., 2002). The use of an elongational flow spinning technique which induces molecular orientation in the spinneret produces highly oriented, highly crystalline low defect fibers, properties that are desirable for carbon fiber precursors. This involves the use of hyperbolically converging dies where the induced orientation can be supplemented and the relaxation impeded by the application of a controlled tension in the air gap and coagulation bath (Collier[5], et al., 2005). One prime consideration for carbon fiber precursors is the degree and size of defects. The elongational flow imposition of orientation inside the hyperbolic dies is especially effective since defects are compressed by the die walls rather than expanded in free surface drawing. By comparing these fibers spun using differing rheological parameters, an understanding of how the cellulose fibers orient and crystallize under different conditions can be determined. This knowledge can be complemented by further understanding of how the use of new catalysts for carbonization will increase the carbon fiber quality and yield (Nimlos, et al., 2003). Building on work by researchers in this area, the specific objectives of the present project are to:

- Determine the rheological behavior of cellulose/[C_4mim]Cl solutions by understanding the characteristics of cellulose, [C_4mim]Cl and the cellulose/[C_4mim]Cl solution.
- Spin single fibers from the IL solutions through a hyperbolically converging die.
- Determine the effects of cellulose concentration, processing temperature, elongational strain rate, draw ratio and coagulation bath composition by measuring the microscopic appearance at the micro and nano levels; tenacity and crystallinity, morphology and the crystal form of the fibers.

Ultimately this should demonstrate that the use of ILs can produce quality cellulose fibers without the harmful environmental emission of current production processes. In order to achieve this goal, an in-depth knowledge of the interactions between cellulose and, the ionic liquid used throughout this study, is needed to better

understand the morphology and the rheological characteristics of the cellulose fibers spun from a cellulose/[C_4mim]Cl solution.

The longer range interest in ILs includes the higher thermal stability and potentially easier recovery. Due to the solubility characteristics of ILs it may be possible to use less chemically treated sources as feedstocks, e.g. bagasse, saw-grass. Recovery of by-products from less chemically treated sources either by solvent extraction of the cellulose and/or phase separation during regeneration, could be an additional benefit.

Chapter 2 – Background

2.1 Cellulose Characteristics

2.1.1 Structure of Cellulose, Hemicelluloses, Lignin

Cellulose, hemicelluloses and lignin are found in the fiber wall of a plant. Lignin is the chemical compound that fills the spaces between the cellulose and hemicellulose components in the cell wall. It is the most abundant organic polymer on Earth after cellulose. The amount of each compound in the fiber wall varies with location within the wall and with the plant species (Rydholm, 1965). A typical fiber wall of wood, as illustrated in Figure 2.1, consists of a middle lamella which is stiff and heavily lignified, a primary wall, an outer secondary wall, a main secondary wall and an inner secondary wall. However, this basic structure can vary slightly with different species of trees and grassy plants.

Generally, the concentration of lignin is the highest in the outer layers of the fiber wall. Hemicelluloses, although located throughout the fiber, are also predominant in the outer layers of the fiber wall. However, the opposite is true for cellulose. Cellulose increases in concentration in the layers closer to the center of the fiber or in the lumen (Rydholm, 1965). Use of other cellulosic sources for the similar lyocell process has been investigated by this group and could be involved in a continuation of this research but is not part of this research (Collier[4], et al., 2000 and Dever, et al., 2003).

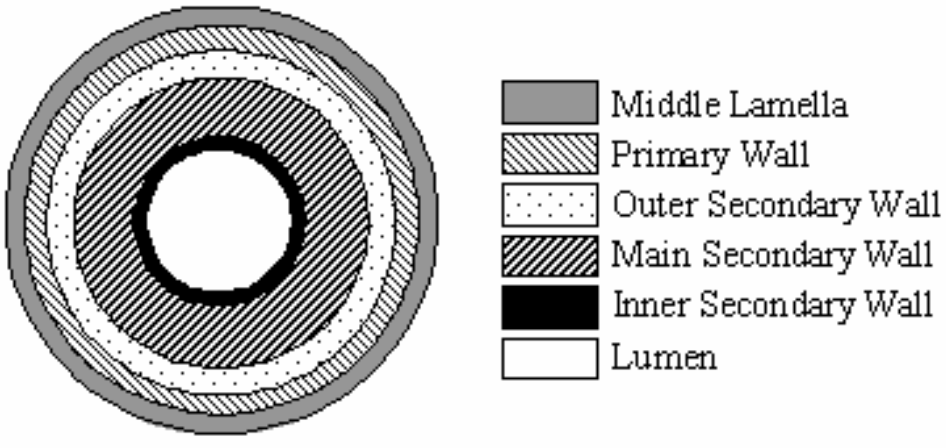

Figure 2.1: Diagram of a fiber wall.

Lyocell, also called NMMO/water, is an environmentally friendly solvent that dissolves cellulose. In commercial processes the cellulose in the solution is precipitated by spinning into a low concentration of NMMO in water. The NMMO is then recovered from the water solution by filtration, dewatering and evaporation to the near monohydrate form and recycled. NMMO is also biodegradable so any remaining NMMO that is not recovered from the water solution is not harmful to the environment. Theoretically, the spinning of a cellulose/ionic liquid solution should behave in the same manner as the cellulose/NMMO solution due to the similar characteristics between them.

Cellulose production occurs in all plant life however other organisms such as certain bacteria, cellular slime molds, amoeba, some fungi and green algae also produce forms of cellulose (Brown, 2003). As shown in Figure 2.2, cellulose consists of glucose monomers with a β-1,4 linkages, with a typical degree of polymerization being approximately 500 units (Flory, 1953).

Cellulose occurs in a number of crystalline forms, the two natural forms called cellulose I and cellulose II. The other remaining forms result from the processing of the cellulose I and II (Brown, 2003). In cellulose I, the more common of the two natural forms, the chains are oriented in a parallel fashion. Cellulose II chains are anti-parallel which allows for additional hydrogen bonding. The crystal structures of cellulose I and cellulose II can be seen in Figure 2.3. The additional hydrogen bond in cellulose II causes it to be more thermodynamically stable however, natural cellulose II is rare, and it is only produced by algae and bacteria (Brown, 2003).

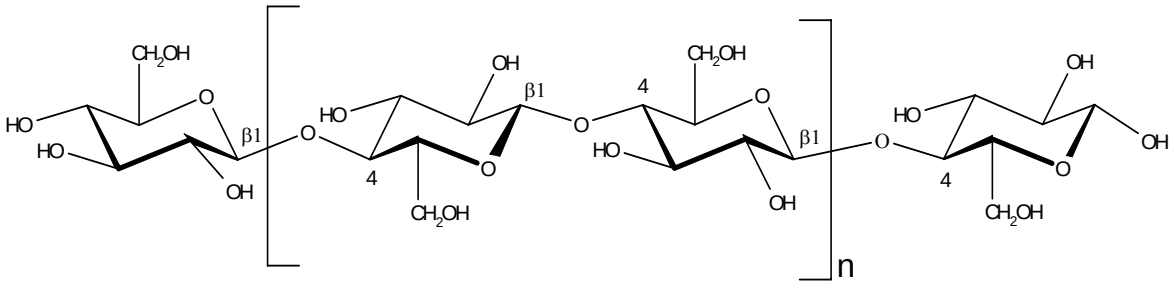

Figure 2.2: Cellulose polymer chain, n ranges from 400 to 6000 units.

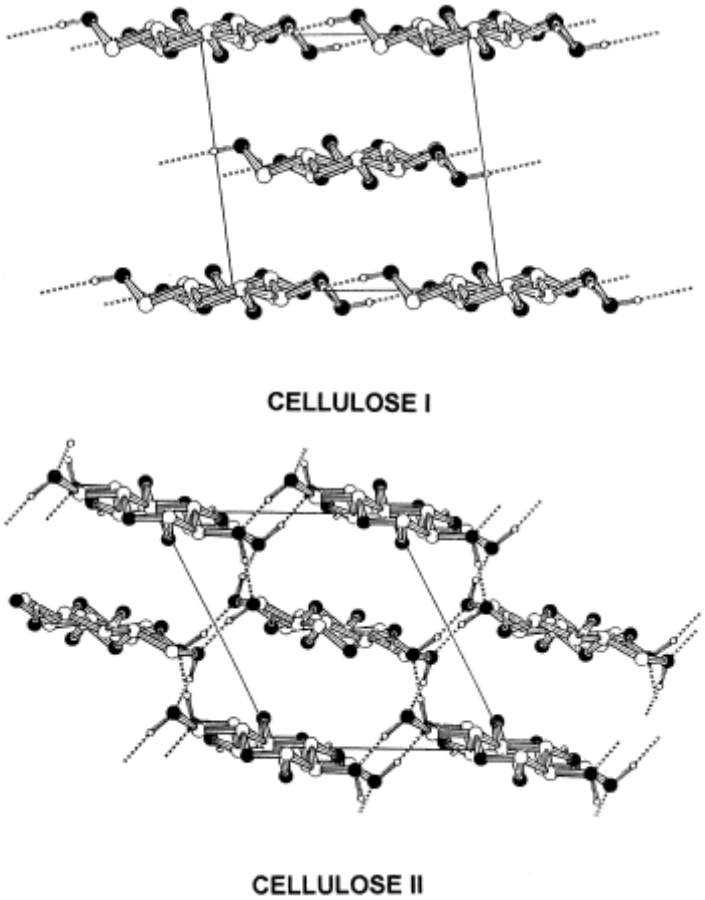

Figure 2.3: The crystal structure of cellulose I and II viewed along the chain axis. The dashed lines represent the intermolecular hydrogen bonds. (Northolt, et al., 2001)

The complete understanding of the nature of cellulose chain structure is an active area of research. Using forms of cellulose, such as cellobiose, as well as native and processed cellulose, calculations on conformational energy can determine the three-dimensional structure of a cellulose chain (Simon[1], et al., 1988). This method can also be applied to groups of cellulose chains (Simon[2], et al., 1988).

Cellulose I can also be synthesized by aligning glucan chains that have the same polarity and chain conformation by the micellar aggregation of a partially purified enzyme (Lee. et al., 1994). Achieving cellulose synthesis is one step in understanding its structure as well as its chemical nature. Studies have been done to determine the structure of cellulose but it is still largely unknown how cellulose interacts with ILs although some theories have been suggested to explain this interaction much remains to be done.

2.1.2 Cellulose Dissolution

In traditional commercial processes cellulose based polymers were dissolved following the reaction of its hydroxyl groups to create ether or ester linked substituents that reduce hydrogen bonding and disrupt crystallinity. However, there are only a limited number of solvents that can dissolve cellulose directly. These solvents include calcium thiocyanate/water, dimethyl acetamide/LiCl, NMMO·H_2O, iron titrate and most recently several dialkylimidazolium salts, also referred to as ILs (Berger, 2001).

In ILs cellulose dissolves due to the formation of strong specific interactions between the cellulose hydroxyl and the ionic liquid. These interactions disrupt the intermolecular hydrogen bonding of the cellulose and thus allow for dissolution (Swatloski[1], et al., 2002). Precipitation of the cellulose from the IL occurs with the addition of water, ethanol or acetone (Swatloski[1], et al., 2002). The OH groups on these non-solvent compounds compete with the cellulose OH bonding and due to the size of these compounds the cellulose-ionic liquid bond are disrupted.

The cellulose dissolution in ILs and the precipitation by water is similar to that of the lyocell spinning process. The phase separation that occurs in the lyocell and IL processes should have an affect on the orientation and crystallinity of the fiber. Retention of orientation after exiting the die and deformation is dependent on the rate of relaxation versus the induced phase change. The flow of lyocell solutions through a converging die may enhance phase separation, cellulose crystallization as well as microfibers formation and high orientation (Collier[1], et al.). A similar response is expected for IL solutions.

A study done on the affect of the phase separation in the lyocell system on the spun fiber indicates that as a fiber enters the coagulation bath, the precipitation of cellulose occurs through diffusion of nonsolvent and solvent in a state of nonequilibrium where spinodal decomposition (i.e. the phase separation of an unstable mixture) occurs (Mortimer, et al., 1996). The quenching of the spun fiber in the coagulation bath first affects the surface of the fiber and can put the system in either an unstable or metastable state. "If the system is in an unstable state, it decays to two coexisting metastable states leading to an interconnected structure of the two phases, one of which is rich in solvent and the other rich in polymer" (Mortimer, et al., 1996). The similarities between lyocell and the cellulose/[C_4mim]Cl solution used in this research, suggests that a phase

separation in the IL solution would affect the orientation and crystallinity of the cellulose fibers similar to that in the lyocell process.

2.2 Ionic Liquids Characteristics

ILs are considered a relatively new class of compounds that have gained attention due to unique properties as solvents. These solvents are considered as environmentally benign solvents for their property of no vapor pressure at room temperature thus emitting no harmful vapors during processing. This is similar to the NMMO·H_2O solvent. The lack of vapor pressure in ILs is due to the ionic bonds of the compound, similar to that of ionic salts, e.g. NaCl, KCl, etc. ILs generally have high thermal stability, good chemical stability and low flammability as well (Seddon, 1997). In a physical properties study, ILs were noted to have greater densities than water, higher viscosities than other molecular solvents and a wide liquidus range (Wilkes, 2004). However, the study later points out that a drawback of IL solvents is their tendency to supercool making measurements of melting point difficult to determine, as well as their tendency to thermally decompose at the upper limit of the liquid range. Another study indicates that as the anion of the IL increases, the thermal stability also increases (Fredlake, et al., 2004). As specified in this study, [C_4mim]Cl, has thermal properties indicated in Table 2.1.

Table 2.1: Thermal Properties of 1-butyl-3-methylimidizoluim chloride, [C_4mim]Cl]

Melting Point Temperature (^oC)	41
Glass Transition Temperature (^oC)	-69
Start Temperature of Thermal Decomposition (^oC)	150
Heat Capacity @ 25^oC (J mol^{-1} K^{-1})	322.7
Heat Capacity @ 50^oC (J mol^{-1} K^{-1})	333.7

(Fredlake, et al. 2004)

ILs are now being considered as solvents and in some cases catalysts in organic synthesis reactions such as Diels-Alder cycloadditions, Heck coupling, hydrogenation, and Friedel-Craft reactions (Lévêque, et al., 2002). Currently, ILs have been examined as solvents and catalysts and in many cases ILs show an improved reaction rate, better selectivity and easier reuse.

When comparing these characteristics to other volatile organic solvents, ionic liquids are "truly designer solvents" (Artl, et al., 2003).

Ionic liquids can be prepared in one or more steps. A general starting reaction for ILs is the synthesis reaction of 1-methylimidazole with an alkyl halide, known as Menschutkin quarterisation, as shown in Figure 2.4. To form some of the other ILs, an anion exchange with an ammonium salt, known as a Finkelstein reaction, is performed on compounds formed in the general reaction in Figure 2.5. The focus of this research is the use of $[C_4mim]Cl$ and its formation is often the first step in forming other ionic liquids. From Figure 2.4, if R is butane and X^- is Cl^- from the chlorobutane then the product is $[C_4mim]Cl$, as shown in Figure 2.5 (Lévêque, et al., 2002).

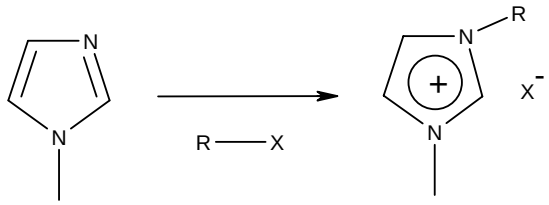

Figure 2.4: Reaction of 1-alkyl-3-methylimidazolium halide.

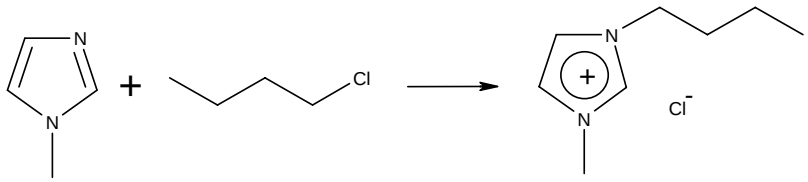

Figure 2.5: Reaction of 1-methylimidazole and chlorobutane to produce $[C_4mim]Cl$.

The specific preparation of $[C_4mim]Cl$ using the reaction can be achieved through several processes. A conventional method is the use of excess solvent, in this case excess chlorobutane (Lévêque, et al., 2002). However, this can prove to be wasteful and alternative methods have been sought. One nearly stoichiometric method is to apply heat to the reactants. This reduces the reaction time from hours to minutes and it reduces the use of large amounts of excess materials. However, the continuous heating and the exothermic nature of the reaction can lead to overheating which will discolor the product. A stronger color indicates a higher level of thermal decomposition (Namboodiri, et al., 2002).

This discoloration typically occurs after an extended exposure to heat and other processing conditions. Within the confines of this research, the mixing and processing times did not effect the coloration of the higher solution concentrations, such as the 12% solution, despite being exposed to heat for a longer time compared to the 8% solutions. Another method of IL preparation is the use of ultrasound as the energy source of a neat reaction. This stoichiometric method reduces the reaction time and lowers the reaction temperature by exposing the reactants in closed containers to irradiation using a sonic bath (Namboodiri, et al., 2002).

The lack of vapor pressure of ILs and $NMMO{\cdot}H_2O$ enables potential reuse once the solute is removed. The recyclability of ILs is another key characteristic that makes them desirable as environmentally benign solvents. In-order for IL to be recycled, the solute in the solution must be removed effectively. The challenge is to use a process that is also considered environmentally benign. A solute (e.g. cellulose) removal process that does not follow this criterion negates the point of using an environmentally benign solvent in the first place. Solute removal in $NMMO{\cdot}H_2O$ and $[C_4mim]Cl$ systems is achieved by dilution with water. Regeneration of the $NMMO{\cdot}H_2O$ and nearly neat $[C_4mim]Cl$ is achieved by removal of the necessary amount of water. This procedure should be effective for $[C_4mim]Cl$.

With the growing interest in ILs, industrial use of these compounds is in the not too distant future and small amounts of ILs will certainly find their way into the environment (Sheldon, 2001). Although the potential benefits of ILs are being studied,

little research has been done their toxicity and biodegradability. Researchers are starting to study the toxicity effects of ILs on mammalian cell lines and enzyme activity as well as on marine species of bacteria, worm, water flea and fish (Bernot, et al., 2005). Though, most research involving the use of ILs focuses on their value in synthesis and separation systems (Swatloski[2], et al., 2004). Due to the immense range of possible ILs, an inexpensive, rapid toxicological screening process is needed.

One study on the toxicity of imidazolium chloride ILs on *Caenorhabditis elegans,* a type of aquatic worm, determined that lengthening the alkyl chain led to a related increase in toxicity/lethality seemingly through surfactant/detergent effects (Swatloski[2], et al., 2004). Another study involving *Daphnia magna*, a water flea, suggests that the toxicity of ILs appears to be related to the imidazolium cation and not to the various anions. The toxicity of imidazolium- based ILs is apparently similar to that of chemicals currently used in manufacturing and disinfection processes e.g., ammonia and phenol. This could indicate that ILs may not be more harmful to aquatic organisms than current volatile organic solvents (Bernot, et al., 2005).

2.3 Interaction of cellulose in [C_4mim]Cl

As noted in section 2.1.2 the dissolving of the cellulose in ionic liquids apparently is driven by the formation of strong specific interactions between the cellulose hydroxyl and the ionic liquid, e.g. [C_4min]Cl, that disrupt the intermolecular hydrogen bonding of the cellulose and thus allowing for solution formation (Swatloski[1], et al., 2002). However, the exact nature of these interactions is still not understood.

A wide range of ILs have been used to dissolve cellulose. The best results of cellulose solution formation were obtained using [C_4mim]Cl apparently because its anion in the ionic liquid bonding state is a strong hydrogen bond acceptor (Swatloski[1], et al., 2002). When cellulose is dissolved in a nonderivitizing solvent like [C_4mim]Cl, the intramolecular hydrogen-bonding of the cellulose hydroxyl groups is disrupted and broken, e.g. by the chloride ion in [C_4mim]Cl. The high chloride activity and concentration of [C_4mim]Cl allows for dissolving of larger amounts of cellulose at a faster rate when compared to traditional solvents (Swatloski[1], et al., 2002).

When water, ethanol or acetone are added to the cellulose/[C_4mim]Cl solution the solubility of cellulose is decreased which is reputed to be from competitive hydrogen-bonding of these components with the IL rather than to the cellulose (Swatloski[1], et al., 2002). With the addition of water to a cellulose/[C_4mim]Cl solution the cellulose is effectively removed from the IL. The best process for removing the water from the IL for its reuse is still being determined, however evaporation or boiling as used in the NMMO system is probably the most promising. In the lyocell process over 99 percent of the NMMO is recovered (Collier[4], et al., 2000).

As mentioned above, liquid-liquid phase separation using water is a clean, energy efficient way to recover a solute, in this case cellulose. Other potential clean solute recovery methods include supercritical carbon dioxide extraction, crown ether extraction and pervaporation and a membrane technique (Schäfer, et al., 2001).

2.4 Polymer Rheology

Polymer liquids, e.g. cellulose/[C_4mim]Cl solution, are complex materials that do not behave rheologically in simple mathematical terms and thus can be defined as non-Newtonian fluids. When in a molten or solution state, polymers that have long chains, tend to become coiled due to entropic consideration and if in a non-dilute solution or melt, they entangle with other neighboring chains. Therefore, knowledge of the deformation and the flow, or rheology of the polymer is more complicated, but necessary in order to spin fibers that have high degrees of orientation and crystallinity. Understanding the effects of elongation, solution viscosity, orientation, shear, strain, strain rate, and relaxation time are crucial in the production of fibers with high crystallinity and orientation.

2.5 Elongational Spinning and the Hyperbolic Die

The hyperbolic die used in this research induces elongational flow in polymer melts and non-dilute solutions including cellulose/[C_4mim]Cl solutions. The die shape

can be defined by Equation (2.1) and since B is very small approximately by Equation (2.2).

$$R^2(z+B)=C \qquad (2.1)$$

$$R^2z=C \qquad (2.2)$$

Where R is the radius at a centerline distance of z from the die entrance and C is a constant that is characteristic of the particular stream surface, for the die shape that is the die wall. At a constant volumetric flow rate, the hyperbolic shape results in a constant elongational strain rate under appropriate processing conditions (Collier[3], 2005). Figure 2.6 illustrates the flow streamlines as the stream function Ψ, and the potential function Φ. Ψ and Φ are orthogonal and in shear free flow Φ is proportional to the isobaric pressure. The stream function and the potential function can be defined by Equations (2.3) and (2.4). Where $\dot{\varepsilon}$ is the elongational strain rate (Collier[3], 2005).

$$\Psi = -\frac{\dot{\varepsilon}}{2} r^2 z \qquad (2.3)$$

$$\Phi = \frac{\dot{\varepsilon}}{2}\left(\frac{r^2}{2} - z^2\right) \qquad (2.4)$$

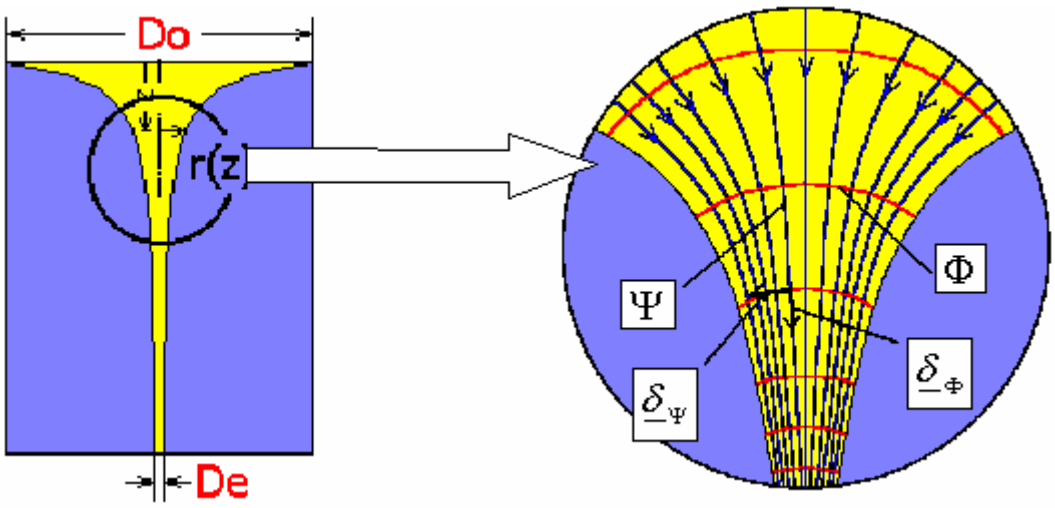

Figure 2.6: The stream function and the potential function in a hyperbolically convergent die (Collier[3], 2005).

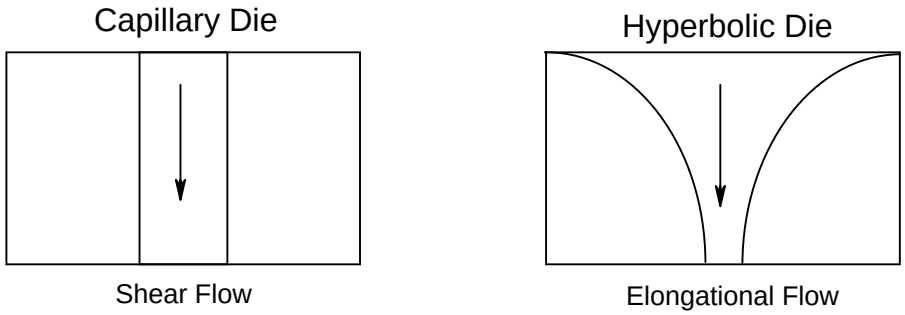

Figure 2.7: Die schematics.

The use of a hyperbolic die enables orientation of the macromolecules, i.e. cellulose, to begin at the entrance of the die and continue to develop as the cellulose solution travels through the die. In a constant diameter capillary die, Figure 2.7a, the orientation that develops within the die is limited by the vorticity induced by the radial gradient of the velocity. In a hyperbolic die, Figure 2.7b, under proper processing conditions, slip is induced at the wall resulting in shear free flow that due to the die geometry results in a linearly accelerating plug flow. As a result, significant orientation is induced without vortices and the only velocity gradient is the streamline direction (Collier[1], et al., 1998). The proper processing conditions result when the orientation number, N_{OR}, is greater than one (Collier[2], et al., 2007).

The orientation number is defined in a later section. As the slip condition is approached from the no slip condition, the flow behavior is essentially the same as in shear free flow except for a decreasing small region near the wall.

2.6 Elongational Viscosity

Elongational viscosity, η_e, determined in a hyperbolic die can be defined by Equation (2.5) below:

$$\eta_e = \frac{\Delta P}{\dot{\varepsilon}\varepsilon_H} \tag{2.5}$$

Where ΔP is the imposed pressure drop from the die entry to the exit, ε_H is the Hencky strain and $\dot{\varepsilon}$ is the elongational strain rate (Collier[1,2] et al., 1998, 2007). Furthermore the elongational strain rate can be defined below as Equation (2.6):

$$\dot{\varepsilon} = (\nu_0 / L)(\exp \varepsilon_H - 1) \tag{2.6}$$

Where L is the centerline length of the die, and ν_o is the initial velocity. The Hencky strain, which will be discussed further in the next section, can be defined below as Equation (2.7):

$$\varepsilon_H = \ln\left(\frac{R_0^2}{R_e^2}\right) \tag{2.7}$$

Where R_o is the entrance radius and R_e is the exit radius of the hyperbolic die (Collier[2], et al., 2007).

The understanding of how elongational viscosity affects the spinning process of cellulose from [C_4mim]Cl is a key step to achieving the goal of this research. Some basic studies involving elongational viscosity suggests that at a steady flow rate of the polymer solution, the elongational viscosity decreases with an increase in the elongational strain rate, whereas the elongational viscosity at a constant strain rate increases with Hencky strain (Collier[3], et al., 2005). Therefore the solution is similar to most polymer melts in that it is strain rate thinning and strain hardening.

2.7 Hencky Strain

The Hencky strain was introduced in Equation (2.7) in the previous section for the hyperbolic geometry. In general the Hencky strain is the natural logarithm of the ratio of an initial length to final length of an element and for a constant volume process this is equivalent to the natural logarithm of the area reduction. As the Hencky strain increases, meaning as the ratio of the entrance radius to the exit ratio increases, the cellulose molecules of the solution will become increasingly oriented. The Hencky strain is one of

the key parameters that affect the orientation of the cellulose fibers. In many characterization devices, (e.g. Meissner type), and orientation processes, (e.g. fiber spinning and fiber drawing), the Hencky strain increases with the process time. In the hyperbolic geometry, the Hencky strain is set by the degree of convergence and the length of the die, therefore, as the degree of convergence and/or length increase, the ε_H increases. In hyperbolic dies the samples are being pushed and compressed against the die wall causing any discontinuities or instabilities in the solution to be compressed. Thus, the hyperbolic die provides more stability to the system than a capillary die and produces fewer and smaller defects compared to free surface elongational deformation processes (Collier[2], et al., 2007).

2.8 Relaxation

Relaxation time is a time constant that is defined as the amount of time needed for polymers with an imposed orientation to return to 0.368 (i.e. 1/e) of its previous state since relaxation is an exponential decay of the orientation. The process time is defined as the amount of time the solution remains in the processing space. Furthermore, the process time, $t_{process}$ in the hyperbolic geometry is defined as Equation (2.8) below (Feigl, et al., 2003):

$$t_{process} = \varepsilon_H / \dot{\varepsilon}\,, \tag{2.8}$$

Shifting of the elongational viscosity curves with temperature indicates that the relaxation time for elongational processes is determined by the same time constant as for shearing processes (Collier[6,7], 2003). The average relaxation time, λ, is defined from dynamic shear rheology in the linear viscoelastic region (Bird, et al., 2001 and Collier[3], et al., 2005). When the system is constrained to the linear viscoelastic region the Maxwell constitutive equation is valid, therefore when the storage modulus equals the loss modulus, the product of the relaxation time and the strain rate is equal to one.

As a result, the relaxation time is given by Equation (2.9) below:

$$\lambda = 1 \Big/ \omega_{crossover} \tag{2.9}$$

Where ω is the angular velocity and using the Cox-Mertz approximation, it is assumed equal to the strain rate in a shearing environment (Collier[3], 2005). In order to lock-in imposed orientation of the polymer molecules, a melt or solution has to go through a phase transition prior to complete relaxation. For melts this is either crystallization or vitrification, for solutions this is preceded or accompanied by phase separation. Relaxation of the molecules oriented in a hyperbolic die can occur in the air gap, i.e. the distance from the die exit to the coagulation bath. Therefore, a smaller air gap and/or faster line speed will reduce the process time for relaxation thus increasing the retained orientation of the fiber. Relaxation can also occur if the phase separation and solidification in the coagulation bath is slow. Applied line tension will impede relaxation in the air gap and coagulation bath.

2.9 Orientation and Orientation Number

If slip at the wall can be induced or nearly induced in a hyperbolic die the orientation of the cellulose molecules will be nearly uniformly increased as they travel through the die. If no slip occurs at the wall, the cellulose molecules that are nearer to the wall will be moving slower than those further toward the centerline. This creates a tumbling effect, i.e. vortices, that reduce the imposed orientation of the molecules. An orientation number has been proposed that represents the amount of orientation occurring in a solution or melt as well as whether or not slip occurs at the die wall (Collier[2], et al., 2007).

The orientation number is a function of the average relaxation time, the elongation strain rate and the Hencky strain and can be defined as Equation (2.10) below:

$$N_{OR} = \lambda \dot{\varepsilon} \varepsilon_H \tag{2.10}$$

Where N_{OR} is the orientation number, and as before, λ is a characteristic relaxation time, ε_H is the Hencky strain and $\dot{\varepsilon}$ is the elongational strain rate. Because of the proportional relations between these parameters, it is expected that imposed orientation should increase as any one of the terms in the product increase as the others are held constant (Collier[2], et al., 2007).

Several studies have recently determined that the elongational rheology was dependent upon both the elongational strain rate and time (Ferguson[1], et al., 1997 and Ferguson[2], et al., 1998). In many instances, the Hencky strain increases with process time. The product $\lambda\varepsilon_H\dot{\varepsilon}$, i.e. the orientation number, is likely to be more broadly applicable than just in hyperbolic die applications. A melt or solution that has a constant elongational strain rate in an isothermal shear free system indicates a hyperbolic shape due to the geometric constrains imposed by a constant elongational strain rate. The nearly constant elongational strain rate is a characteristic of the hyperbolic geometry. Furthermore, the hyperbolic shape represents a minimum in the viscous dissipation term, $\tau:\nabla\mathbf{v}$ and many systems would tend toward this minimum (Collier[2], et al., 2007).

Equation (2.10) indicates the mechanism for the development of orientation is proportional to $\dot{\varepsilon}\varepsilon_H$, divided by the mechanism for relaxation, $1/\lambda$ (Collier[2], et al., 2007). An orientation value of approximately one is an indication that the effects controlling the flow of the system balance. However, an orientation value less than about one suggests the flow is relaxation dominated and for values greater than about one, the flow is orientation dominated with a transition region between. In the hyperbolic die, an orientation number greater than one suggests that slip at the wall is occurring (Collier[2], et al., 2007). The level and distribution of orientation in a fiber should also be dependent upon the orientation number since as the orientation number increases the effect of relaxation will decrease in significance in relation to the simultaneously imposed orientation. As the orientation number approaches one from a lower value, the orientation effect is still strong and significant orientation should still be developing in the majority of the fluid (Collier[2], et al., 2007). The major resistance to flow through the hyperbolic die is due to the body forces of the polymer molecules resisting orientation. A momentum balance suggests that this orientation related body force is orders of magnitude larger

than the forces related to either velocity gradients, shear at the wall, or gravitational effects (Collier[2,3], et al., 2007, 2005).

2.10 Solution Spinning

Polymers that form thermally unstable melts but can be dissolved in low-molecular liquids at high enough concentrations can be used in solution spinning processes. In wet-spinning the polymer is extruded into a liquid non-solvent coagulation bath where it is precipitated from the solvent. The typical range of parameters for wet-spinning consists of polymer solution concentrations of 5% to 30%, extrusion viscosities between 2 to 500 Pa•s, coagulation bath temperatures between 0 to 150^{o}C and take-up velocities between 50 to 100 m/min (Ziabicki, 1976). Polymers that are soluble in volatile solvents can be dry-spun. This means that as the solution is extruded and when, it comes into contact with a stream of hot air or gas, the solvent leaving the polymer fiber vaporizes (Ziabicki, 1976). In dry-jet wet spinning the fibers are first passed thought air or gas and then into a coagulation bath, with concentration, viscosities and take-up velocity controlled by the bath. Because of the characteristics of cellulose and [C_4mim]Cl, a process with an air gap similar to dry-jet wet spinning may be the most appropriate method to use for the purpose of producing fibers even though the solvent is non-volatile. In the air gap the solution can be further attenuated and cooled.

2.11 Carbon Fiber and Precursor Morphology

Although carbon fibers have been in use commercially and industrially for over 40 years, they have been receiving recent attention due to the unique properties in the application of composite materials to additional applications. Composites made from carbon fiber are stronger and lighter than metals such as some grades of steel and aluminum. "Carbon fiber composites have fatigue properties superior to all known metals, and, when coupled with the proper resins, carbon fiber composites are one of the most corrosion resistant materials available" (Walsh, 2001).

Under heated conditions carbon fibers do not melt or soften, thus allowing them to be used in such applications such as rocket nozzles and aircraft brakes where high temperatures are an issue (Walsh, 2001). At room temperatures, carbon fibers do not suffer from stress corrosion or stress rupture failures which is typical of glass or other organic polymer fibers. These properties make carbon fibers ideal for use when, stiffness, lower weight, and exceptional fatigue characteristics are necessary (Chand, 2000). The compressive strength of the carbon fiber will increase with a decrease in orientation, crystallite size, density, and with inter-planar spacing of the precursor fibers used in the processing (Chand, 2000).

The type of precursor used in the production of carbon fibers greatly affects the properties of the carbon fibers. Development of new precursors will lead to the production of carbon fibers with unique properties and potentially lower cost which could lead to new applications for these fibers. It is proposed that for development of successful carbon fiber precursors several things should be considered (Chand, 2000). First, the precursor molecules should have high carbon content, a high molecular weight, be resistant to high temperatures and have high degree of order and orientation. Second, the presence of an aromatic heterocyclic ring in the precursor molecule, where there is only one carbon atom between aromatic rings, is preferred. Finally, the non-carbon atoms such as nitrogen and oxygen should be a part of side groups rather than of main chain for easy release and cyclization (Chand, 2000). Based on these criteria, cellulose would not be considered a prime candidate precursor due to the oxygen atom within the main chain of the molecule. However, due to the recent development of new catalysts, cellulose has enhanced potential as a carbon fiber precursor.

Typically the precursors used in the production of carbon fibers are polyacrylonitrile, pitch, and rayon, phenol, lignin, imides, amides, vinyl polymers, and various naturally occurring cellulosic materials. Polyacrylonitrile, pitch, and rayon are the most commonly used of these precursors (Walsh, 2001). Many other precursors have been tested in the production of carbon fibers. Historically, cellulosic precursor fibers such as cotton, linen, ramie, sisal, hemp, and flax were in use but are now considered of little importance due to the availability of other precursors with better structural and

mechanical properties. However, some current research into the production of carbon fibers using cellulosic fibers indicates that cellulose precursors can possibly enhance the carbon fiber yield by modifying the degradation mechanism (Chand, 2000).

Chapter 3 – Methods

3.1 Theoretical Basis

Several parameters that are fundamental to the spinning process need to be investigated in order to achieve a better understanding of the orientation and crystallinity properties of the manufactured cellulose fibers. These significant parameters include the concentration of cellulose in the ionic liquid, the length of the air gap, the type of die, the elongational strain rate, the drawing and take-up velocity, the composition of the coagulation bath and the temperature at which the solution is spun. Of these parameters, the type of die, drawing ratio, the air gap, solution temperature and the solution concentration are expected to have the greatest impact on the orientation and crystallinity of the resultant fibers. Although the air gap length and the composition of the coagulation bath would have a noticeable effect on the fiber properties, maintaining an adequate level of control of these parameters were too difficult within the confines of the experimental set-up. As the solution travels through the die, the air gap and the coagulation bath, each parameter has a direct effect on the solution by affecting the orientation and relaxation of the molecules thus causing the solution to change significantly. The control of temperature, elongational strain rate, the take-up velocity as well as the cellulose concentration is essential in the production of fibers with high orientation and crystallinity. The interactions between these parameters define the mechanical properties of the fibers. The properties of carbon fibers prepared from cellulose fibers have also been related to the orientation and crystallinity of the original cellulose fibers (Peng, et al., 2003).

From the known properties of cellulose and $[C_4mim]Cl$, as well as the knowledge of how the parameters affect other polymer solutions, the following results can be anticipated. A higher Hencky strain with other parameters constant should result in regenerated cellulose fibers that have higher orientation and mechanical properties. The higher concentration of the cellulose solutions should increase the level of crystallinity in the spun fibers because more molecules will be present within the extrudate as the fiber is forming. A smaller air gap distance at the same line speed will decrease the time for

relaxation of the solution before the orientation is set in the coagulation bath. This lower time for relaxation will enable the cellulose molecules to retain more of their orientation. Applied tension to the fiber line should increase the attenuation and resultant orientation and also inhibit relaxation, thus allowing the molecules of the fiber to retain more orientation. With an increase in the air gap drawing velocity, a higher degree of orientation can be predicted due to the greater amount of tension on the fiber and shorter process time. Also a small amount of solvent in the coagulation bath should increase the crystallinity of the spun fiber during the wet spinning process (Ziabicki, 1976). Therefore, if a small amount of [C_4mim]Cl is present in the coagulation bath, a higher level of crystallinity in the cellulose fiber is predicted based upon the results of spinning lyocell fibers. An increase in the elongational strain rate in the die and/or in the air gap should increase the orientation of the molecules. If the solution moves through the die at a slower strain rate, it has more time to relax within the die. This is consistent with the lower orientation number. Therefore, the level of orientation is reduced. The last parameter, the temperature of the solution will have an effect on the elongational viscosity. An increase in the temperature should decrease both the elongational viscosity and the relaxation time constant. That latter also decreases the orientation number.

3.2 Mixing of the Ionic Liquid Solutions

For each spinning session, approximately 70 grams of the [C_4mim]Cl/cellulose solution was mixed, which was used for the viscosity measurements and the spinning process. The dissolving pulp was finely ground to remove any clumps that would not dissolve uniformly. For Step One, the continuous fiber spinning, three dissolving pulps; 670, 1720 and 3900 degree of polymerization (DP), were tested at various concentrations in order to determine the solution that would result in the best viscosity for the spinning process. The degree of polymerization is the number of glucose units in the cellulose molecule and that number times 162 equals the molecular weight. The dissolving pulp was then dried in an oven at 90^{o}C for approximately one hour to remove any excess water that the dissolving pulp might have accumulated during the storage process. The [C_4mim]Cl was stored in a desiccator to prevent accumulation of water.

The dissolving pulp was then weighed for the desired percent cellulose concentration in the [C_4mim]Cl/cellulose solution. To prevent thermal degradation during the mixing and spinning process, propyl gallate was added (Rosenau, et al., 2004). The propyl gallate was weighed to be approximately 1% of the weight of the dissolving pulp used in the solution.

The [C_4mim]Cl/cellulose solution was mechanically mixed using a Brabender Half-Size mixer at approximately 90^{o}C until the solution was visually clear. The amount of time that the [C_4mim]Cl/cellulose solution remained in the mixer depended on the concentration of the solution being mixed as well as the dissolving pulp. A solution with a smaller amount of dissolving pulp that had a higher molecular weight required less mixing time compared to a solution with a higher amount of dissolving pulp that had a lower molecular weight. Thus the mixing time ranged from approximately 30 minutes, for low concentrations as well as high dissolving pulps, to 2 hours, for high concentrations and lower dissolving pulps. In order to aid in the mixing of a homogenous solution, a small amount of the [C_4mim]Cl was added to the Brabender followed by a small amount of the dissolving pulp. This prevented any [C_4mim]Cl from leaking from the bottom of the Brabender where the two halves of the mixer are connected. The remaining [C_4mim]Cl was added while the rollers were rotating at 50 RPM. The [C_4mim]Cl was melted before the remaining dissolving pulp was added to the mixer in small amounts at a time to prevent any compaction of the dissolving pulp. If the dissolving pulp was too compact it would not thoroughly dissolve in the solution leaving small clumps of the dissolving pulp remaining in the solution.

The solution was considered thoroughly mixed when a clear appearance and the desired viscoelastic characteristics were observed, indicating that the cellulose had dissolved in the [C_4mim]Cl. The viscoelastic characteristic was visually observed by stringiness when a small amount was withdrawn on a spatula. The level of viscoelasticity also depended on the percent of cellulose in the solution. During the mixing process a large amount of air was mixed into the solution. These air bubbles affected the spinning process by causing breaks in the spinning line. To prevent this, when the solution was removed from the Brabender and placed in a glass jar, the jar was then placed in a small

desiccator which was attached to a vacuum pump. While the solution was still hot, the air bubbles were removed. The removal of the air bubbles was determined to be a vital step during spinning experiments of Step One.

3.3 Complex Viscosity Measurements

The complex viscosity for each solution was tested using the Rheometric Scientific ARES rheometer. Each solution was tested using 25 mm diameter parallel plates, a minimum of two times at temperatures of 80^{o}C, 90^{o}C and 100^{o}C. The dynamic moduli of G' and G" as well as the complex viscosity (η) were measured over a frequency range of 0.1 to 100 s^{-1}. The data were then graphed and two curve fit models, the Carreau and the Cross model, were used to determine the required variables to shift the data to one temperature reference. These models are further described in Chapter four.

3.4 Elongational Viscosity Measurements

The elongational viscosity was tested using the Rheometric Scientific ACER capillary rheometer. Solutions containing 8%, 10% and 12% cellulose were tested at temperatures of 80^{o}C, 90^{o}C and 100^{o}C with three Hencky strain rates of 8.4, 7 and 6. The elongational viscosity was measured for a minimum of five elongational strain rates ranging from 0.5 to 100 s^{-1}. The data were then graphed using the shift variables determined for the complex viscosity using the Carreau model in order to shift the results to one temperature reference.

3.5 Spinning

Spinning was done using the ACER capillary rheometer where the IL/cellulose solution was preheated in order to load into the ACER barrel. This was done to minimize the formation of air bubbles in the solution during the transfer from the jar to the barrel. The barrel and the Hencky 7 die with the additional diameter plate and the screens that

attached to the barrel were preheated to the desired temperature of the run. Due to the viscosity of the solution, when loading, it would remain near the top of the barrel however, over time the solution would travel down the length of the barrel and thermally equilibrate with the set barrel temperature. A schematic of the spinning set-up is illustrated in figure 5.3.

Once the IL/cellulose solution reached thermal equilibrium, the ram was attached and moved to a position in the barrel where it was in contact with the solution. The elongational strain rates were then set from lowest to highest based on the experimental parameters. The solution was then extruded into the coagulation bath and drawn under two submerged stationary spools before being spun onto the collection spool. The spinner was set to the desired experimental parameters and varied throughout the spinning session. The collection spool was then soaked in water for approximately two days before being rinsed and dried.

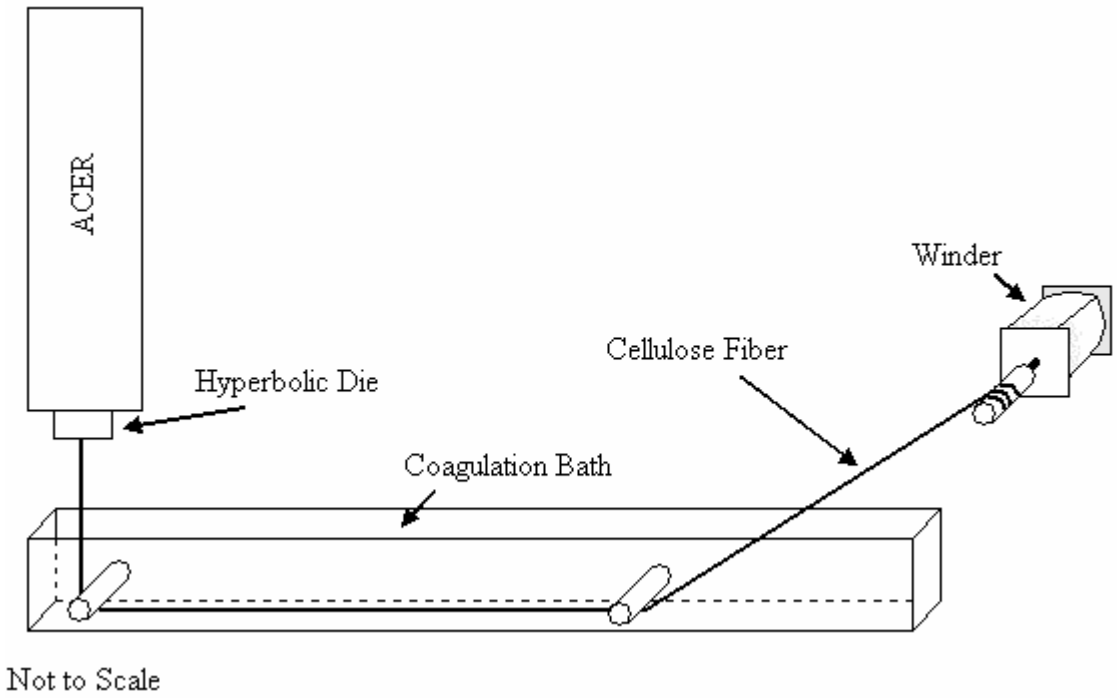

Figure 3.1: Schematic of wet spinning

3.6 SEM Imagery

The first step in using the scanning electron microscope (SEM) for the image analysis is the sample preparation. First, a small portion of fibers was cut and placed onto the stage. The stage was then placed into the SPI – Module Sputter Coater for a gold coating. The gold coating was applied in order to prevent the buildup of a surface charge inside the microscope thus enabling a clearer picture. This process was done for all the runs.

Once prepared, the samples were placed, six at a time into the SEM. The samples were set at a distance of 6 millimeters from the electron source which was set at 3 kilovolts. This enabled a better resolution at lower magnification. A higher voltage would increase the magnification allowing for a clearer picture but over time this would compromise the sample by creating an electrical charge. The goal of the SEM images was to verify the surface morphology of the fibers and to determine the fiber diameter using the measuring analysis software, [1]SCION Image®.

3.7 Crystallinity and Orientation Measurements

The crystallinity measurements were determined using Wide Angle X-Ray Scatter (WAXS) equipment as well as the curve fit software called [2]Pro Fit®. To prepare each sample for testing the fibers were overlapped to form a small rectangular bundle where the layers of the fibers added up to several millimeters in thickness. Each sample bundle was attached to the aluminum stage and the x, y and z coordinates were measured for correct scanning to occur. Overall the fibers in the bundles were somewhat oriented parallel to one another but there was still a level of disorientation due to the spinning process which caused the fibers to be at slight angles to each other which could be described as a cross-hatched pattern. The WAXS was run at 45 kV and 40 mA. The beginning angle was 5^{o} and the stopping angle was 35^{o}. This range was determined from the first run which indicated that the intensity peaks only occurred within this range. All of the WAXS input parameters used for all the runs are listed in Appendix D.

[1]SCION Image is made by Scion Corporation
[2]Pro Fit is made by QuantumSoft

After each scan was completed, the generated intensity peak graph was imported into the curve fit software, Pro Fit®. This software determine the area under the first and second main intensity peaks as well as the amorphous region. The areas were then used to determine a crystallinity index for the sample. The peak fitting was done at least three times to obtain three crystallinity measurements for each sample.

The birefringence was determined by measuring the polarimetry using an optical microscope with crossed polarizing filters. Between the crossed polarizers, the fiber sample appeared bright against the isotropic background. A compensator was then used to determine the angle or rotation for each fiber which was a key variable in the calculation of the birefringence disscused further in Section 4.7.

3.8 Tensile Strength Measurements

The first step of testing the tensile strength of each sample was to determine the denier. Denier is defined as mass in grams per 9,000 meters of fiber. It is a unit of measure for the linear mass density of fibers. The denier was needed for each fiber tested in order to determine the correct tenacity. Ten fibers were selected from throughout each sample. Each fiber was inserted into the Vibromat M in order to determine the denier. A precision weight was attached to the end of each fiber based on the approximate denier. A pulse of vibration was then sent through the fiber and based on the weight attached, the Vibromat determined the denier.

With the weights still attached to the fiber, it was clamped into the Instron 4400R which determined the tenacity by measuring the amount of load needed to break the fiber over a measured distance. The software measured the load versus displacement curves and values of average displacement at the maximum, the average load at the maximum, the average linear density, the average percent strain at the maximum, the average tenacity at the maximum and the average modulus were determined for each run based on all the fibers tested at a 15 millimeter gage length.

3.9 Experimental Design

3.9.1 Step One – Continuous Fiber Spinning

The first step in the experimental process was to find the parameters that would enable the spinning of continuous fibers. As each spinning session progressed, the extruded fibers would continuously break. It was believed that the solutions were not homogenous and therefore breakage would start in the region of the fiber where the cellulose content was lower. Another possible cause for the fiber breakage was the die type used. The Hencky 7 hyperbolic die used in the initial runs had an exit diameter of 0.6 mm which in many spinning applications is considered relatively large. With a larger diameter die opening and a limiting drawing force, the elongational strain rate in the air gap was not as high; thereby reducing the level of orientation in the fibers. The extrusion rate and take-up velocity also had to be lower for a larger diameter die which also reduced the degree of orientation. A lower level of orientation would account for the breaks in the fiber. A third cause could be that the N_{OR} was near one and instabilities occurred at or near the die exit. The N_{OR} was calculated where possible and estimated for other concentrations. Table 3.1 illustrates the estimate of the elongational stain rate and the velocity for a given orientation number and various solution concentrations at different temperatures. As seen in Table 3.1, N_{OR} could be increased by increasing the strain rate or the relaxation time. The relaxation time increases with concentration and decreases with temperature.

Table 3.1: Orientation Number Calculations for Cellulose in Ionic Liquids

					N_{OR} = 1	N_{OR} = 10
Solution Concentration	Temp. (^oC)	$w_{crossover}$ (1/s)	relaxation time (s)	ram velocity (m/s)	Strain rate (1/s)	strain rate (1/s)
12%	90	50.55	0.020	1.65E-04	7.22	72.21
15%	80	5.58	0.179	1.82E-05	0.80	7.97
15%	90	35.28	0.028	1.15E-04	5.04	50.39
15%	100	87.52	0.011	2.85E-04	12.50	125.03
Approximate						
10%	90	~110	0.009	3.58E-04	15.71	157.14

In order to spin a continuous fiber, several parameters were modified for the subsequent test runs. In the first run a 10% solution using dissolving pulp 670 was mechanically mixed in the Brabender. Initially the solution was mixed at 80^{o}C however; the cellulose was clumping and not dissolving. Therefore the mixing temperature was increased to 90^{o}C and mixed until the solution was clear in appearance although several small clumps of cellulose remained in the solution. Fibers were obtained of this solution at 95, 105 and 110 ^{o}C with an elongational strain rate of 1.5 to1.75 s^{-1} however, the fibers were not continuous. During the spinning process the take-up velocity seemed to be too fast for the extruded fibers. Therefore, a new take-up winder was suggested. The new winder with lower speeds was tested on the next spinning session.

The second session again used dissolving pulp 670 for a 10% solution. Fibers were obtained at 80^{o}C and 110^{o}C and an elongational strain rate of 2.0 to 2.5 s^{-1}, and the fibers were not continuous. The spinning began at 110^{o}C and the temperature was decreased with moderate success. Although the new winder was slower, breakage in the fiber was still occurring, most likely due to the impurities in the solution during mixing.

The concentration and the dissolving pulp for the third session remained the same as before except that the system was modified by the addition of a series of screens at the top of the Hencky 7 die in order to remove the impurities from the solution before entering the die. Fibers were obtained at 85, 95, 100 and 115 ^{o}C and an elongational strain rate of 1.5 to 2.0 s^{-1}. However, the fibers were still not continuous but with the addition of the screens the fibers were able to be spun for longer times. The use of a dissolving pulp with a high molecular weight was suggested for the next session.

For the fourth session a 3% solution of dissolving pulp 3900 was mixed. Using the new winder and the screens, better spinnability was achieved. However, the 3% solution appeared to have experienced thermal degradation and the resulting fibers were not smooth in appearance like the fibers spun for the dissolving pulp 670 solutions'. Again, a new dissolving pulp at a higher concentration was used for the next session.

Dissolving pulp1720 was used for the fifth session and a 5% solution was mixed. The use of the new dissolving pulp increased the spinnability to a desirable level however, the resulting fibers had a flattened shape. The flatness of the fibers was

believed to be the result of the spinning and or soaking of the fibers after they were extruded. It was believed that when the fibers were soaked on the godet, the IL was dissolved from fibers causing shrinking of the fibers. Also suggested was that the fibers were contracting on the spool due to relaxation thus causing the flattening. Another possibility was that the fibers did not have sufficient time in the water bath before being pulled thus causing the flatness. The next session tested these theories.

The parameters for the sixth session remained the same as the previous session. This session was done to determine the cause of the flat fibers. First, fibers were spun on to the spool and then allowed to soak and dry on the spool. Second, fibers were spun and then allowed to soak on the spool but were removed from the spool for drying. Third, fibers were spun but removed from the spool for soaking and drying. The fibers all remained flat. This suggested that the fibers were not in the coagulation bath long enough before being drawn. The set-up of the coagulation bath did not make it possible for the extruded fiber to have an increased time in the water before being drawn. Therefore, a slower elongational strain rate and take-up velocity were suggested. To achieve this, a smaller exit diameter was needed. The Hencky 7 die was modified with the addition of a linear converging machined plate 3 mm thick. The entrance diameter of the plate matched the exit diameter of the die and reduced linearly to the exit diameter of 0.3 mm, thus reducing the exit diameter by half. With the addition of the new plate, the Hencky strain rate was increased from 7 to 8.4.

The final session tested the new Hencky strain rate on a 10% solution mixed with dissolving pulp 670. Although the previous dissolving pulp of 1720 increased the spinnability of the fibers, the visual appearance was not smooth. The initial sessions had smooth fibers with dissolving pulp 670 but not continuous spinning. Therefore, with the addition of the screens, the new winder, and the smaller diameter, it was believed that the original dissolving pulp would enable continuous spinning.

The conclusion of Step One determined that continuous spinning can be achieved with 10% dissolving pulp 670 using the new winder, the filtering screens, a Hencky strain rate of 8.4, the temperature at 100^{o}C and the elongational strain rate of 1.5 s^{-1}. These

values were then used as the default parameters for the experiments of Step Two described in more detail in the following sections.

3.9.2 Step Two – Modifications of the Parameters

3.9.2.1 Experimental Design for Experiment 1

To test the effect of the parameter modifications on the fibers, two sets of experiments were run. In the first experiment, the concentration of the cellulose in the solution was kept constant at 10% and the temperature, elongational strain rate and the take-up velocity were varied. In the second experiment, the temperature was kept constant at 100^{o}C and the cellulose concentration, the elongational strain rate and the take-up velocity were varied. Therefore, Experiment 1 is a temperature variation with a constant concentration and Experiment 2 is a concentration variation with a constant temperature.

The runs were set up based on the following process (Cochran, et al., 1957). For the first experiment, with the concentration of the solution remaining constant, three parameters were chosen to be tested and each with a range of five values. To code the runs, each parameter was labeled as X_1 through X_4 and each value for the parameters was assigned a number of -1.682, -1, 0, 1, or 1.682. The 1.682 value was based on the experimental design for using a central composite design for a second-order fit of the data and requiring rotatability which is required in order to predict the same variance at difference measurement points. An experiment with three independent variables is essentially like having a cube with corners with xyz coordinates of 1,1,1; -1,1,1; -1,-1,1 etc. In a second-order model extra points are added on the coordinates that are equidistant from the center as are the corners. Therefore, the additional points are a distance alpha away. The value of alpha depends on the points in the factorial design and if alpha equals the fourth root of the number of points than the design is rotatable. So, for three variables there are 8 points and the fourth root of 8 is 1.682 (Montgomery, 1997). This is illustrated in Table 3.2. The coded value corresponds to the set up of the runs in the matrix in Table 3.3. For example, the -1 appearing in the first row of the table for the X_1 parameter of Run 1 indicates that for Run 1 the X_1 parameter has Value 2.

The process described above was applied to the parameters and values of this research which is illustrated in Tables 3.4 and 3.5. In Table 3.3, the parameters are defined as follows: X_1 is the elongational strain rate ($\dot{\varepsilon}$); X_2 is the take up velocity (v) and X_3 is the solution temperature (T). Therefore by using the matrix from Table 3.3 the parameter values for each run have been determined as shown in Table 3.5. Since runs 16 through 20 are repeats of run 15 they are excluded in the testing and are used to determine the variance.

Table 3.2: Code Assignment for Experiment 1

Parameter	Coded Value				
	-1.682	-1	0	1	1.682
X_1	Value 1	Value 2	Value 3	Value 4	Value 5
X_2	Value 1	Value 2	Value 3	Value 4	Value 5
X_3	Value 1	Value 2	Value 3	Value 4	Value 5

Table 3.3: Matrix for Experiment 1

Run #	Parameters			Run #	Parameters		
	X_1	X_2	X_3		X_1	X_2	X_3
1	-1	-1	-1	11	0	-1.682	0
2	1	-1	-1	12	0	1.682	0
3	-1	1	-1	13	0	0	-1.682
4	1	1	-1	14	0	0	1.682
5	-1	-1	1	15	0	0	0
6	1	-1	1	16	0	0	0
7	-1	1	1	17	0	0	0
8	1	1	1	18	0	0	0
9	-1.682	0	0	19	0	0	0
10	1.682	0	0	20	0	0	0

Table 3.4: Coded Variable Definition for Experiment 1

Parameter	Coded Value				
	-1.682	-1	0	1	1.682
X_1	$\dot{\varepsilon}_1$	$\dot{\varepsilon}_2$	$\dot{\varepsilon}_3$	$\dot{\varepsilon}_4$	$\dot{\varepsilon}_5$
X_2	v_1	v_2	v_3	v_4	v_5
X_3	T_1	T_2	T_3	T_4	T_5

Table 3.5: Parameter Values for the Experiment 1

Run #	Parameters			Run #	Parameters		
	X_1	X_2	X_3		X_1	X_2	X_3
1	$\dot{\varepsilon}_2$	v_2	T_2	11	$\dot{\varepsilon}_3$	v_1	T_3
2	$\dot{\varepsilon}_4$	v_2	T_2	12	$\dot{\varepsilon}_3$	v_5	T_3
3	$\dot{\varepsilon}_2$	v_4	T_2	13	$\dot{\varepsilon}_3$	v_3	T_1
4	$\dot{\varepsilon}_4$	v_4	T_2	14	$\dot{\varepsilon}_3$	v_3	T_5
5	$\dot{\varepsilon}_2$	v_2	T_4	15	$\dot{\varepsilon}_3$	v_3	T_3
6	$\dot{\varepsilon}_4$	v_2	T_4				
7	$\dot{\varepsilon}_2$	v_4	T_4				
8	$\dot{\varepsilon}_4$	v_4	T_4				
9	$\dot{\varepsilon}_1$	v_3	T_3				
10	$\dot{\varepsilon}_5$	v_3	T_3				

3.9.2.2 Experimental Design for Experiment 2

For the second experiment, with temperature remaining constant, two parameters were chosen to be tested and each will have a range of five values. To code the runs, each parameter was labeled as X_1 and X_2 and each value for the parameters was assigned a number of -1.414, -1, 0, 1, or 1.414. This range of numbers was based on the experimental design for two independent variables. Like the experimental design for three variables instead of having a cube, two variables would have a square with the corners at xy coordinates of 1,1; -1,1 etc. for four points each equidistant from the center. Therefore, for two variables, 4 points are used and the fourth root of 4 is 1.414.

(Montgomery, 1997). This is illustrated in Table 3.6. The coded value then corresponds to the set up of the runs in the matrix in Table 3.7.

The process described above was applied to the parameters and values of this research which is illustrated in Tables 3.8 and 3.9. In Table 3.8, the parameters are defined as follows: X_1 is the elongational strain rate ($\dot{\varepsilon}$) and X_2 is the take up velocity (v). Therefore by using the matrix from Table 3.7 the parameter values for each run were determined as shown in Table 3.9. This design was applied to an 8% and a 12% cellulose/IL solution.

Table 3.6: Code Assignment for Experiment 2

Parameter	Coded Value				
	-1.414	-1	0	1	1.414
X_1	Value 1	Value 2	Value 3	Value 4	Value 5
X_2	Value 1	Value 2	Value 3	Value 4	Value 5

Table 3.7: Matrix for Experiment 2

Run #	Parameters		Run #	Parameters	
	X_1	X_2		X_1	X_2
1	-1	-1	6	1.414	0
2	1	-1	7	0	-1.414
3	-1	1	8	0	1.414
4	1	1	9	0	0
5	-1.414	0			

Table 3.8: Coded Variable Definition for Experiment 2

Parameter	Coded Value				
	-1.414	-1	0	1	1.414
X_1	$\dot{\varepsilon}_1$	$\dot{\varepsilon}_2$	$\dot{\varepsilon}_3$	$\dot{\varepsilon}_4$	$\dot{\varepsilon}_5$
X_2	v_1	v_2	v_3	v_4	v_5

3.9.2.3 Parameter Values

The values used for each parameter range were determined based on the results and analysis obtained from Step One. Table 3.10 lists the values used for each run. With the parameter values established and using Tables 3.5 and 3.9, all the experimental runs were defined and listed in Table 3.11.

This set of runs will be known as the *Step Two Runs* which were analyzed by determining the morphology at the micro and nano levels; and calculating the tenacity and crystallinity of the fibers by the techniques illustrated in the previous sections

Table 3.9: Parameter Values for the Experiment 2

Run #	Parameters		Run #	Parameters	
	X_1	X_2		X_1	X_2
1	$\dot{\varepsilon}_2$	v_2	6	$\dot{\varepsilon}_5$	v_3
2	$\dot{\varepsilon}_4$	v_2	7	$\dot{\varepsilon}_3$	v_1
3	$\dot{\varepsilon}_2$	v_4	8	$\dot{\varepsilon}_3$	v_5
4	$\dot{\varepsilon}_4$	v_4	9	$\dot{\varepsilon}_3$	v_3
5	$\dot{\varepsilon}_1$	v_3			

Table 3.10: Parameter Values for Step Two Runs

Parameter	Parameter Values for Experiment 1 Coded Values				
	-1.682	-1	0	1	1.682
$\dot{\varepsilon}$	1.0795	1.25	1.5	1.75	1.9205
v	26.59	30	35	40	43.41
T	90	94.0547	100	105.945	110
Parameter	Parameter Values for Experiment 2 Coded Values				
	-1.414	-1	0	1	1.414
$\dot{\varepsilon}$	1.1465	1.25	1.5	1.75	1.8535
v	27.93	30	35	40	42.07

Table 3.11: Definition of all Experimental Runs

Session #	Run #	Conc.	Temp (^oC)	Elong. Strain Rate (s^{-1})	Velocity (% of total RPM)	Velocity (m/min)
1	1	10	100	1.08	35	71
1	2	10	100	1.5	~27	~46
1	3	10	100	1.5	35	71
1	4	10	100	1.5	~43	~98
1	5	10	100	1.92	35	71
2	6	10	94.1	1.25	30	56
2	7	10	94.1	1.25	40	88
2	8	10	94.1	1.75	30	56
2	9	10	94.1	1.75	40	88
3	10	10	105.9	1.25	30	56
3	11	10	105.9	1.25	40	88
3	12	10	105.9	1.75	30	56
3	13	10	105.9	1.75	40	88
4	14	10	90	1.5	35	71
5	15	10	110	1.5	35	71
6	16	8	100	1.15	35	71
6	17	8	100	1.25	30	56
6	18	8	100	1.25	40	88
6	19	8	100	1.5	~28	~50
6	20	8	100	1.5	35	71
6	21	8	100	1.5	~42	~95
6	22	8	100	1.75	30	56
6	23	8	100	1.75	40	88
6	24	8	100	1.85	35	71
7	25	12	100	1.15	35	71
7	26	12	100	1.25	30	56
7	27	12	100	1.25	40	88
7	28	12	100	1.5	~28	~50
7	29	12	100	1.5	35	71
7	30	12	100	1.5	~42	~95
7	31	12	100	1.75	30	56
7	32	12	100	1.75	40	88
7	33	12	100	1.85	35	71

Chapter 4 – Results

4.1 Complex Viscosity

Before the spinning of the solutions took place, the complex viscosity and the dynamic moduli were measured and graphed for 8%, 10% and 12% solutions. From the generated graphs, temperature shifting was completed using two curve fit models. The first curve fit model used was the Carreau model which is represented below as equation 4.1 (Macosko, 1994).

$$\eta = \eta_o \left(1 + (\lambda\omega)^2\right)^{\frac{n-1}{2}} \tag{4.1}$$

Where, η is the complex viscosity as a function of the frequency (ω), η_o is the zero shear viscosity, λ is the relaxation time and n is a rate constant. The second curve fit model used was the Cross model which is represented below as equation 4.2 (Macosko, 1994).

$$\eta = \eta_o \Big/ \left(1 + (\lambda\omega)^{1-n}\right) \tag{4.2}$$

From these parameters, the temperature shift value (a_T) can be calculated from the following equation 3.4 (Collier[6] et al., 2003 and Bird et al., 2001).

$$a_T = \frac{T\eta_o(T_o)}{T_o\eta_o(T)} \tag{4.3}$$

Where T is the temperature of the data being shifted, T_o is the temperature to which the data is being shifted. The shift value is then applied to the data to obtain the reduced complex viscosity curve as well and the reduced dynamic moduli curve. A polynomial fit was then done on the reduced complex viscosity curves from each model to determine which model had the highest R^2 value. The R^2 is a coefficient of determination which by definition is the proportion of variability in a data set that is accounted for by a statistical model (i.e. an R^2 value of 1 indicates that the fitted model explains all variability in y, while R^2 value of 0 indicates no relationship between the graphed variables). A complete table with all the R^2 values for each session is listed in Appendix A.

The ΔH values for all the sessions were also calculated from equation 4.4 below.

$$\Delta H = R\ln(a_T) \Big/ \left(\frac{1}{T} - \frac{1}{T_o}\right) \qquad (4.4)$$

Where R is equal to 1.987 10^{-3} kCal per mole Kevin and the temperature is in Kelvin. Based on these results it was determined that the Cross model had the best results. Therefore the data variables obtained from the model were used for the remainder of the calculations done.

4.1.1 Complex Viscosity of the 8%, 10% and 12% Solutions

The complex viscosity for the solution concentrations at the three temperatures over the frequency is represented as Figure 4.1. The graph illustrates that as the frequency increased the complex viscosity of the cellulose/IL solution decreased. This graph also illustrates that the increase in temperature decreased the complex viscosity. The increase in the concentration of the solution increased the complex viscosity compared to lower concentrations, the higher concentrations of solution also followed the same trend in relation to the temperature as lower concentrations.

Also observed in this graph is a trend indicating a larger difference in the solution at 100^{o}C in comparison to 80^{o}C and 90^{o}C. This indicates that the solutions run at 100^{o}C had a lower viscosity due to possible degradation of the solution. Also observed was a smaller difference in the viscosity in the 12% solution in comparison to the 8% and 10% solutions. This indicates that the 12% solution had a lower viscosity than expected for this concentration. The figure suggests that the 12% solution has had some thermal degradation as well. The graphs for all complex viscosity of Sessions 1 through 7 are shown in Appendix A.

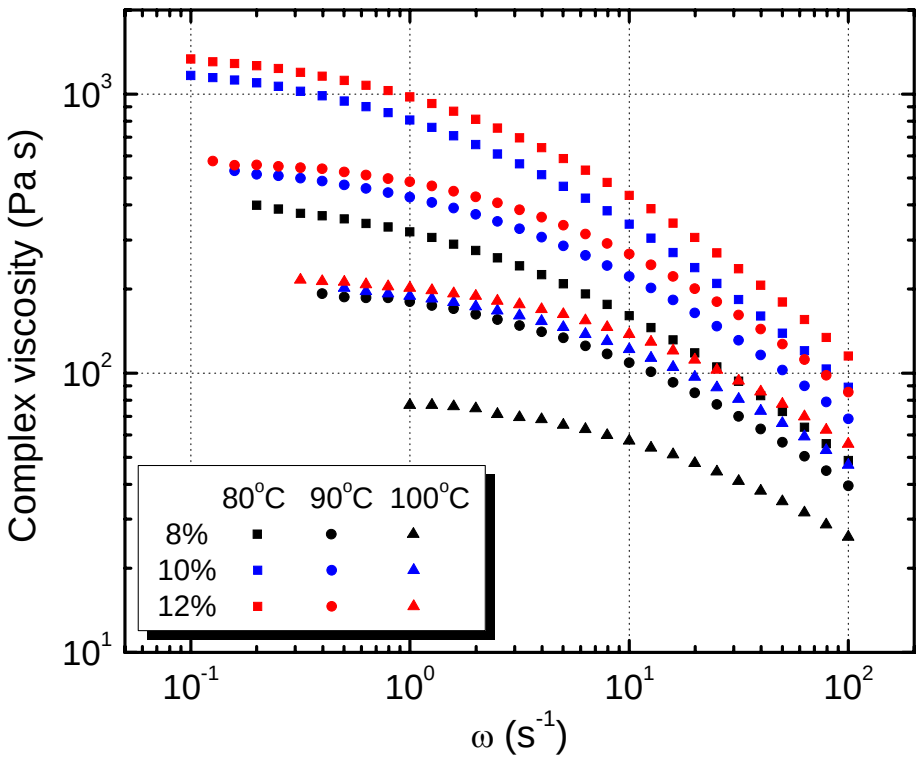

Figure 4.1: Complex viscosity of all solutions at 80°C, 90°C and 100°C.

4.1.2 Temperature Shift

The shift factor (a_T) was used to transpose the 80°C and the 100°C complex viscosity curves onto the 90°C curve for each of the concentrations. The temperature shift was calculated from equation 4.5 shown below.

$$T_o\eta \big/ a_T T = \eta_{a_T} \qquad (4.5)$$

Where T_o is the temperature that the data is being shifted to, T is the temperature of the shifted data, a_T is the shift factor, η is the viscosity of the data being shifted and η_{aT} is the reduced complex viscosity. The frequency was shifted by multiplying the original frequency by the shift factor for each curved that was shifted. Figure 4.2 illustrates the reduced complex viscosity curves for each concentration.

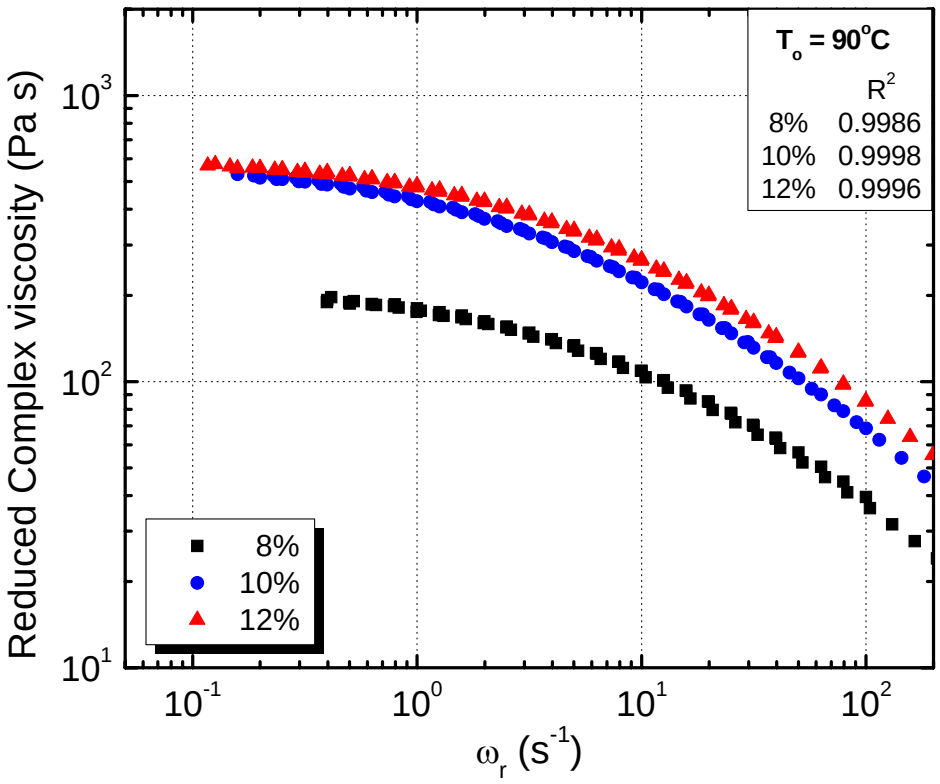

Figure 4.2: Reduced complex viscosity of all solutions at 80°C, 90°C and 100°C.

This figure illustrates that the 80°C and the 100°C curve transposed with a close fit onto the 90°C where the R^2 values for all the sessions for both the Cross and Carreau model ranged from 0.9974 to 0.9998 thus suggesting that temperature shift had a high accuracy. It was observed that the 12 % solution had a reduced complex viscosity that was close, just slightly higher, than the 10% solution. This indicates that the 12% solution, as suggested previously, had a level of thermal degradation thus lowering the viscosity closer to the 10% solution. Another possibility is a difference in the solution characteristics between 8% and the 10% and 12% solutions. There could be liquid crystal formation at some concentrations and not others or a two phase system that causes the 10% and 12% to have similar viscosities at low strain rates. A complete list of the shift factors as well as the R^2 values calculated for the shifted curves is in Appendix A.

The dynamic moduli for each solution were also shifted by shifting the frequency in the same manner as the frequency shift for the complex viscosity. Figure 4.3 illustrates the dynamic moduli for each solution versus the reduced angular velocity.

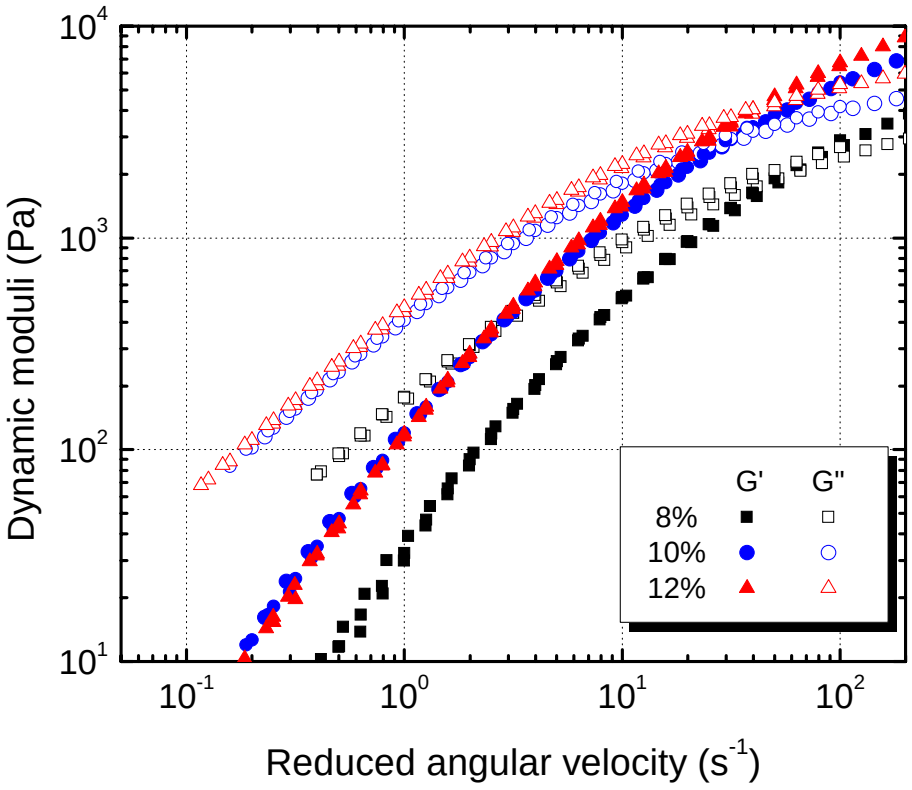

Figure 4.3: Dynamic moduli verses reduced angular velocity of all solutions.

As the angular velocity was increased the dynamic moduli for each solution also increased. Also as the concentration of cellulose in the solution was increased, the G' and G" curves increased; however, the increase in the concentration decreased the crossover point of these two curves. This means that the increase in concentration increased the relaxation time since the relaxation time is the inverse of the crossover point.

4.1.3 Temperature Comparison

Figures 4.4 to 4.9 represent the temperature comparison of the complex viscosity as well as the dynamic moduli for each of the solution concentrations. The trends in all of the graphs show a smaller difference in the 12% solution when compared to the 10% than with the 10% compared to the 8% solutions. This can be seen in both the complex viscosity curves as well as the dynamic moduli curves.

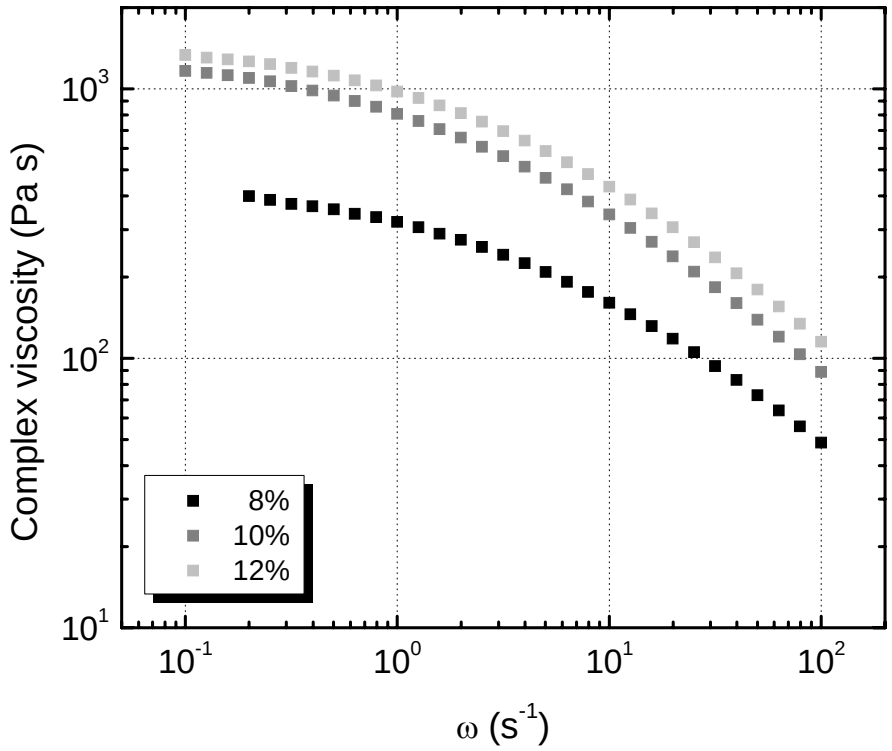

Figure 4.4: Complex viscosity of all solutions at 80°C.

Also observed is a smaller difference in the 12% solution when compared to the other solutions at the higher temperatures than at the lower temperatures. This suggests that the increase in the temperature decreased the complex viscosity for all the solutions but there was a greater decrease in the 12% solution overall, thus supporting what was observed from Figures 4.1 to 4.3. As stated previously, this is an indication that the 12% solution had a higher rate of thermal degradation than the 10% and 8% solutions and that all the solutions had a higher rate of thermal degradation at 100°C.

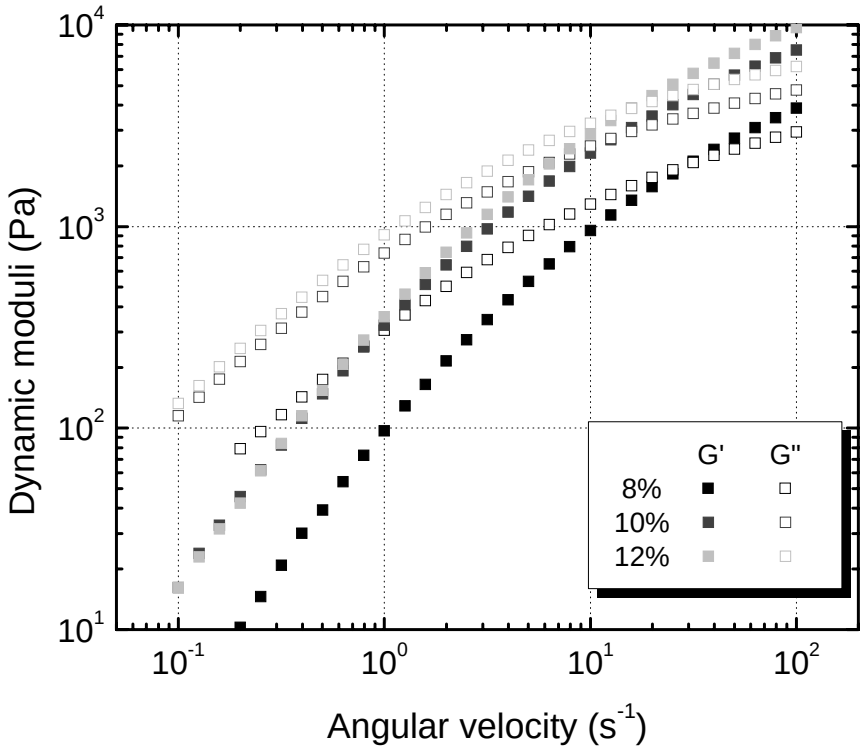

Figure 4.5: **Dynamic moduli of all solutions at 80°C.**

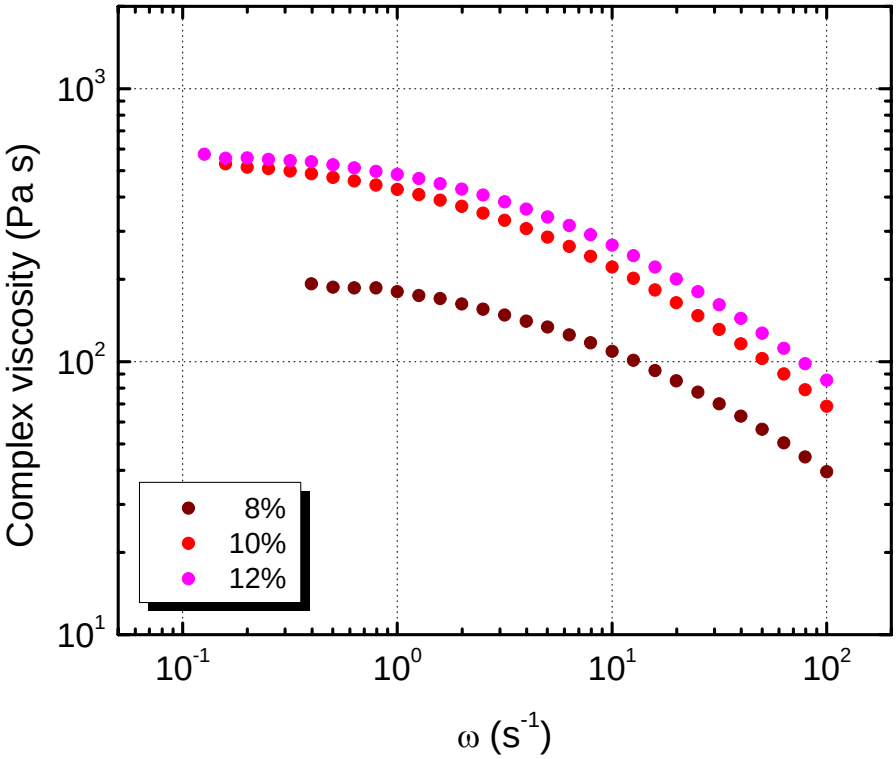

Figure 4.6: **Complex viscosity of all solutions at 90°C.**

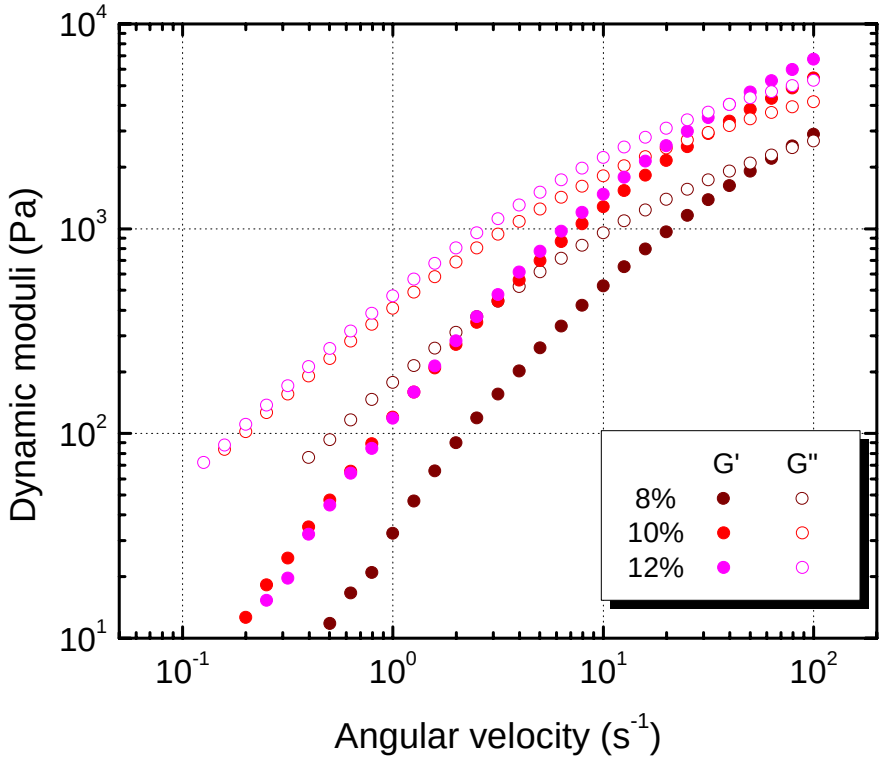

Figure 4.7: **Dynamic moduli of all solutions at 90°C.**

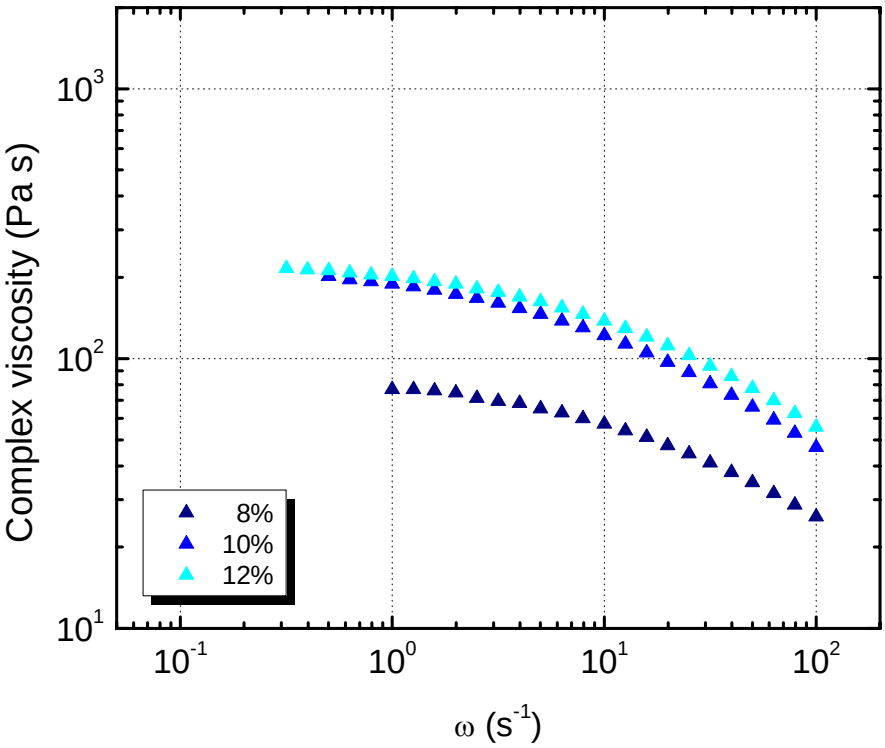

Figure 4.8: **Complex viscosity of all solutions at 100°C.**

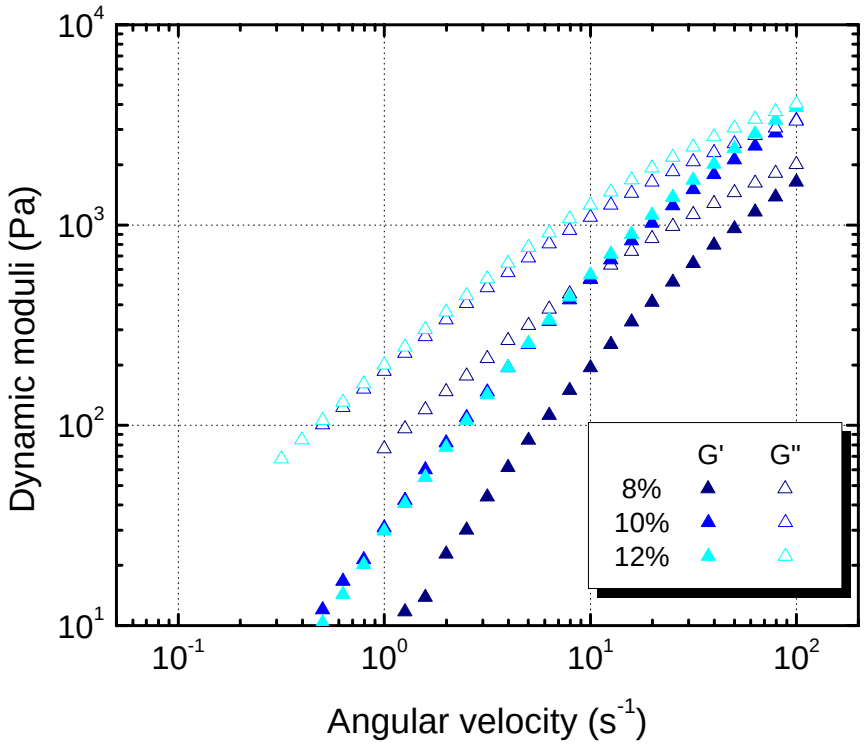

Figure 4.9: Dynamic moduli of all solutions at 100°C.

4.2 Elongational Viscosity

4.2.1 Temperature Shift

The second step in the viscosity study was to measure the elongational viscosity of the 8%, 10% and 12% solutions at 80°C, 90°C, and 100°C for three dies with Hencky strain rates of 6, 7 and 8.4. The runs for each solution using each die were graphed at each temperature and are shown in Appendix B. Using the same temperature shift values (a_T) as calculated from the complex viscosity, the curves were shifted to the reference temperature of 90°C. Figures 4.10 to 4.12 represent the temperature shifted reduced elongational viscosity of each solution for each die. The individual graphs for each solution at each Hencky strain rate illustrating the temperature shift are also in Appendix B.

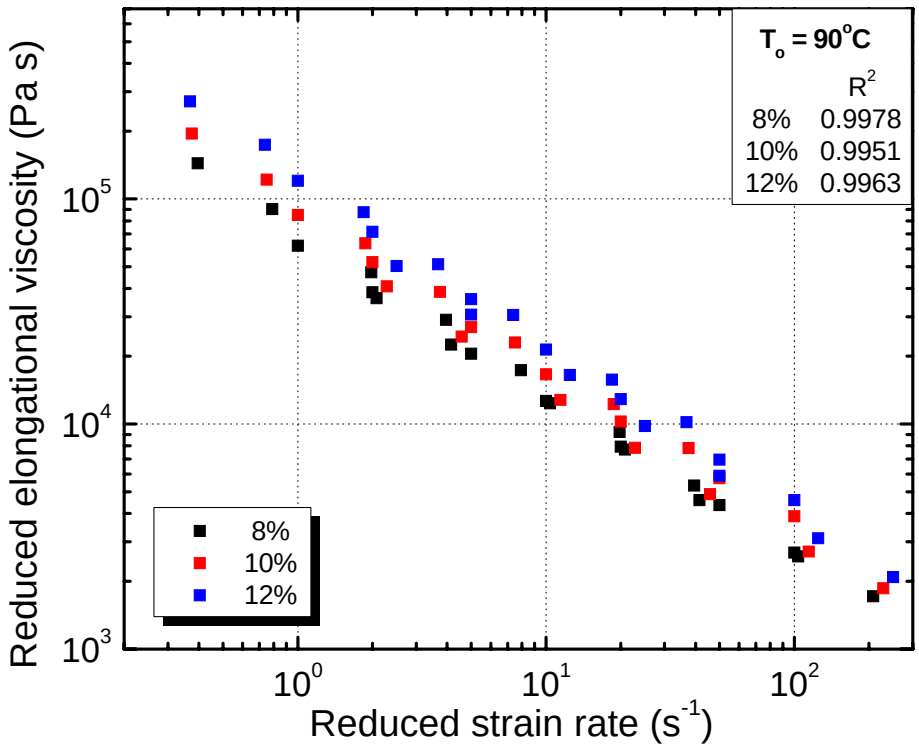

Figure 4.10: **Temperature shifted reduced elongational viscosity of all solutions for a H6 die.**

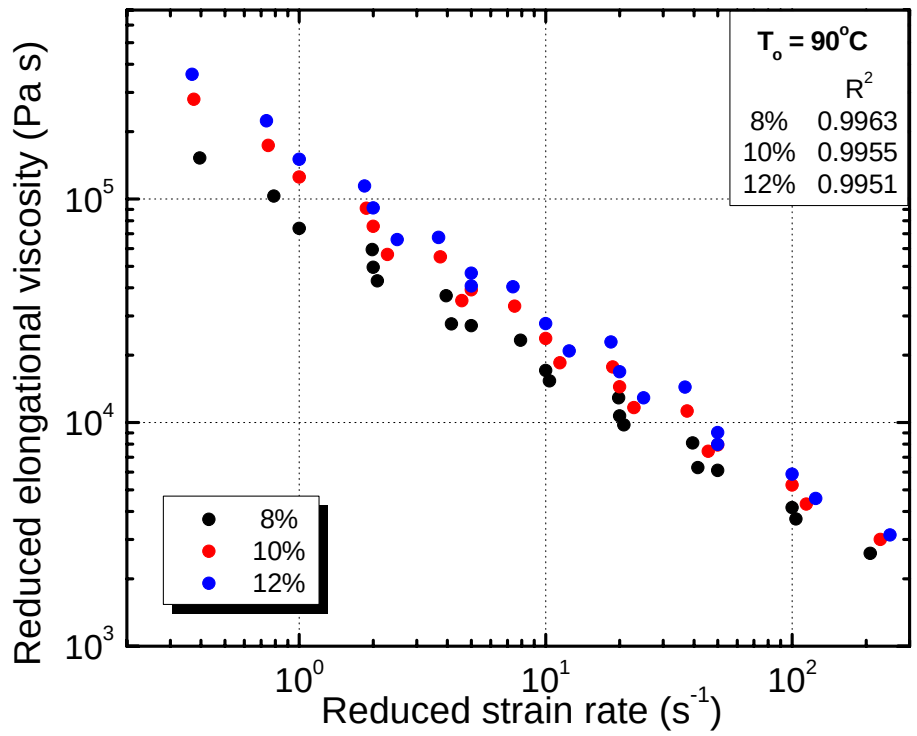

Figure 4.11: **Temperature shifted reduced elongational viscosity of all solutions for a H7 die.**

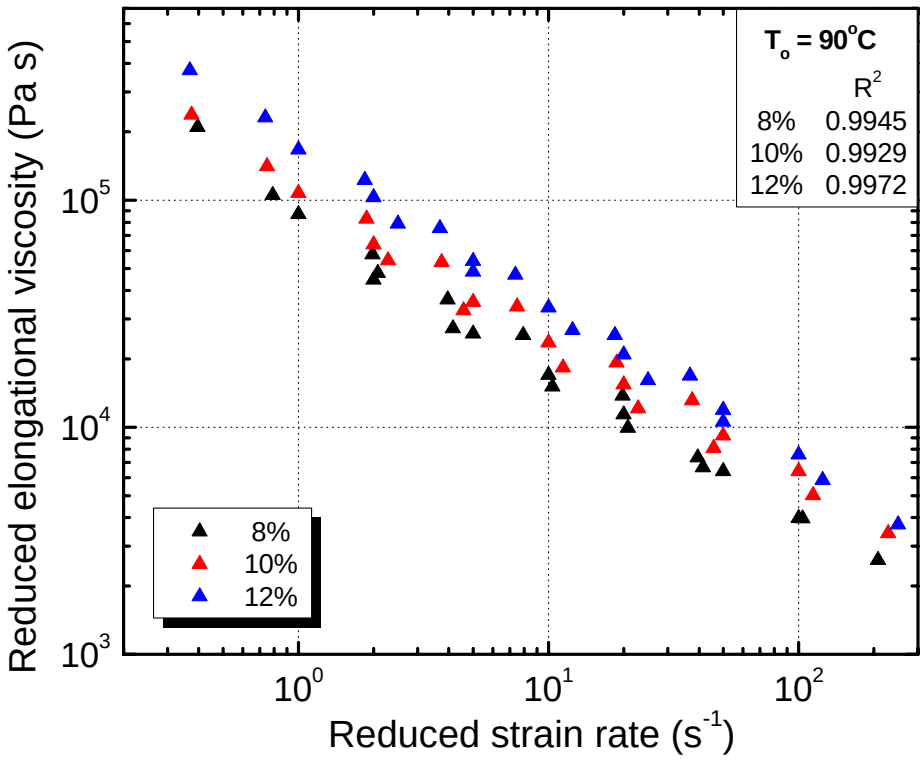

Figure 4.12: Temperature shifted reduced elongational viscosity of all solutions for a H8.4 die.

Each of these figures illustrates that for each Hencky strain rate, the 8% solution had the lowest reduced elongation viscosity, whereas the 12% solution had the highest. This can be explained based on the concentration of the solutions. The lower amount of cellulose in the 8% solution would reduce the viscosity of the solution as observed in the figures. The complete listing of the R^2 values for the temperature shifting is in Table 1B of Appendix B. The R^2 values range from 0.9929 for the 10% solution using a H8.4 die to 0.9978 for the 8% solution using a H6 die. All these values indicate that the temperature shift for each solution for each die is accurate. The 8%, 10% and 12% are not as different in elongation as in shear and the pattern is not as indicative of degradation as in shear. This set of facts could suggest two phases at the higher percentages since a phase separation would influence shear much more than elongational flow. In shear a lower viscosity phase tend to go to the external surface thereby lubricating and reducing the drag at the wall. This does not occur in elongational flow.

4.2.2 Hencky Strain Shifting

The elongational viscosity data were also shifted to a reference Hencky strain rate using two methods (Collier[7] et al., 2003). The first method is based on the relaxation time ratio shown as equation 4.6.

$$\left(a_H\right)_1 = \frac{\left(TR-3\right)\varepsilon_{H_o}}{\left(TR-3\right)_o \varepsilon_H} \tag{4.6}$$

Here the $(TR\text{-}3)_o$ and the ε_{Ho} are taken at the reference Hencky strain, in this case 7. TR represents the Trouton Ratio which equals η_e/η_s, where η_e is the elongational viscosity and the η_s is the shear viscosity at an $\dot{\varepsilon}$ of zero. The Hencky shift factor was then used to calculate the reduced elongational viscosity, equation 4.7, and the reduced strain rate, equation 4.8.

$$\left(\eta_e\right)_r = \frac{\eta_e}{a_H^2} \tag{4.7}$$

$$\left(\dot{\varepsilon}\right)_r = a_H \dot{\varepsilon} \tag{4.8}$$

The second method is based upon the orientational viscosity ratio shown as equation 4.9.

$$\left(a_H\right)_2 = \frac{\eta_e\left[\dot{\varepsilon}_o, \varepsilon_H\right] - 3\eta_s}{\eta_e\left[\dot{\varepsilon}_o, \varepsilon_{H_o}\right] - 3\eta_s} \tag{4.9}$$

The Hencky shift factor for this method was then used to again calculate the reduced elongational viscosity, equation 4.10, and the reduced strain rate, equation 4.11.

$$\left(\eta_e\right)_r = \eta_e \frac{\varepsilon_{H_o}}{a_H \varepsilon_H} \tag{4.10}$$

$$\left(\dot{\varepsilon}\right)_r = a_H \dot{\varepsilon} \tag{4.11}$$

The R^2 analysis of the shifted data was compared for each method, and method 2 was found to yield the best results for all the data. A complete list of the R^2 values is in Table 2B and the graphs for both methods are in Appendix B. The graphs of Hencky strain shifting of each solution using the Method 2 equations are also shown as Figures 4.13 to 4.15.

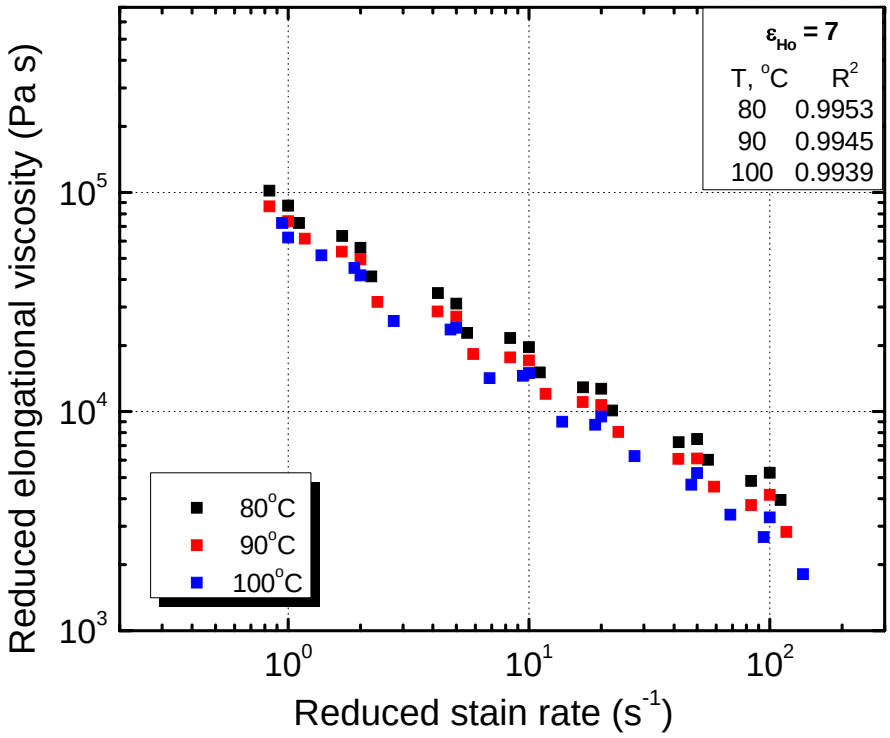

Figure 4.13: **Hencky strain shifted reduced elongational viscosity of an 8% solution at all temperatures – Method 2.**

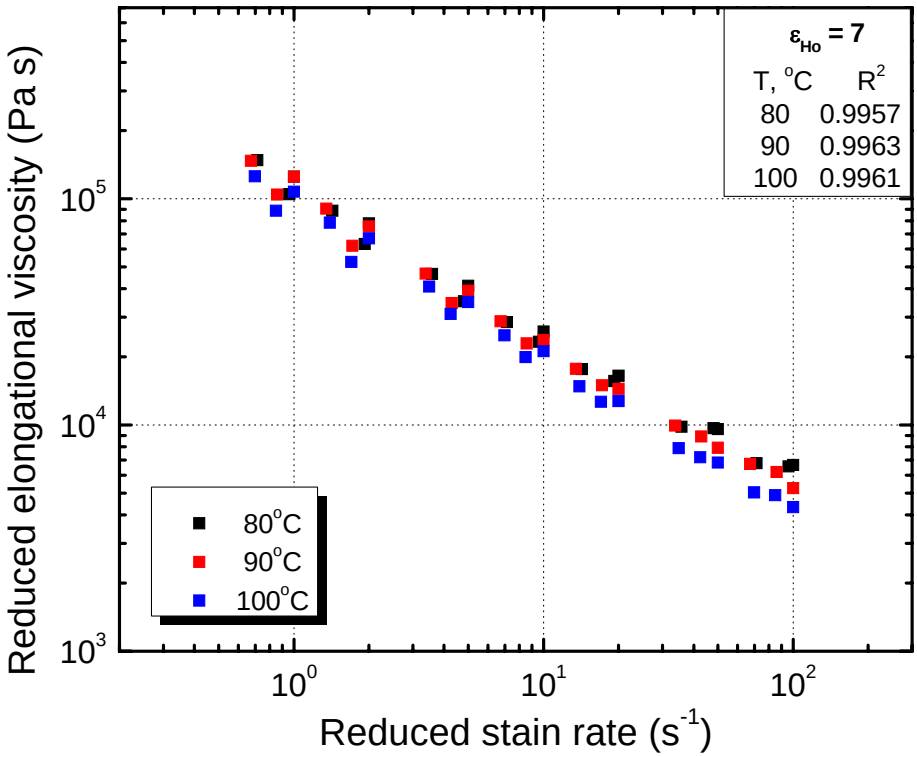

Figure 4.14: **Hencky strain shifted reduced elongational viscosity of a 10% solution at all temperatures – Method 2.**

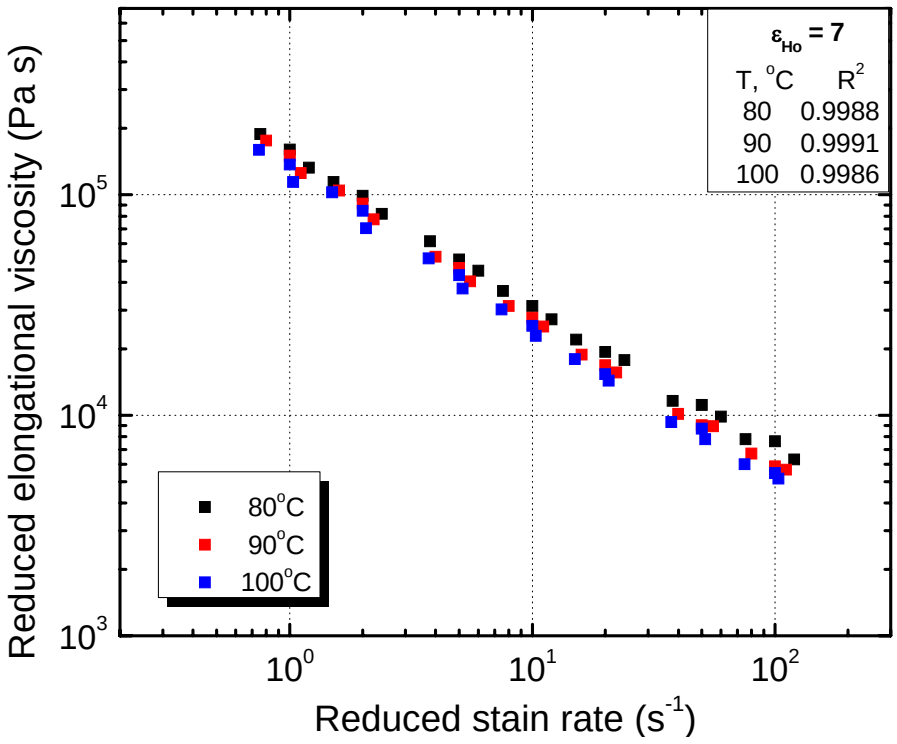

Figure 4.15: Hencky strain shifted reduced elongational viscosity of a 12% solution at all temperatures – Method 2.

Each of these figures illustrates that for each solution the lowest reduced elongation viscosity curve was at 100°C, whereas the highest was for 80°C. This indicates that the increase in the temperature decreased the elongational viscosity which was expected. Also observed in the figures is the smaller difference in the elongation viscosity between the temperatures at the lower strain rates; thus, suggesting that at these lower strain rates, the temperature does not affect the elongational viscosity as greatly. The complete listing of the R^2 values for the Hencky strain rate shifting is in Table 2B of Appendix B. The R^2 values range from 0.9939 for the 8% solution at 100°C to 0.9991 for the 12% solution at 90°C. All these values indicate that the Hencky strain rate shift for each solution is accurate.

The final step was to simultaneously shift both the temperature as well as the Hencky strain rate to a reference temperature of 90°C and a reference Hencky strain rate of 7 using equations 4.12 and 4.13 (Collier[7] et al., 2003).

$$(\eta_e)_{r1[T,H]} = \frac{\eta_e T_o}{a_T T}\frac{1}{(a_H)_1^2} \quad \text{and} \quad (\dot{\varepsilon})_{r1[T,H]} = a_T (a_H)_1 \dot{\varepsilon} \tag{4.12}$$

$$(\eta_e)_{r2[T,H]} = \frac{\eta_e T_o}{a_T T}\frac{\varepsilon_{H_o}}{(a_H)_2 \varepsilon_H} \quad \text{and} \quad (\dot{\varepsilon})_{r2[T,H]} = a_T (a_H)_2 \dot{\varepsilon} \tag{4.13}$$

The simultaneous shifting was also done for both methods and the individual comparison graphs for each solution are shown in Appendix B. The R^2 results again indicated that the most accurate method is Method 2. Figure 4.16 illustrates the shifting using the equations from Method 2 for all three solutions. This figure illustrates that the 8% solution had lowest reduced elongation viscosity where as the 12% solution had the highest. Again this can be explained based on the concentration of the solutions. The lower amount of cellulose in the 8% solution would reduce the viscosity of the solution as observed in the figure. The R^2 values indicate that the temperature shifted and the Hencky strain rate shifted data for 10% solution were the least accurate when compared to the 8% and 12% solutions. However, since all of the R^2 values were greater than 0.99, it can be concluded that all the data are in an acceptable accuracy range.

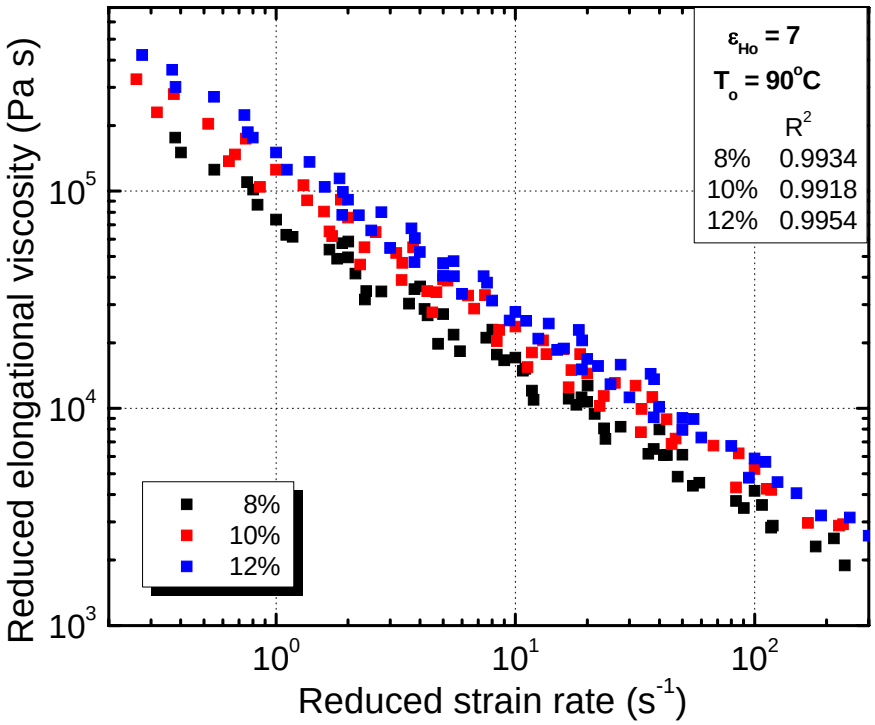

Figure 4.16: Reduced elongational viscosity for all solutions.

4.3 Draw Ratio Calculations

Two of the input parameters used for the spinning experiments were the elongational strain rate and the take-up velocity of the spinner. By calculating the draw ratio for each run, these two parameters were combined and used as a single parameter, the draw ratio, which was paired with the temperature change for Experiment 1 and the concentration change for Experiment 2, in the regression analysis of the crystallinity, orientation number, denier, average maximum load and the tenacity of the fiber.

Using the entrance radius of the die and the new exit radius from the 3 mm plates shown in Figure 4.17, a new Hencky strain rate was calculated based on equation 2.7. This new Hencky strain rate for the die with an additional plate was found to be 8.4, which was used for all the remaining calculations. Also using the entrance and the exit radii, a ratio between the entrance and exit velocities was determined from equation 4.14.

$$v_o R_o^2 \pi = v_d R_e^2 \pi \qquad (4.14)$$

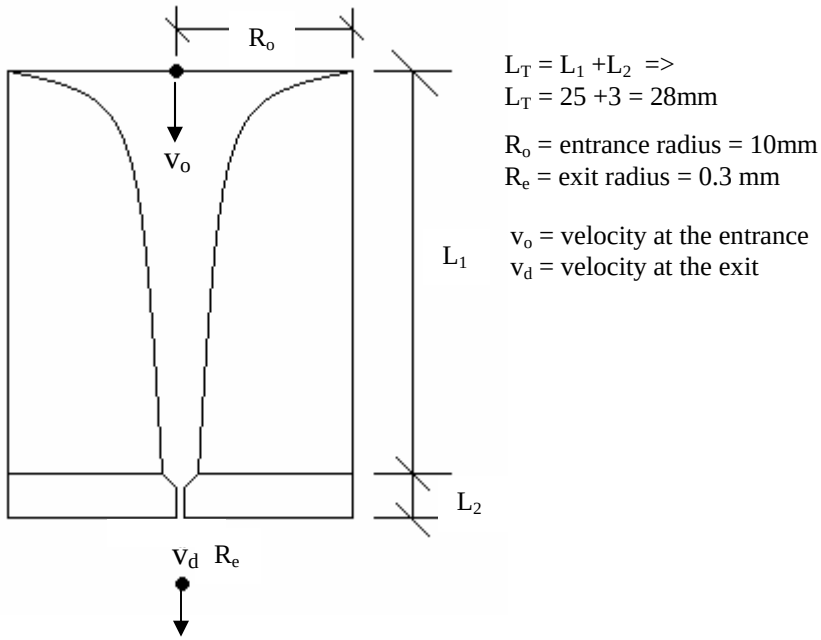

Figure 4.17: Diagram of for the draw ratio calculations.

From equation 2.6, the entrance velocity was derived as shown in equation 4.15

$$v_o = \frac{\dot{\varepsilon} L_T}{\left(e^{\varepsilon_H} - 1\right)} \tag{4.15}$$

The $\dot{\varepsilon}$ is based on the value indicated for each of the runs. Therefore the draw ratio, D_r, which is defined as the take-up velocity divided by the velocity at the die exit, can be derived as shown in equation 4.16.

$$D_r = \frac{v_t}{v_d} = \frac{v_t R_e^2 \left(e^{\varepsilon_H} - 1\right)}{\dot{\varepsilon} L_T R_o^2} \tag{4.16}$$

The take-up velocity like the elongational strain rate is based on the values for each individual run.

4.4 Image Analysis – SEM Results

The SEM image analysis enabled the surface area of the fibers to be viewed at a micro level thus indicating the effect that the concentration and the draw ratio had on the surface of the fiber. Figures 4.18 and 4.19 represent two runs at low and high draw ratios where the concentration and the temperature remained constant. In Figure 4.18, at the lower draw ratio, the fibers appear smooth and somewhat round in shape. However, in Figure 4.19 the fibers appear to be flat in shape but still smooth. This indicates that an increase in the draw ratio stretches the fibers to a flatter shape which is not as desirable for carbon fiber precursors as a round fiber. The flattening could also be due to a shorter time in the air gap causing the fibers to be hotter and more deformable upon contacting the first spool in the coagulation bath.

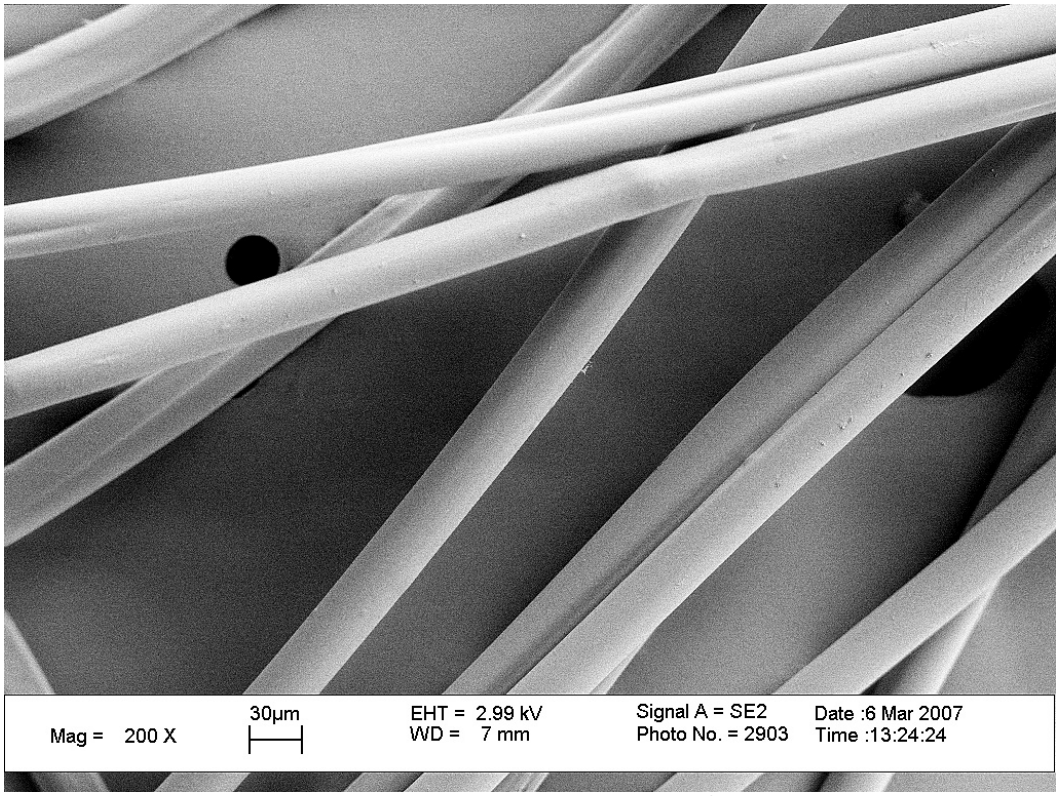

Figure 4.18: Run #2 – 10% solution, 100°C, D_r = 18.2

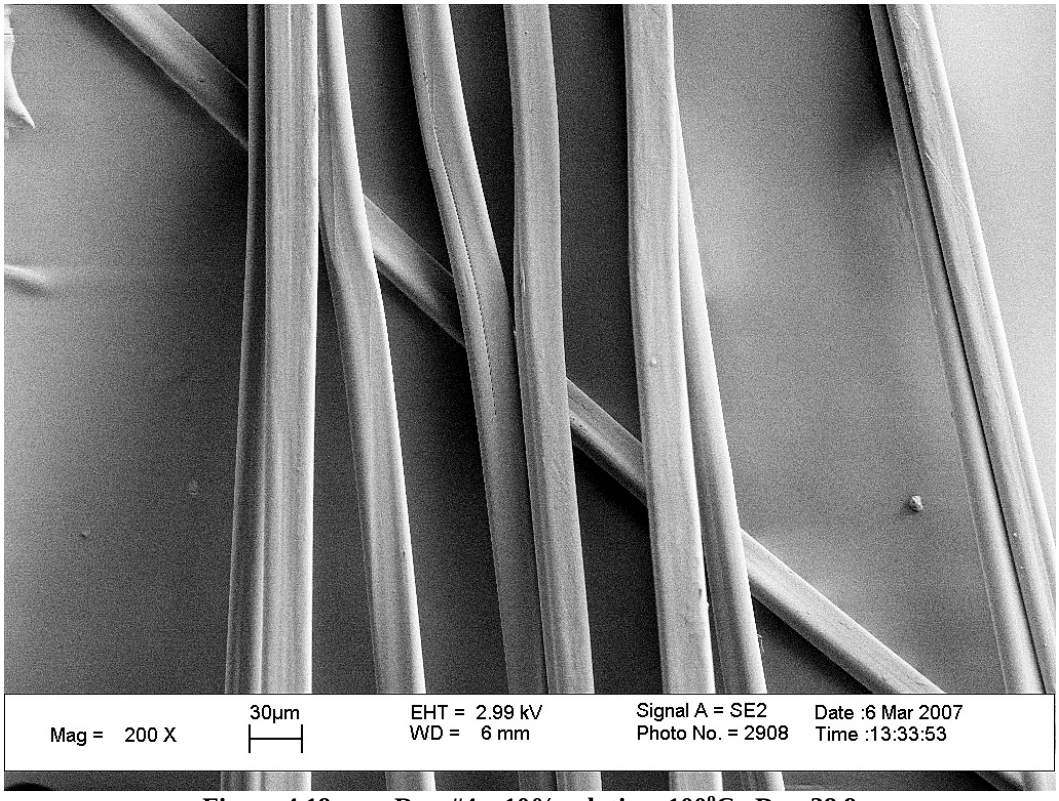

Figure 4.19: Run #4 – 10% solution, 100°C, D_r = 38.9

Figures 4.20 and 4.21 represent two runs at low and high concentrations where the draw ratio and the temperature remained constant. In Figure 4.20, at the higher concentration, the fibers appear smooth and round in shape. However, in Figure 4.21 the fibers appear to be flat in shape and crenulated on the surface, indicating that the lower concentration fibers may be more deformable when they contact the first spool in the coagulation bath. This indicates that a higher solution concentration, fibers are rounder in appearance and smooth which is desirable for carbon fiber precursors. The SEM images at magnifications 200X and 150X for each run are in Appendix C.

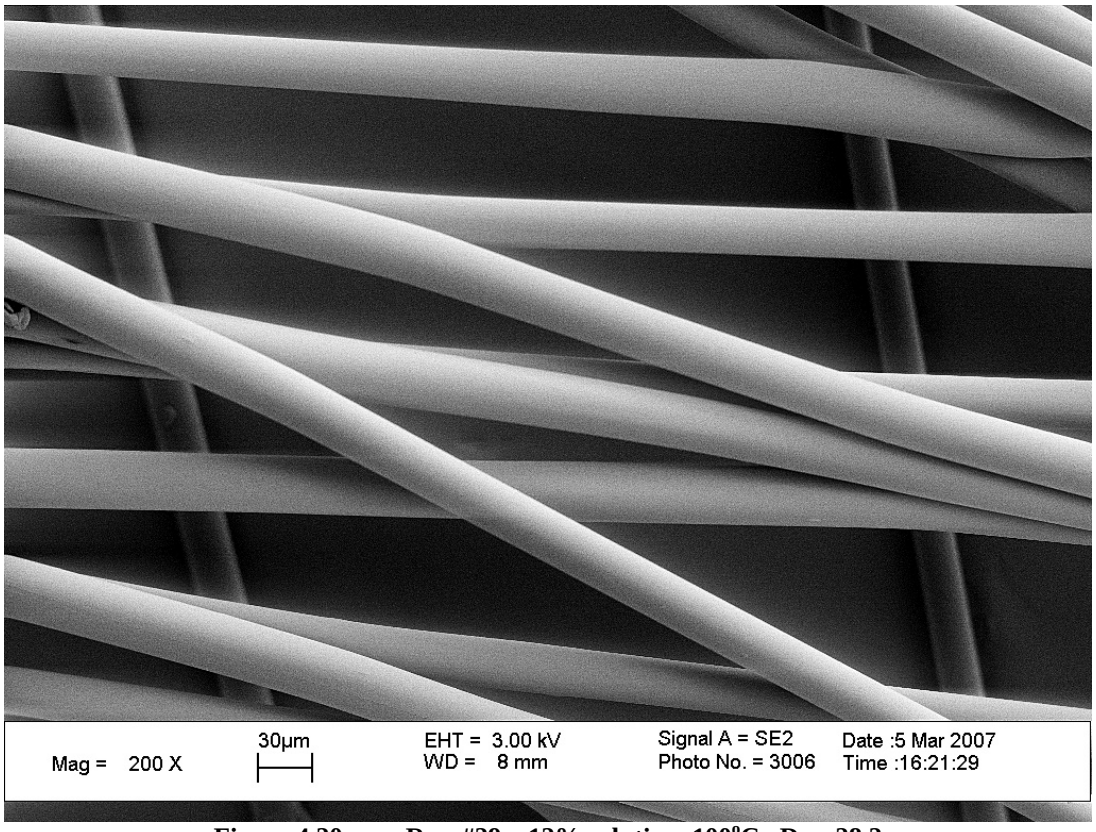

Figure 4.20: Run #29 – 12% solution, 100°C, D_r = 28.2

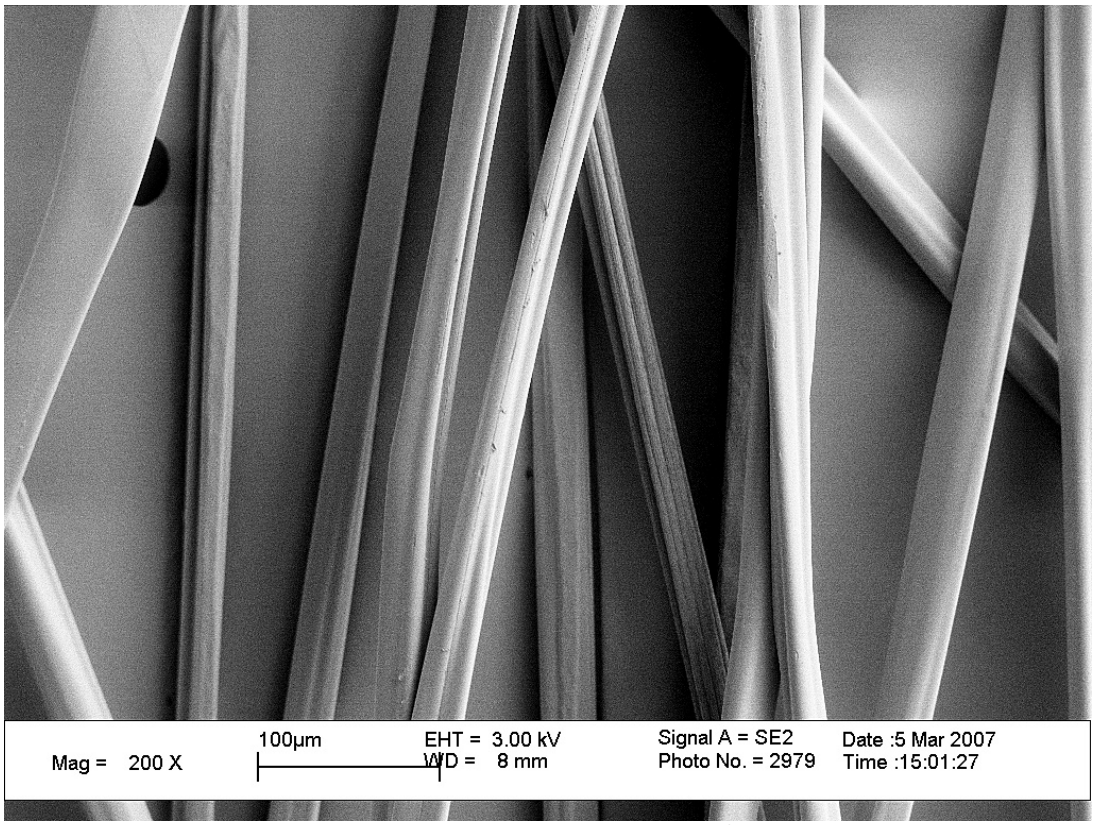

Figure 4.21: Run #20 – 8% solution, 100°C, D_r = 28.2

4.5 Regression Analysis

In order to fully understand the effects that the run parameters had on the results of each of the fiber runs, a multiple quadratic regression was preformed for crystallinity, orientation number, linear density, average maximum load on the fiber and tenacity. This provided a response surface to illustrate the effect that temperature, concentration and draw ratio had on the aforementioned results. For each of the regression analyses, the z-axis was a dependent variable, i.e. crystallinity, orientation number, linear density, average maximum load on the fiber or tenacity, and the y-axis was the independent variable draw ratio and the x-axis was also an independent variable, either temperature or concentration depending on the experiment.

The coefficients for the regression equation were solved for each measurement, i.e. crystallinity, and a matrix for the surface was solved. The actual measurements were

then plotted for the comparison. The general regression equation used is shown below as equation 4.17.

$$z = \beta_o + \beta_1 x + \beta_2 y + \beta_3 x^2 + \beta_4 y^2 + \beta_5 xy \qquad (4.17)$$

Where z represents the measurement analyzed in the regression, x represents the temperature or the solution concentration, y represents the draw ratio and the β's are the equation coefficients. Table 4.1 lists the regression equations used for all the surface graphs in the following sections. The regression analysis was completed in [1]Excel® and then graphed in [2]Origin 7.5®

Table 4.1: Regression Equations for all Experimental Measurements

Description	Regression Equation
Crystallinity Index with Temperature and D_r Variation	$CI = 5.453 - 9.881E^{-2}T + 2.091E^{-3}D_r + 5.148E^{-4}T^2 + 1.378E^{-4}D_r^2 - 5.362E^{-5}TD_r$
Crystallinity Index with Concentration and D_r Variation	$CI = 0.6964 - 1.020E^{-2}C - 1.082E^{-3}D_r + 1.329E^{-3}C^2 + 1.250E^{-4}D_r^2 - 2.178E^{-4}CD_r$
Tenacity with Temperature and D_r Variation	$Ten = 35.09 - 6.293E^{-1}T + 7.566E^{-2}D_r + 2.968E^{-3}T^2 + 6.612E^{-5}D_r^2 - 7.058E^{-4}TD_r$
Tenacity with Temperature and CI Variation	$Ten = 24.71 - 0.5040T + 12.94CI + 2.159E^{-3}T^2 - 8.540CI^2 + 1.670E^{-2}TCI$
Tenacity with Concentration and D_r Variation	$Ten = -0.3690 + 4.762E^{-1}C - 3.147E^{-2}D_r - 2.026E^{-2}C^2 + 8.207E^{-4}D_r^2 - 4.793E^{-4}CD_r$
Tenacity with Concentration and CI Variation	$Ten = -1.001 + 4.977E^{-1}C - 7.807E^{-1}CI - 2.638E^{-2}C^2 + 1.107CI^2 + 9.258E^{-2}CCI$
f_H with Temperature and $N_{OR(die)}$ Variation (10% only)	$f_H = -28.50 + 0.4951T + 54.63N_{OR(die)} - 2.117E^{-3}T^2 - 24.70N_{OR(die)}^2 - 0.4587T N_{OR(die)}$
f_H with Temperature and $N_{OR(die)}$ Variation (8% and 10%)	$f_H = -18.78 + 0.3309T + 35.17N_{OR(die)} - 1.424E^{-3}T^2 - 14.86N_{OR(die)}^2 - 0.2955T N_{OR(die)}$
f_H with Temperature and $N_{OR(Tot)}$ Variation	$f_H = -2.781 + 5.126E^{-2}T + 0.5152N_{OR(Tot)} - 2.019E^{-4}T^2 - 1.048E^{-2}N_{OR(Tot)}^2 - 4.081E^{-3}T N_{OR(Tot)}$
Tenacity with Temperature and $N_{OR(Tot)}$ Variation	$Ten = 62.70 - 1.080T - 1.769N_{OR(Tot)} + 4.782E^{-3}T^2 + 2.700E^{-2}N_{OR(Tot)}^2 + 1.536E^{-2}T N_{OR(Tot)}$

[1] Excel is made by Microsoft
[2] Origin 7.5 is made by OriginLab Corp.

4.6 Crystallinity Analysis

The crystallinity was calculated using a peak integration method. Using the intensity curves for the WAXS, the two peaks as well as the amorphous peak were determined with curve fitting software and corrected for background noise. The area under the two main peaks as divided by the total area under the curve, this included the amorphous region, to obtain the crystallinity index. The peak fitting software was run a minimum of three times in the same x-ray scan to obtain the peak areas for the crystallinity calculations. The calculated crystallinity was then averaged for each sample.

4.6.1 Wide Angle X-Ray Scatter Intensity Curves

Based on the crystallinity calculations the highest and lowest runs were Run #25 and Run #19, respectively. Figures 4.22 and 4.23 represent the intensity peaks for these runs. The intensity curve graphs for all of the runs are shown in Appendix D.

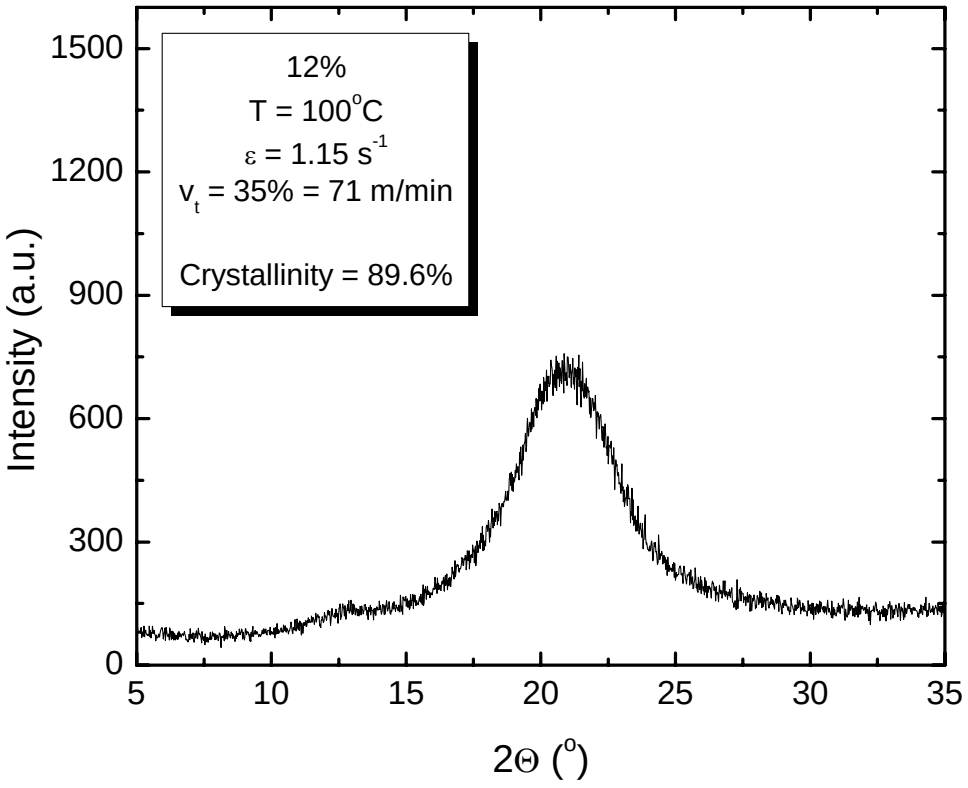

Figure 4.22: X-ray intensity peak for Run #25

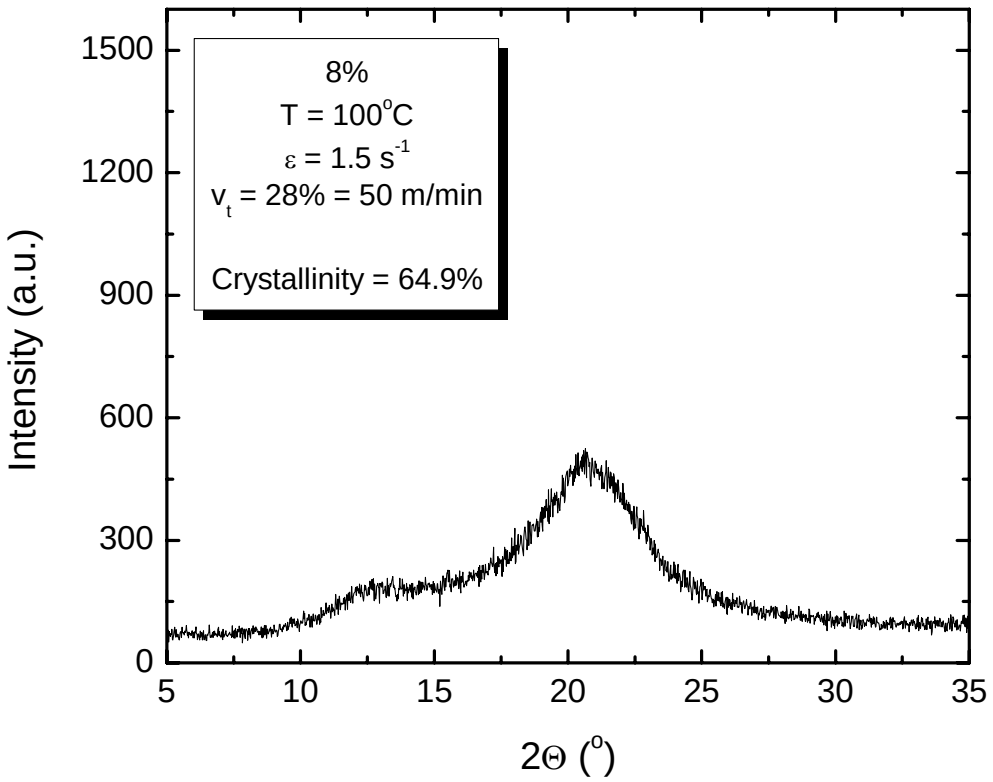

Figure 4.23: X-ray intensity peak for Run #19

The intensity of the peaks varied widely from run to run with no visible pattern that was correlated with the input parameters. The intensity was measured with arbitrary units therefore when graphed on different scales all the peak patterns were of the same shape. Run #25 shown above had the highest calculated crystallinity but did not have the highest peak intensity. If graphed on a smaller scale, the peaks would be more pronounced. However for consistency, all of the intensity curves had the same scaling, as seen in Appendix D.

Run #19, shown above in Figure 4.23, had the lowest calculated crystallinity. Although the peaks for Run #19 are smaller than the peaks for Run #25, no conclusion about the crystallinity can be made from these figures. For example, Run #15 and Run #30 shown in Appendix D had higher peaks than Run #25 but had a lower calculated crystallinity of 82.6% and 74.1%, respectively. Overall, the crystallinity ranged from 64.9% to 89.6%. Because of these results, a visual comparison of the intensity curves is apparently not conclusive.

4.6.2 Crystallinity Regression Curves

4.6.2.1 Temperature Variation – Experiment 1

Figure 4.24 represents the surface curve obtained from the regression analysis for the effect temperature and draw ratio had on crystallinity, where the draw ratio was calculated from changes in the take-up velocity as well as the elongational strain rate. This graph illustrates that the temperature had a low point in crystallinity at approximately 100^{o}C, which then increased as the temperature increased and decreased. Also observed in this figure is the increase in crystallinity as the draw ratio increases. At the lower draw ratios, the crystallinity levels out indicating that it will decrease only to a certain level depending on the draw ratio, this can be more easily observed in Figure 4.26. The goal of the fiber spinning is to have a highly crystalline fiber. Therefore, this figure suggests that temperatures greater and less than 100^{o}C and high draw ratios would achieve the goal.

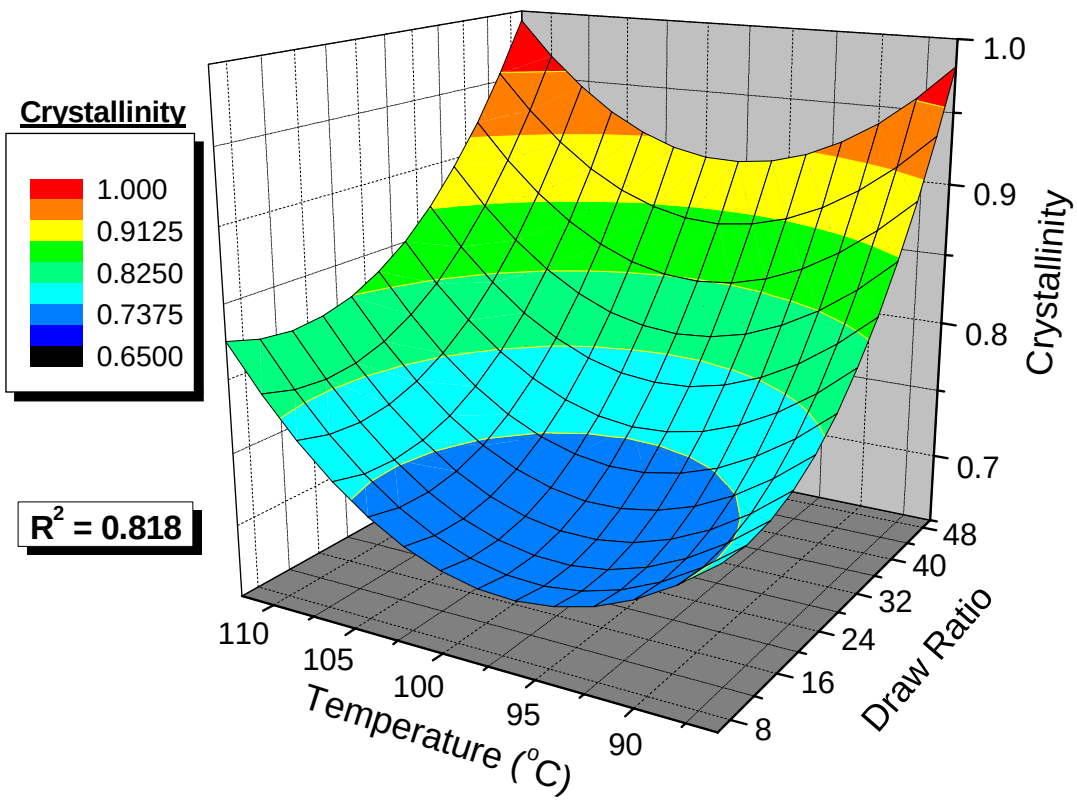

Figure 4.24: The effect of temperature and draw ratio on the crystallinity of a 10% solution.

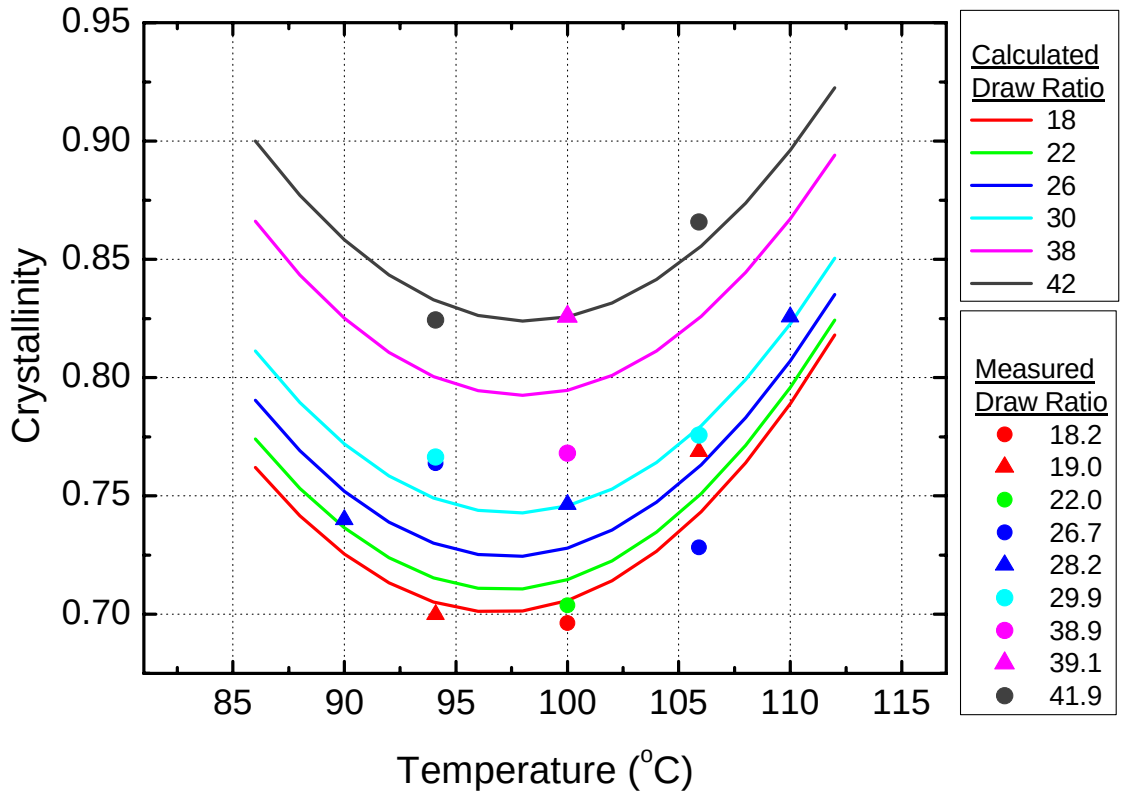

Figure 4.25: The effect of temperature on the crystallinity for a 10% solution at measured and calculated draw ratios.

Figure 4.25 represents the effect of temperature on the crystallinity where the lines are the calculated draw ratios based on the regression analysis and the points represent the crystallinity for the runs in Experiment 1 which was previously described in Section 3.9.2.1 as the runs with the variation in temperature while holding the concentration constant. The graph clearly shows the dip in the crystallinity at approximately 97°C. In order to compare the regression results with the actual results, the "calculated lines" from the regression analysis equation and the "measured points" from the test results are shown . The points indicate that the measured draw ratios fit the calculated draw ratio curves relatively well where the closest measurement to calculation is for the draw ratio of 22.0.

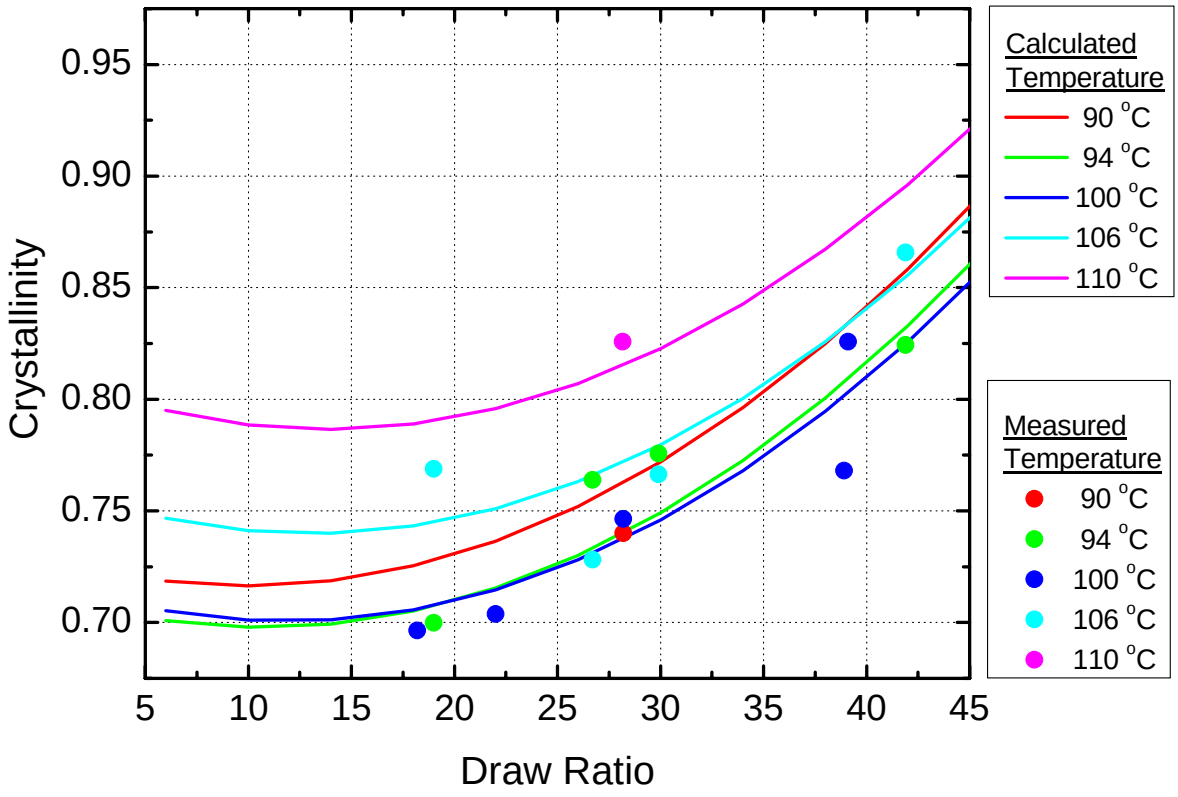

Figure 4.26: The effect of draw ratio on the crystallinity for a 10% solution at measured and calculated temperatures.

Figure 4.26 represents the effect of draw ratio on the crystallinity. The graph shows a decrease in the crystallinity as the draw ratio decreases. The points indicate that the measured temperatures fit the calculated temperature curves relatively well where the closest measurement to calculation is for the temperature of 100^{o}C.

Based on these two figures the run with the highest crystallinity was Run #11 with a crystallinity of 86.6%, run at a temperature of 106^{o}C, a draw ratio of 41.9 and a concentration of 10%. The lowest crystallinity was observed to be Run #2 with a crystallinity of 69.6%, run at a temperature of 100^{o}C and a draw ratio of 18.2.

4.6.2.2 Concentration Variation – Experiment 2

Figure 4.27 represents the surface curve obtained from the regression analysis for the effect solution concentration and draw ratio had on crystallinity. This graph illustrates that the lowest crystallinity occurs at low solution concentrations and low draw ratios. This means that a higher solution concentration at a high draw ratio would yield fibers with the desired high crystallinity. As previously stated, the goal of the fiber spinning is to have a highly crystalline fiber, therefore based on Figures 4.24 and 4.27, a high concentration solution spun at a high temperature or low temperature and a high draw ratio would yield highly crystalline fibers.

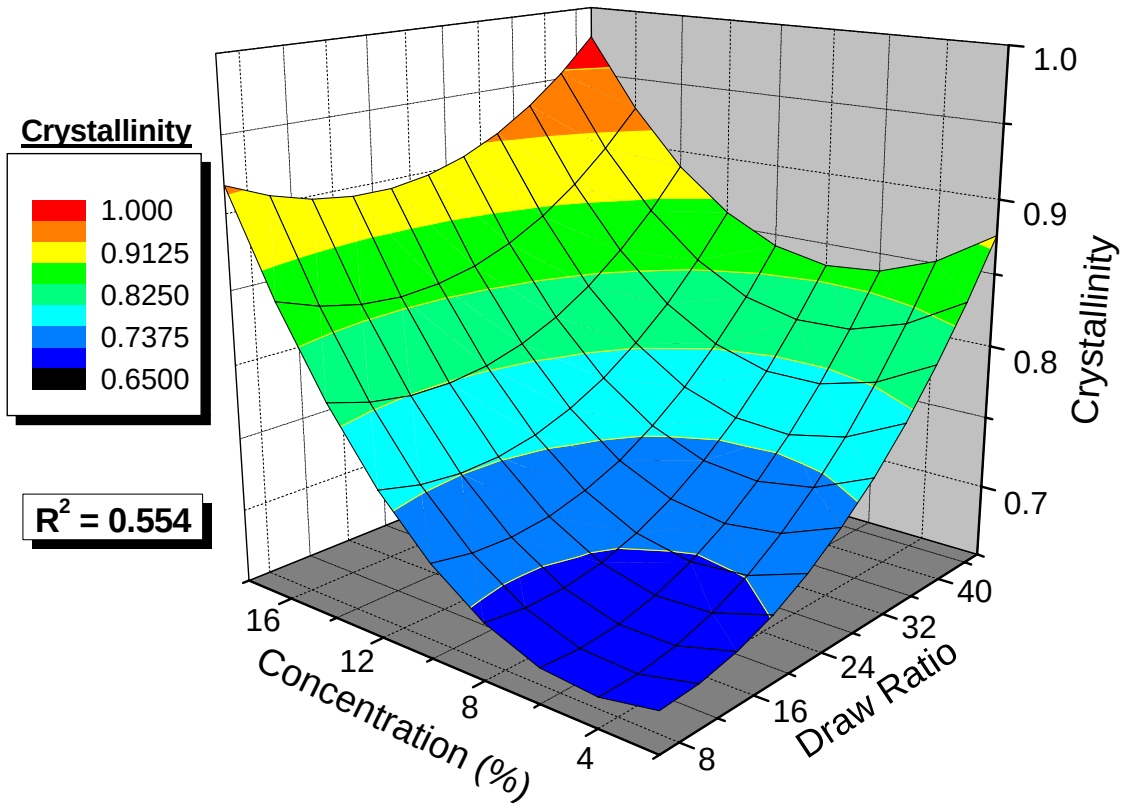

Figure 4.27: The effect of solution concentration and draw ratio on the crystallinity at 100°C.

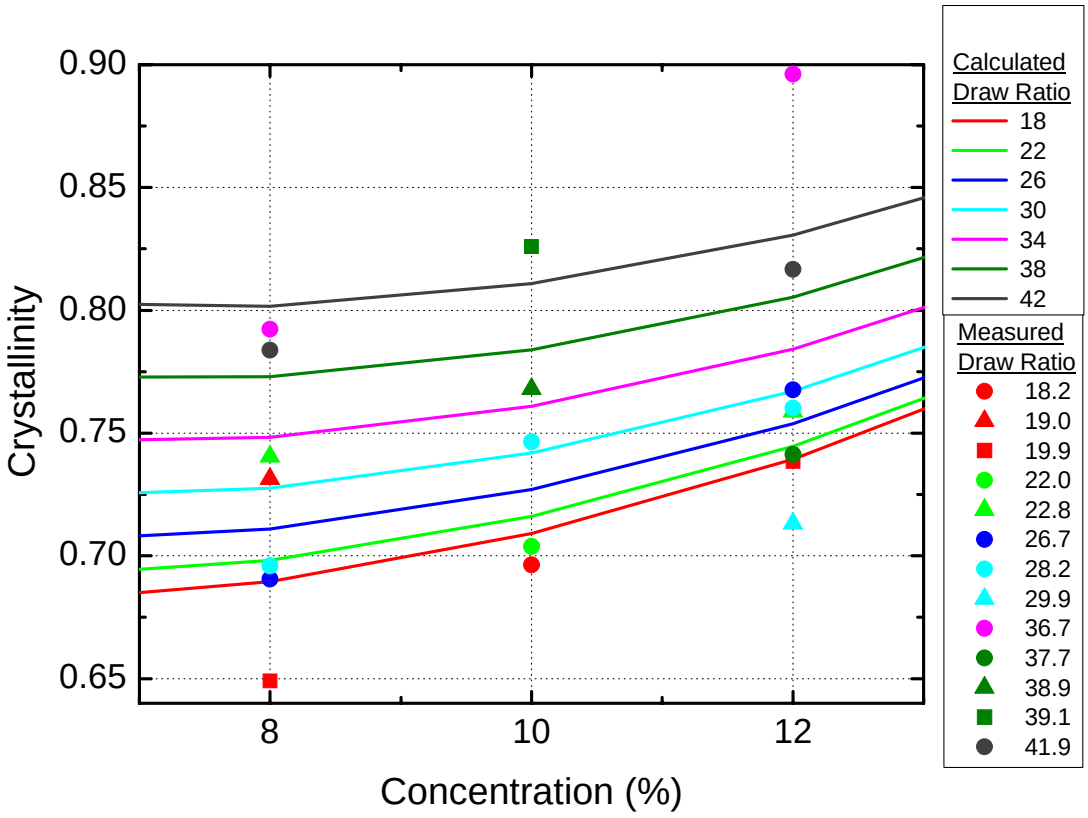

Figure 4.28: The effect of solution concentration on the crystallinity at 100°C for measured and calculated draw ratios.

Figure 4.28 represents the effect of concentration on the crystallinity where the lines are the calculated draw ratios based on the regression analysis and the points represent the measured crystallinity for the runs in Experiment 2 which was previously described in Section 3.9.2.2 as the runs with the variation in concentration while holding the temperature constant. The graph illustrates the increase in crystallinity as the concentration increases. Also observed is a smaller difference in the crystallinity at lower draw ratios. This again suggests that the fibers will maintain a set level of crystallinity regardless of how low the draw ratio is. The points indicate that the measured draw ratios somewhat fit the calculated draw ratio curves where the closest measurement to calculation is for a draw ratio of 28.2. However, there are several measured draw ratio points that do not match the curves, especially for the lower concentrations.

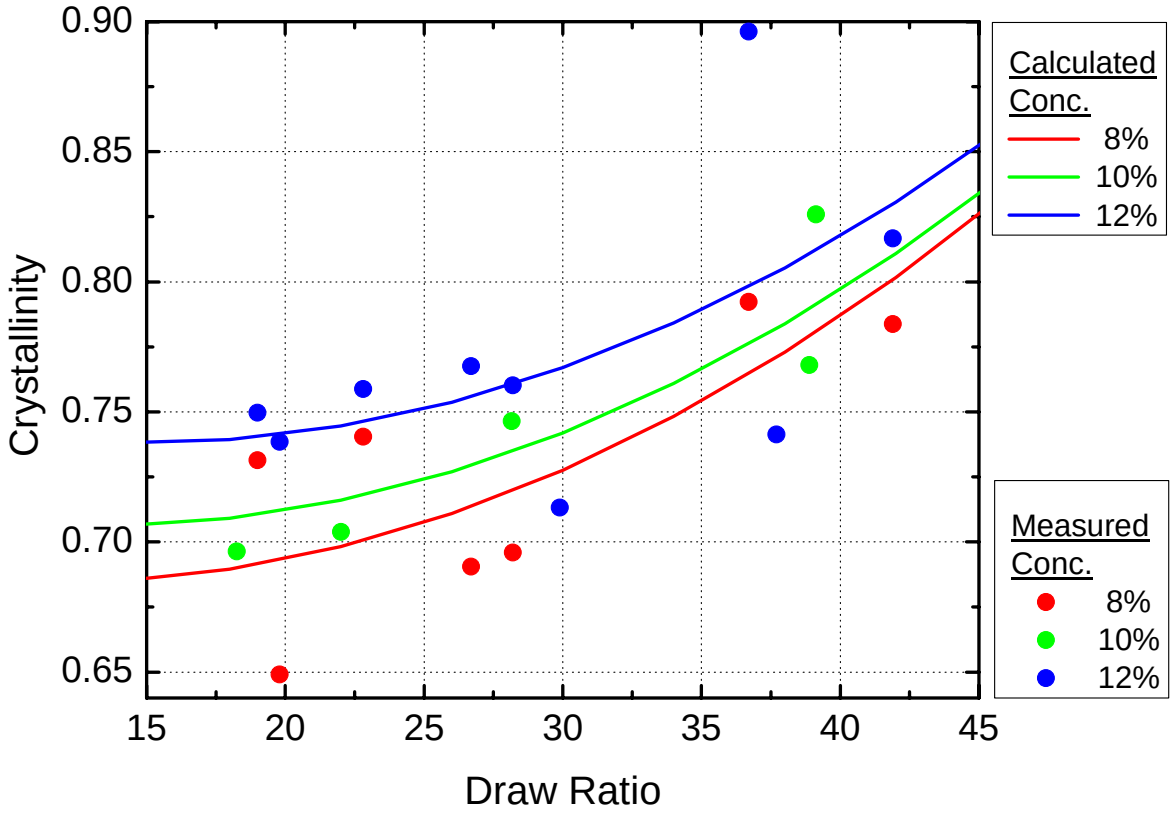

Figure 4.29: The effect of draw ratio on the crystallinity at 100°C for measured and calculated solution concentrations.

Figure 4.29 represents the effect of draw ratio on the crystallinity. The graph clearly shows a decrease in the crystallinity as the draw ratio decreases with a larger difference in the crystallinity for the concentrations at the lower draw ratios. The measured concentration points indicate that the 10% concentration fit the calculated concentration curve the closest and the 8% concentration appeared to be the furthest from the calculated concentration curve.

Based on these two figures the run with the highest crystallinity was Run #25 with a crystallinity of 89.6%, run at a temperature of 100°C, a draw ratio of 36.7 and concentration of 12%, however this point appears to be an outlier point based on the distance it is from the calculated 12% concentration curve. Therefore, Run #1 with a crystallinity of 82.6%, was the run with the next highest crystallinity, within experiment 2. It was run at a temperature of 100°C, a draw ratio of 39.1 and a concentration of 10%. In Figure 4.24, the lowest crystallinity appears to occur at a temperature of 100°C

however, the measured results indicate otherwise. This could suggest that the effect of temperature on the crystallinity is not as significant as expected. Based on visual observation of the of the results, it does appear that the crystallinity does increase as the temperature increases however it should be noted that the highest as well as the lowest crystallinity occurs at 100°C. The lowest crystallinity was observed to be Run #19 with a crystallinity of 64.9%, run at a temperature of 100°C, a draw ratio of 19.8 and a concentration of 8%. All of the crystallinity results are listed in Table 2D of Appendix D.

4.7 Birefringence and Orientation Factor Analysis

The first step in determining an orientation factor was to measure the birefringence of fibers from each run. The angle of rotation, *2i*, was measured for each fiber and used to find the phase difference, Γ, which also incorporates the constant values of the compensator used in the angle measurements. Therefore, the birefringence, Δn, was calculated based on equation 4.17 where *d* is the diameter of the fiber being tested. The measured birefringence was then used to calculate the Herman's orientation factor, f_H shown in equation 4.18 where Δ^o is the maximum or intrinsic birefringence of cellulose (White, et al., 1983). A Herman's orientation factor equal to one indicates that the fiber is perfectly oriented whereas a factor of zero indicates that there is no orientation within the fiber.

$$\Delta n = \Gamma / d \tag{4.17}$$

$$f_H = \Delta n / \Delta^o \tag{4.18}$$

The maximum birefringence for cellulose was found to have several values; 0.056 (Bingham, 1964), 0.061 (Lenz, et al., 1992) and 0.081 (Kong et al., 2005). For the calculation of the orientation factor shown in Tables 4.2 and 4.3, 0.061 was used for the maximum birefringence of the cellulose. Although the value presented by Kong was higher, the method used to determine the maximum birefringence was questionable therefore, 0.061 was used for the calculations.

Table 4.2: Birefringence Results for Experiment 1

Run #	Δn	Herman's orientation factor (f_H)	Run #	Δn	Herman's orientation factor (f_H)
1	0.030	0.497	9	0.040	0.652
2	0.035	0.581	10	0.032	0.531
3	0.039	0.646	11	0.036	0.585
4	0.032	0.526	12	0.036	0.586
5	0.036	0.593	13	0.036	0.590
6	0.040	0.656	14	0.045	0.732
7	0.033	0.548	15	0.027	0.445
8	0.038	0.630			

Table 4.3: Birefringence Results for Experiment 2

Run #	Δn	Herman's orientation factor (f_H)	Run #	Δn	Herman's orientation factor (f_H)
16	0.033	0.540	26	0.046	0.749
17	0.018	0.291	27	0.041	0.674
18	0.031	0.509	28	0.041	0.664
19	0.032	0.522	29	0.023	0.382
20	0.028	0.460	30	0.039	0.647
22	0.034	0.553	31	0.033	0.539
24	0.033	0.541	32	0.034	0.550
25	0.041	0.672	33	0.036	0.587

Figure 4.30 represents the effect of temperature, total orientation number, tenacity and crystallinity index on the Herman's orientation factor. The straight line in each graph represents the regression line based on the measured values. This figure indicates the following; an increase in temperature decreased the fiber orientation, an increase in orientation number showed an increase in the fiber orientation, an increase in the tenacity increased the fiber orientation and the increase in crystallinity decreased the fiber orientation which was opposite was what was expected.

The orientation factor ranged from 0.291 for Run #17 to 0.749 for Run #26. This indicates that the fibers obtained were slightly oriented to moderately oriented. Also observed was a small increase in the level of orientation as the concentration increased however, this was a general trend and there were exceptions.

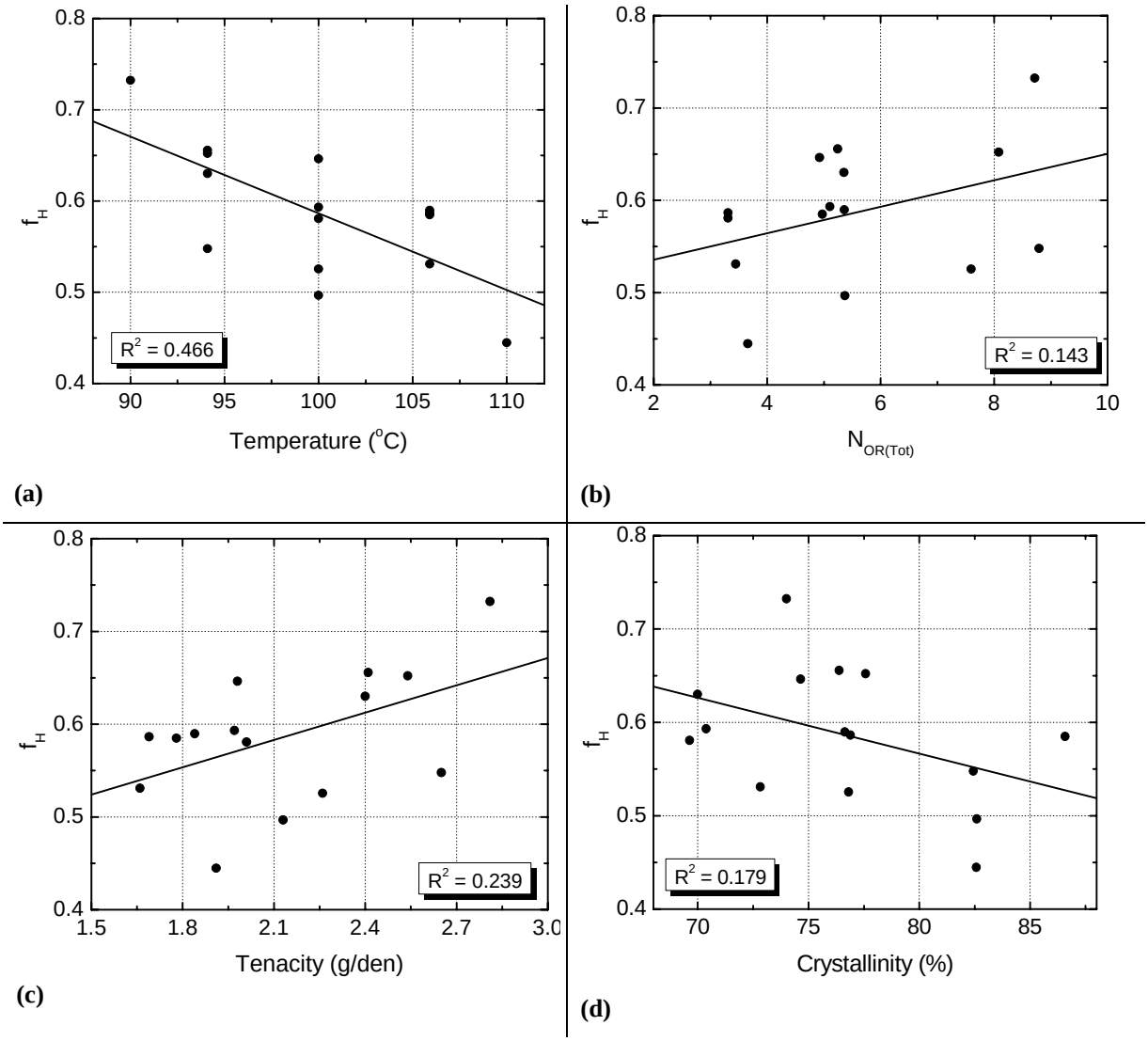

Figure 4.30: Effect of (a) temperature, (b) total orientation number, (c) tenacity and (d) crystallinity on the Herman's orientation factor for cellulose fibers.

4.8 Tensile Strength Analysis

4.8.1 Fiber Breakage Curves – Load verses Displacement

A minimum of ten fibers were used for the tensile strength testing. Each fiber was broken at a 15 mm gage length and the results were plotted on the same graph for comparison. The linear density, the maximum load and the tenacity calculation were averaged from the results of all the fibers tested. However any fibers that gave results dissimilar to the other test results were considered outliers and were disregarded from the total averages of the fiber results. A complete table of the results and the breakage curves for all the runs are in Appendix E. The figures in Appendix E that have missing fibers from the chorological order appearing in the legend, were fibers that were excluded from the averages because they would have skewed the results.

4.8.2 Average Linear Density

The average linear density and was also correlated to temperature, concentration and draw ratio. This was done to determine the effect of each parameter on the linear density. Because the linear density was not a normalized value like the tenacity, the results obtained, as well as some brief explanations can be found in Appendix F. The tenacity results which are more relevant are included in the following sections.

4.8.3 Tenacity Regression Curves

4.8.3.1 Temperature Variation – Experiment 1

Figure 4.31 represents the surface regression curve of the fiber tenacity as affected by the change in temperature and draw ratio. This graph illustrates that at low temperatures and high draw ratios, the fiber tenacity is higher. The goal of the fiber spinning is to have a fiber with a high tenacity, again indicating the strength of the fiber. Therefore, Figure 4.31 suggests that lower temperatures and higher draw ratios would achieve this goal.

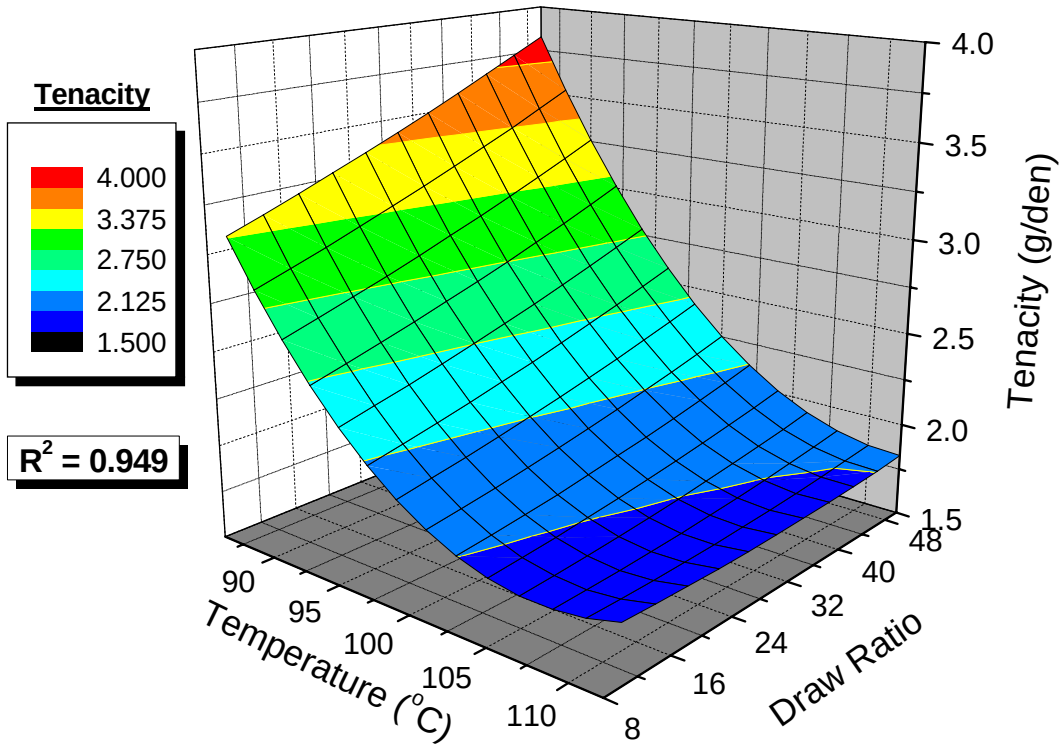

Figure 4.31: The effect of temperature and draw ratio on the fiber tenacity for a 10% solution.

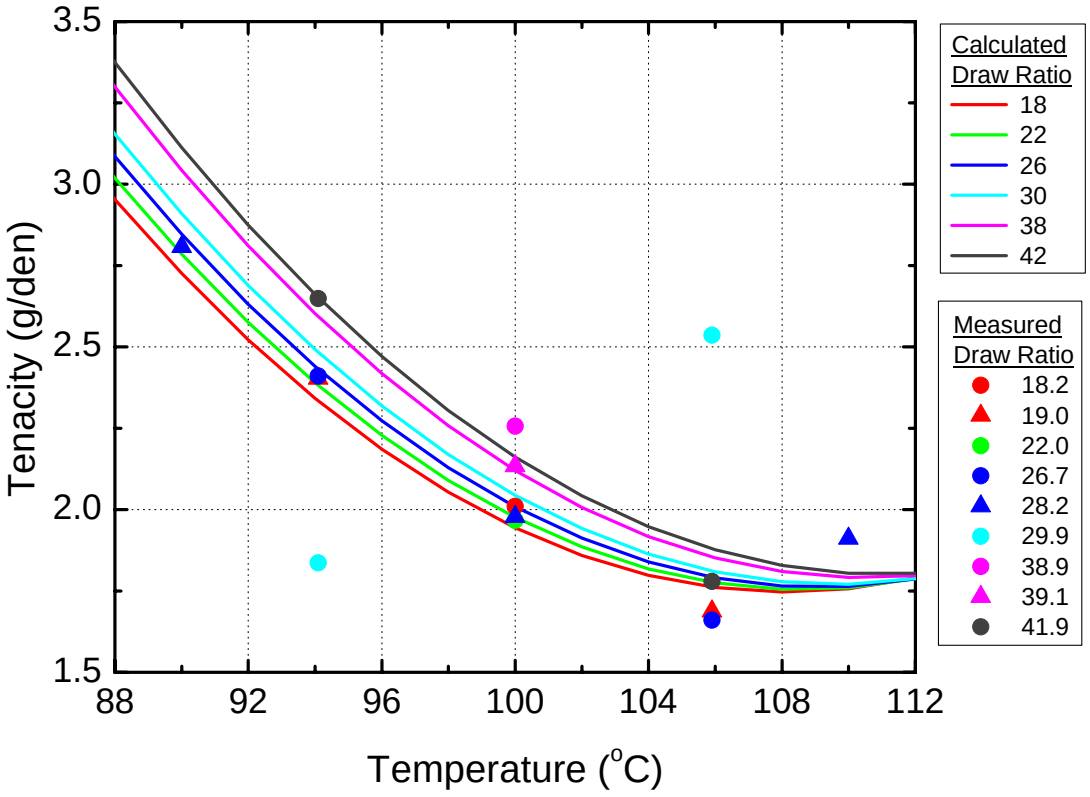

Figure 4.32: The effect of temperature on the fiber tenacity for a 10% solution at measured and calculated draw ratios.

Figure 4.32 represents the effect of temperature on the fiber tenacity where the lines are the calculated draw ratios based on the regression analysis and the points represent the measured draw ratios for the runs in Experiment 1. The graph indicates a decrease in the tenacity as temperature increases. Also observed is a smaller difference in the tenacity, for all the draw ratios, at higher temperatures indicating that the fibers will maintain a certain level of tenacity regardless of the increase in the temperatures. The points indicate that the measured draw ratios do not fit the calculated draw ratio curves well with exception to the draw ratio point of 26.7.

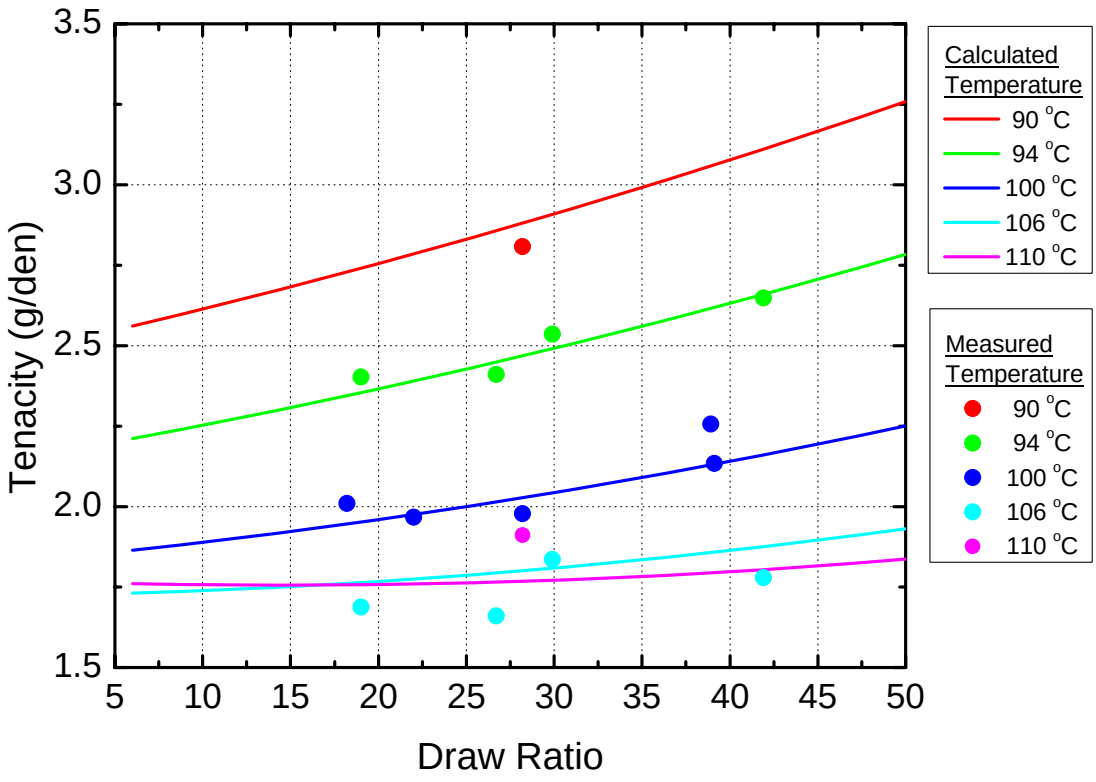

Figure 4.33: The effect of draw ratio on the fiber tenacity for measured and calculated temperatures.

Figure 4.33 represents the effect of draw ratio on the fiber tenacity. The graph illustrates that tenacity increases as the draw ratio increases. The graph also shows a smaller difference in the tenacity and the lower draw ratios. The points indicate that the measured temperatures fit calculated temperature curves relatively well.

Based on Figures 4.32 and 4.33, the run with the highest tenacity was Run #14 with a tenacity of 2.808 g/den, run at a temperature of 90^{o}C, a draw ratio of 28.2 and a concentration of 10%. The lowest tenacity was observed to be Run #10 with a tenacity of 1.660 g/den, run at a temperature of 106^{o}C, a draw ratio of 26.7 and a concentration of 10%.

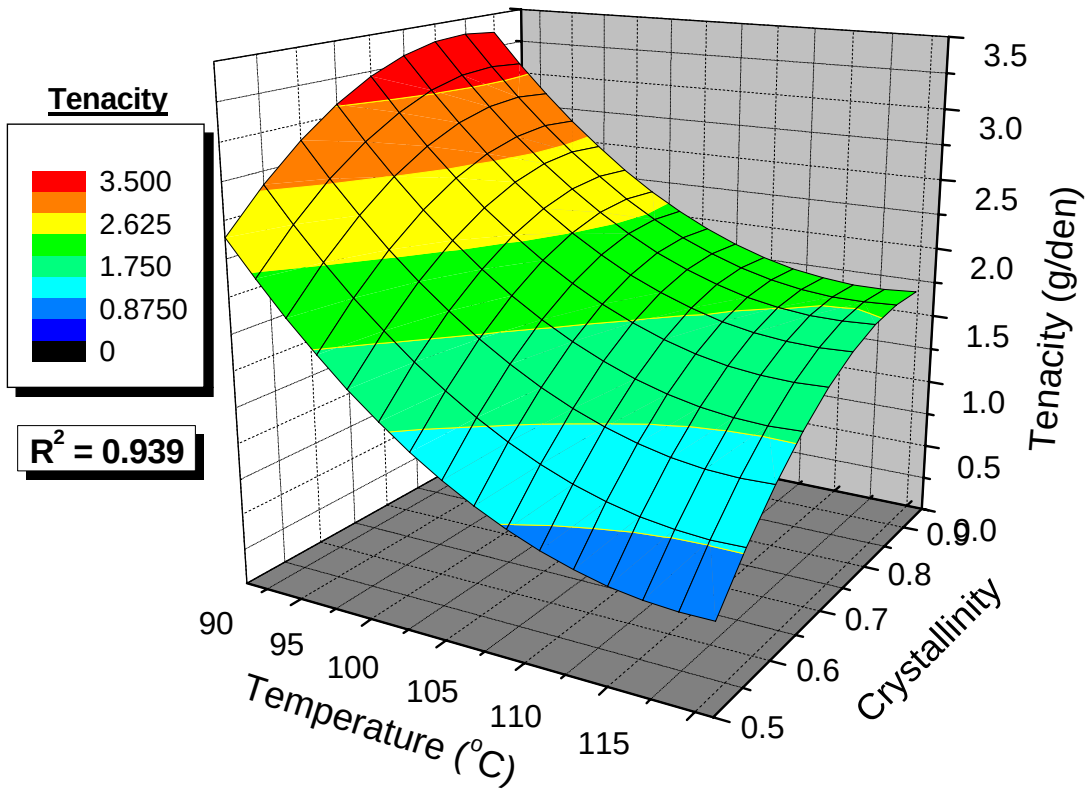

Figure 4.34: The effect of temperature and crystallinity on the fiber tenacity for a 10% solution.

Figure 4.34 represents the effect that the variation of temperature and crystallinity had on the fiber tenacity. As illustrated in this graph, a lower temperature and a high crystallinity will produce fibers with a high tenacity. Also observed as the crystallinity is decreased, there is a greater decrease in the fiber tenacity at lower temperatures than compared to the higher temperatures. Also at higher temperatures there is less of a difference in the tenacity of the fiber. This indicates that lower temperatures have a greater effect the tenacity of the fiber.

4.8.3.2 Concentration Variation – Experiment 2

Figure 4.35 represents the surface regression curve for effect solution concentration and draw ratio had on the fiber tenacity. This graph illustrates that the highest tenacity occurs at high concentrations and high draw ratios. This means that a high solution concentration at a high draw ratio would yield stronger fibers. As previously stated, the goal of the fiber spinning is to have a fiber with a high tenacity. Therefore, based on Figures 4.31 and 4.35, higher concentrations, higher draw ratios and lower temperatures would achieve this goal.

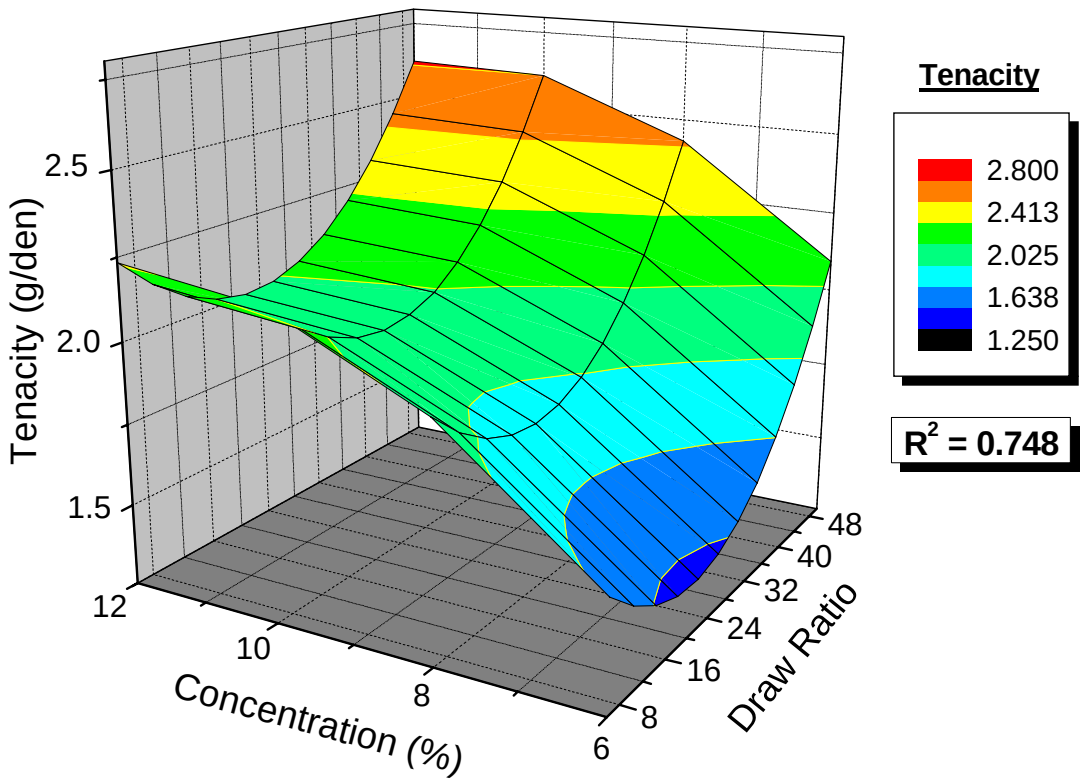

Figure 4.35: The effect of concentration and draw ratio on the fiber tenacity at 100°C.

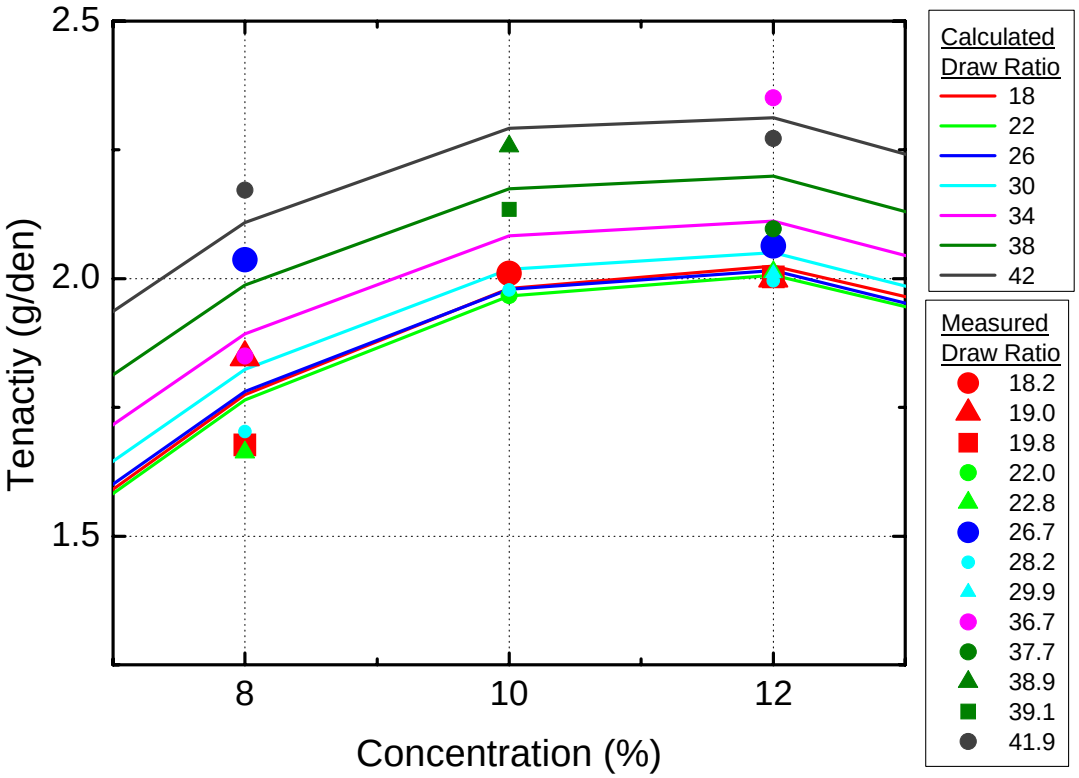

Figure 4.36: The effect of concentration on the fiber tenacity at 100°C for measured and calculated draw ratios.

Figure 4.36 represents the effect of concentration on the tenacity of fiber where the lines are the calculated draw ratios based on the regression analysis and the points represent the measured draw ratio points for the runs in Experiment 2. The graph indicates an increase in the tenacity of the fiber as concentration increases. At the higher concentrations, the tenacity appears to level off indicating that the fibers maintain a certain strength of the concentration. Also observed, at lower draw ratios, the tenacity did not vary as widely in comparison to the higher draw ratios. The points indicate that the measured draw ratios somewhat fit calculated draw ratio curves.

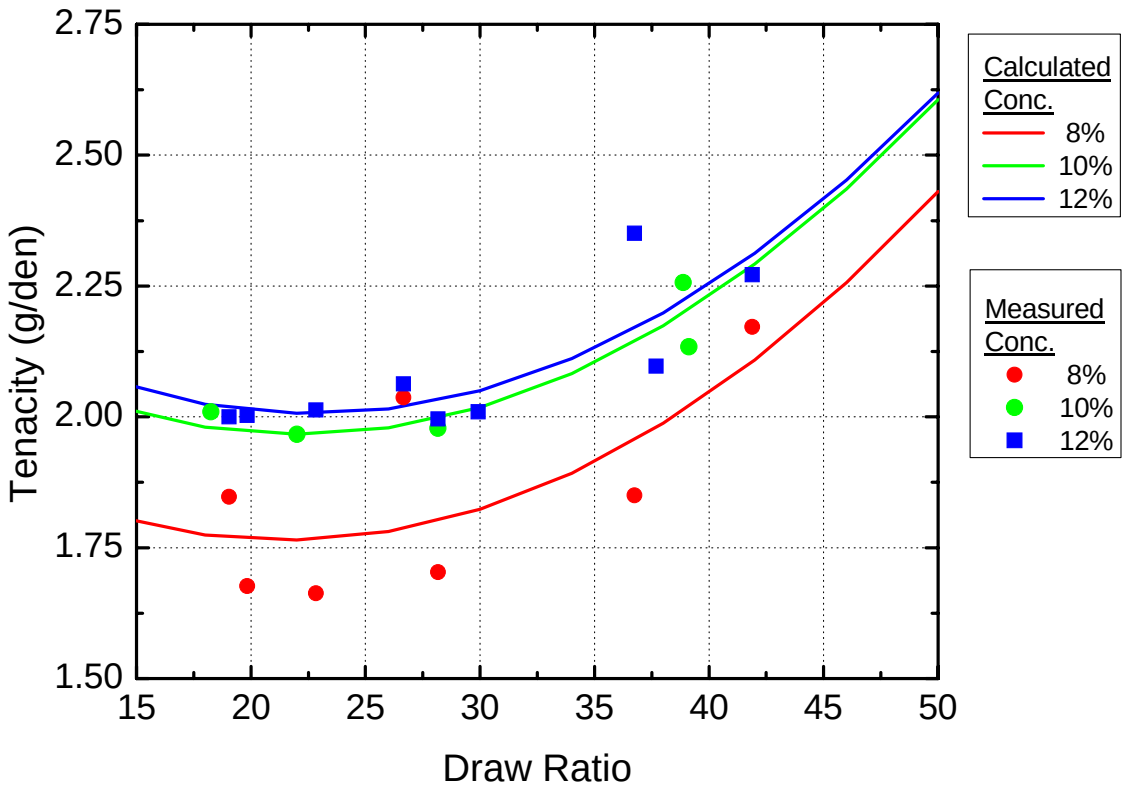

Figure 4.37: The effect of draw ratio on the fiber tenacity at 100°C for measured and calculated solution concentrations.

Figure 4.37 represents the effect of draw ratio on the fiber tenacity. The graph shows an increase in the tenacity as the draw ratio increases. The points indicate that all of the measured concentration points appear to follow the calculated concentration curves. However, there is less of a difference between the 12% curve compared with the 10% curve than the 10% curve compared to the 8% curve. This could be an indication of possible thermal degradation or liquid crystal formation at some concentrations and not others or the occurrence of a two-phase system.

Based on Figures 4.36 and 4.37, the run with the highest tenacity was Run #25 with a tenacity of 2.351 g/den, run at a temperature of 100°C, a draw ratio of 36.7 and a concentration of 12%. The lowest tenacity was observed to be Run #24 with a tenacity of 1.663 g/den, run at a temperature of 100°C, a draw ratio of 22.8 and a concentration of 8%.

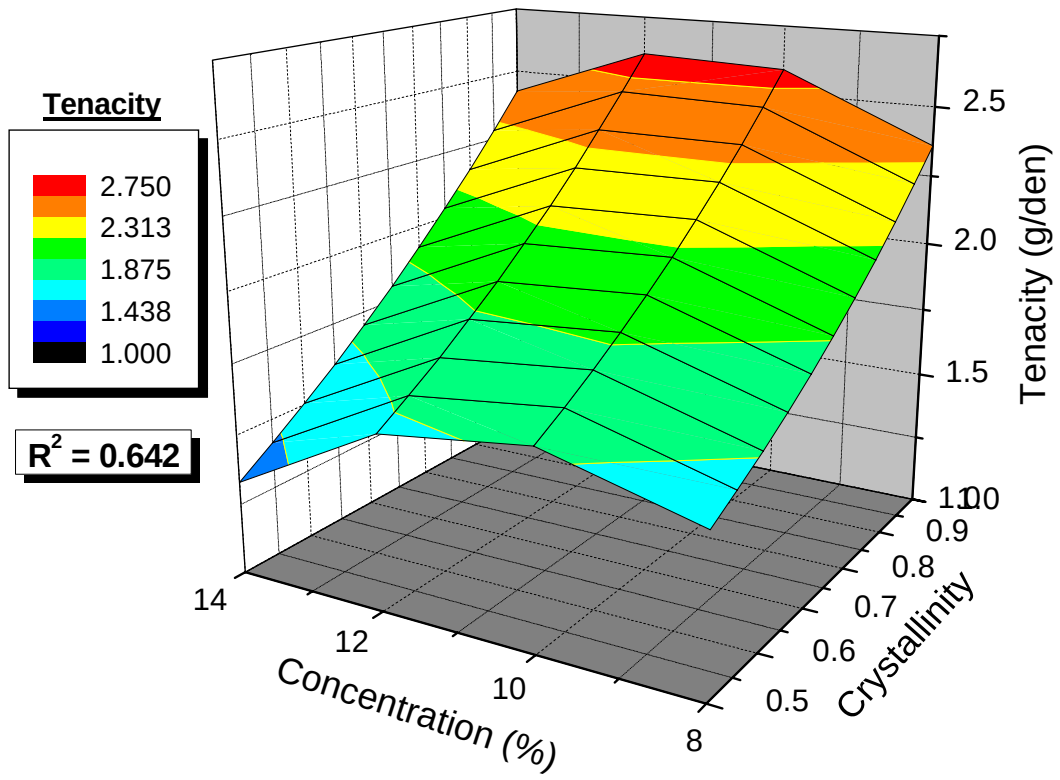

Figure 4.38: The effect of concentration and crystallinity on the fiber tenacity at 100°C.

Figure 4.38 represents the effect the variation of concentration and crystallinity had on the fiber tenacity. As illustrated in this graph, a high concentration and a high crystallinity will produce fibers that have a high tenacity. Also observed, as the crystallinity decreased, there is a greater decrease in fiber tenacity at a higher solution concentrations than compared to the lower concentrations. This indicates that an increasing concentration will have a greater impact on the fiber tenacity than the crystallinity.

Overall, based on Figures 4.34 and 4.38 when correlating the crystallinity to the fiber tenacity, it can be determined the low temperatures, mid to lower solution concentrations and high crystallinity will yield a fiber with a high tenacity.

4.9 Orientation Number Analysis

4.9.1 Calculations

Before the orientation numbers could be analyzed they had to be calculated based on the experimental input parameters. Three orientation numbers were calculated and correlated with the fiber tenacity and crystallinity. The first orientation number was calculated for the orientation within the die itself. Equation 4.19 represents the orientation number of the die, $N_{OR(die)}$.

$$N_{OR(die)} = \lambda \varepsilon_H \dot{\varepsilon} \qquad (4.19)$$

Where the relaxation time (λ) was calculated based on the G' and G" crossover points for the complex viscosity data shown in Table 4.4. The Hencky strain rate (ε_H) was calculated from the die entrance radius and the die exit radius and the elongational strain rate ($\dot{\varepsilon}$) was an initial parameter.

The second orientation number was calculated for the orientation of the fiber in the air gap. Equation 4.20 represents the orientation number of the air gap, $N_{OR(AG)}$.

$$N_{OR(AG)} = \lambda \varepsilon_{H(AG)} \dot{\varepsilon}_{(AG)} \qquad (4.20)$$

Table 4.4: Calculated and measured relaxation times for all runs.

Run #	Conc.	Temp [T] (^oC)	Relaxation time [λ] (s)	Run #	Conc.	Temp [T] (^oC)	Relaxation time [λ] (s)
1	10	100	1.23E-02	17	8	100	8.47E-03
2	10	100	1.23E-02	18	8	100	8.47E-03
3	10	100	1.23E-02	19	8	100	8.47E-03
4	10	100	1.23E-02	20	8	100	8.47E-03
5	10	100	1.23E-02	22	8	100	8.47E-03
6	10	94.1	**1.69E-02**	24	8	100	8.47E-03
7	10	94.1	**1.69E-02**	25	12	100	1.57E-02
8	10	94.1	**1.69E-02**	26	12	100	1.57E-02
9	10	94.1	**1.69E-02**	27	12	100	1.57E-02
10	10	105.9	**9.70E-03**	28	12	100	1.57E-02
11	10	105.9	**9.70E-03**	29	12	100	1.57E-02
12	10	105.9	**9.70E-03**	30	12	100	1.57E-02
13	10	105.9	**9.70E-03**	31	12	100	1.57E-02
14	10	90	2.23E-02	32	12	100	1.57E-02
15	10	110	**8.50E-03**	33	12	100	1.57E-02
16	8	100	8.47E-03				

Where bold represents a relaxation time calculated from a linear regression.

The Hencky strain rate ($\varepsilon_{H(AG)}$) was calculated from the radius of the fiber at the beginning of the air gap and the radius of the fiber at the end of the air gap. It should be noted that the radius of the fiber at the beginning of the air gap is the same as the exit radius of the die. The elongational strain rate ($\dot{\varepsilon}_{(AG)}$) was calculated based on Equation 2.6 and taking into account the length of the air gap and that the initial velocity of the air gap is the same as the exit velocity of the die. Although the fibers are cooling in the air gap and therefore their relaxation time is increasing, the same relaxation times are used for the calculations related to the air gap as were used for the die calculations.

Finally, the third orientation number was calculated for the orientation of both the die and the fiber in the air gap. Equation 4.21 represents the total orientation number, $N_{OR(Tot)}$.

$$N_{OR(Tot)} = \lambda \varepsilon_{H(Tot)} \dot{\varepsilon}_{(Tot)} \qquad (4.21)$$

The Hencky strain rate ($\varepsilon_{H(Tot)}$) was calculated from the radius of the entrance of the die and the radius of the fiber at the end of the air gap. When the elongational strain rate ($\dot{\varepsilon}_{(Tot)}$) was calculated the initial velocity at the die entrance and the total length of the die and the air gap combined was taken into account.

A schematic representing the orientation number equations as well the equations used for the Hencky strain rates and elongational strain rates can be found in Appendix G. The orientation numbers for all of the runs as well as additional correlations to tenacity and crystallinity are also listed in Appendix G.

4.9.2 Herman's Orientation Factor Correlations with Orientation Numbers

Figure 4.39 represents the correlations of the Herman's orientation factor with the orientation number for the die. Part (a) of the figure represents the correlation for the 10% solution data, and part (b) represents the correlation for the 8% and 10% solution data. This graph indicates that as the orientation number increases the orientation factor also increases. This supports the definition of the orientation number as being an indication of the level of orientation induced in the die. Also represented are the R^2 values where the best correlation of the orientation factor to the die orientation number includes both the 8% and 10% solutions.

Figure 4.40 represents the correlations of the Herman's orientation factor with the orientation numbers for the die, the air gap and the total. Each correlation is for the 8%, 10% and 12% solutions excluding runs #17, #26 and #29 which are considered outlier points and would alter the fit of the data. The R^2 values indicate that the die orientation number had the best correlation followed by the total orientation. The correlation with the orientation number in the die also indicates that inclusion of the 12% solution data significantly decreases the correlation. This is consistent with the apparent difference of the 12% solution compared to the 8 and 10% solutions noted earlier. This suggests that the level of orientation in the fiber is strongly affected by the die as indicated for the R^2 values.

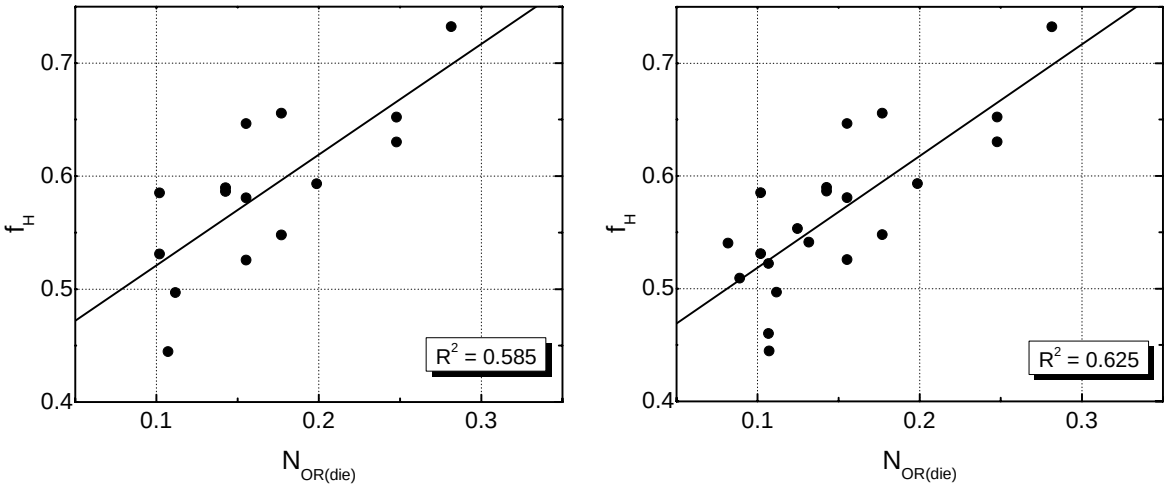

Figure 4.39: Herman's orientation factor versus the die orientation number for (a) 10% solution (b) 8% and 10% solutions.

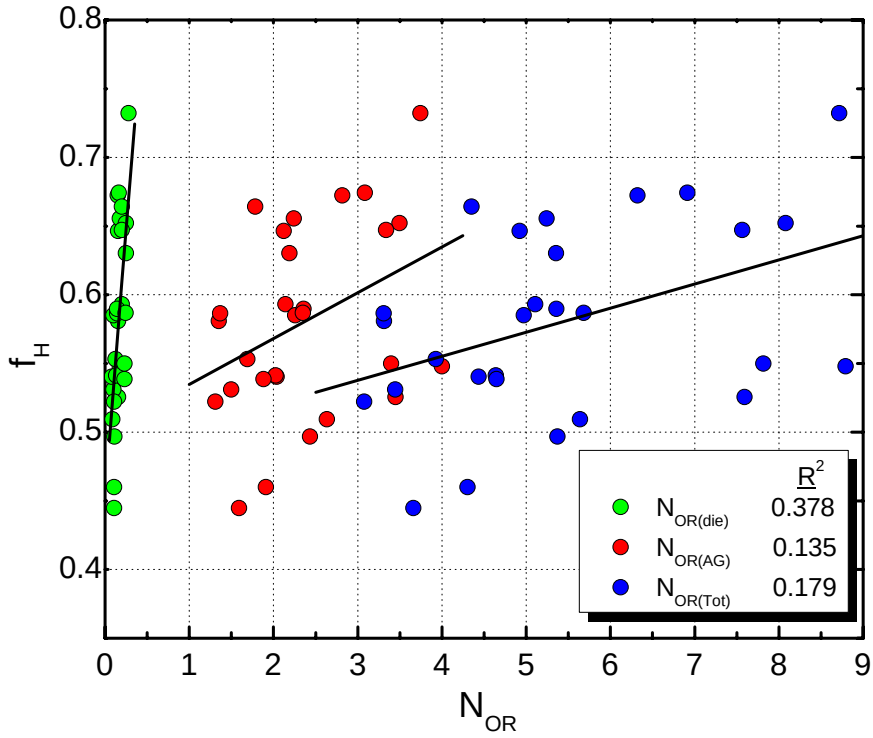

Figure 4.40: Herman's orientation factor versus orientation numbers for 8%, 10% and 12% solutions.

Figure 4.40 illustrates that the Herman's orientation factor correlates better with what is happening in the die than in the die, and the air gap combined even with the inclusion of the 12% data.

Figures 4.41 and 4.42 represent the surface regression curve for the effect of the temperature and the die orientation number on the Herman's orientation factor for the fibers. Note that the temperature scale in Figures 4.41, 4.42 and 4.43 has been inverted compared to previous figures to better illustrate the responses. Figure 4.41 represents the results of just the 10% solution and Figure 4.42 represents the results for the 8% and 10% solutions. The graphs indicate that in general lower temperatures increases the orientation of the fiber. The comparison of the two reveals that the correlation using just the 10% solution was better than using both the 8% and 10% solutions. This is opposite of what was determined from Figure 4.39. The addition of temperature to the correlation of orientation factor and orientation number increased the R^2 value for the 10% solution. This suggests that temperature plays a significant role on the level of orientation of the fiber.

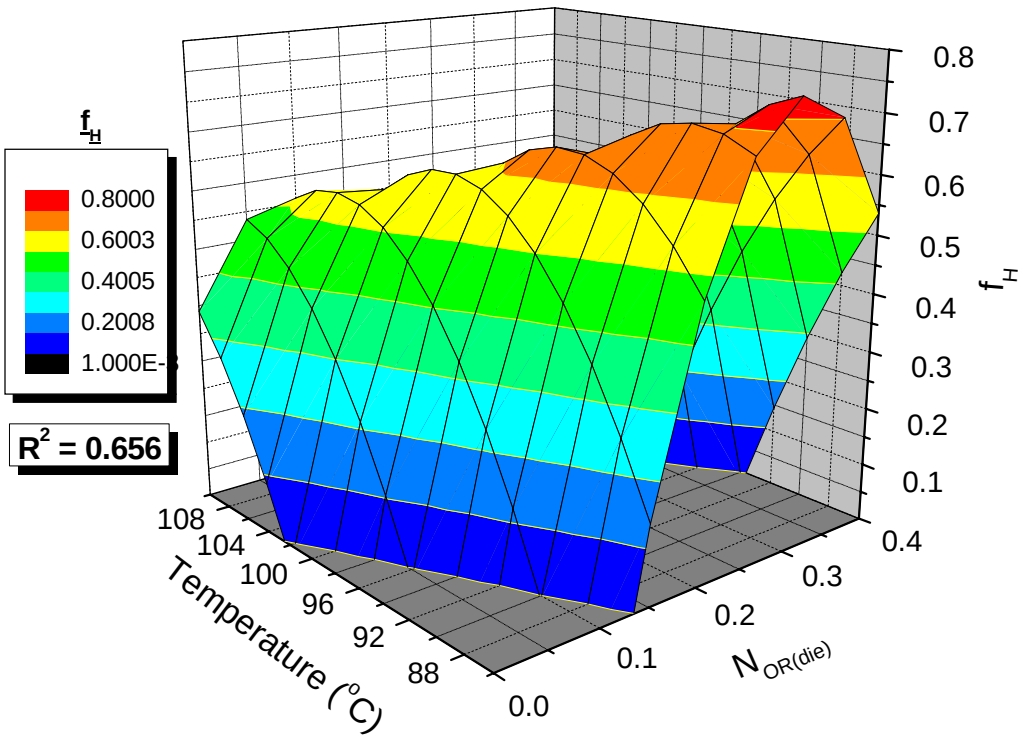

Figure 4.41: **Effect of temperature and die orientation number of the Herman's orientation factor for a 10% solution.**

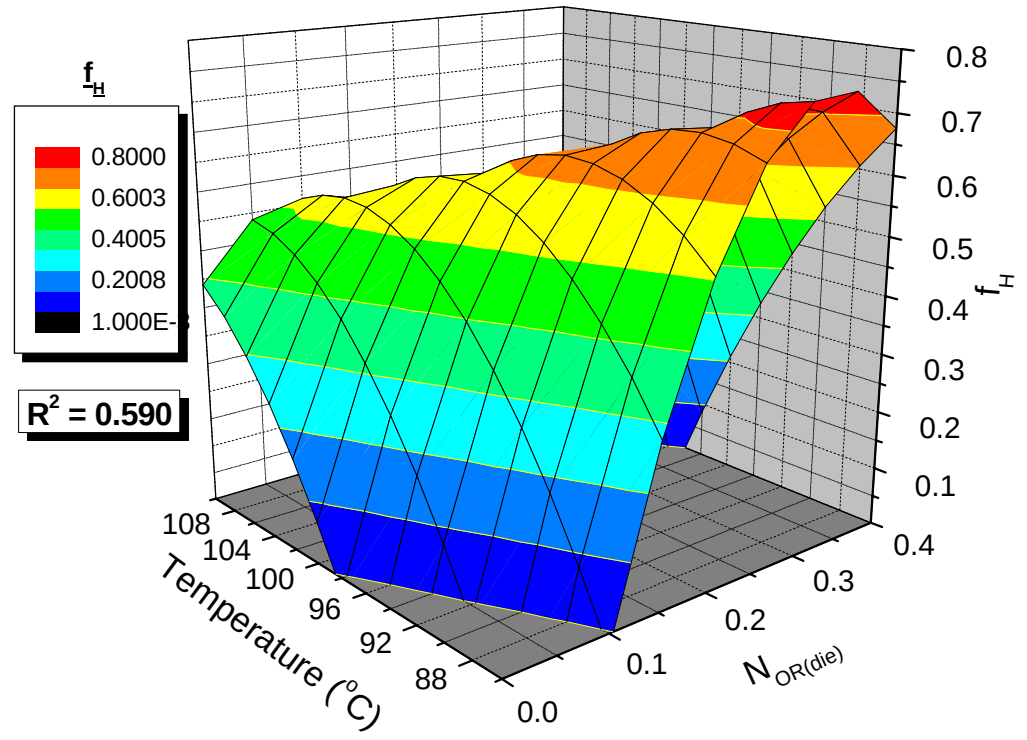

Figure 4.42: **Effect of temperature and die orientation number of the Herman's orientation factor for 8% and 10% solutions.**

Figure 4.43 represents the surface regression curve for effect of the temperature and total orientation number on the Herman's orientation factor of the fibers for a 10% solution. As the orientation number increases, it theoretically represents the level of orientation within the fiber. Therefore, it would be expected that an increase in the orientation factor of the fiber would also increase the orientation number. The graph illustrates that in general, at lower temperatures, the orientation factor increased when the orientation number increased.

The comparison of Figure 4.41 to Figure 4.43 confirms that the Herman's orientation factor correlates better with what is happening in the die. All of these figures suggest that there is a good connection with the orientation number, especially in the die and with the actual orientation of the fiber. The folding of the curves, i.e. the decrease of the Herman's orientation factor at higher temperatures and orientation numbers in Figures 4.41 to Figures 4.43 indicates a significant temperature effect. This suggests that relaxation of orientation in the air gap and coagulation bath becomes increasingly influential at higher temperatures when significant orientation was imposed in the die. Apparently at the higher temperatures the effect of relaxation on the orientation induced in the die and induction of additional orientation in the air gap is dominant over imposition of additional orientation in the air gap. It appears that, particularly in the air gap with a free surface, at the higher temperatures there is an increasing competition between relaxation and induction of additional orientation by draw down. However relaxation in the die is inhibited by the constraining walls. The rate of relaxation is apparently dependent on level of orientation, temperature and physical boundary constraints.

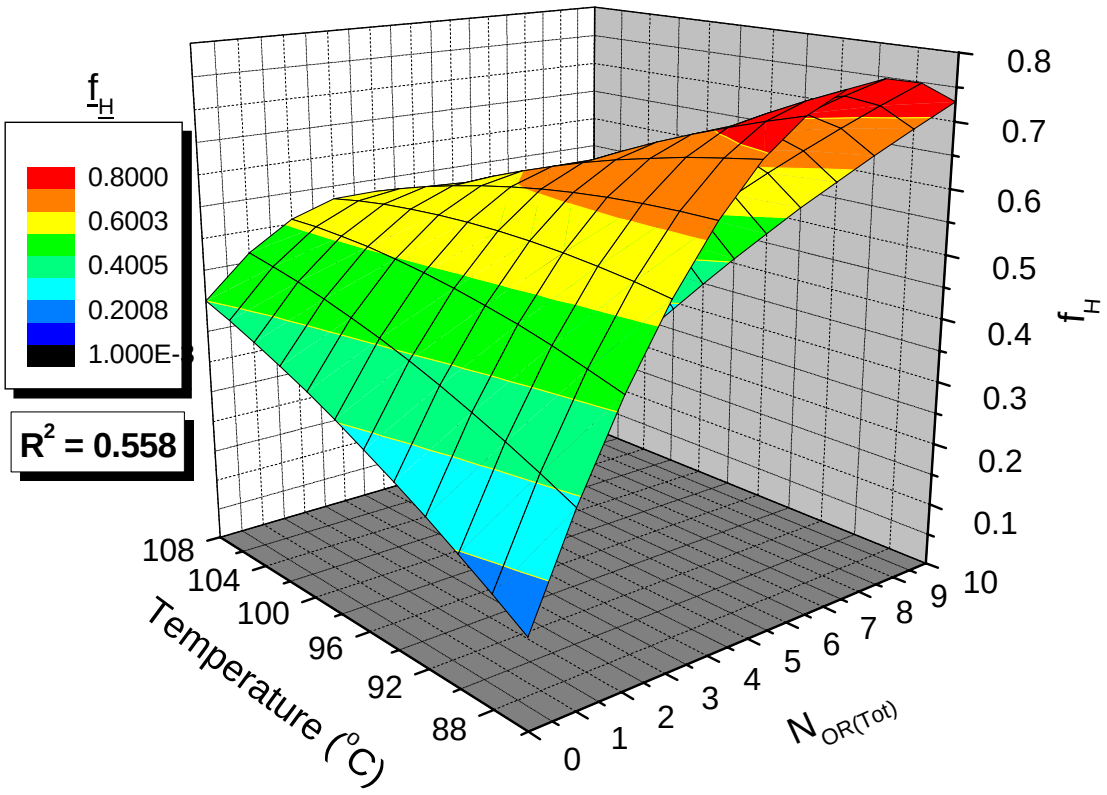

Figure 4.43: The effect of temperature and orientation factor on the total orientation number for a 10% solution.

4.9.3 Tenacity Correlations with Total Orientation Number

Figure 4.44 represents the linear and parabolic correlations for the orientation numbers of the die, air gap and total with the tenacity for the variation in temperature. This figure illustrates a significant increase in orientation number for the air gap as well as the total, thus suggesting that the orientation number within the die is not as significant. Also observed in this figure is a general increasing trend of the tenacity as the orientation number increases. The comparison between the linear and parabolic regression R^2 values indicates that the parabolic curve had a more accurate fit to the actual data points.

Figure 4.45 represents the addition of temperature to the correlation of tenacity and orientation number. As indicated by the high R^2 value, the correlation between the tenacity and the orientation number is increased with the addition of temperature to the correlation.

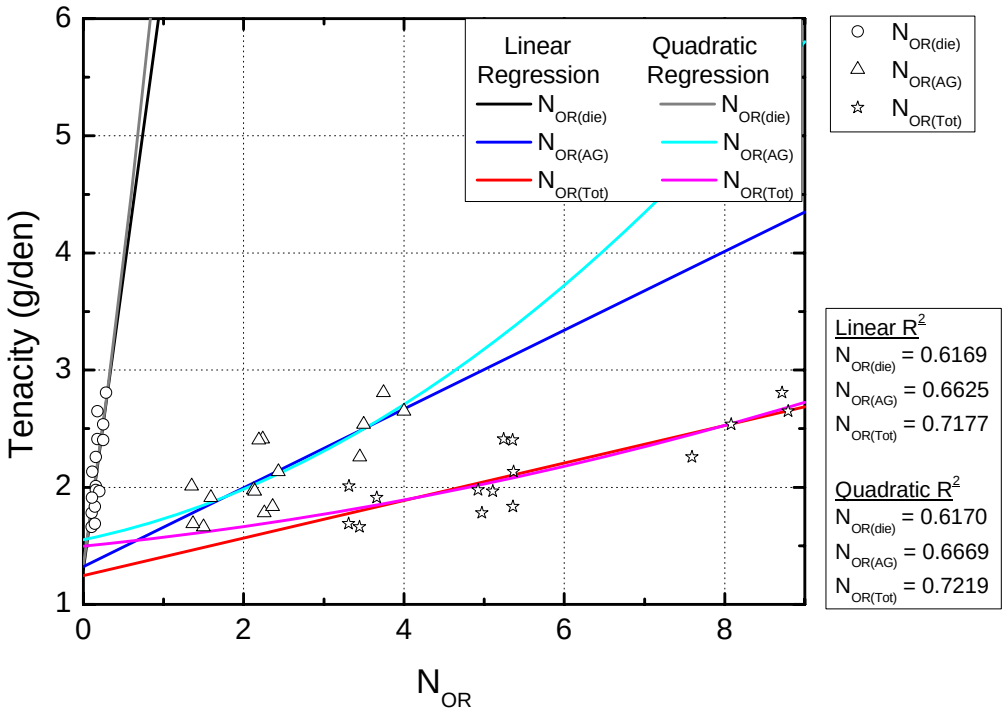

Figure 4.44: **Tenacity versus all orientation numbers at a constant 10% solution concentration for linear and quadratic regressions.**

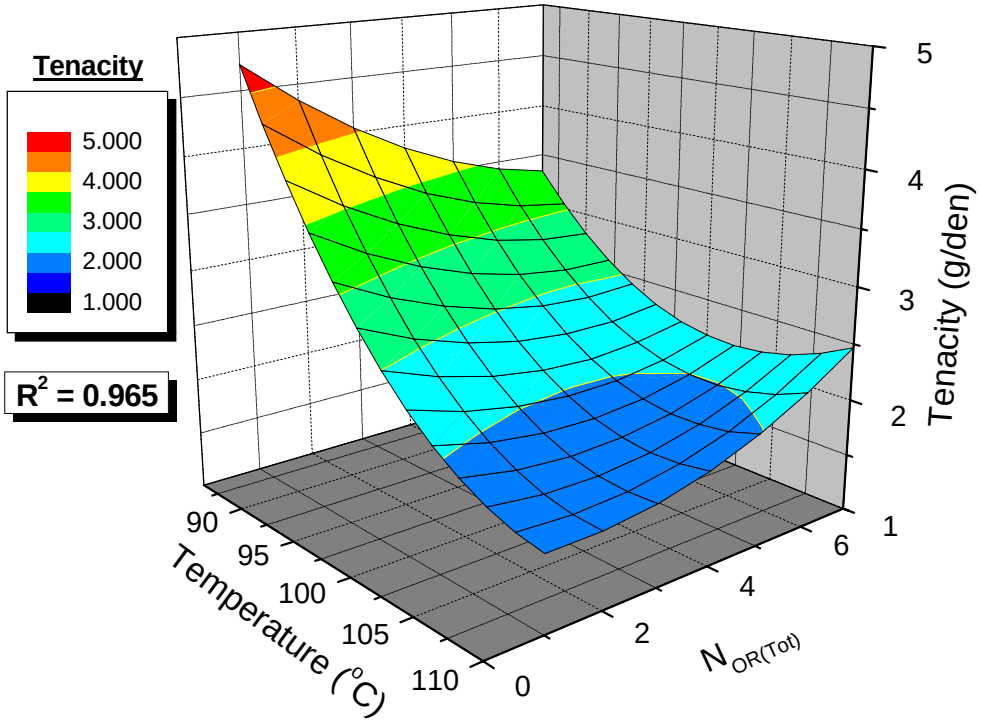

Figure 4.45: **The effect of temperature and total orientation number on the tenacity of a 10% solution.**

Chapter 5 – Discussion

5.1 Complex Viscosity

The graphs of Section 4.1 illustrate the effects of temperature and solution concentration variation on the complex viscosity. The results for the complex viscosity of the 8%, 10% and 12% cellulose/[C_4mim]Cl solutions at 80°C, 90°C and 100°C were as expected. As indicated in the results, the increase in temperature decreased the viscosity of the solutions. These results confirm the already known conclusion that for almost all viscose solutions, an increase in temperature of the solution will decrease the viscosity.

Also illustrated in the graphed results is the effect of the solution concentration on the complex viscosity which indicates that as the solution concentration is lowered, the lower the complex viscosity of the solution will become. Again the results confirm the intuitive conclusion that the less cellulose dissolving pulp added to the [C_4mim]Cl, the more liquid it will remain thus the lower viscosity as seen in Figure 5.1 (Watson, 2006).

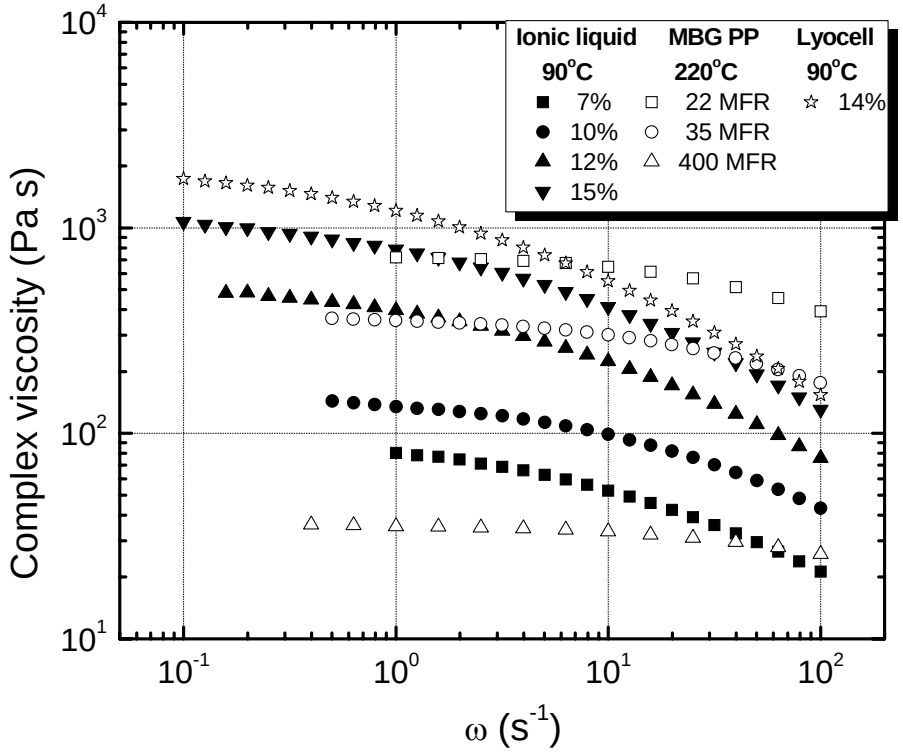

Figure 5.1: Complex viscosity comparison graph of hand mixed ionic liquid solutions, MBG PP and Lyocell for 90°C (Watson, 2006).

Also represented in Figure 5.1 is a comparison evaluation of the results with other recorded data sets. This graph represents the complex viscosity of various solution concentrations of lyocell, melt blowing grade (MGB) polypropylene and manually mixed cellulose/[C_4mim]Cl solutions. Figure 5.1 illustrates the same trend for lyocell and the cellulose/[C_4mim]Cl solutions although the [C_4mim]Cl solutions are lower in viscosity. In Figure 5.2, the complex viscosities of the mechanically mixed [C_4mim]Cl solutions used in this research were transposed onto Figure 5.1 for a more in depth comparison.

It can be observed that the mechanically mixed solutions, shown in red, blue and green, have higher viscosities than the manually mixed solutions. The difference in the viscosities of the manually mixed and the mechanically mixed is most likely due to a more thorough mixing thus resulting in a higher viscosity. The higher viscosity can be seen especially with the 8% and 10% solutions. However, the 12% solution for this research is lower than expected. As the figures in Section 4.1 illustrate, the 12% solution had a reduced complex viscosity that was close, just slightly higher, than the 10% solution.

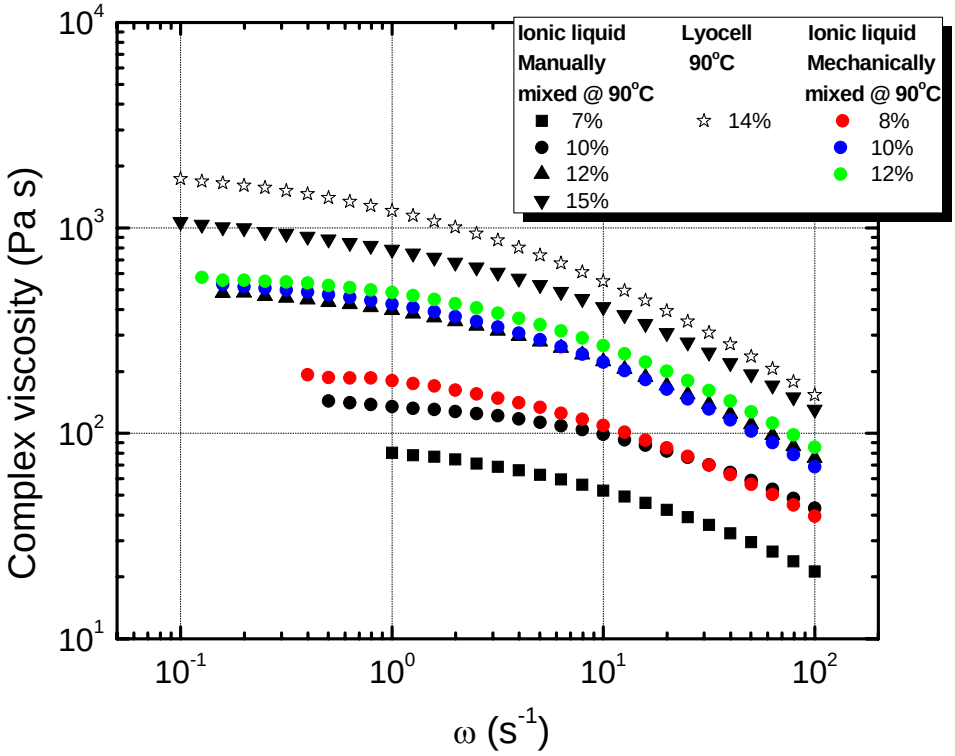

Figure 5.2: Complex viscosity comparison graph with the data from Figure 5.1 with the transposed data from Figure 4.1 at 90°C.

This indicates that the 12% solution, as suggested previously, had a level of thermal degradation thus lowering the viscosity closer to the 10% solution. The mixing time for the 12% solution was of necessity longer than the 8 and 10% solutions to achieve a good solution. Another possibility is a difference in the solution characteristics between 8% and the 10% and 12% solutions. There could be liquid crystal formation at some concentrations and not others or a two-phase system that causes the 10% and 12% to have similar viscosities at low strain rates.

As previously stated in Section 4.1, the complex viscosity for each solution concentration was temperature shifted to the reference temperature of 90^{o}C and the R^2 values were all about 0.99 indicating an extremely accurate correlation. Therefore, based on the R^2 values and the comparison data from Figures 5.1 and 5.2 it was determined that the complex viscosities for the solutions used in this research were acceptable.

5.2 Elongational Viscosity

The graphs of Section 4.2 illustrate the effects of temperature and solution concentration variation as well as Hencky strain rate on the elongational viscosity. The results for the elongational viscosity of the 8%, 10% and 12% cellulose/[C_4mim]Cl solutions at 80^{o}C, 90^{o}C and 100^{o}C as well as for Hencky strain rates of 6, 7 and 8.4 were as expected.

As indicated in the results, is the effect of the solution concentration on the elongational viscosity, which indicates that the as the solution concentration is decreased, the lower the elongational viscosity of the solution becomes. The results confirms the intuitive conclusion that the less cellulose dissolving pulp added to the [C_4mim]Cl, the more liquid it will remain thus the lower viscosity. Also observed in the results is that the increase in temperature, decreased the viscosity of the solutions. Again, these results confirm the already well known conclusion that for almost all viscose solutions, an increase in temperature of the solution will decrease the viscosity.

The effect of the Hencky strain rate variation was also observed and it was found that the lower Hencky strain rates also reduced the elongational viscosity. The larger exit diameter of the die with the same inlet diameter, thus the lower Hencky strain rate, would

correspond to a lower orientational force to overcome thereby allowing the solution to flow more freely thus reducing the elongational viscosity.

The two shifting methods were done to ensure the most accurate results possible. Both methods had high R^2 values that allow each to be acceptable on an individual basis. However, Method 2 had slightly higher R^2 values; this indicates that the orientational viscosity ratio of Method 2 had more of an effect on the results than the relaxation time ratio of Method 1.

As previously stated in Section 4.2, the elongational viscosity for each solution concentration was temperature shifted to the reference temperature of 90^{o}C and Hencky strain shifted to 7. The R^2 values were all about 0.99 indicating an extremely accurate correlation. Therefore, based on the viscosity measurements, both complex and elongational, shown in Section 4.1 and 4.2, as well as based on the high R^2 values for all shift results, it was determined that the viscosity for the solutions used in this research were acceptable.

5.3 SEM Images

Based on the comparison of all the SEM images for all the runs, it was determined that the temperature did not have as high of an effect as the draw ratio and the concentration of the fiber appearance. This was due to the similar surface appearance of fiber spun at the same draw ratio but under difference temperatures. However, the increase in the draw ratio had a significant effect on the fibers. As the draw ratio was increased the fibers became flatter suggesting the fibers did not have adequate time to set before being stretched.

The concentration of the solution also affected the resulting fiber. The SEM images indicated that the lower solution concentrations caused the surface of the fiber to appear rough and striated. This suggests that the fiber had a higher quantity of [C_4mim]Cl within the fiber that was not removed during the spinning process through the coagulation bath. Therefore, during the soaking stage after the fiber was spun, it "deflated" as the remaining [C_4mim]Cl was released from the fiber.

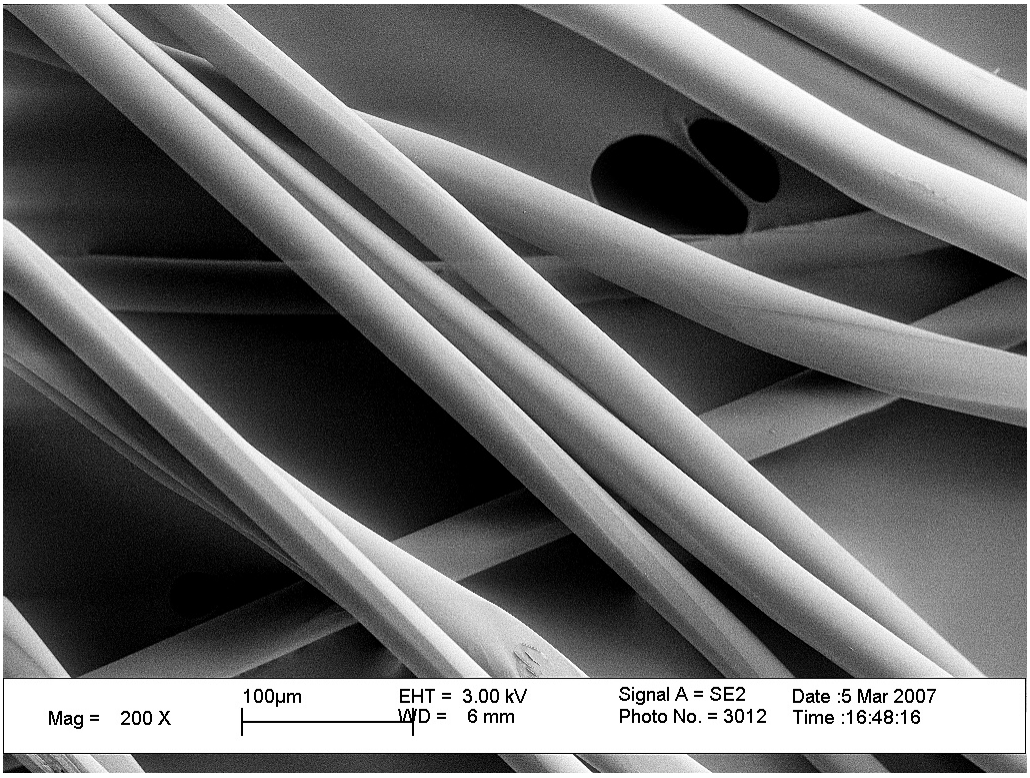

Figure 5.3: Run #31 – 12% solution, T = 100°C, $\dot{\varepsilon}$ = 1.75 s^{-1}, v_t = 56 m/min, D_r = 19.0

The highest quality fiber based on appearance would be a high concentration fiber spun at a low draw ratio. Therefore Run #31, had the best surface appearance, shown in Figure 5.3.

5.4 Crystallinity

The optimal cellulose pre-cursor for a carbon fiber would have a high crystallinity. The analysis of the crystallinity results for both Experiment 1 and Experiment 2 indicate that a high draw ratio, a high temperature and a high solution concentration would yield a fiber with a high crystallinity. The figures in Section 4.6 indicate that the draw ratio seems to have a greater effect on the crystallinity than the temperature, indicating that as the fiber was being spun at the higher draw ratios, the cellulose molecules were being oriented more parallel to one another thus increasing the crystallinity. Also indicated in the figures was the increase in crystallinity as the solution concentration increased suggesting that the amount of molecules within the fibers due to

the concentration affected the level of crystallinity. The analysis of the crystallinity indicates that this parameter did not correlate as highly as expected which is likely a result of the crystallinity being more affected by fiber orientation, defect structure and lateral order.

Therefore based on the results shown in Section 4.6, disregarding the outlier point of 89.6, the crystallinity for all of the runs ranged from 69.6% to 86.6%. Lyocell fibers have a crystallinity in the range of 64.04% to 72.56 % (Peng et al., 2003). This indicates that the crystallinity for the fiber spun from [C_4mim]Cl solutions is comparable to the crystallinity of Lyocell fibers, if not slightly higher.

5.5 Birefringence and Orientation Factor

By measuring the birefringence, the Herman's orientation factor was calculated which is in indicator of the level of orientation within the fiber. It was found that the fiber orientation ranged from slightly oriented to moderately oriented indicating that the orientation within the fibers was not a high as anticipated. The analysis of the data revealed several parameters that effected the orientation of the fiber.

First, the increase in the temperature during the spinning process decreased the fiber orientation, thus suggesting that thermal relaxation and perhaps degradation could have affected the orientation of the molecules. The thermal degradation of the solution would likely reduce the length of the cellulose chains. This suggests that temperature during the spinning process is a key parameter affecting the properties of the fiber.

The second observation is the increase in the total orientation number as the Herman's orientation factor increased. This supports the definition of the orientation number being an indication of the orientation of the fiber. A fiber produced with a high orientation number would be expected to have a high orientation factor. However, this is the general trend, the results obtained from the calculations reveal that there are exceptions.

The analysis of the relationship between crystallinity and the orientation factor indicated a decreasing trend overall. This was not expected. Generally, a high level of orientation is an indication that the crystallinity is also high. However, in this case the

opposite in true. Again this supports the conclusion that the crystallinity was affected by many unforeseeable factors and is not a good indicator of level of orientation within the fiber. Finally, it was observed that as the orientation factor of the fiber increased, the tenacity of the fiber also increased. This suggests that fibers with a high orientation factor would be stronger as a result of the cellulose molecules being more closely packed.

The orientation factor was also correlated with the orientation number of the die as well as the total orientation number which revealed that the orientation factor had a better correlation to the die orientation number than to the air gap orientation number or the total orientation number. This suggests that the level of orientation in the fiber is being imposed and retained primarily in the die. The competing orientation development, the relaxation in the air gap and coagulation bath do not contribute as much to the orientation in the final fibers. Also, at higher temperatures relaxation is dominant.

When temperature was incorporated into the correlations of orientation factor and orientation numbers the resulting graphs illustrated an arc pattern or what could be described as “folding back”. This was most likely an effect of relaxation of orientation imposed predominantly in the die becoming increasingly dominant at higher temperature over induction of additional orientation during draw down in the air gap and in the coagulation bath.

5.6 Tenacity

The optimal cellulose pre-cursor would have high fiber tenacity. Tenacity is an indication of fiber strength. The analysis of the correlation results of the effect of temperature, concentration and crystallinity, shown in Section 4.8.3, indicate that a higher orientation number in the die, high draw ratio, low temperature, high concentration and a high crystallinity results in a fiber with a high tenacity.

Based on the figures in this section, the draw ratio and orientation number in the die appeared to have the greatest effect on the tenacity, more so than that temperature or the concentration. A high draw ratio for the fibers during the spinning process thus increasing the orientation of the cellulose molecules imposed in the die and inhibiting relaxation, increased the strength of the fiber. Low temperatures are also optimal because

of reduced thermal relaxation and possible degradation that would weaken the fiber. A high concentration also affects the tenacity of the fiber by increasing the amount of cellulose molecules within the extruded fibers. The higher content of cellulose molecules would increase the tenacity of the fiber.

Also observed was the relationship between the fiber crystallinity and the tenacity. When the fiber had a higher crystallinity, the tenacity was also higher. However, as mentioned previously, the increase in crystallinity decreased the level of orientation in the fiber again indicating that there are several factors affecting the crystallinity of the fiber. As a result, the level of crystallinity in the fiber is not a good indication of the tenacity of the fiber.

Therefore based on the results, the fiber tenacity for all of the runs ranged from 1.66 to 2.81 g/den. Based on some studies conducted with Lyocell fibers, the tenacity can range from 4.8 to 6.9 g/den depending on the conditions of spinning (Peng et al., 2003 and Fink et al., 2001). This indicates that the tenacity for the fibers spun from $[C_4mim]Cl$ solutions are lower than the tenacity of Lyocell fibers. This lower tenacity is likely the result of the level of orientation in the fiber being lower than expected, which could be the result of a lower orientation number in this experimental setup than that for lyocell fibers.

5.7 Orientation Number

The optimal cellulose pre-cursor would have an orientation number greater than one that indicates that the fiber is in an orientation dominant mode, which results in significant orientation (Collier[2] et al., 2007). However, an orientation number near one, results in a transition region that gives flow instabilities in the hyperbolic die. This causes some data scatter and surface roughening of the fiber (Collier[2] et al., 2007). When the orientation number is less than one it appears that the elongational flow is in a relaxation dominant mode in which developing orientation is relaxing as it develops (Collier[2] et al., 2007). The results in Section 4.7 indicate for all the runs, that orientation number for the die were in a relaxation dominated state due to the orientation numbers being significantly less than one as tabulated in Appendix E.

However, the orientation number of the fiber in the air gap ranged from 1.31 to 4.00 and the orientation number for the combined die and the air gap ranged from 3.08 to 8.79. All of which are greater than one indicating that the within the air gap the fibers should be in an orientation dominate state, thus causing a significant increase in the orientation of the fiber. As noted however that at higher temperatures relaxation becomes dominant in the air gap and coagulation bath. Perhaps the transition to an orientation dominant regime occurs at a lower orientation number when the fiber is constrained by the die walls than when it is draw down in a free boundary region. All of the data on orientation number previous to this study has been on flow through converging dies. A much smaller die exit diameter with the same entrance diameter or a higher strain rate would increase the orientation number in the die for this material. Also, the orientation number correlated with temperature accounts for the fact that the fiber is cooling and relaxing at different rates in the air gap as well as the coagulation bath for different extrusion temperatures. Relaxation and cooling rates are important to maintaining orientation imposed in the die as well as externally.

5.8 R^2 values for Regression Correlations

Tables 5.1 and 5.2 represent the R^2 values for all the correlations done between the different variables, both dependent and independent. Table 5.1 shows the regression correlation R^2 values for crystallinity, tenacity and the total orientation number Each of these parameters, with the exception of crystallinity being correlated to itself, was correlated to the temperature/draw ratio, the concentration/draw ratio, temperature/crystallinity, and the concentration/crystallinity.

The R^2 values ranged from 0.532 to 0.993. The temperature correlations were found to have higher R^2 values than the concentration correlations. This suggests that the concentration had a greater effect on the parameters due to the decrease in the R^2 values. Overall, the correlations of the parameters to the draw ratio were better than the correlations to the crystallinity.

Table 5.1: Summary of the R^2 values for all the regression correlations.

Parameter	Regression Correlations		
	Crystallinity	Tenacity	f_H
Temperature and D_r	0.818	0.949	--
Concentration and D_r	0.554	0.748	--
Temperature and Crystallinity	--	0.939	--
Concentration and Crystallinity	--	0.642	--
Temperature and $N_{OR(die)}$ for 10% soln.	--	--	0.590
Temperature and $N_{OR(die)}$ for 8% and 10% soln.	--	--	0.558
Temperature and $N_{OR(Tot)}$ for a 10% soln.	--	--	0.656
Temperature and $N_{OR(Tot)}$	--	0.965	--

Table 5.2: Summary of the R^2 values for all the orientation number regression correlations.

Parameter	Regression Correlations							
	Temperature Variation – Constant 10% solution				*Concentration – Constant 100°C*			
	Tenacity		Crystallinity		Tenacity		Crystallinity	
	Linear	Parabolic	Linear	Parabolic	Linear	Parabolic	Linear	Parabolic
$N_{OR(die)}$	0.617	0.617	0.224	0.290	0.049	0.093	8.21E-05	0.026
$N_{OR(AG)}$	0.6625	0.6669	0.0595	0.0660	0.4182	0.4257	0.2521	0.5139
$N_{OR(Tot)}$	0.7177	0.7219	0.0309	0.0342	0.4064	0.4304	0.2215	0.5144

The R^2 values in Table 5.2 represent the linear and quadratic correlations of all the orientation numbers to the tenacity and the crystallinity. Overall, these values were much lower than desired. However, the tenacity was the most accurate for the orientation numbers that accounted for the air gap and the R^2 values were much lower for the correlations with the crystallinity.

This table indicates that the temperature and orientation number had the most impact on the tenacity. Even with some values indicating that there was little correlation between parameters; one should consider the number of variables within the experiments that could affect the outcome. There are many unforeseen influences that could shape the results of an already complex wet-spinning system. Therefore, without further refining of the spinning system the results will not be as accurate as desired.

5.9 Summary

The optimal cellulose carbon fiber pre-cursor with be highly oriented and highly crystalline. Table 5.3 shows the runs that yielded the highest and lowest values for all the

parameters. Some runs appear in the highest and lowest categories repeatedly, for example, Runs #7, #14 and #25 are listed several times for having values the would suit the optimal. On the other hand, Runs #2, #10, #16 and #19 are shown to repeatedly have properties that do not meet the optimal.

However, when choosing the parameter set that would best meet the ideal goal, it could not be based on the run that was repeated the most often in Table 5.3. When analyzing the effect to the temperature, concentration and the draw ratio on the fiber properties it was observed that there was no right set of parameters that would give the optimal fibers. Several factors had to be considered, mainly what parameters had the greatest effect on the fiber. These parameters were determined to be the tenacity and the orientation of the fiber.

Therefore, the analysis of these results revealed that the overall run with the highest tenacity and the highest orientation factor was Run #14, a 10% solution spun at 90^{o}C with a draw ratio of 28.17. Table 5.4 represents the list the measured results of this run. Figure 5.4 through 5.6 are the SEM image, WAXS intensity peak and fiber breakage graph for Run # 14.

Table 5.3: Summary of highest and lowest run results for all variables.

Results	**Experiment 1** *Temperature variation, constant 10% solution*				**Experiment 2** *Concentration variation, constant 100^{o}C*			
	Highest Run	Value	Lowest Run	Value	Highest Run	Value	Lowest Run	Value
Crystallinity (%)	#11	86.6	#2	69.6	#25	89.6	#19	64.9
f_H	#14	0.73	#15	0.44	#26	0.75	#17	0.29
Tenacity (g/den)	#14	2.81	#10	1.66	#25	2.35	#24	1.66
$N_{OR(die)}$	#14	0.282	#10	0.102	#33	0.245	#16	0.082
$N_{OR(AG)}$	#7	4.00	#2	1.35	#4	3.45	#19	1.31
$N_{OR(Tot)}$	#7	8.79	#12	3.31	#32	7.82	#19	3.08

Table 5.4: Parameters and results for Run #14.

Run #	Con.	Temp [T] (^{o}C)	Draw Ratio [D_r]	CI (%)	Relax-ation time [λ] (s)	$N_{OR(die)}$	$N_{OR(AG)}$	$N_{OR(Tot)}$	Lin. Den. (den)	Ten. (g/den)
14	10	90	28.17	74	2.23E-2	0.282	3.75	8.72	7.64	2.81

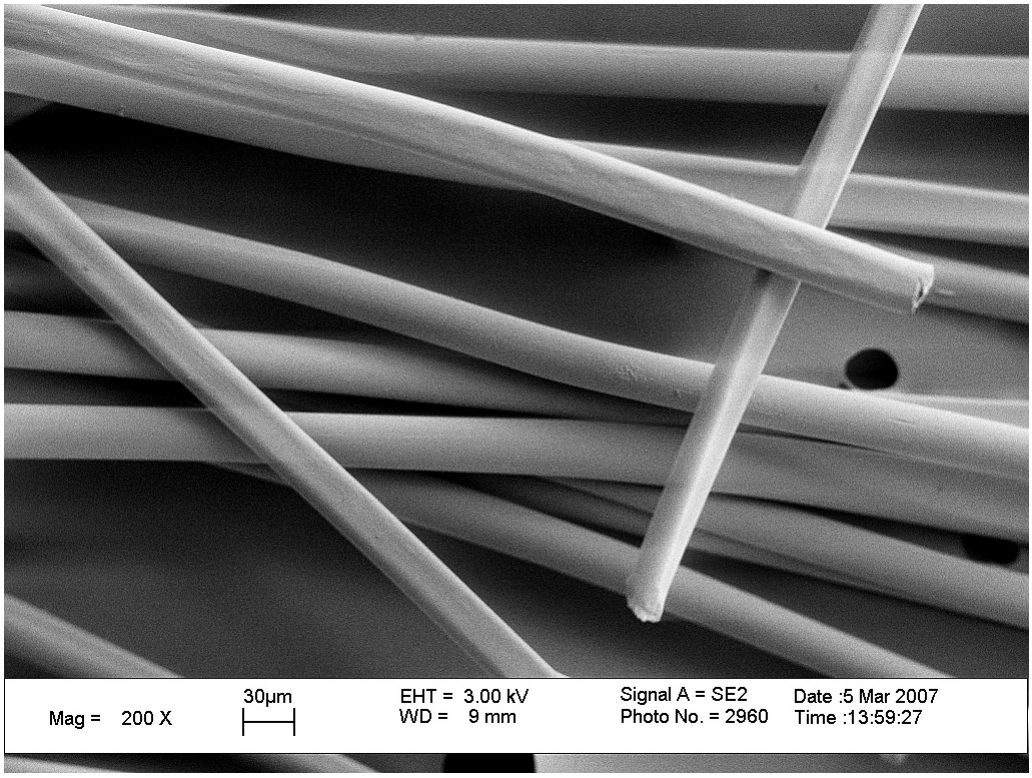

Figure 5.4: SEM image of Run #14

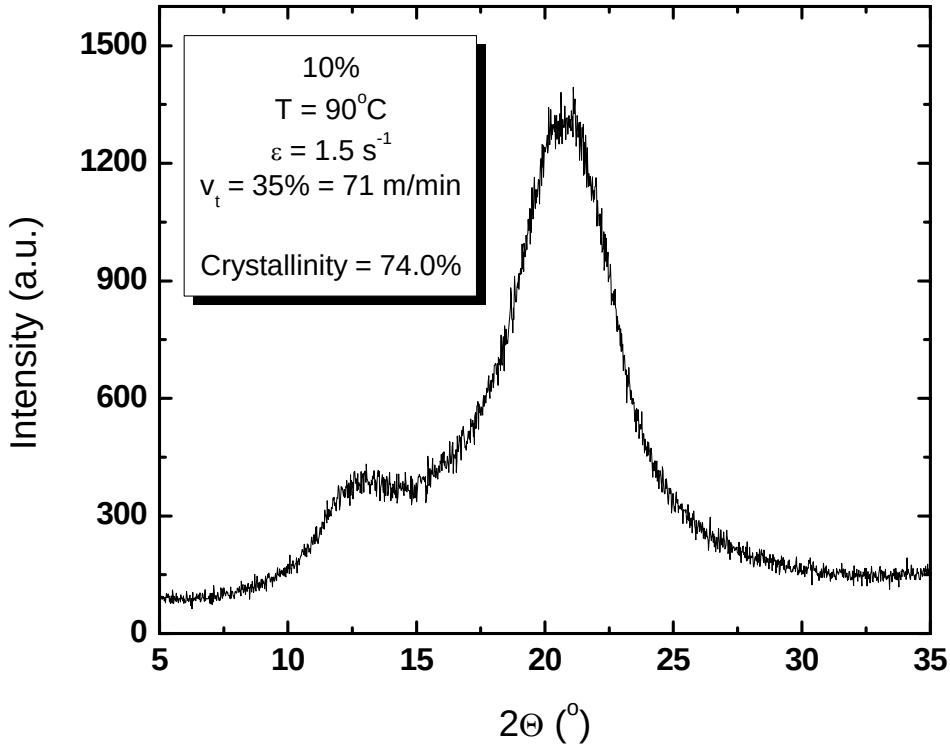

Figure 5.5: WAXS Intensity scan of Run #14.

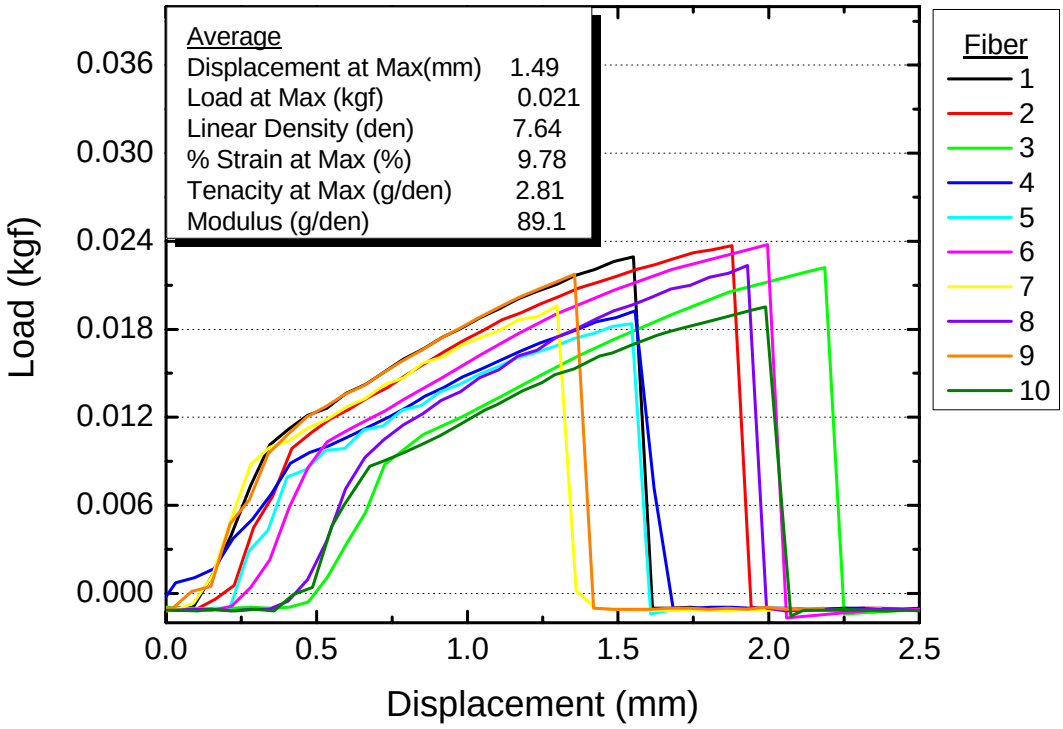

Figure 5.6: Load verses displacement of Run #14.

Chapter 6 – Conclusion

The primary goal of this research was to spin highly oriented and highly crystalline cellulose fibers from an $[C_4mim]Cl$ solution. These fibers, in addition to their environmentally advantageous processing, have potential as precursors for carbon fibers. One prime consideration for carbon fiber precursors is the degree and size of defects. Therefore, by using the elongational flow spinning technique to induce molecular orientation in the spinneret enabled the production of highly oriented, highly crystalline fibers. The effect of spinning conditions on fiber properties was then determined.

The key steps of this research was to first determine the rheological behavior of cellulose/$[C_4mim]Cl$ solutions by understanding the characteristics of cellulose, $[C_4mim]Cl$ and the cellulose/$[C_4mim]Cl$ solution. Secondly, a continuous single fiber was spun from the cellulose/$[C_4mim]Cl$ solutions through the hyperbolically converging die in order to prove the experimental methodology. Finally, the effects of cellulose concentration, processing temperature and draw ratio were determined by measuring the microscopic appearance, the tenacity and the crystallinity for the resulting fibers.

The results of the rheological study for the complex and elongational viscosities revealed that viscosity of the cellulose/[C4mim]Cl solution decreased when exposed to higher temperatures, at lower concentrations and at low Hencky strain rates. A smaller difference in the viscosity in the 12% solution in comparison to the 8% and 10% solutions was observed for the complex viscosity. This indicates that the 12% solution had a lower viscosity than expected for this concentration. This difference is more noticeable in the reduced complex viscosity that was close, just slightly higher, than the 10% solution. This suggests that the 12% solution had a level of thermal degradation thus lowering the viscosity closer to the 10% solution. Another possibility is a difference in the solution characteristics between 8% and the 10% and 12% solutions. There could be liquid crystal formation at some concentrations and not others or a two phase system that causes the 10% and 12% to have similar viscosities at low strain rates. This is most likely the cast, since the difference in the 12% solution was not apparent in the elongational viscosity results. The effects of liquid crystal formation and/or two phase systems are more noticeable in complex viscosity analysis.

It can be concluded from the analysis of the cellulose fibers spun from the [C_4mim]Cl solutions, that the temperature, solution concentration and the draw ratio had a significant effect on the fiber properties, especially the fiber tenacity and the orientation factor as well as the orientation number. It should also be noted that the draw ratio in the air gap when coupled with temperature gave the highest correlation with the tenacity. The calculation of the orientation number in the air gap included the draw down ratio through the Hencky strain and also the strain rate and relaxation time of the polymer. The orientation number calculation for the air gap used the same relaxation time as was used for the fluid in the die even though the filament was cooling rapidly in the air gap. This would contribute to inaccuracy of orientation number for the air gap and total orientation numbers. Therefore, the orientation number in the air gap should be much larger due to the temperature dependence of the relaxation time, consistent with the draw down in the air gap along with temperature being the most important variables.

The combination of the draw down ratio and temperature did indirectly take into account the effect of the changing polymer characteristic relaxation, hence a good correlation with the mechanical properties. Apparently, the converging flow in the die was important in developing a nearly homogeneous extrudate that could then be elongated without failure in the air gap since using a constant diameter die rather than a converging die did not allow stable drawdown. However, the draw down in the air gap was the dominant effect once sufficiently homogeneous extrudates were formed.

It is important to realize that tenacity of the fibers, that is the ratio of the average maximum load to the linear density, is probably the best indication of the quality of the fibers. This quality would include the degree of orientation and low level of defects, both important characteristics for carbon fiber precursors and other applications. The Herman's orientation factor, which is an indication of the level or orientation in the fiber, is also a good indication of fiber quality. However, the lower orientation factor indicates that the fibers are not at highly oriented as desired which could be the reason the tenacity was lower than expected. Furthermore the crystallinity is apparently not as well correlated with temperature and draw ratio; therefore probably not as good an indicator of

fiber quality since it would be affected by orientation as well as defect structure and lateral order.

Based upon the analysis of the results it was determined that fibers spun from a high concentration solution at approximately 90^{o}C at a medium draw ratio would yield the fiber properties desirable for a carbon fiber precursor, i.e. as high tenacity and a high orientation factor. The final test will be to produce an adequate amount of continuous fiber using the determined parameters for the production of carbon fibers.

In addition to the production of carbon fibers, other future studies could include several of the following ideas; the effect of temperature change in the air gap on the orientation number by modeling the heat transfer from the filament where the time in the air gap, diameter of filament as a function of position in the air gap and the starting and ending temperatures are known. Furthermore the temperature dependence of the relaxation time could be estimated from the data presented and then fit to the temperature profile of the filament in the air gap. The result would be a longitudinal and radial temperature profile. The radial profile would likely have a rather similar shape for time in the air gap so an average longitudinal profile may be satisfactory. In conclusion, this research revealed that it is possible to spin an oriented, highly crystalline fiber using elongational flow spinning techniques as well as determining what parameters in the spinning process that would be ideal.

LIST OF REFERENCES

LIST OF REFERENCES

Arlt, W., Seiler, M., Jork, C., (2003), "New Classes of Compounds for Chemical Engineering: Ionic Liquids and Hyperbranched Polymers" *Technical University of Berlin*.

Bird, R.B., Stewart, W.E., Lightfoot, E.N., (2001), Transport Phenomena, 2nd Ed., Wiley Publishing, New York, NY.

Berger, R.D., (2001), "Characterization and Comparison of Hydrophilic and Hydrophobic Room Temperature Ionic Liquids Incorporating the Imidazolium Cation." *Green Chemistry,* **3(4):** 156-164.

Bernot, R.J., Brueseke, M.A., Evans-White, M.A., Lamberti, G.A., (2005), "Acute and Chornic Toxicity of Imidazolium-based Ionic Liquids on *Daphnia magna," Environmental Toxicology and Chemistry*, **24(1):** 87–92.

Bingham, B.E.M., (1964), "A Study of the Fine Structure of Regenerated Cellulose Fibers." *Die Makromolekulare Chemie*, **77(1):** 139-152.

Brown, R.M., Jr., (2003), "Cellulose Structure and Biosynthesis: What is in Store for the 21st Century?" *J. of Polymer Science: Part A Polymer Chem.*, **42(2):** 487-495.

Chand, S., (2000), "Review: Carbon Fibers for Composites." *J. of Materials Science*, **35(6):** 1303-1313.

Cochran, W.G., Cox, G.M., (1957), Experimental Designs, 2nd Ed., Wiley Publishing, New York, NY.

[1]Collier, J.R., Romanoschi, O., Petrovan, S.J., (1998), "Elongational Rheology of Polymer Melts and Solutions." *J. of Applied Polymer Science,* **69(12):** 2357-2367.

[2]Collier, J.R., Petrovan, S.J., Hudson, N., Wie, X., (2007), "Elongational Rheology by Different Methods and Orientation Number." *J. of Applied Polymer Science,* 105(6): 3551-3561.

[3]Collier, J.R., (2005), "Analysis of Flow Through Semi-Hyperbolically Convergent die in Hyperbolical Coordinates." *ChE 547 – Transport Phenomena Class Notes*, University of Tennessee – Knoxville.

[4]Collier, B.J., Dever, M., Petrovan, S., Collier, J.R., Li, Z., Wei, X., (2000), "Rheology of Lyocell Solutions from Different Cellulose Sources." *J. of Polymers and the Environment,* **8(3):**151-154.

[5]Collier, J.R., Petrovan, S., Patil, P., Collier, B.J., (2005), "Elongational rheology of fiber forming polymers." *J. of Materials Science,* **40(19):** 5133 – 5137.

[6]Collier, J.R., Petrovan, S., Patil, P., Collier, B.J., (2003), "Temperature Shifting of Convergent Flow Measured Effective Elongational Viscosity." *J. of Applied Polymer Science,* **87(9):** 1387 – 1396.

[7]Collier, J.R., Petrovan, S., Patil, P., Collier, B.J., (2003), "Hencky Strain Shifting of Convergent Flow Measured Effective Elongational Viscosity." *J. of Applied Polymer Science,* **87(9):** 1397 – 1404.

Dever, M., Collier, B.J., Petrovan, S., Collier, J.R., (2003), "Lyocell Solutions from Undervalued Cellulose Sources." *Clothing and Textiles Research Journal*, **21(4):** 167-173.

Feigl, K, Tanner, F. X., Edwards B. J., Collier, J. R., (2003), "A numerical study of the measurement of elongational viscosity of polymeric fluids in a semi-hyperbolically converging die." *J. of Non-Newtonian Fluid Mechanics*, **115(2-3):** 191.

[1]Ferguson, J, Hudson, N.E., Odriozola, M. A., (1997), "The interpretation of transient extensional viscosity data." *J. of Non-Newtonian Fluid Mechanics,* **68(2-3):** 241-257.

[2]Ferguson, J, Hudson, N.E., J. Forsyth, J., (1998), "Transient extensional rheology and the influence of strain history." *J. of Non-Newtonian Fluid Mechanics*, **79(2-3):** 213-223.

Fink, H.P., Weigel, P., Purz, H.J., Ganster, J., (2001), "Structure formation of regenerated cellulose materials from NMMO-solutions." *Progress in Polymer Science*, **26(9):** 1473-1524.

Flory, P.J. (1953), Principles of Polymer Chemistry. Cornell University Press, New York, pg. 85.

Franks, N.E., Varga, J.K., (1979), US Patent 4145532.

Fredlake, C. P., Crosthwaite, J.M., Hert, D.G., Aki, S.N.V.K., Brennecke, J.F., (2004), "Thermophysical Properties of Imidazolium-Based Ionic Liquids." *J. of Chemical Engineering Data,* **49 (4):** 954-964.

Kong, K., Eichhorn, S.J., (2005), "Crystalline and Amorphous Deformation of Process-Controlled Cellulose-II Fibres." *Polymer*, **46(17):** 6380-6390.

Kreze, T., Strnad, S., Stana-Kleinschek, K., Ribitsch, V., (2001), "Influence of aqueous medium on mechanical properties of conventional and new environmentally friendly regenerated cellulose fibers." *Materials Research Innovations*, **4(2-3):** 107–114.

Lee, J.H., Brown, R.M., Jr., Kuga, S., Shoda, S., Kobayahi, S., (1994), "Assembly of Synthetic Cellulose I." *Biochemistry,* **91:** 7425-7429.

Lenz, J., Schurz, J., Wrentschur, E., (1992), "Comparative Characterization of Solvent Spun Cellulose and High Wet Modulus Viscose Fibres by Their Long Periods, *Acta Polmerica*, **43(6):** 307-312.

Lévêque, J. M., Luche, J. L., Pétrier, C., Roux, R., Bonrath, W., (2002), "An Improved Preparation of Ionic Liquids by Ultrasound." *Green Chemistry*, **4(4):** 357-360.

Macosko, C. W., (1994), Rheology. Principles, Measurements, and Applications, Wiley-VCH, New York, NY.

Montgomery, D.C., (1997), Design and Analysis of Experiments. 4th Ed., Wiley Publishing, New York, NY., pg 601.

Mortimer, S.A., Péguy, A.A., (1996), "Methods for Reducing the Tendency of Lyocell Fibers to Fibrillate." *J. of Applied Polymer Science*, **60(3):** 305-316.

Namboodiri, V. V. and Varma, R. S., (2002), "Solvent-Free Sonochemical Preparation of Ionic Liquids." *Organic Letters*, **4(18):** 3161-3163.

Nimlos, M.R., Blanksby, S.J., Ellison, G.B., Evans, R.J., (2003), "Enhancement of 1,2-dehydration of alcohols by alkali cations and protons: a model for dehydration of carbohydrates." *J. of Analytical and Applied Pyrolysis*, **66(1-2):** 3-27.

Northolt, M.G., Boerstoel, H., Maatman, H., Huisman, R., Veurink, J., Elzerman, H., (2001), "The Structure and Properties of Cellulose Fibres Spun from an Anisotropic Phosphoric Acid Solution." *Polymer*, **42(19):** 8249-8264.

Peng, S., Shao, H., Hu, X., (2003), "Lyocell Fibers as the Precursor of Carbon Fibers." J. *of Applied Polymer Science*, **90(7):** 1941–1947.

Rosenau, T., Potthast, A., Adorjan, I., Hofinger, A., Sixta, H., Firgo, H., Kosma, P., (2004), "Cellulose solutions in *N*-methylmorpholine-*N*-oxide (NMMO) – degradation processes and stabilizers." *Cellulose*, **9(3-4):** 283-291.

Rydholm, S.A., (1965), Pulping Processes. Interscience Publishers., New York, NY., 42-166.

Schäfer, T., Rodrigues, C. M., Afonso, C.A.M., Crespo, J.G., (2001), "Selective Recovery of solutes from Ionic Liquids by Pervaporation-A Novel Approach for Purification and Green Processing." *ChemComm Communications*, **17:** 1622-1623.

Seddon, K.R., (1997), "Ionic Liquids for Clean Technology." *J. of Chemical Technology and Biotechnology*, **68(4):** 351-356.

Shariq K, A.E., Yamaki, M., (1999), "Carbon Fibers." *Chemical Economics Handbook-SRI International*, **542:** 4000.

Sheldon, R., (2001), "Catalytic reactions in ionic liquids," *Chemical Communications*, 2001, **23:** 2399–2407.

[1]Simon, I., Scheraga, H.A., (1988), "Structure of Cellulose. 1. Low-Energy Conformation of Single Chains." *Macromolecules*, **21(4):** 983-990.

[2]Simon, I., Glasser, L., Scheraga, H.A., (1988), "Structure of Cellulose. 2. Low-Energy Crystalline Arrangements." *Macromolecules*, **21(4):** 990-998.

[1]Swatloski, R. P., Spear, S. K., Holbrey, J.D., Rogers, R.D., (2002), "Dissolution of Cellulose with Ionic Liquids." *J. of the American Chemical Society*, **124(18):** 4974-4975.

[2]Swatloski, R. P., Holbrey, J.D., Memon, S.B., Caldwell, G.A., Caldwell, K.A., Rogers, R.D., (2004), "Using *Caenorhabditis elegans* to probe toxicity of 1-alkyl-3-methylimidazolium chloride based ionic liquids," *Chemical Communications*, **6:** 668–669.

Walsh, P.J., (2001), "Carbon Fibers." *ASM Handbook*, **21:** 35-40.

Watson, J.L., (2006), "Rheology of 1-butytl-3-methylimidizoluium chloride Cellulose Solutions." Master's Thesis, University of Tennessee, Knoxville, TN.

White, J.L., Spruiell, J.E., (1983), "The Specification of Orientation and its Development in Polymer Processing." *Polymer Engineering and Science*, **23(5):** 247-256.

Wilkes, J. S., (2004), "Properties of Ionic Liquid Solvents for Catalysis." *J. of Molecular Catalysis A: Chemical*, **214(1):** 11-17.

Ziabicki, A., (1976), Fundamentals of Fibre Formation. The Science of Fibre Spinning and Drawing. Wiley-Interscience Publications., London, England.

APPENDIX A

Complex Viscosity

Table 1A: R^2 and ΔH values from the Carreau and Cross fit models for all sessions.

Session	Model	Shift Factor	Temperature (K)			R^2 for a_T	ΔH (kCal/mol)	R^2 for ΔH
			353.18	363.18	373.18			
1	Carreau	a_T =>	2.272	1	0.4011	0.9997	22.76	0.9989
	Cross	a_T =>	2.325	1	0.3908	0.9995	23.40	0.9989
2	Carreau	a_T =>	2.291	1	0.3772	0.9993	23.69	0.9980
	Cross	a_T =>	2.371	1	0.3754	0.9998	24.19	0.9986
3	Carreau	a_T =>	2.278	1	0.3458	0.9996	24.79	0.9966
	Cross	a_T =>	2.351	1	0.3404	0.9991	25.40	0.9966
4&5	Carreau	a_T =>	2.214	1	0.3940	0.9994	22.67	0.9981
	Cross	a_T =>	2.289	1	0.3920	0.9996	23.16	0.9987
6	Carreau	a_T =>	2.078	1	0.3956	0.9986	21.81	0.9965
	Cross	a_T =>	2.149	1	0.4012	0.9974	22.04	0.9978
7	Carreau	a_T =>	2.398	1	0.3702	0.9994	24.52	0.9986
	Cross	a_T =>	2.499	1	0.3685	0.9996	25.11	0.9992
8%	Carreau	a_T =>	2.078	1	0.3956	0.9974	21.81	0.9965
	Cross	a_T =>	2.149	1	0.4012	0.9986	22.04	0.9978
10%	Carreau	a_T =>	2.285	1	0.3748	0.9997	23.74	0.9979
	Cross	a_T =>	2.345	1	0.3741	0.9998	24.10	0.9984
12%	Carreau	a_T =>	2.398	1	0.3702	0.9994	24.52	0.9986
	Cross	a_T =>	2.499	1	0.3685	0.9996	25.11	0.9992

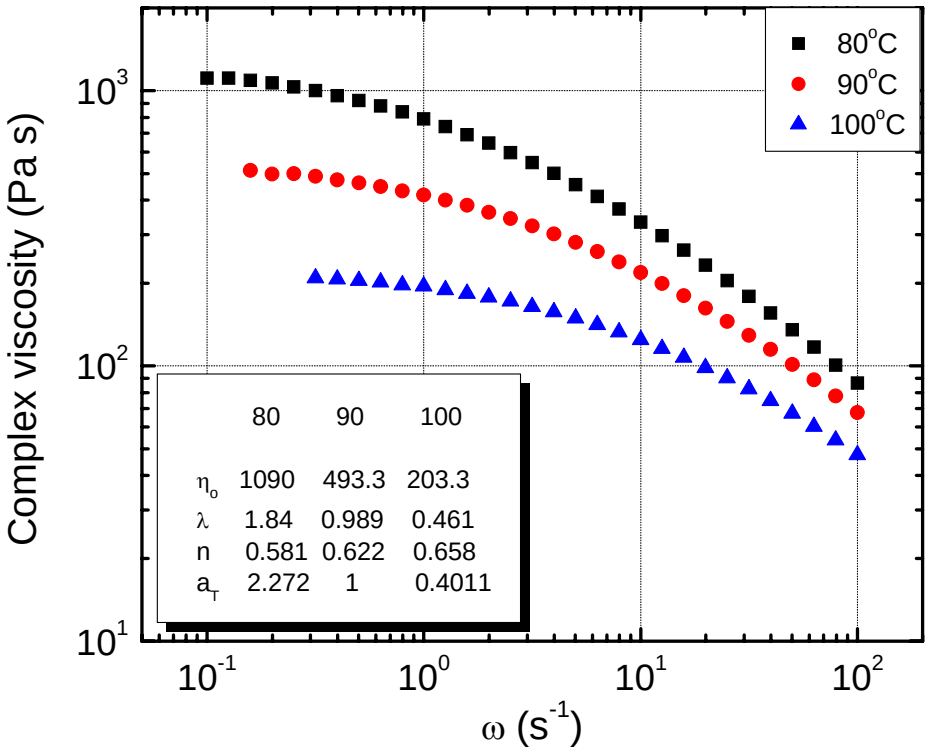

Figure A1: Session 1 – Complex viscosity for a 10% solution.

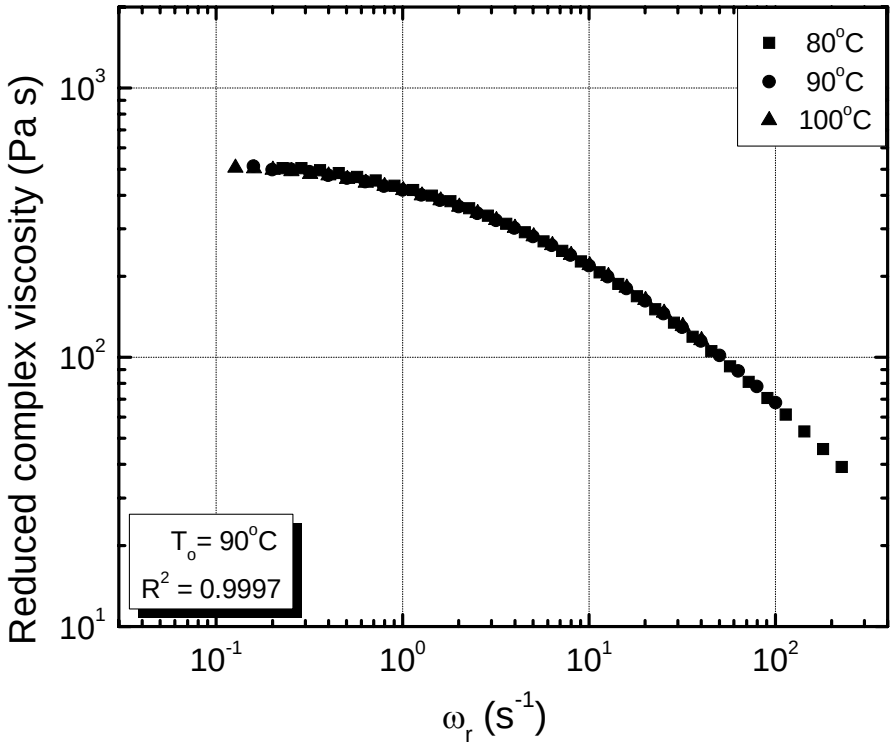

Figure A2: Session 1 – Temperature shifted reduced complex viscosity for a 10% solution using Cross model.

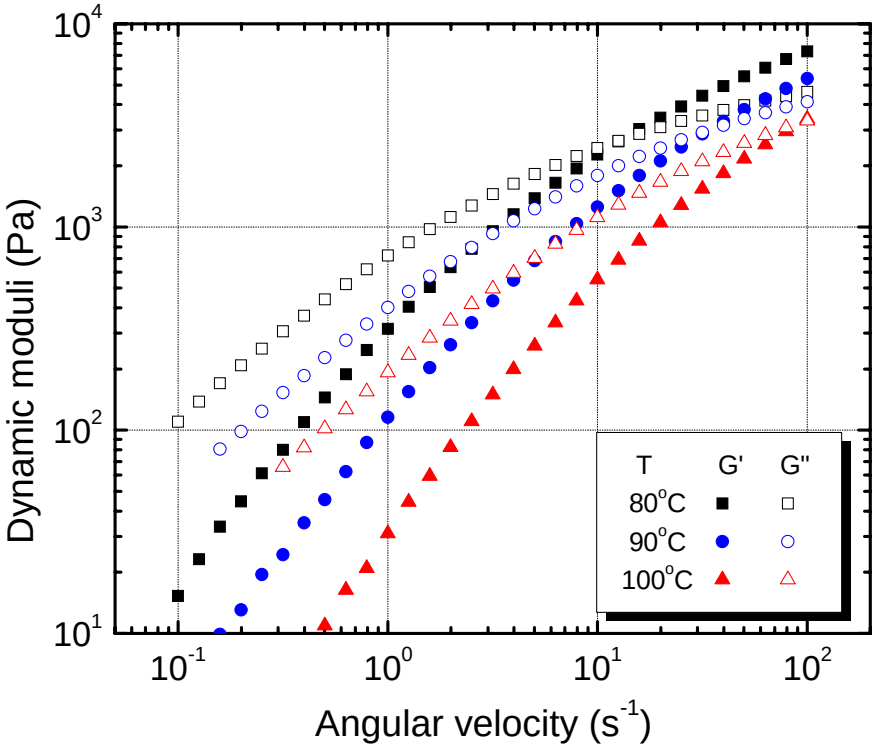

Figure A3: Session 1 – Dynamic moduli for a 10% solution.

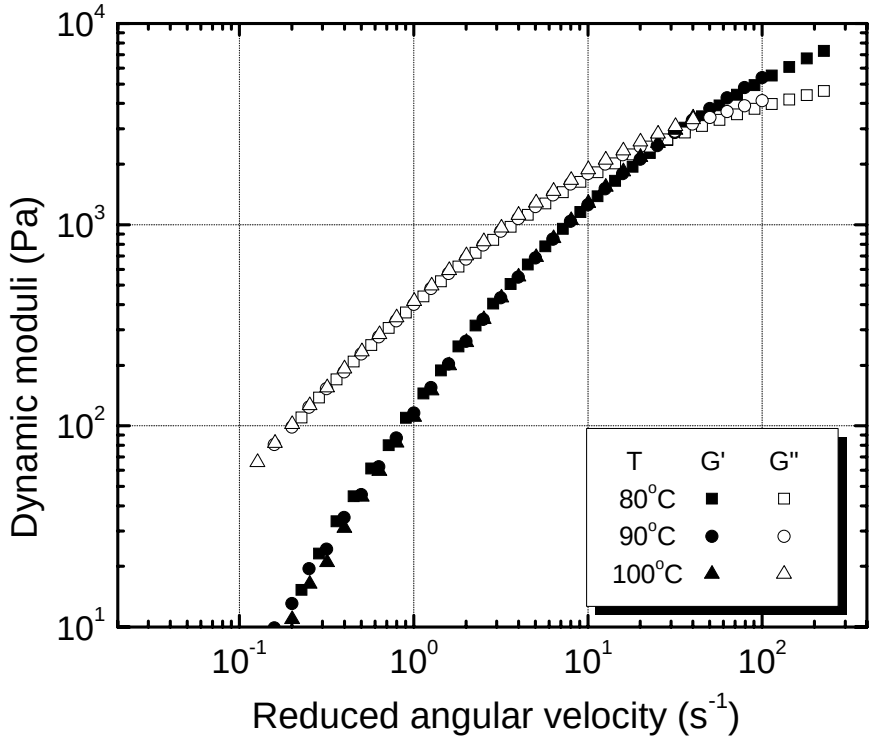

Figure A4: Session 1 – Dynamic moduli at reduced angular velocity for a 10% solution using Cross model.

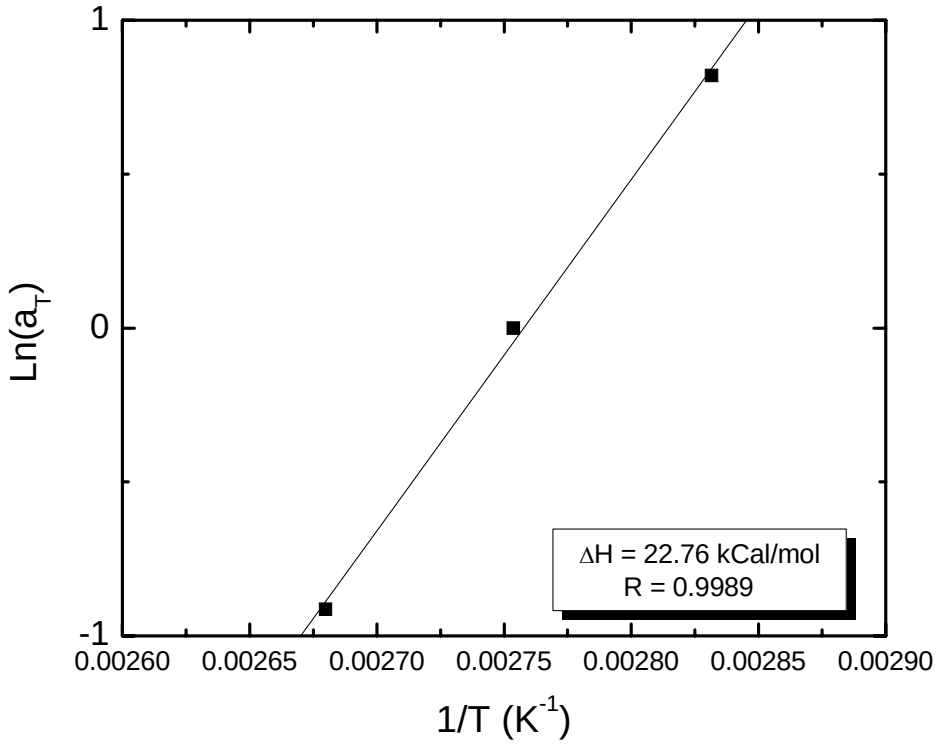

Figure A5: Session 1 – Natural log of a_T verses the temperature inverse for a 10% solution.

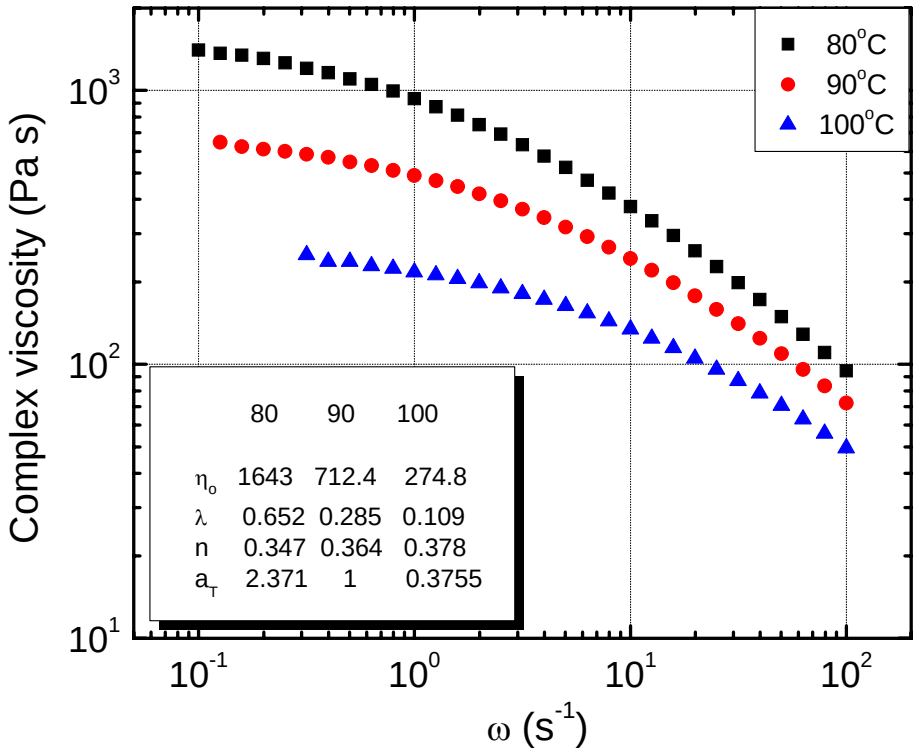

Figure A6: Session 2 – Complex viscosity for a 10% solution.

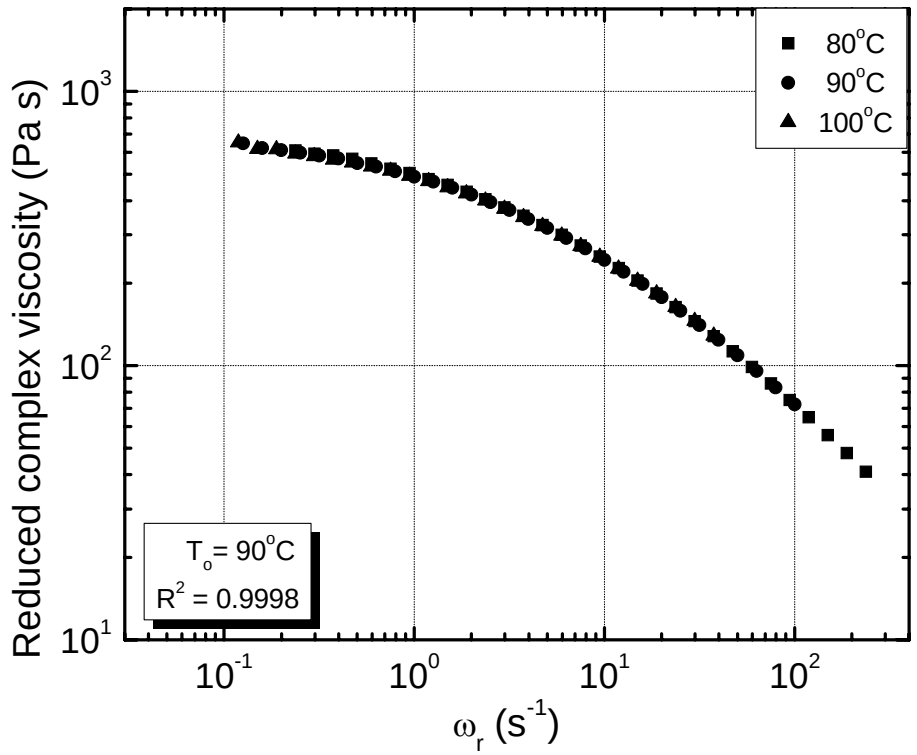

Figure A7: Session 2 – Temperature shifted reduced complex viscosity for a 10% solution using Cross model.

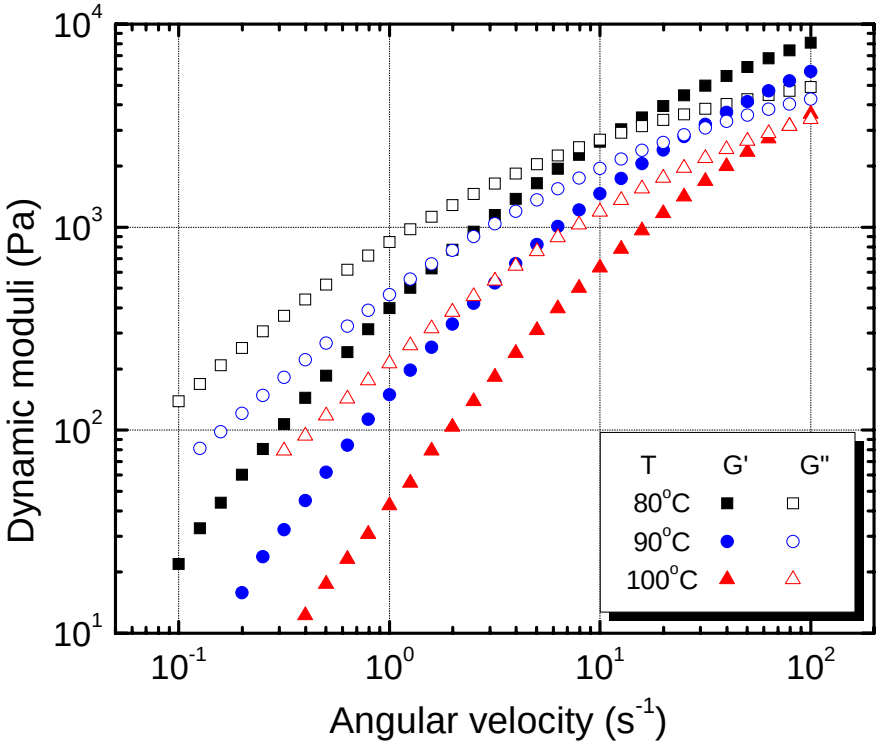

Figure A8: Session 2 – Dynamic moduli for a 10% solution.

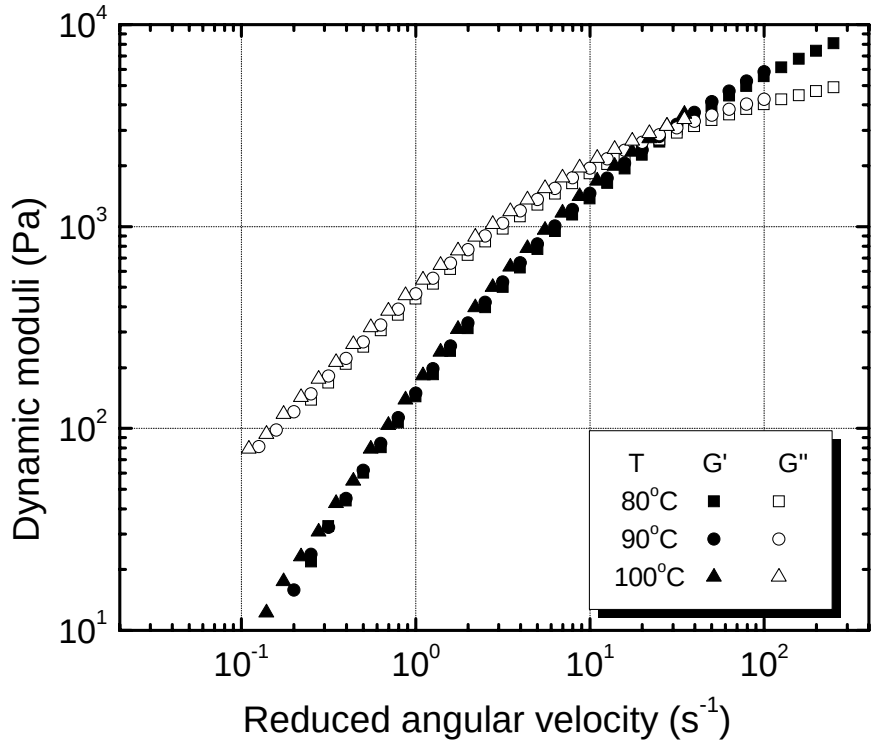

Figure A9: Session 2 – Dynamic moduli at reduced angular velocity for a 10% solution using Cross model.

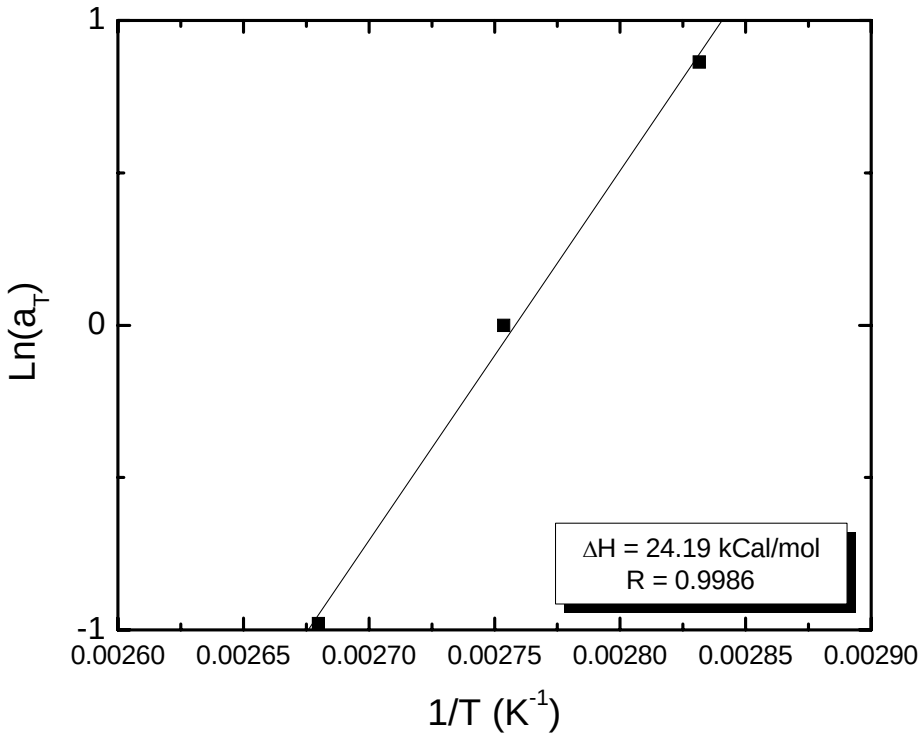

Figure A10: Session 2 – Natural log of a_T verses the temperature inverse for a 10% solution.

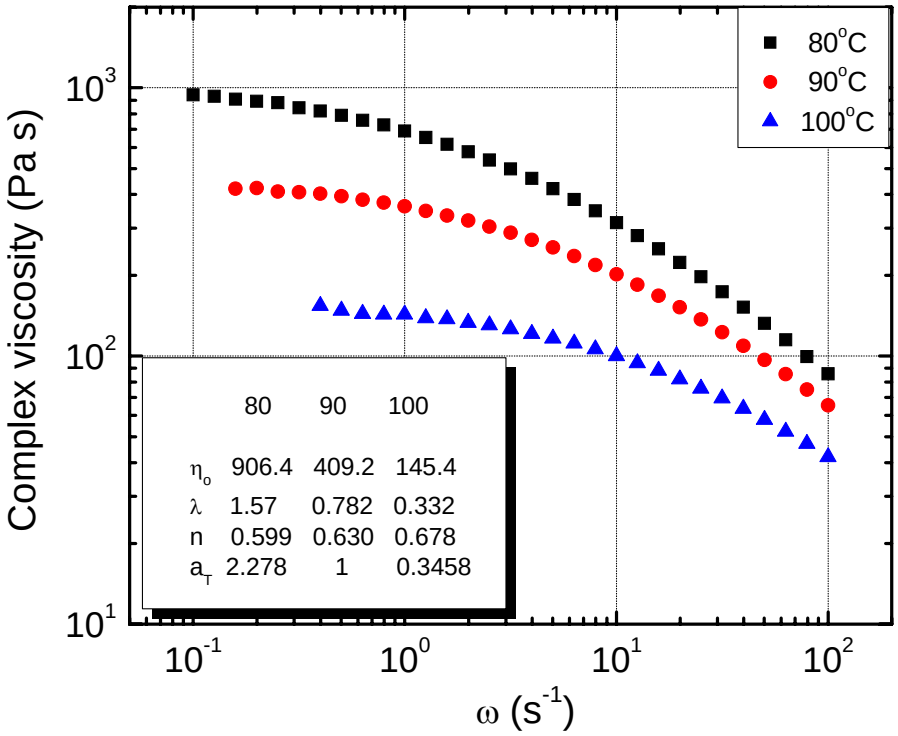

Figure A11: Session 3 – Complex viscosity for a 10% solution.

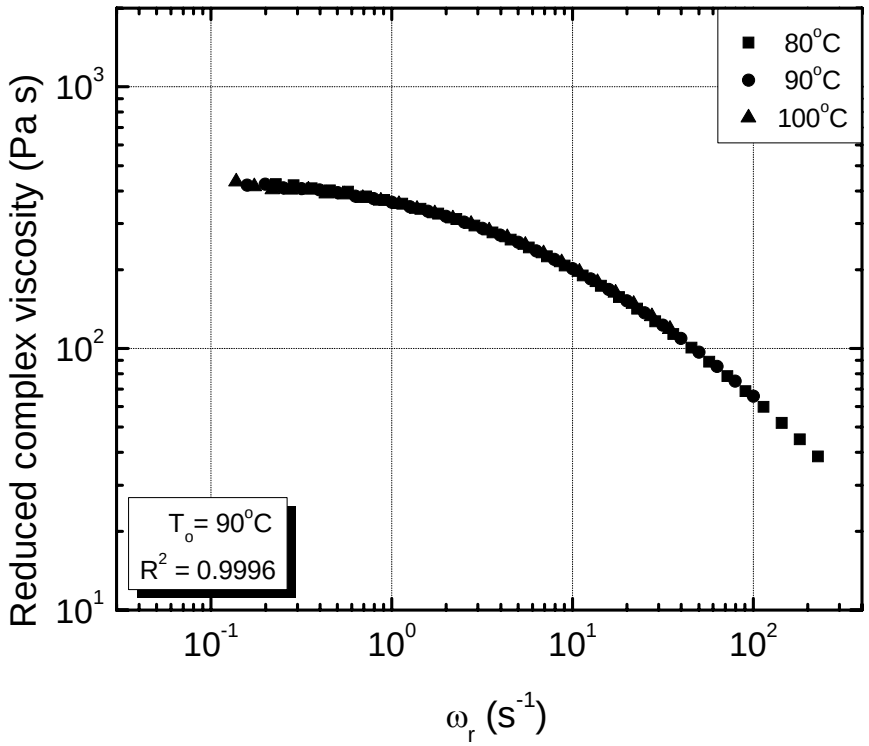

Figure A12: Session 3 – Temperature shifted reduced complex viscosity for a 10% solution using Cross model.

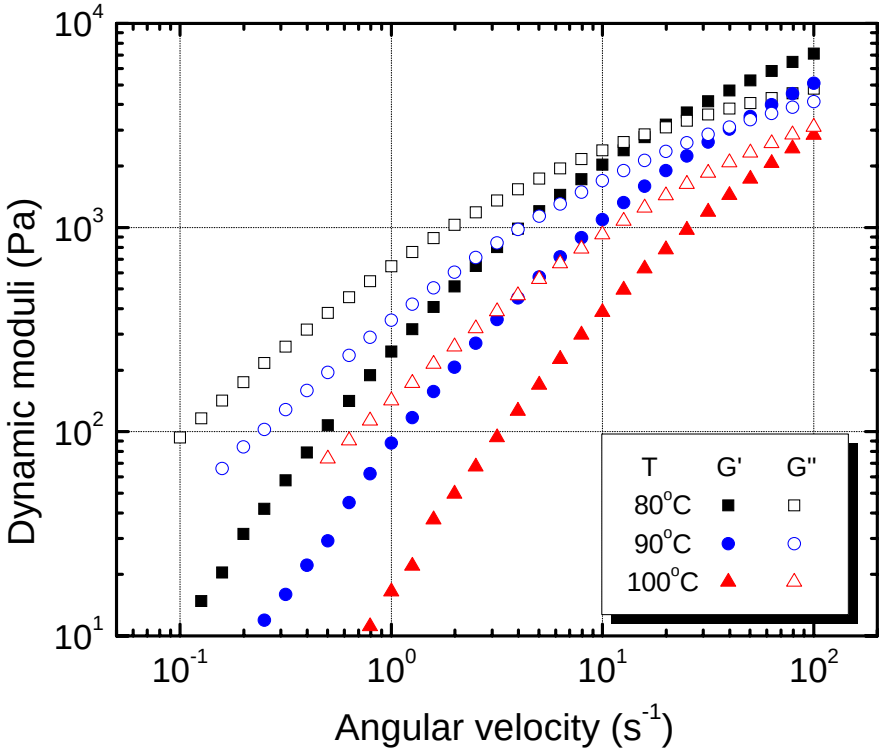

Figure A13: Session 3 – Dynamic moduli for a 10% solution.

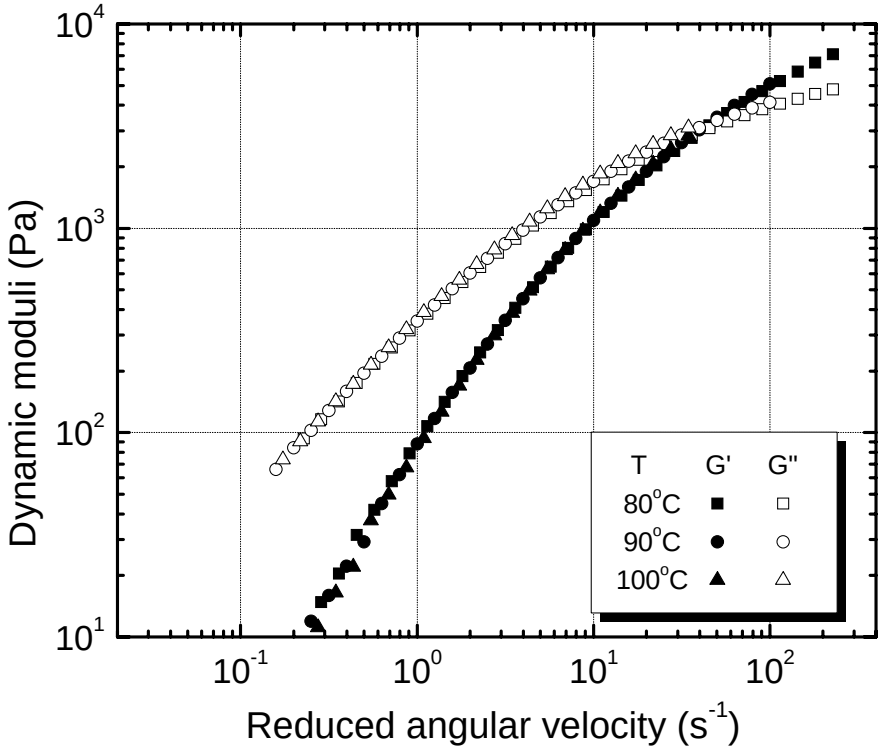

Figure A14: Session 3 – Dynamic moduli at reduced angular velocity for a 10% solution using Cross model.

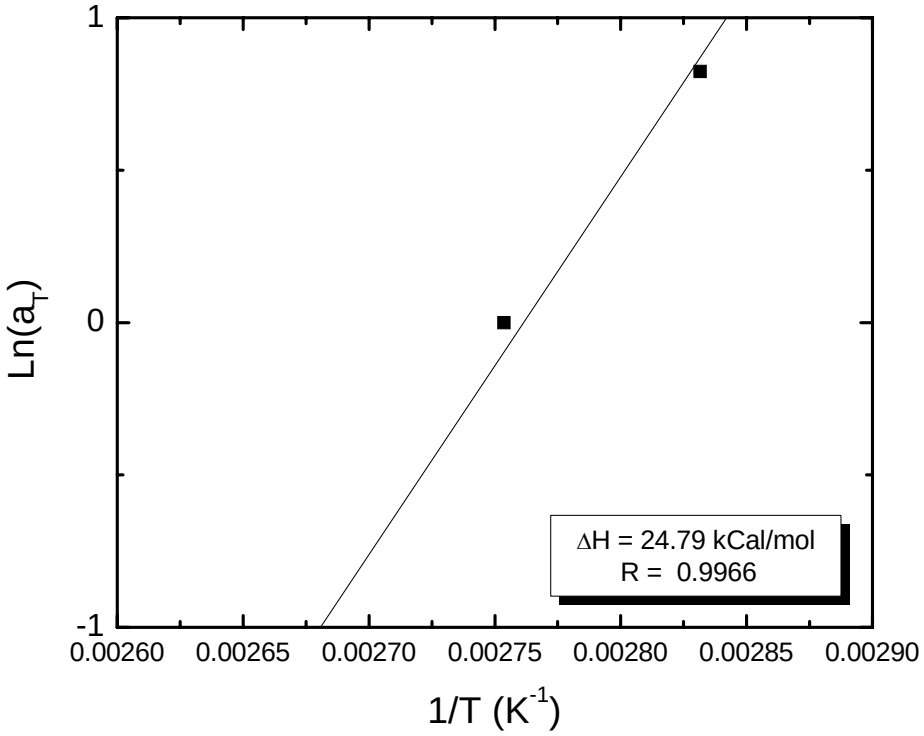

Figure A15: Session 3 – Natural log of a_T verses the temperature inverse for a 10% solution.

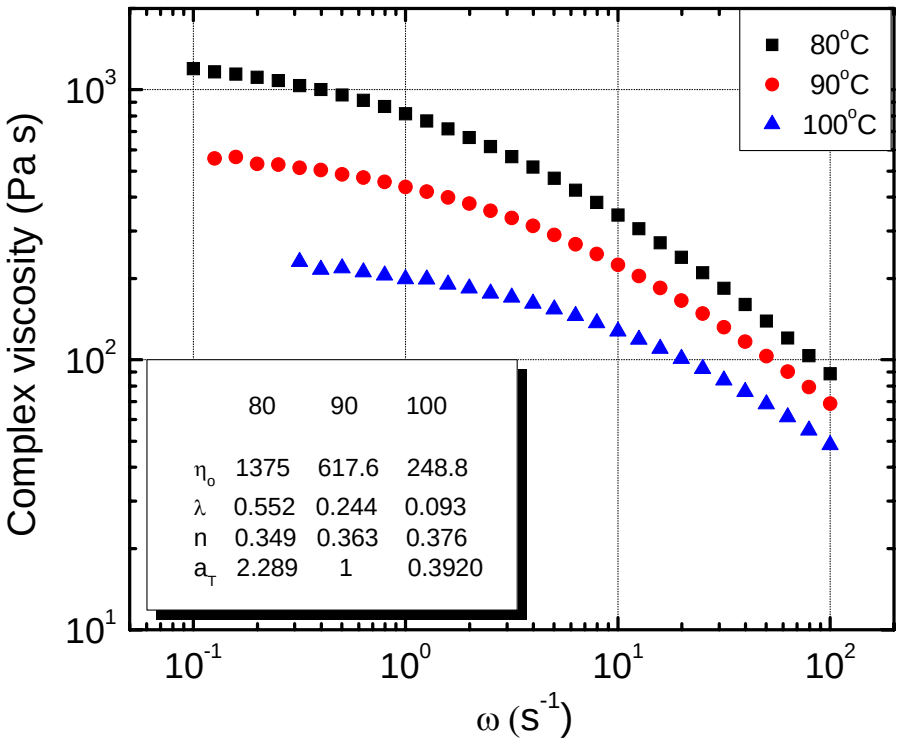

Figure A16: Sessions 4&5 – Complex viscosity for a 10% solution.

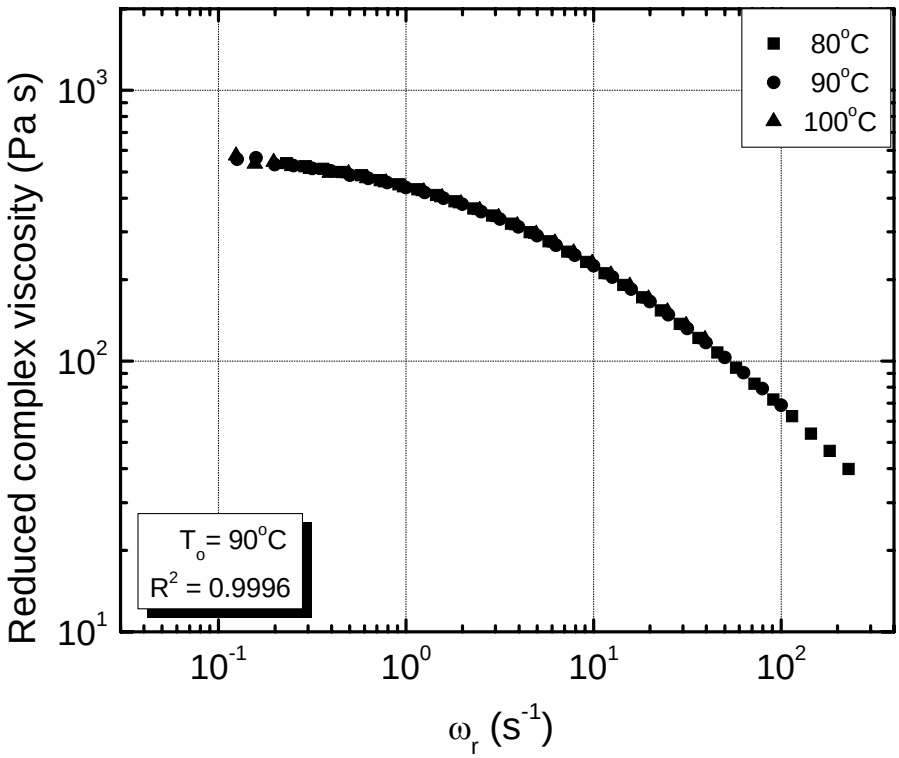

Figure A17: Sessions 4&5 – Temperature shifted reduced complex viscosity for a 10% solution using Cross model.

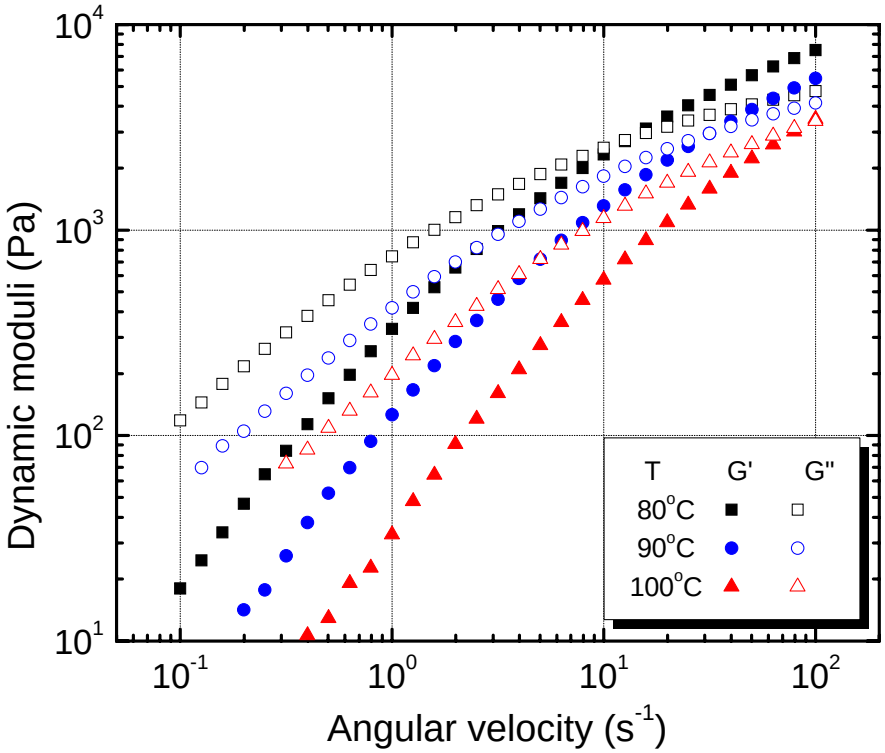

Figure A18: Sessions 4&5 – Dynamic moduli for a 10% solution.

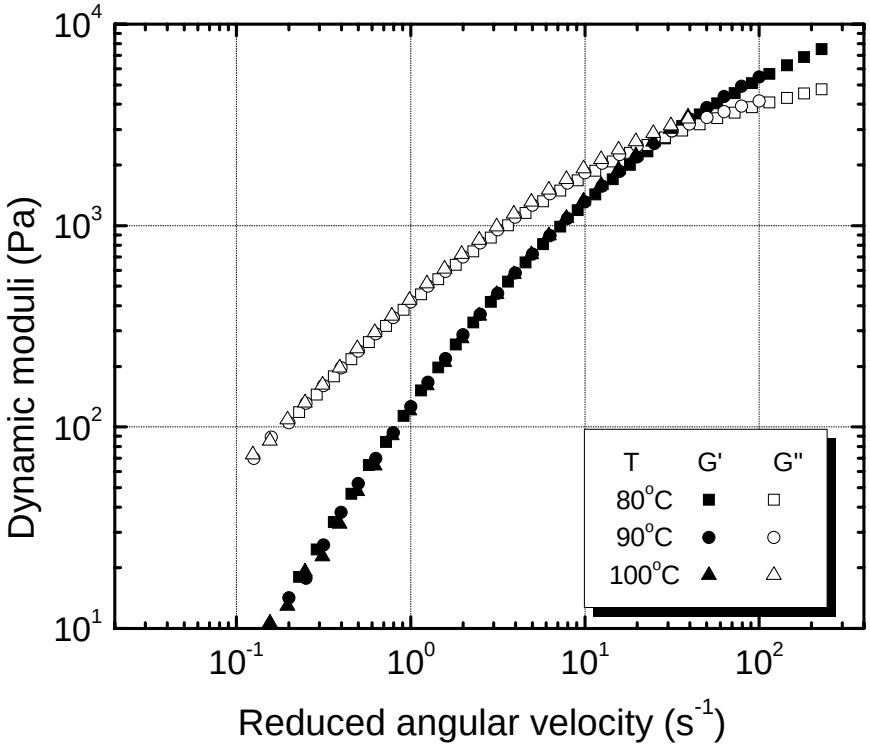

Figure A19: Sessions 4&5 – Dynamic moduli at reduced angular velocity for a 10% solution using Cross model.

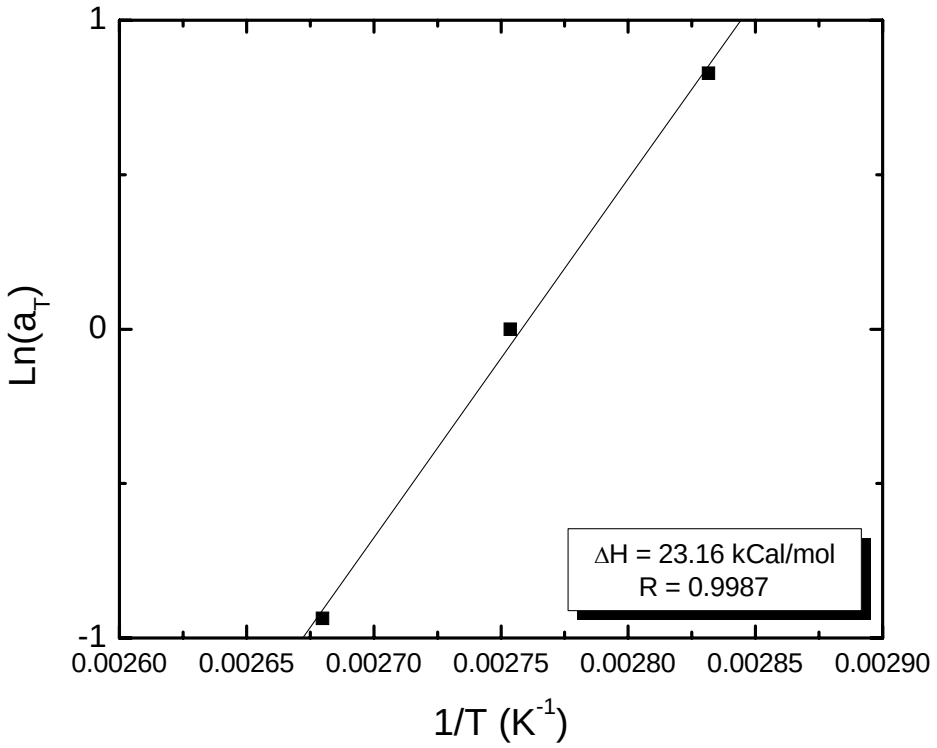

Figure A20: Sessions 4&5 – Natural log of a_T verses the temperature inverse for a 10% solution.

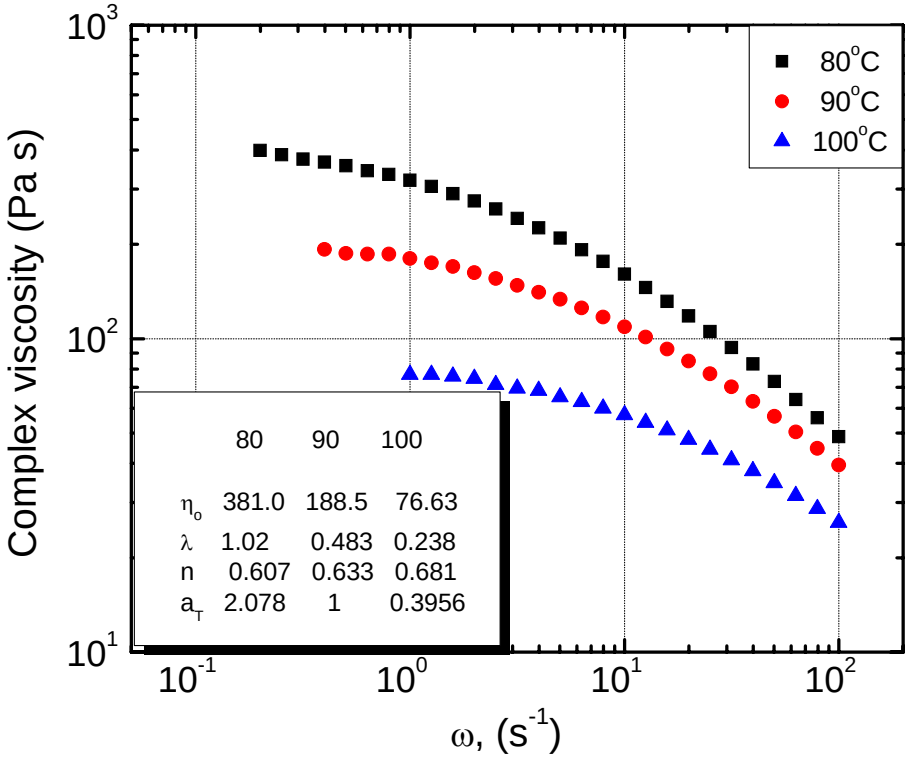

Figure A21: Session 6 – Complex viscosity for an 8% solution.

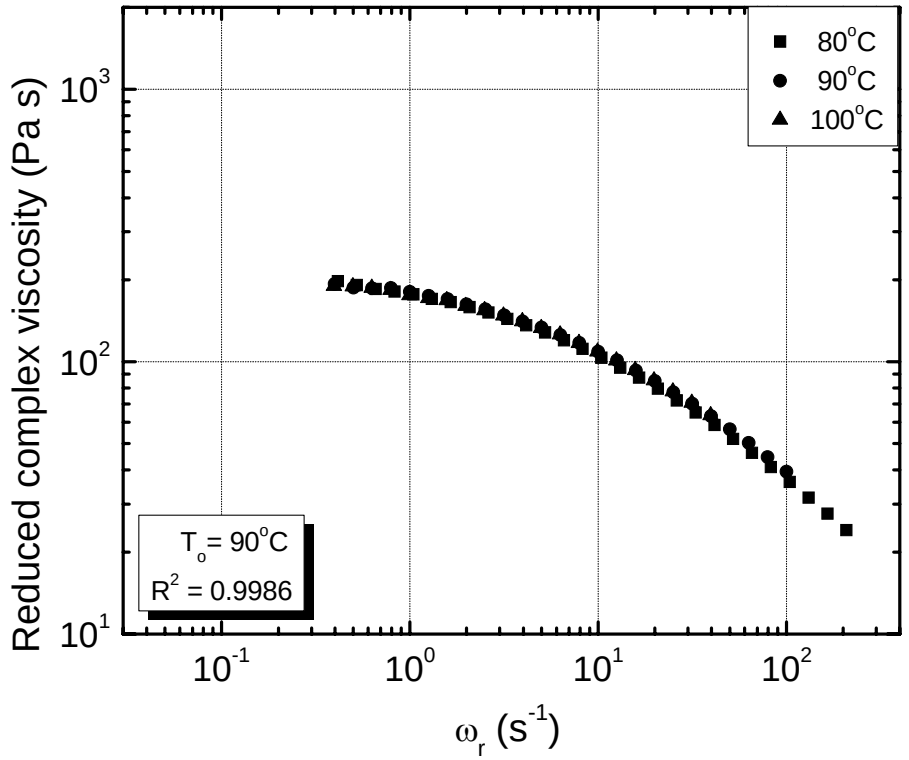

Figure A22: Session 6– Temperature shifted reduced complex viscosity for an 8% solution using Cross model.

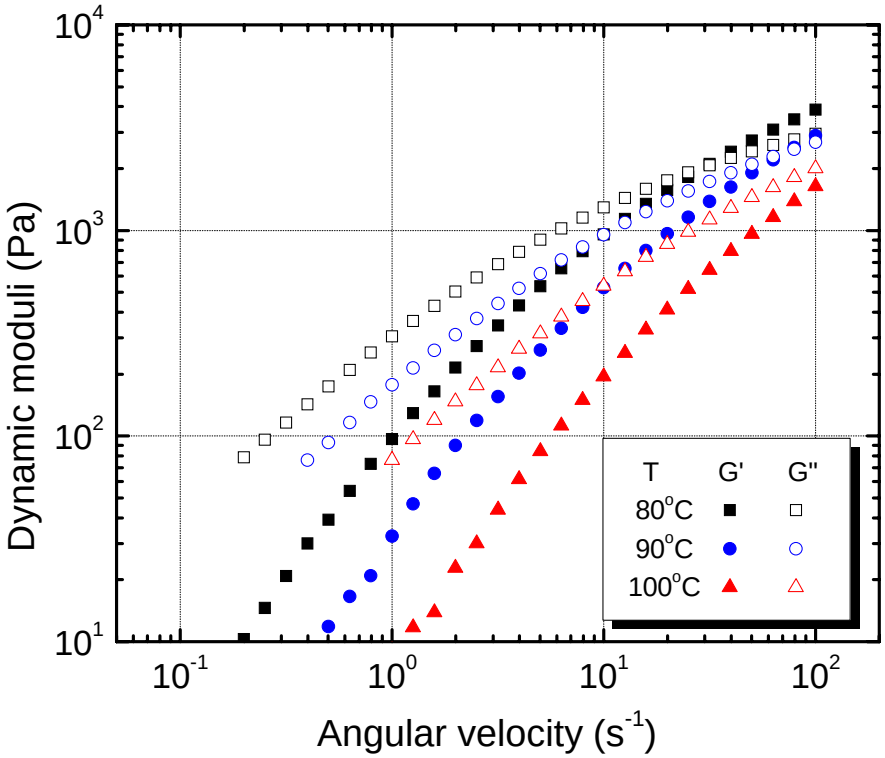

Figure A23: Session 6 – Dynamic moduli for an 8% solution.

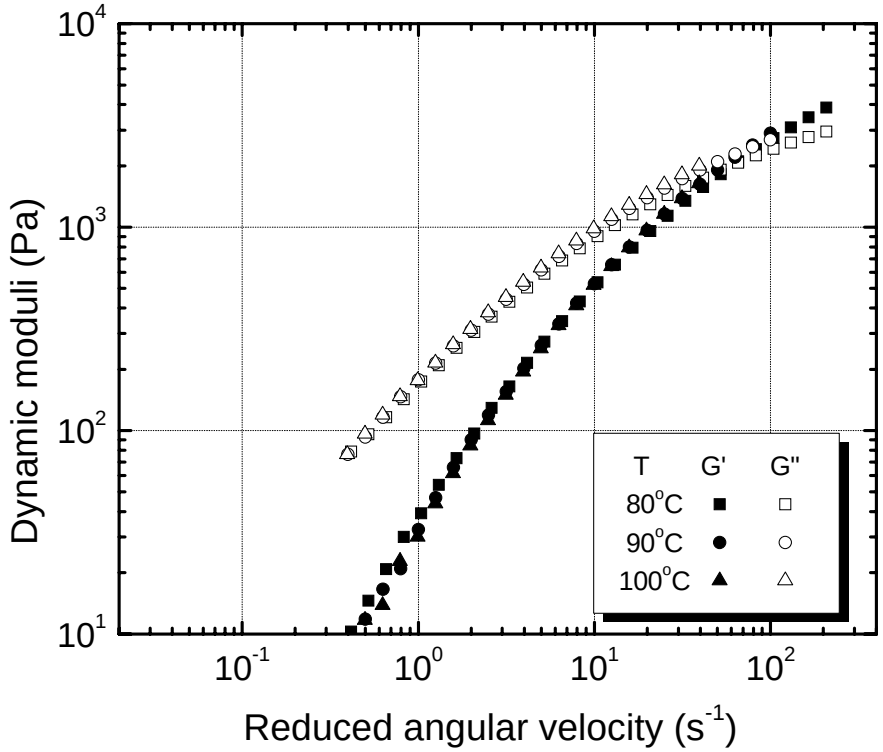

Figure A24: Session 6 – Dynamic moduli at reduced angular velocity for an 8% solution using Cross model.

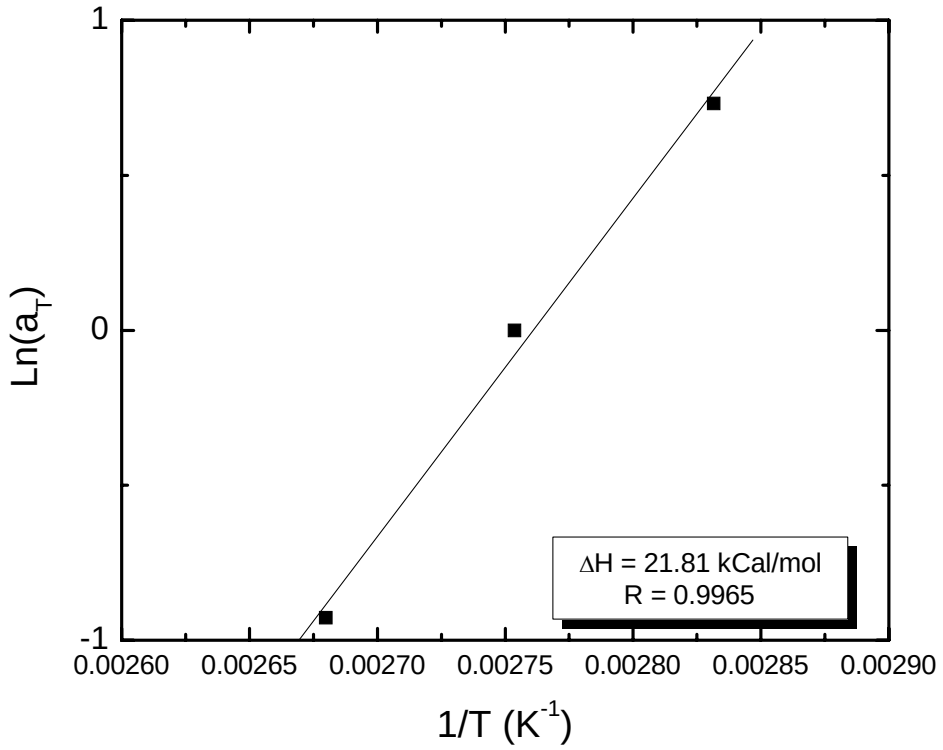

Figure A25: Session 6 – Natural log of a_T verses the temperature inverse for an 8% solution.

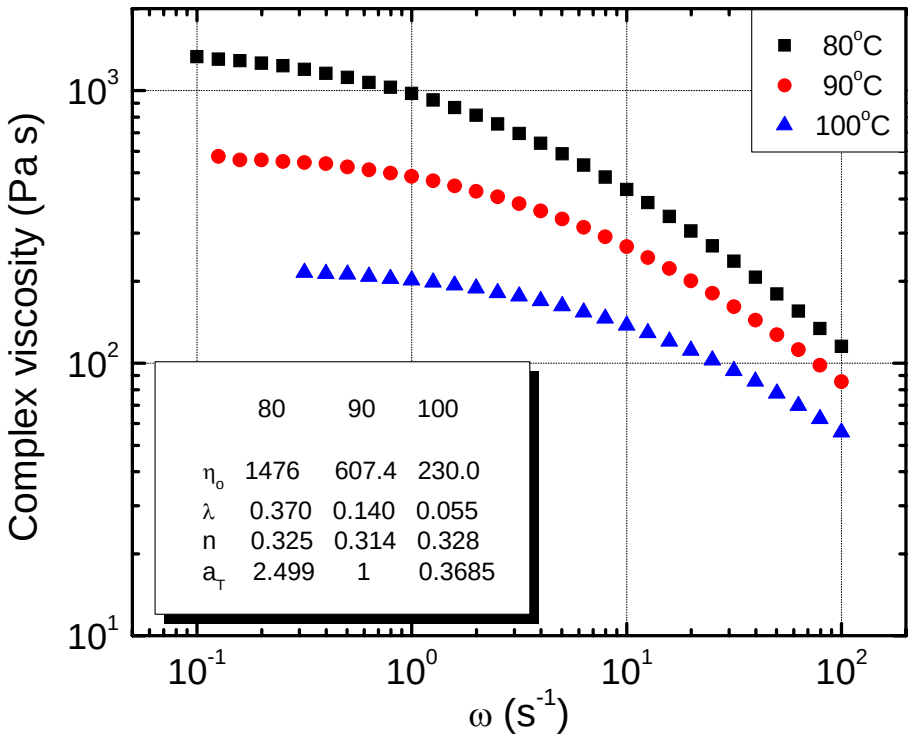

Figure A26: Session 7 – Complex viscosity for a 12% solution.

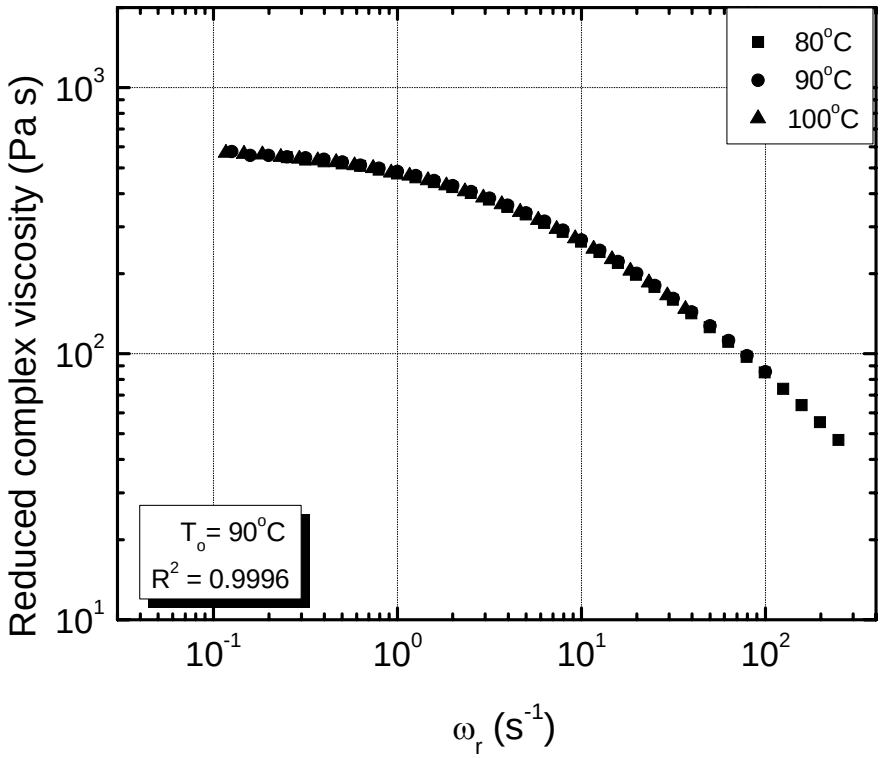

Figure A27: Session 7– Temperature shifted reduced complex viscosity for a 12% solution using Cross model.

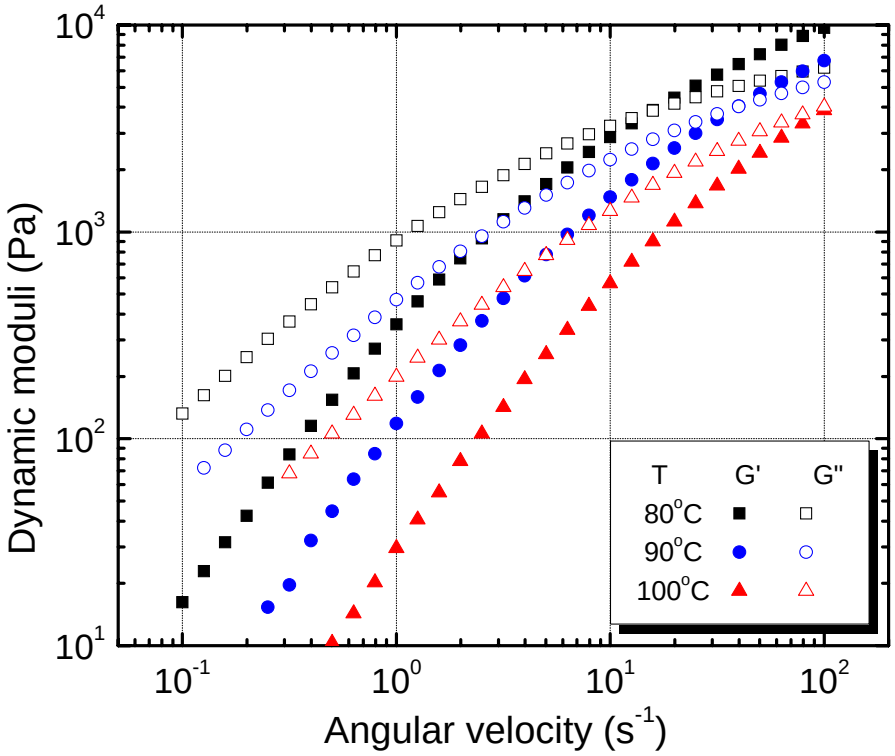

Figure A28: Session 7 – Dynamic moduli for a 12% solution.

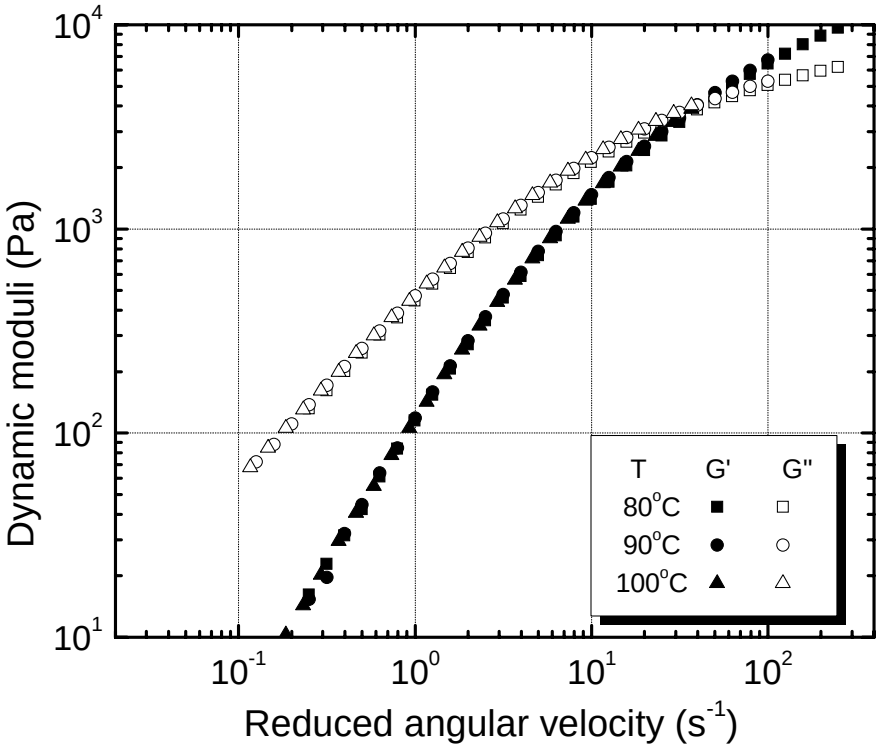

Figure A29: Session 7 – Dynamic moduli at reduced angular velocity for a 12% solution using Cross model.

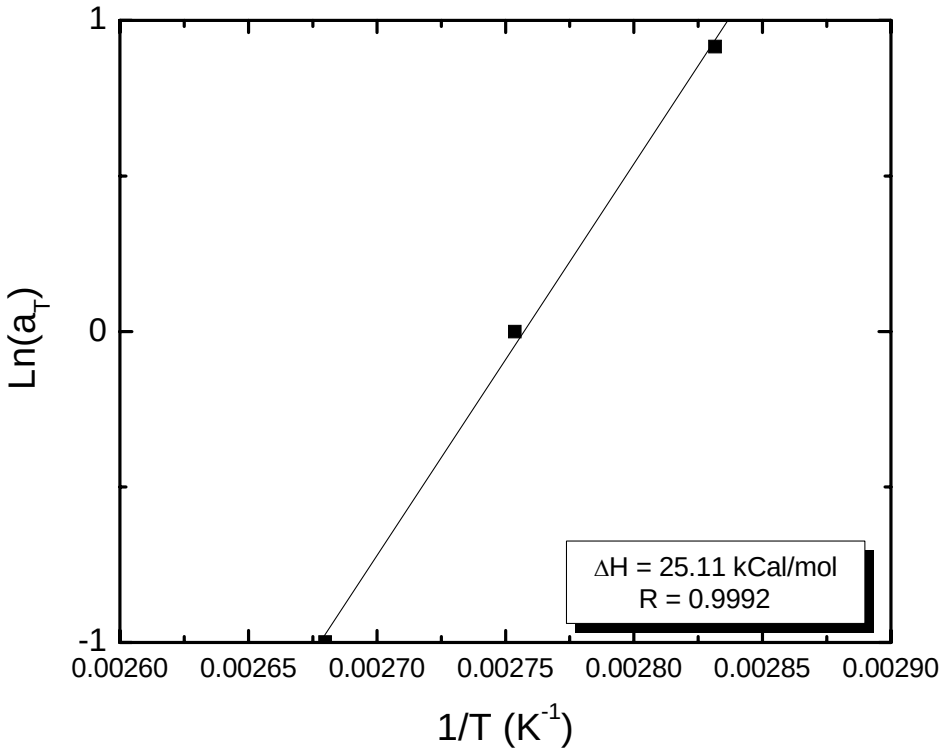

Figure A30: Session 7 – Natural log of a_T verses the temperature inverse for a 12% solution.

APPENDIX B

Elongational Viscosity

Table 1B: R^2 values and temperature shift values for elongational viscosity results.

Conc. %	Hencky Die	Temperature (K)			R^2 for a_T
		353.18	363.18	373.18	
8	H6	2.078	1	0.3956	0.9978
10	H6	2.285	1	0.3748	0.9951
12	H6	2.499	1	0.3685	0.9963
8	H7	2.078	1	0.3956	0.9963
10	H7	2.285	1	0.3748	0.9955
12	H7	2.499	1	0.3685	0.9951
8	H8.4	2.078	1	0.3956	0.9945
10	H8.4	2.285	1	0.3748	0.9929
12	H8.4	2.499	1	0.3685	0.9972

Table 2B: R^2 values and Hencky strain shift values for elongational viscosity results.

Conc. %	Temp (K)	Method	Hencky Strain			R^2 for a_H
			6	7	8.4	
8	353.18	1	0.9783	1	0.9243	0.9859
		2	0.8385	1	1.109	0.9953
8	363.18	1	0.9758	1	0.9792	0.9900
		2	0.8364	1	1.175	0.9945
8	373.18	1	1.102	1	1.146	0.9875
		2	0.9443	1	1.376	0.9939
10	353.18	1	0.8333	1	0.8001	0.9765
		2	0.7143	1	0.9601	0.9957
10	363.18	1	0.7870	1	0.7150	0.9767
		2	0.6745	1	0.8580	0.9963
10	373.18	1	0.8136	1	0.7079	0.9774
		2	0.6974	1	0.8495	0.9961
12	353.18	1	0.8847	1	0.9993	0.9890
		2	0.7583	1	1.199	0.9988
12	363.18	1	0.9322	1	0.9255	0.9849
		2	0.7990	1	1.111	0.9991
12	373.18	1	0.8734	1	0.8607	0.9870
		2	0.7486	1	1.033	0.9986

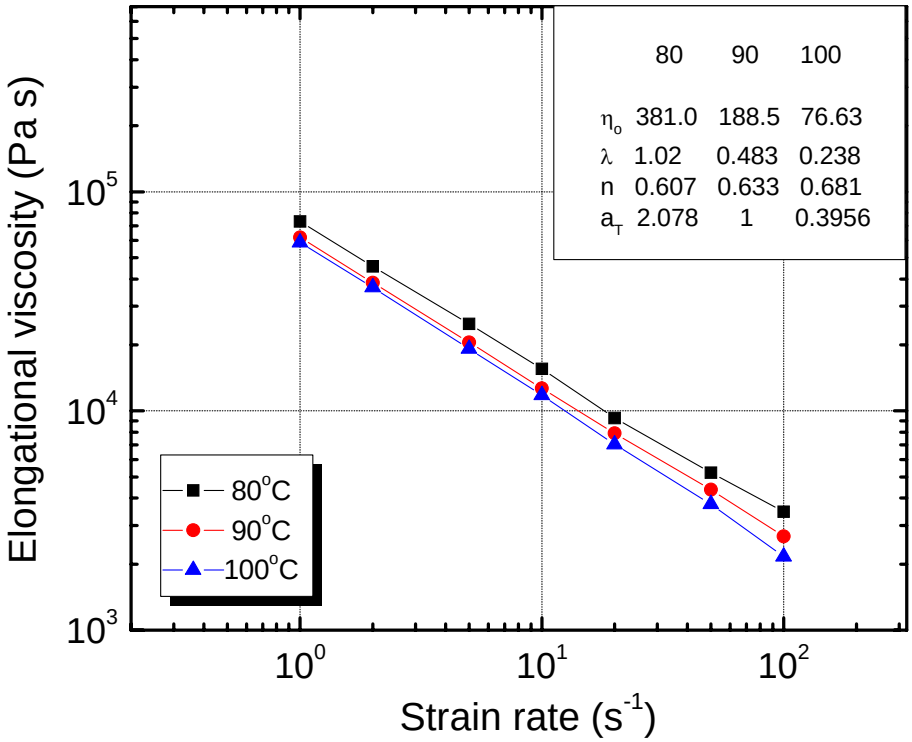

Figure B1: Elongational viscosity of an 8% solution at 80°C, 90°C and 100°C using a H6 die.

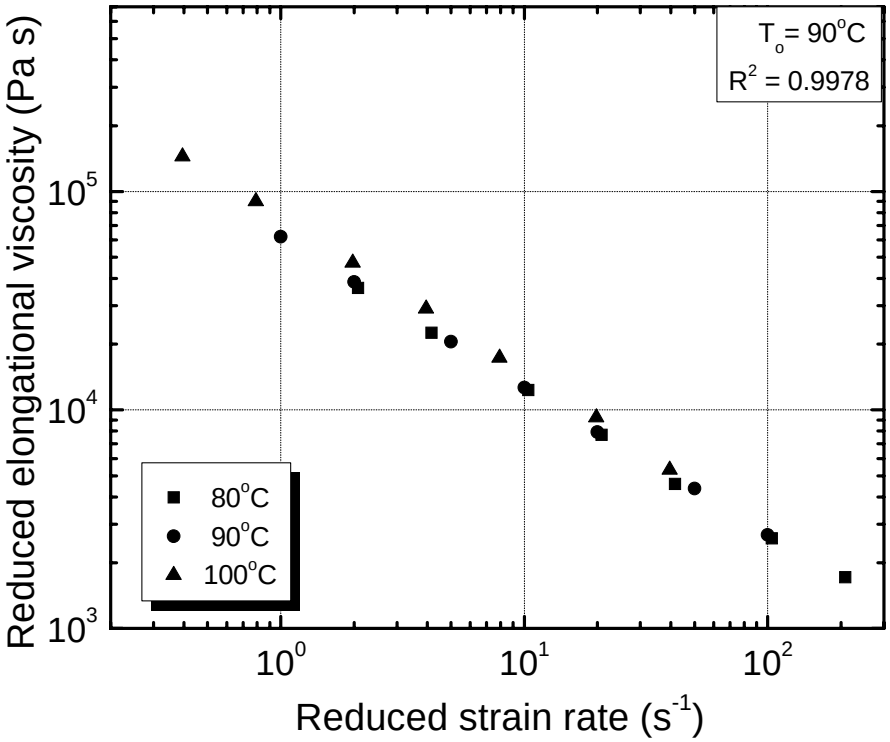

Figure B2: Temperature shifted reduced elongational viscosity of an 8% solution using a H6 die.

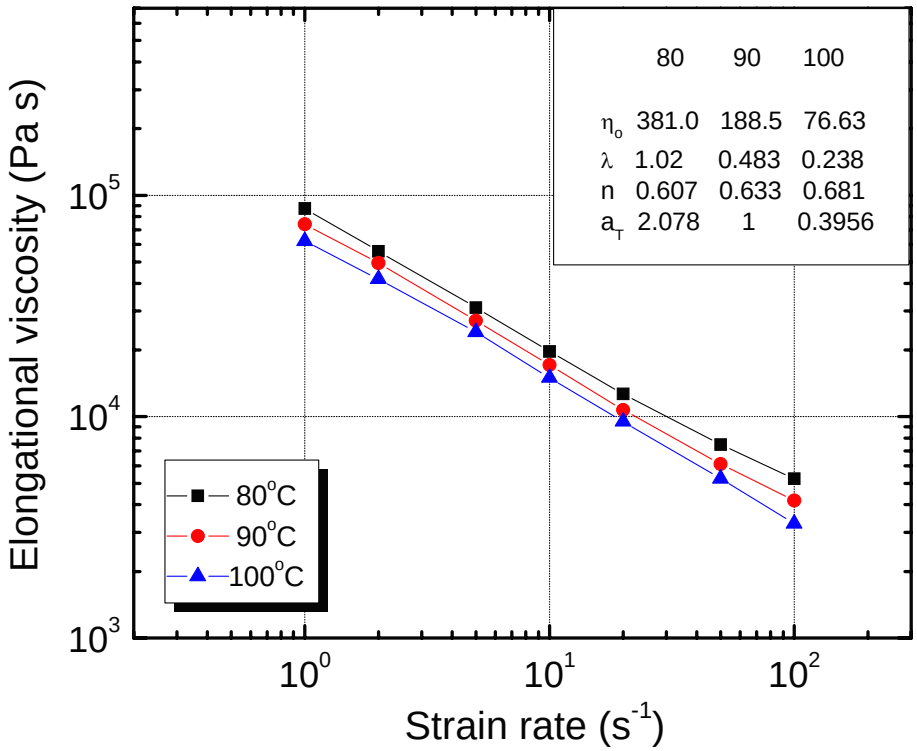

Figure B3: Elongational viscosity of an 8% solution at 80°C, 90°C and 100°C using a H7 die.

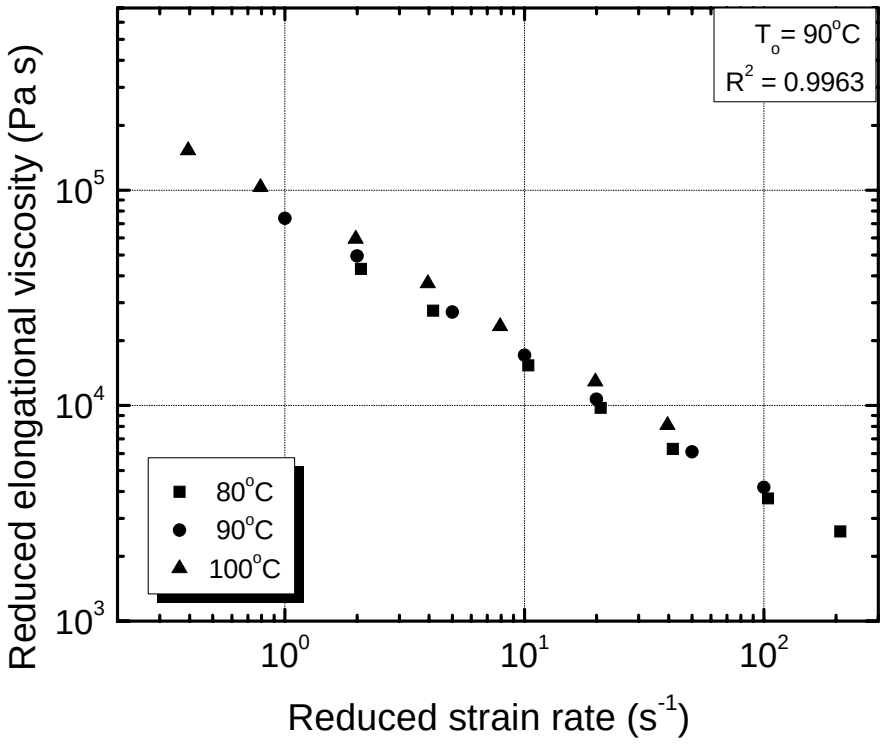

Figure B4: Temperature shifted reduced elongational viscosity of an 8% solution using a H7 die.

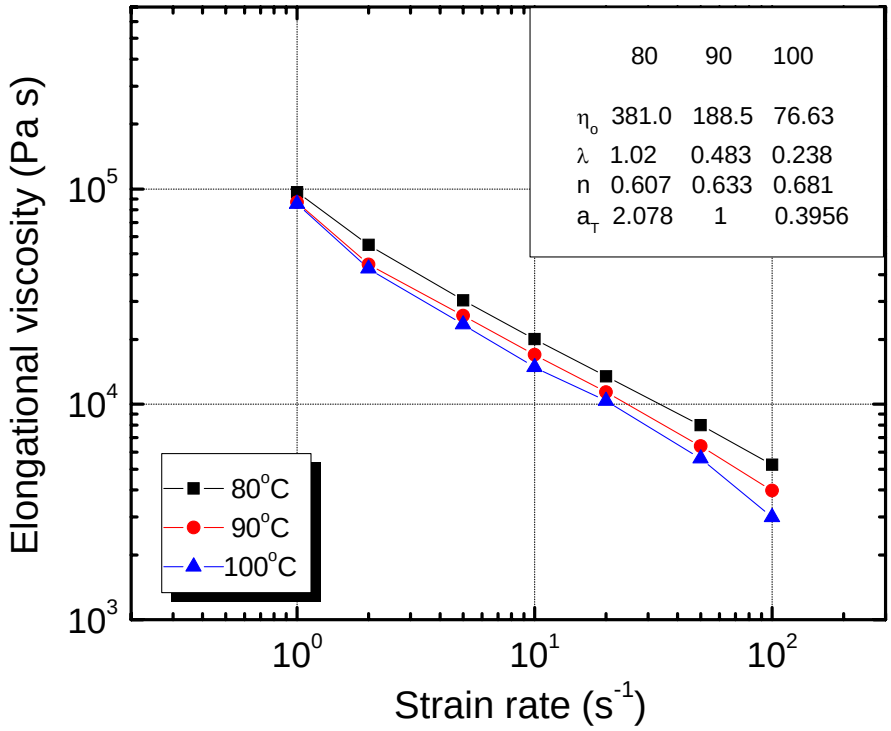

Figure B5: Elongational viscosity of an 8% solution at 80°C, 90°C and 100°C using a H8.4 die.

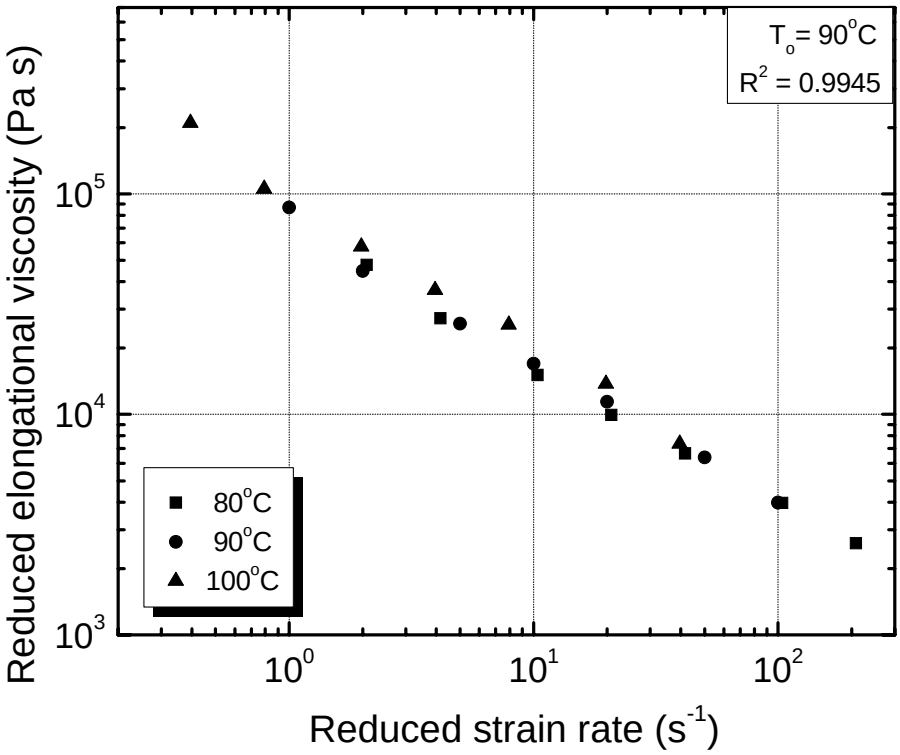

Figure B6: Temperature shifted reduced elongational viscosity of an 8% solution using a H8.4 die.

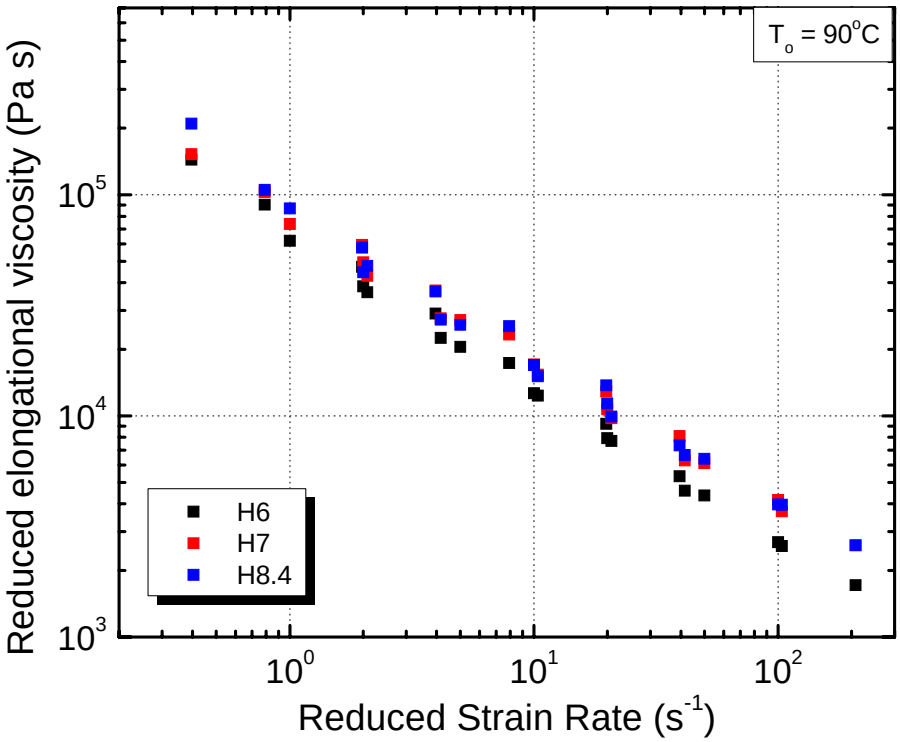

Figure B7: Temperature shifted reduced elongational viscosity of an 8% using all dies.

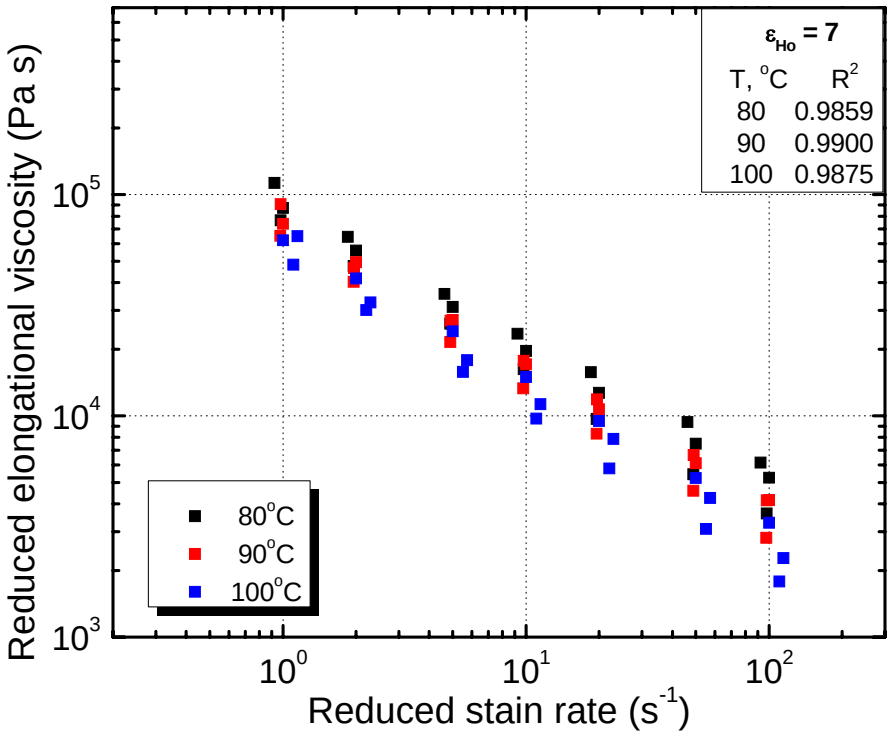

Figure B8: Method 1 Hencky shifted reduced elongational viscosity of an 8% solution at all temperatures.

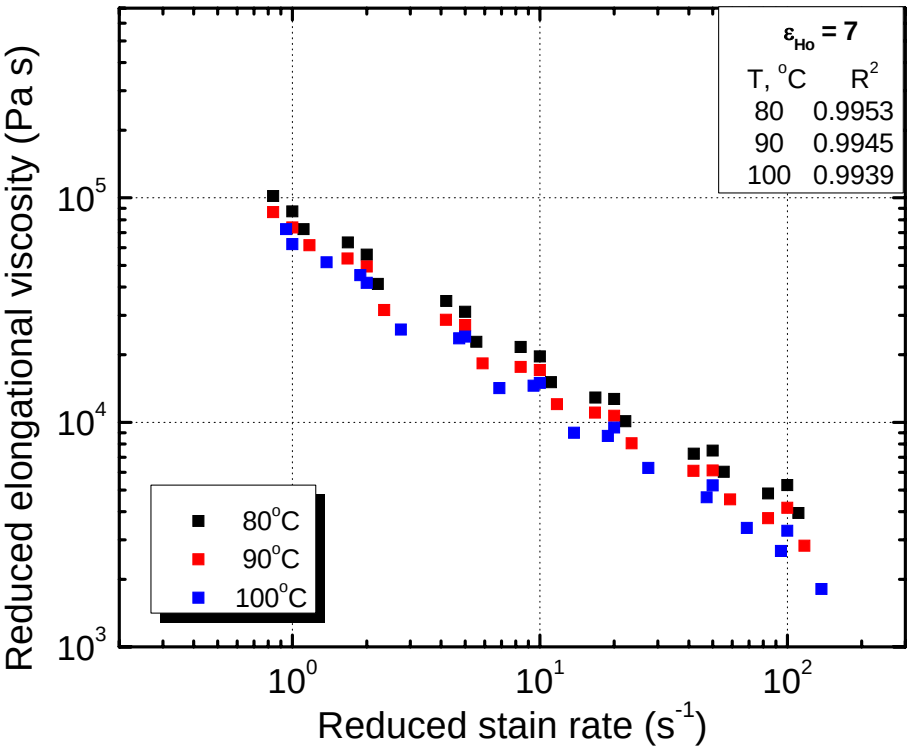

Figure B9: Method 2 Hencky shifted reduced elongational viscosity of an 8% solution at all temperatures.

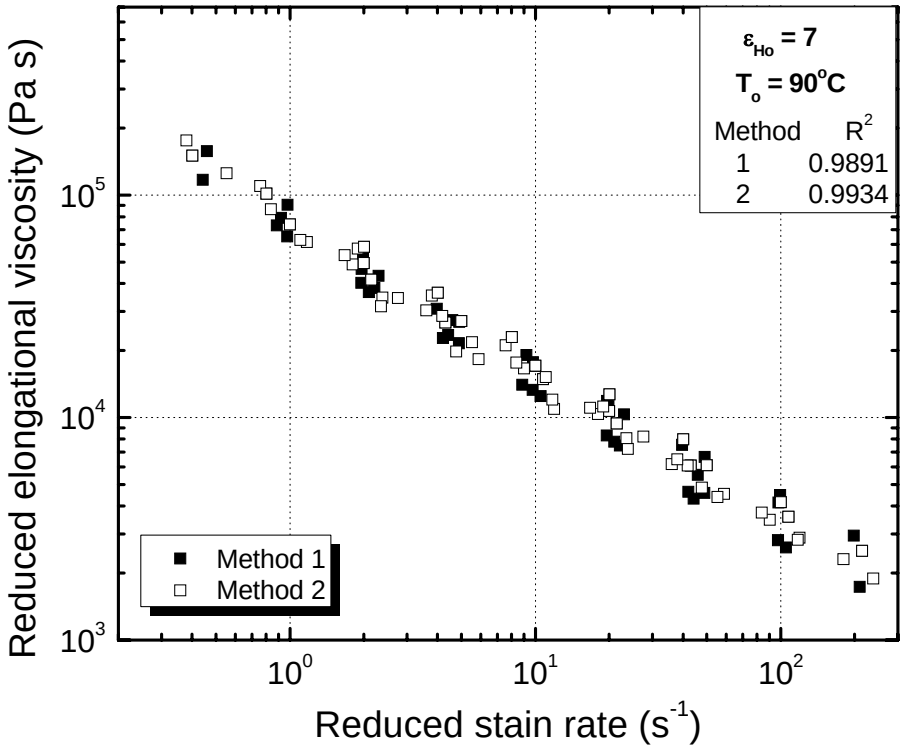

Figure B10: Method 1 and 2 comparison for Hencky strain and temperature shift for an 8% solution.

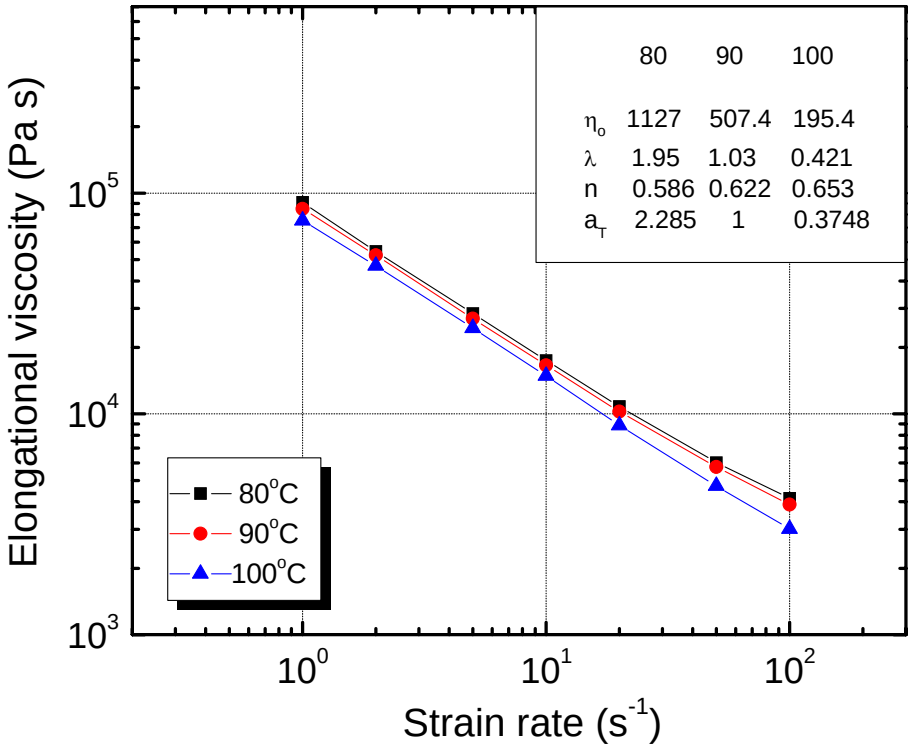

Figure B11: Elongational viscosity of a 10% solution at 80°C, 90°C and 100°C using a H6 die.

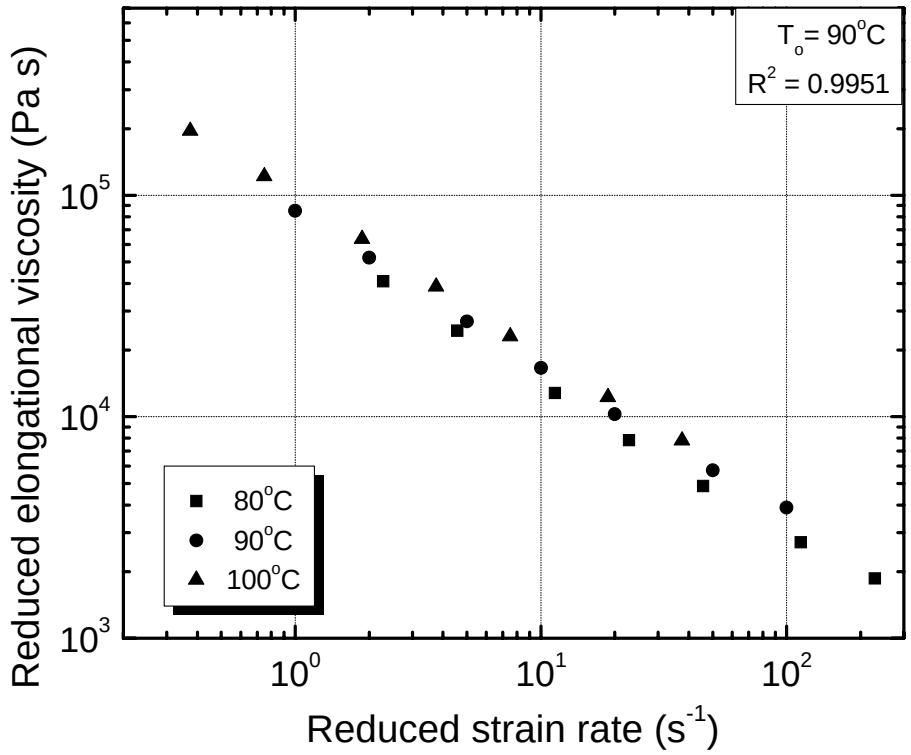

Figure B12: Temperature shifted reduced elongational viscosity of a 10% solution using a H6 die.

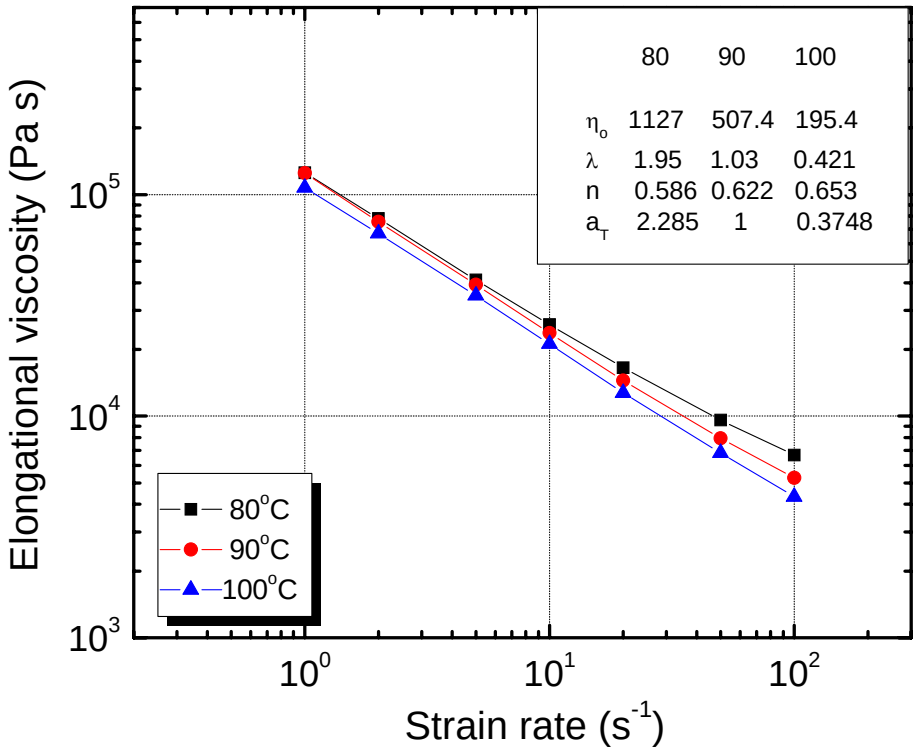

Figure B13: Elongational viscosity of a 10% solution at 80°C, 90°C and 100°C using a H7 die.

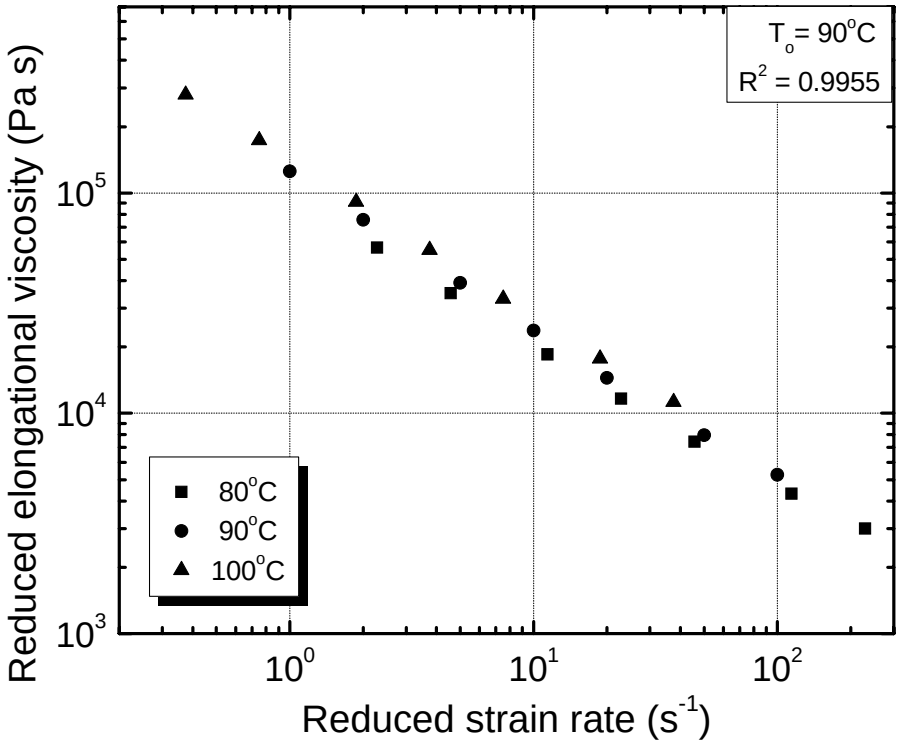

Figure B14: Temperature shifted reduced elongational viscosity of a 10% solution using a H7 die.

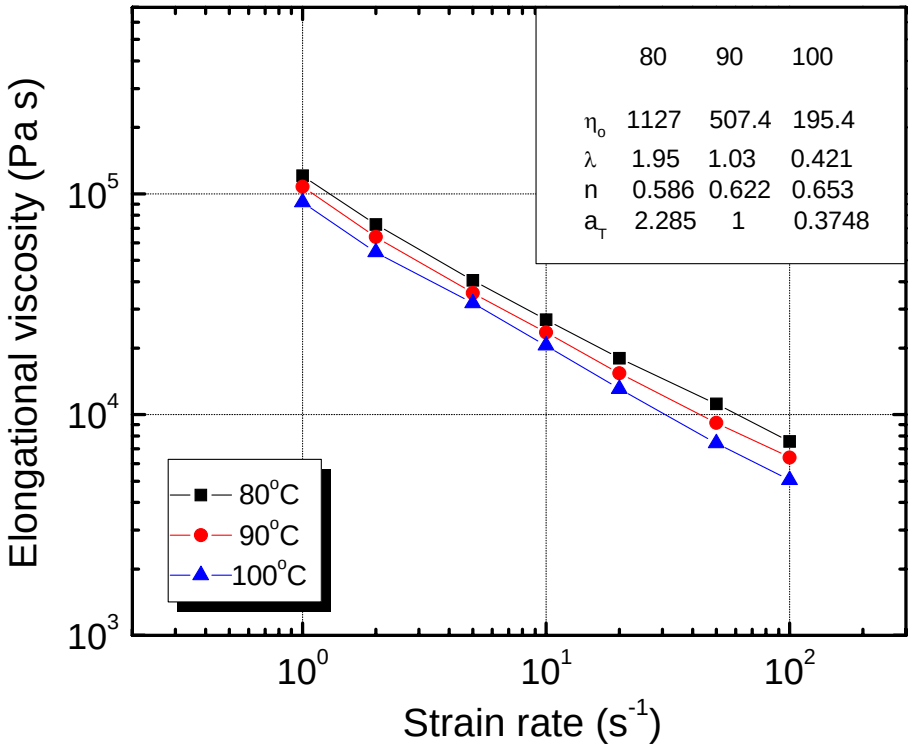

Figure B15: Elongational viscosity of a 10% solution at 80°C, 90°C and 100°C using a H8.4 die.

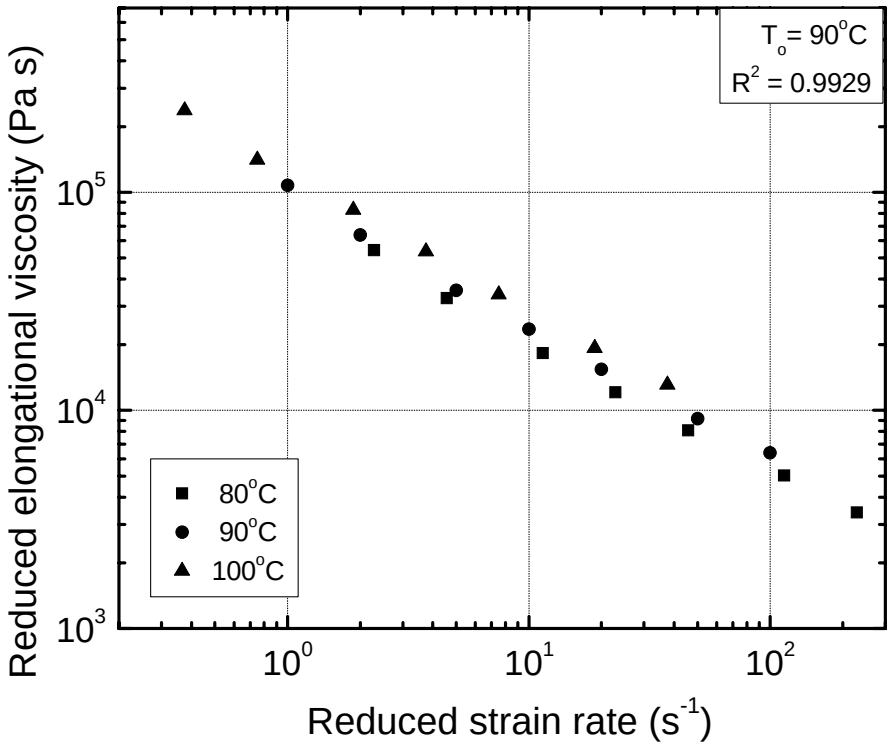

Figure B16: Temperature shifted reduced elongational viscosity of a 10% solution using a H8.4 die.

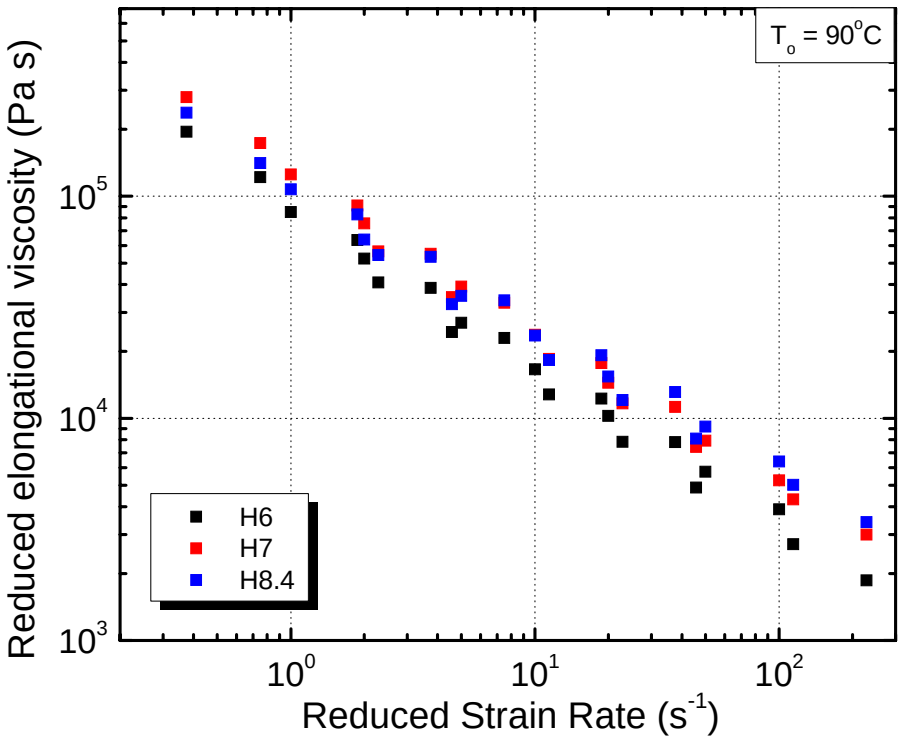

Figure B17: Temperature shifted reduced elongational viscosity of a 10% solution using all dies.

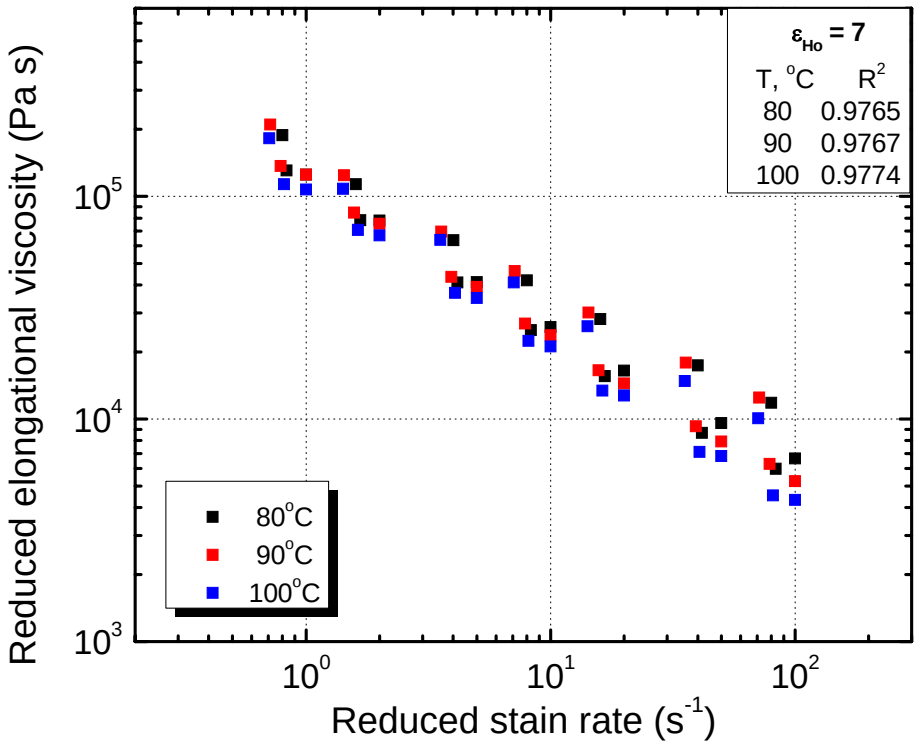

Figure B18: Method 1 Hencky shifted reduced elongational viscosity of a 10% solution at all temperatures.

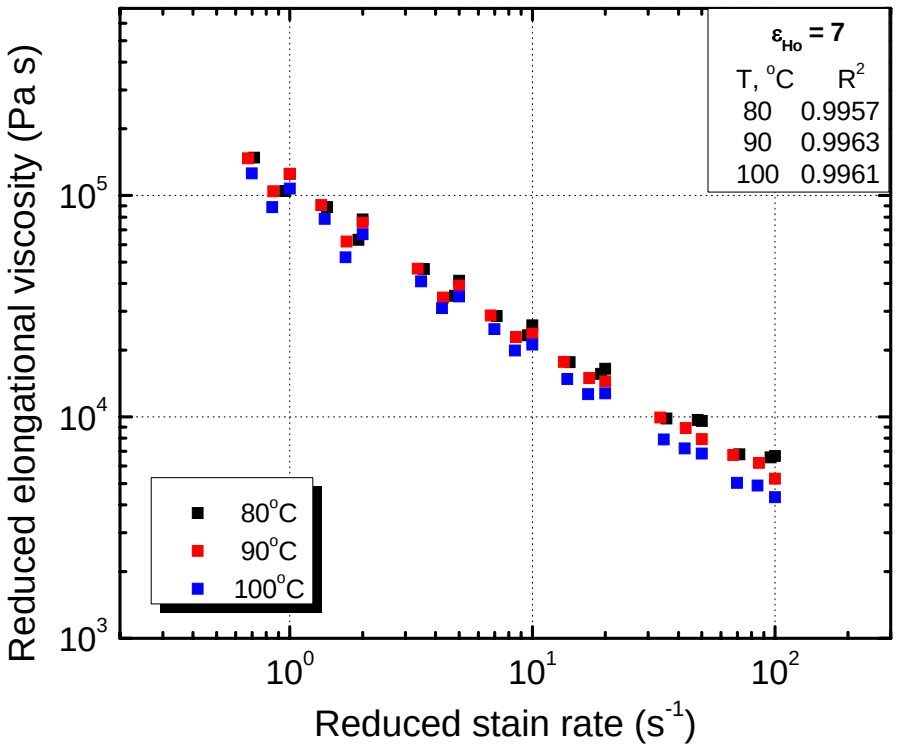

Figure B19: Method 2 Hencky shifted reduced elongational viscosity of a 10% solution at all temperatures.

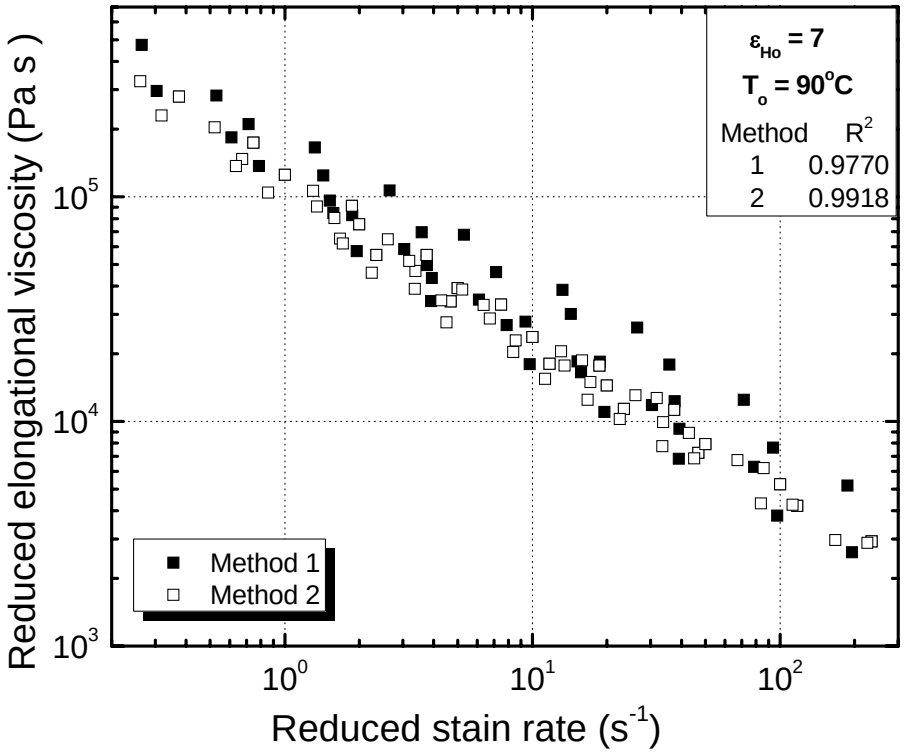

Figure B20: Method 1 and 2 comparison for Hencky strain and temperature shift for a 10% solution.

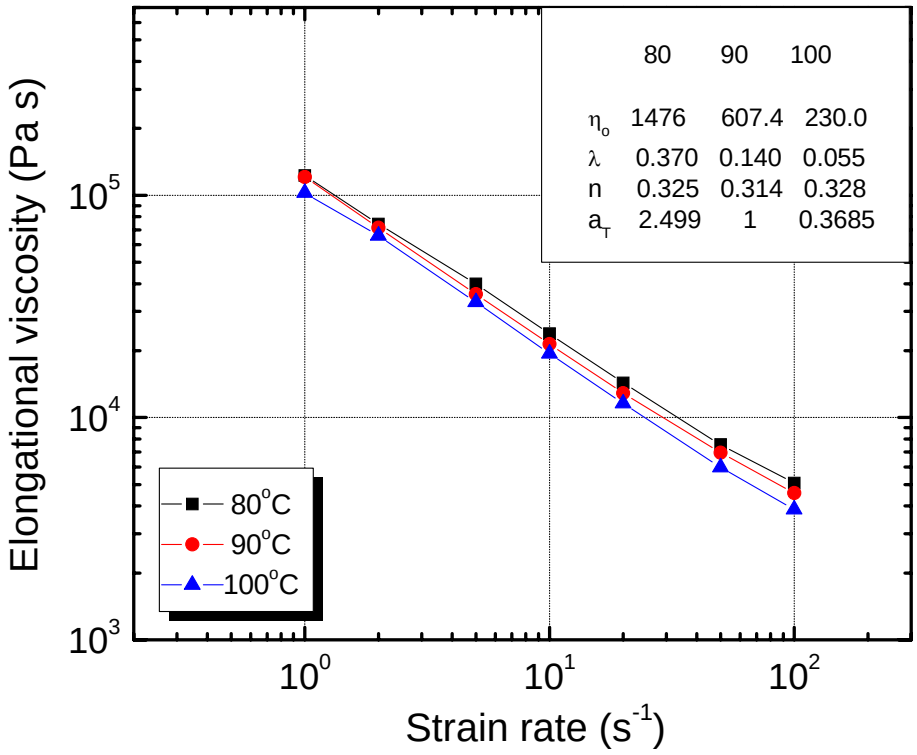

Figure B21: Elongational viscosity of a 12% solution at 80°C, 90°C and 100°C using a H6 die.

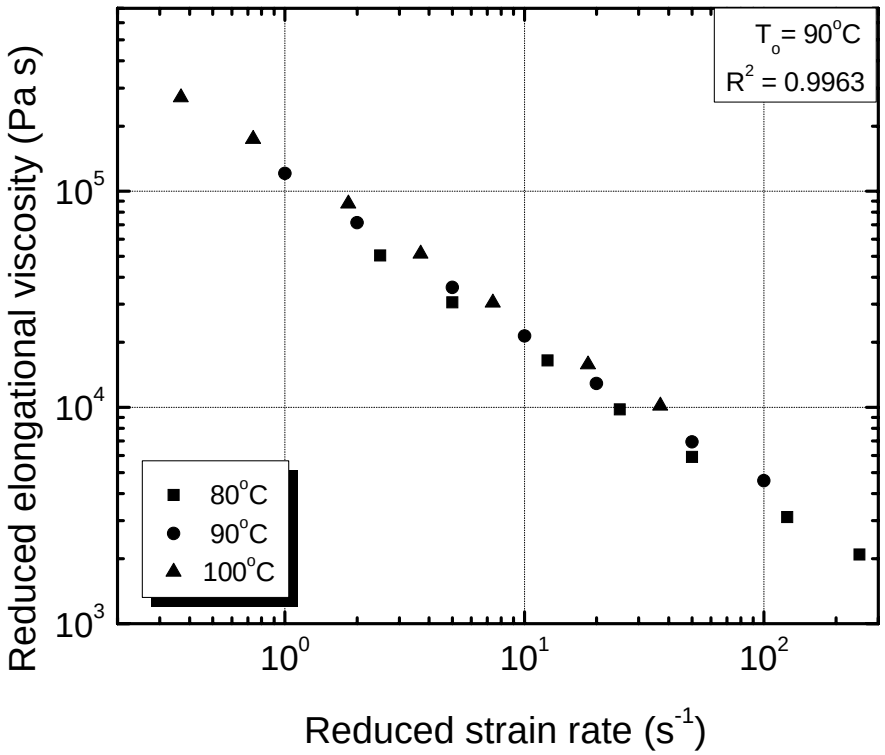

Figure B22: Temperature shifted reduced elongational viscosity of a 12% solution using a H6 die.

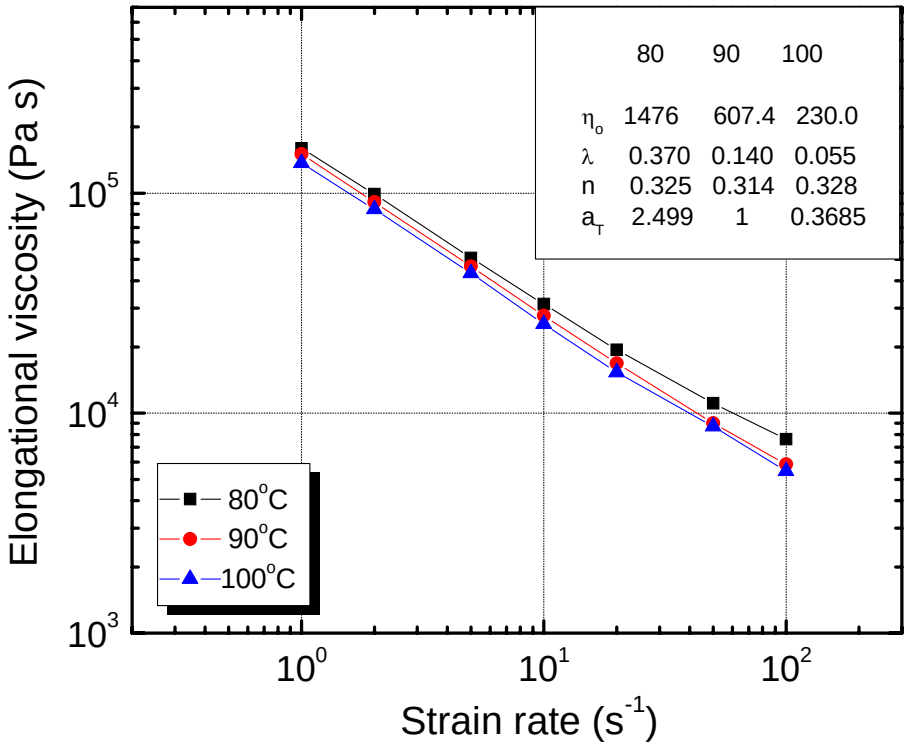

Figure B23: Elongational viscosity of a 12% solution at 80°C, 90°C and 100°C using a H7 die.

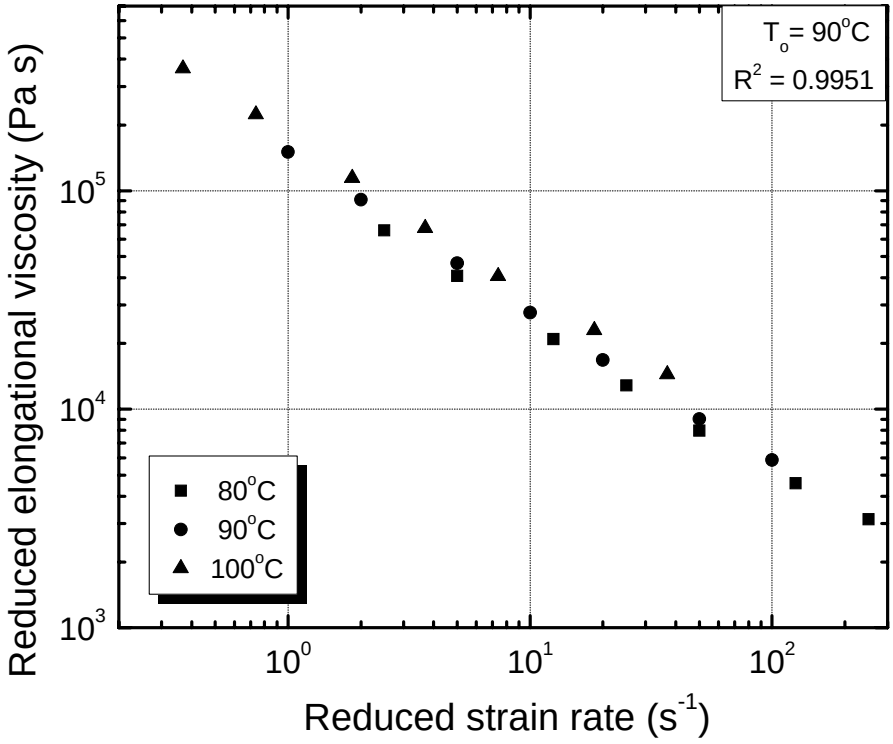

Figure B24: Temperature shifted reduced elongational viscosity of a 12% solution using a H7 die.

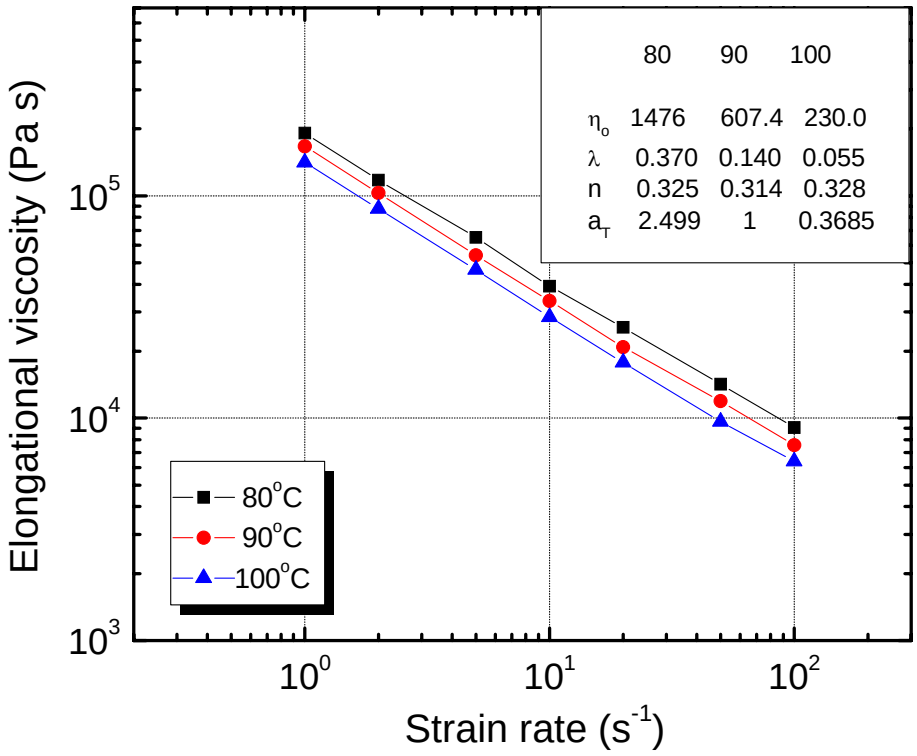

Figure B25: Elongational viscosity of a 12% solution at 80°C, 90°C and 100°C using a H8.4 die.

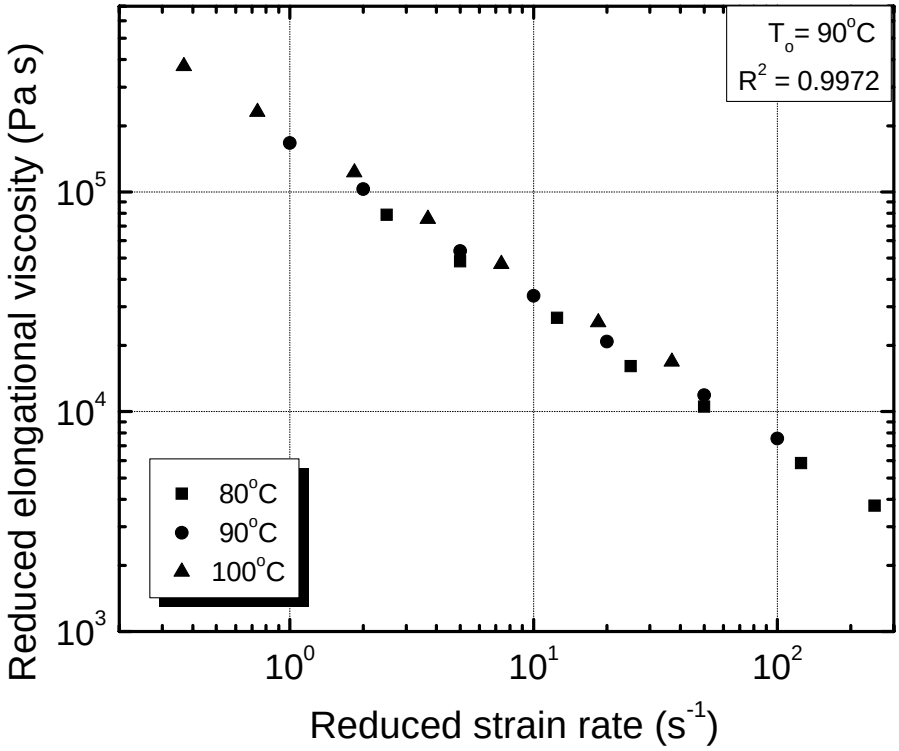

Figure B26: Temperature shifted reduced elongational viscosity of a 12% solution using a H8.4 die.

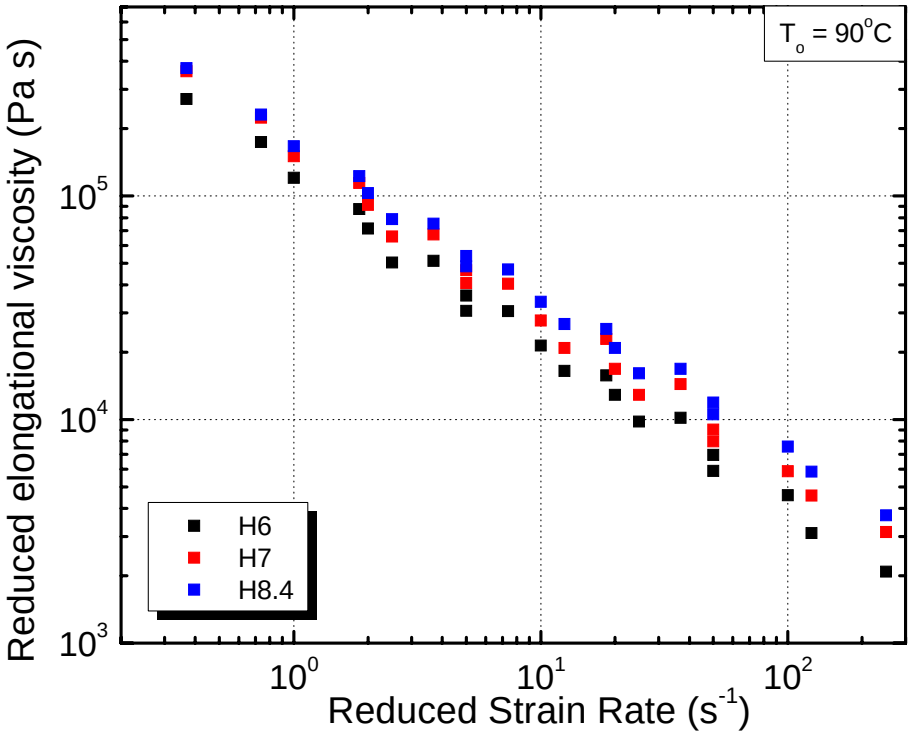

Figure B27: Temperature shifted reduced elongational viscosity of a 12% solution using all dies.

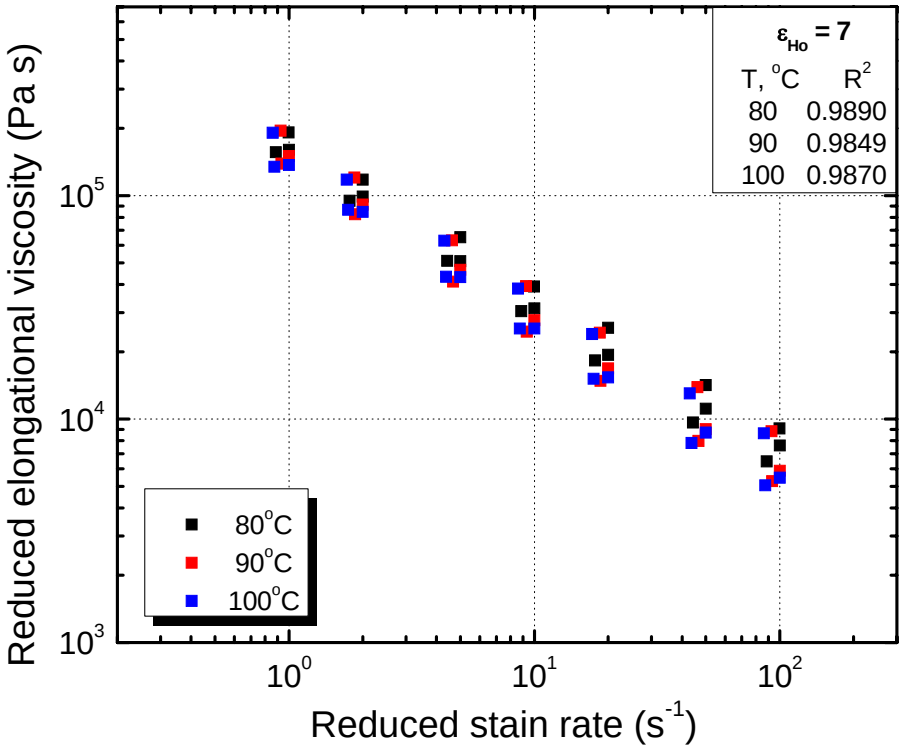

Figure B28: Method 1 Hencky shifted reduced elongational viscosity of a 12% solution at all temperatures.

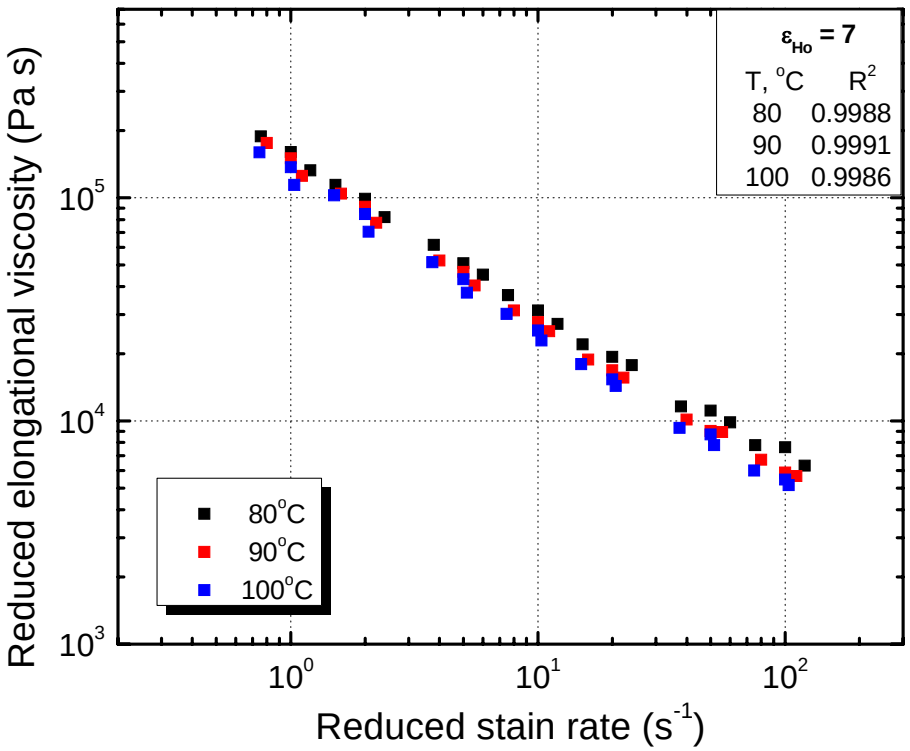

Figure B29: Method 2 Hencky shifted reduced elongational viscosity of a 12% solution at all temperatures.

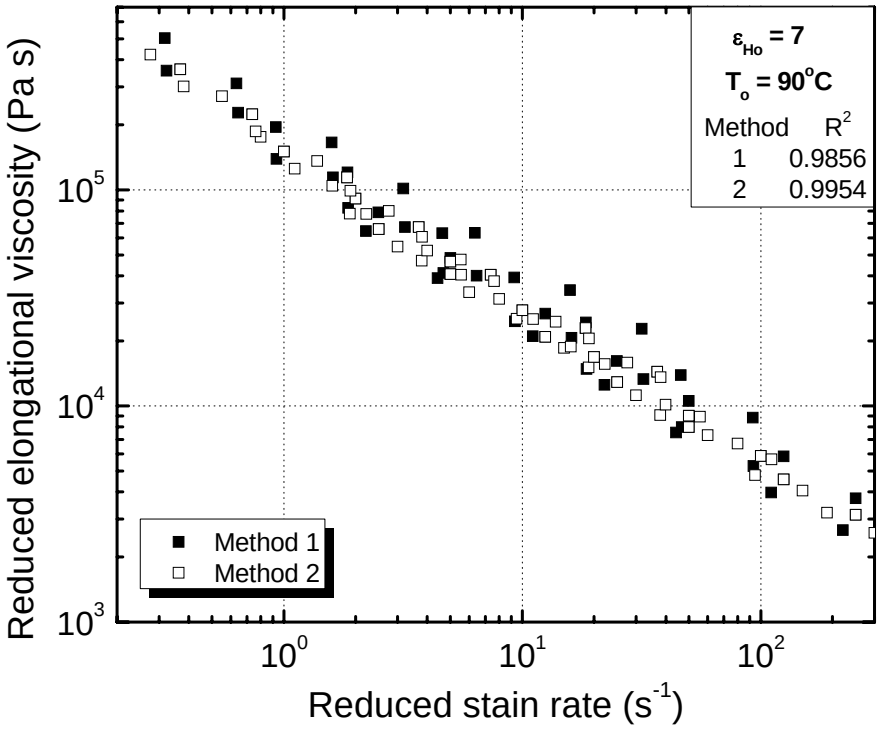

Figure B30: Method 1 and 2 comparison for Hencky strain and temperature shift for a 12% solution.

APPENDIX C

SEM Images

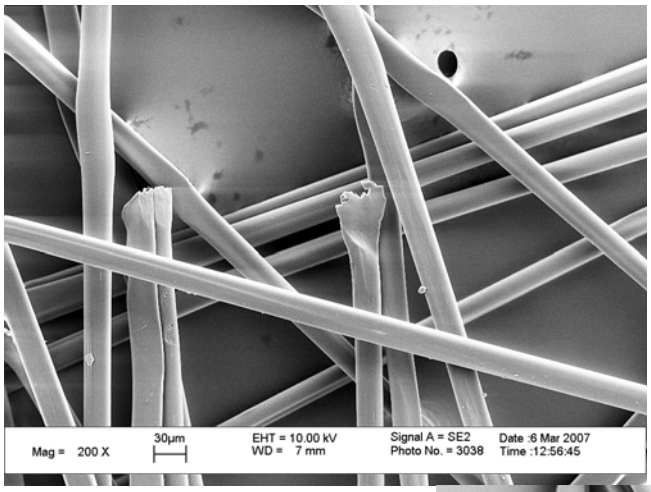

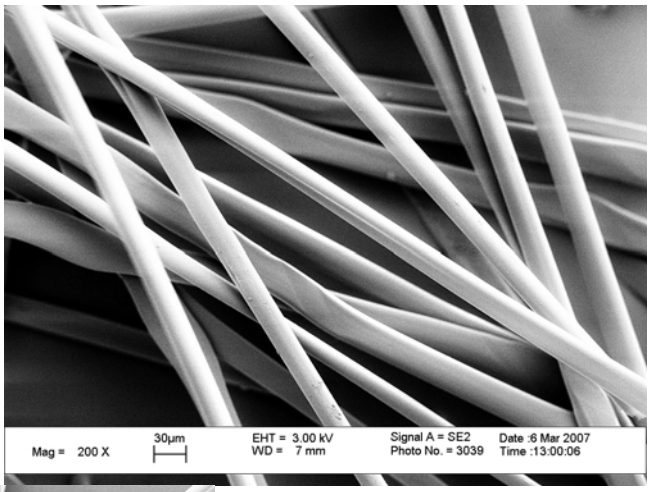

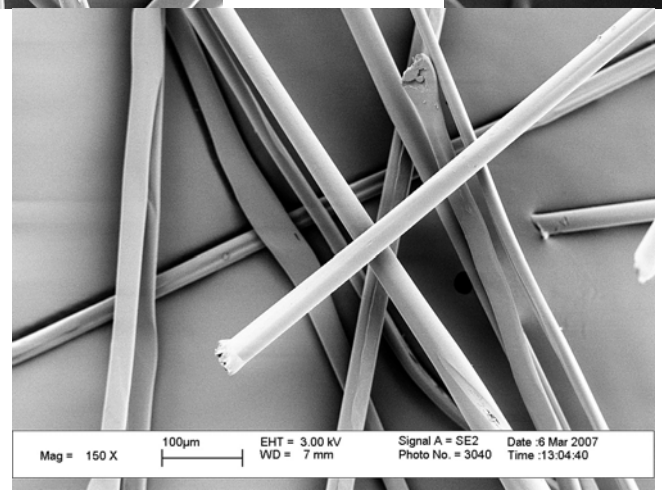

Figure C1: Session #1 - Run#1, 10%, T = 100°C, $\dot{\varepsilon}$ = 1.08 s^{-1}, v_t = 71 m/min, D_r = 39.1

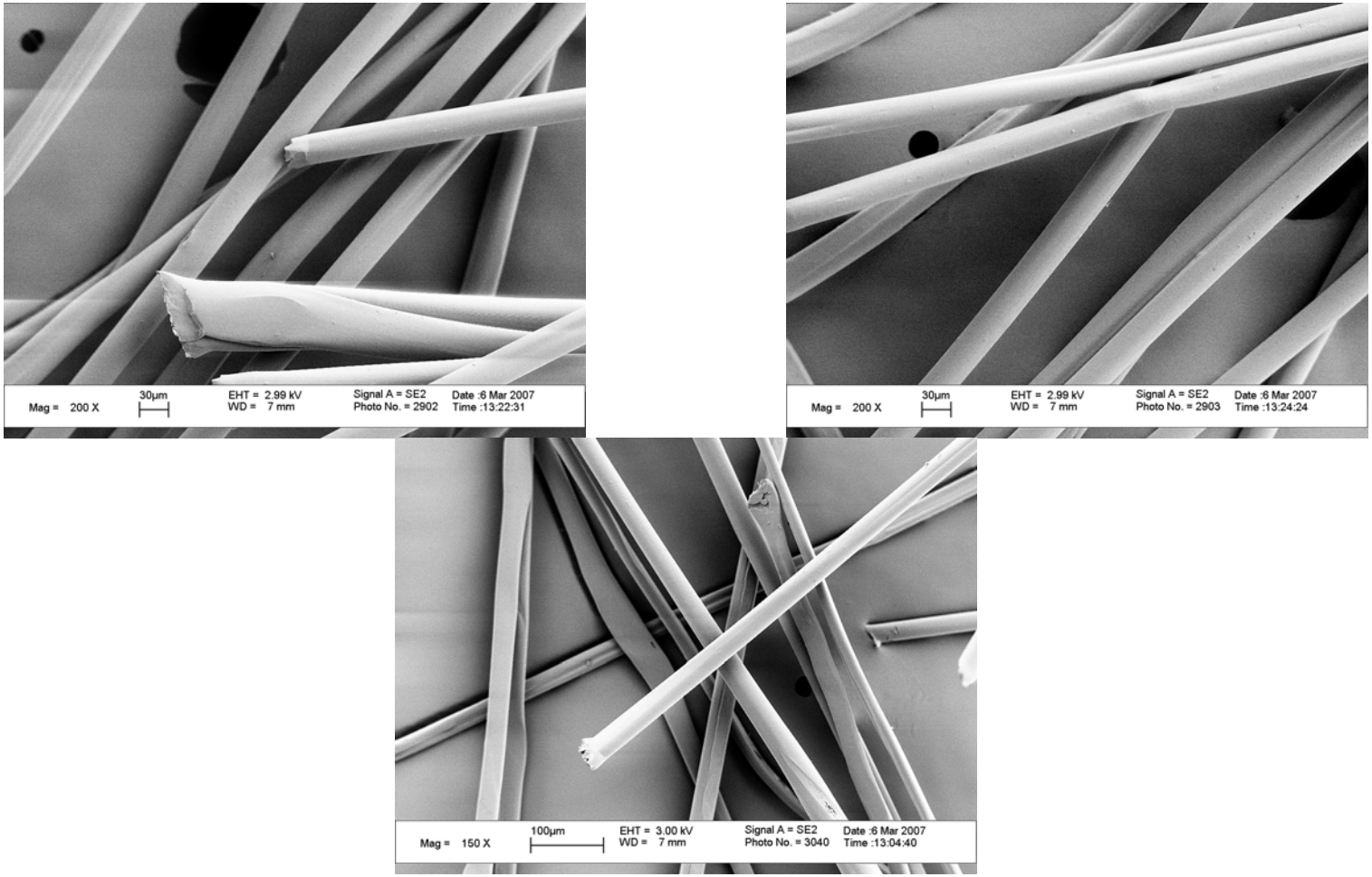

Figure C2: Session #1 - Run#2, 10%, T = 100°C, $\dot{\varepsilon}$ = 1.5 s^{-1}, v_t = ~46 m/min, D_r = 18.2

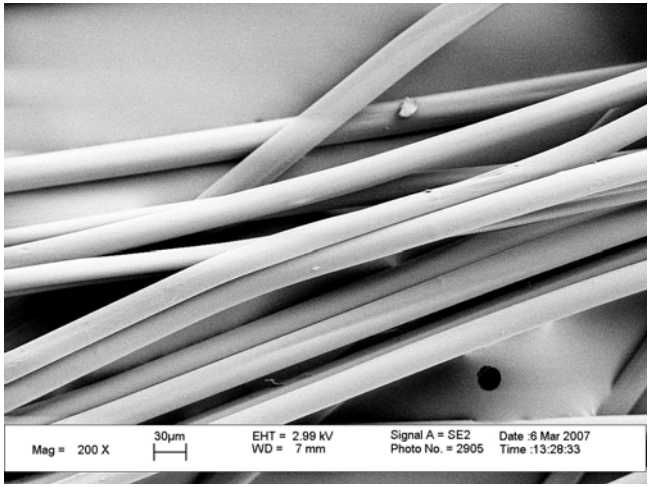

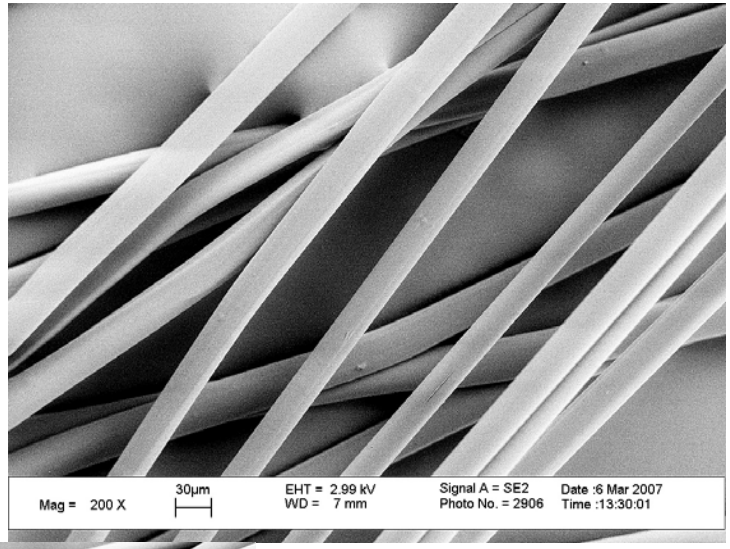

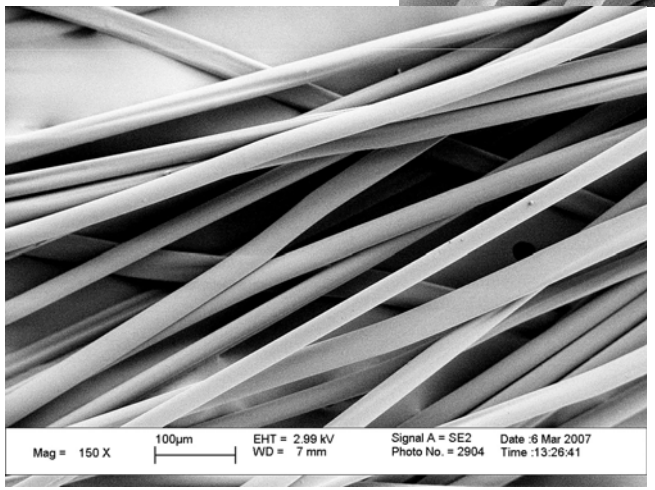

Figure C3: Session #1 - Run#3, 10%, T = 100 ^{o}C, $\dot{\varepsilon}$ = 1.5 s^{-1}, v_t = 71 m/min, D_r = 28.2

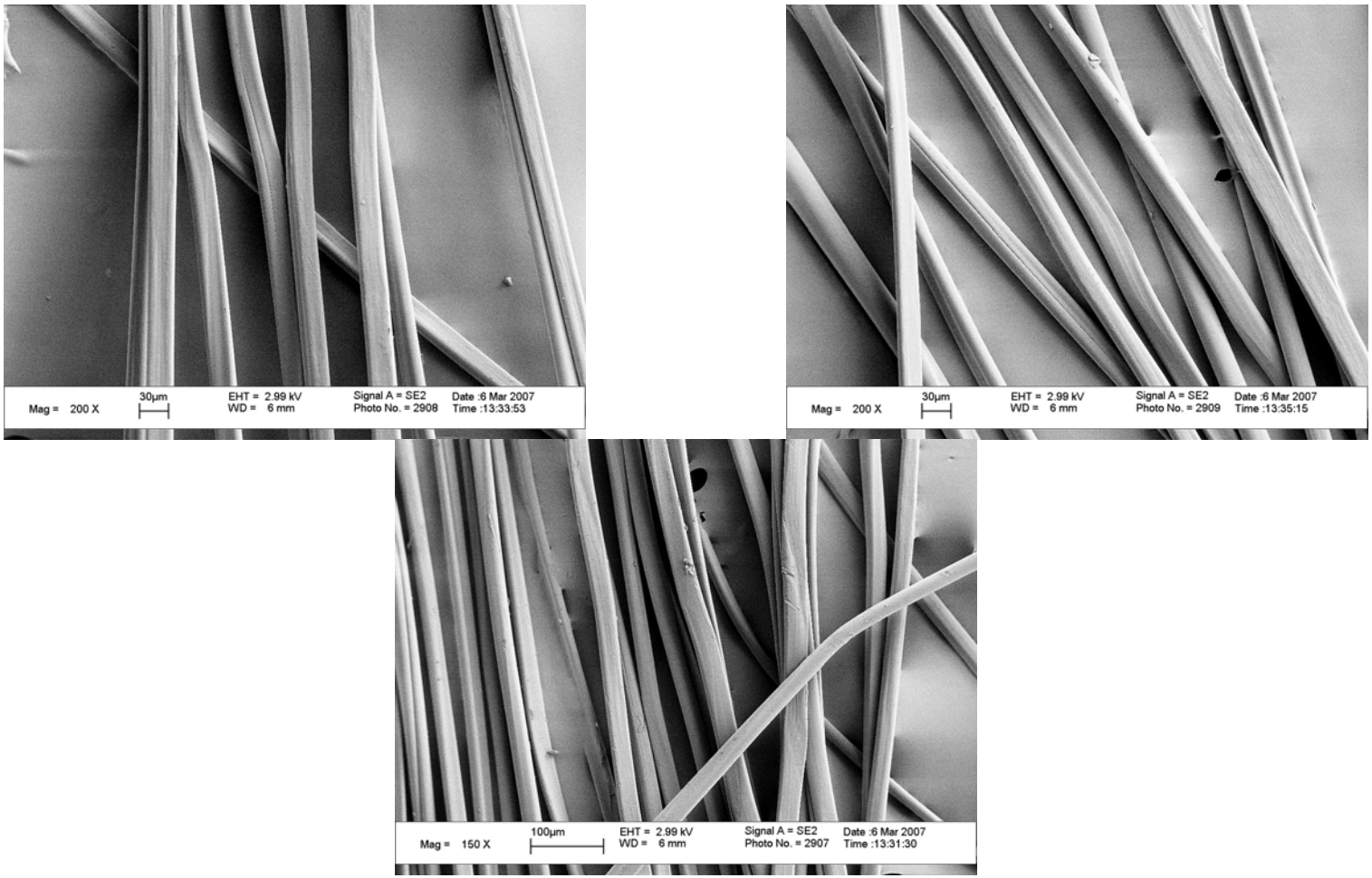

Figure C4: Session #1 - Run#4, 10%, T = 100°C, $\dot{\varepsilon}$ = 1.5 s^{-1}, v_t = 98 m/min, D_r = 38.9

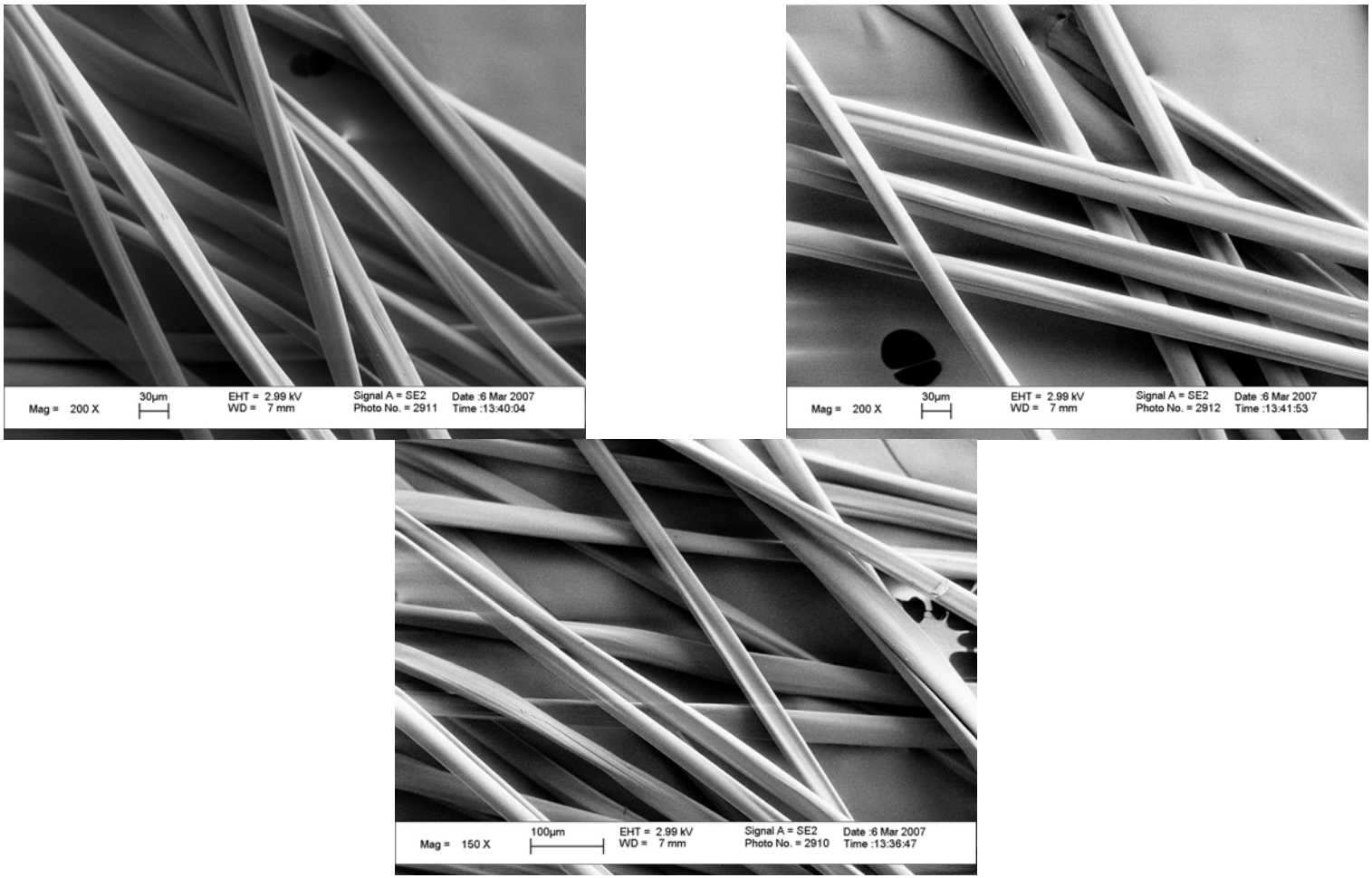

Figure C5: Session #1 - Run# 5, 10%, T = 100°C, $\dot{\varepsilon}$ = 1.92 s^{-1}, v_t = 71 m/min, D_r = 22.0

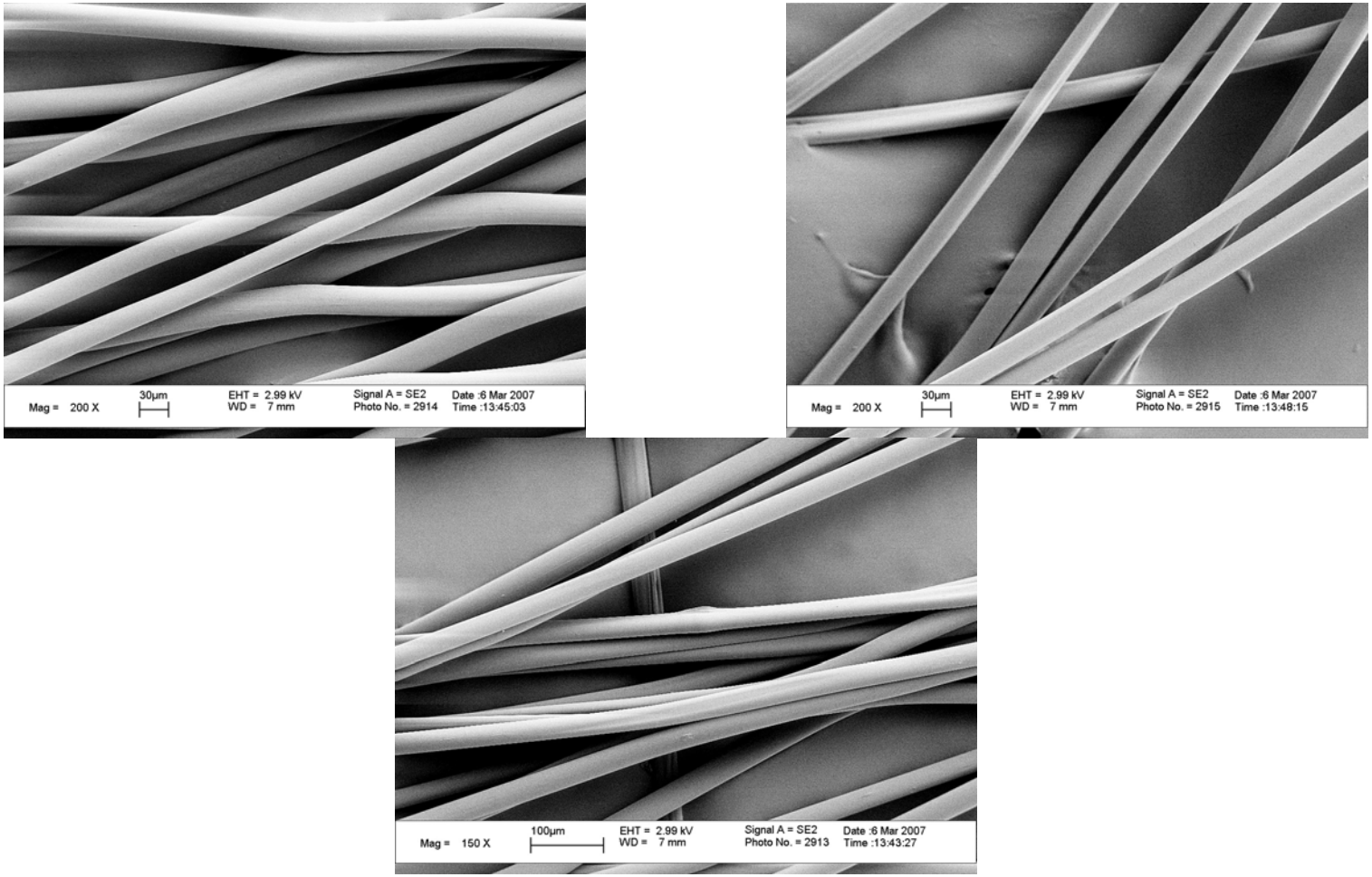

Figure C6: Session #2 - Run#6, 10%, T = 94.1°C, $\dot{\varepsilon}$ = 1.25 s^{-1}, v_t = 56 m/min, D_r = 26.7

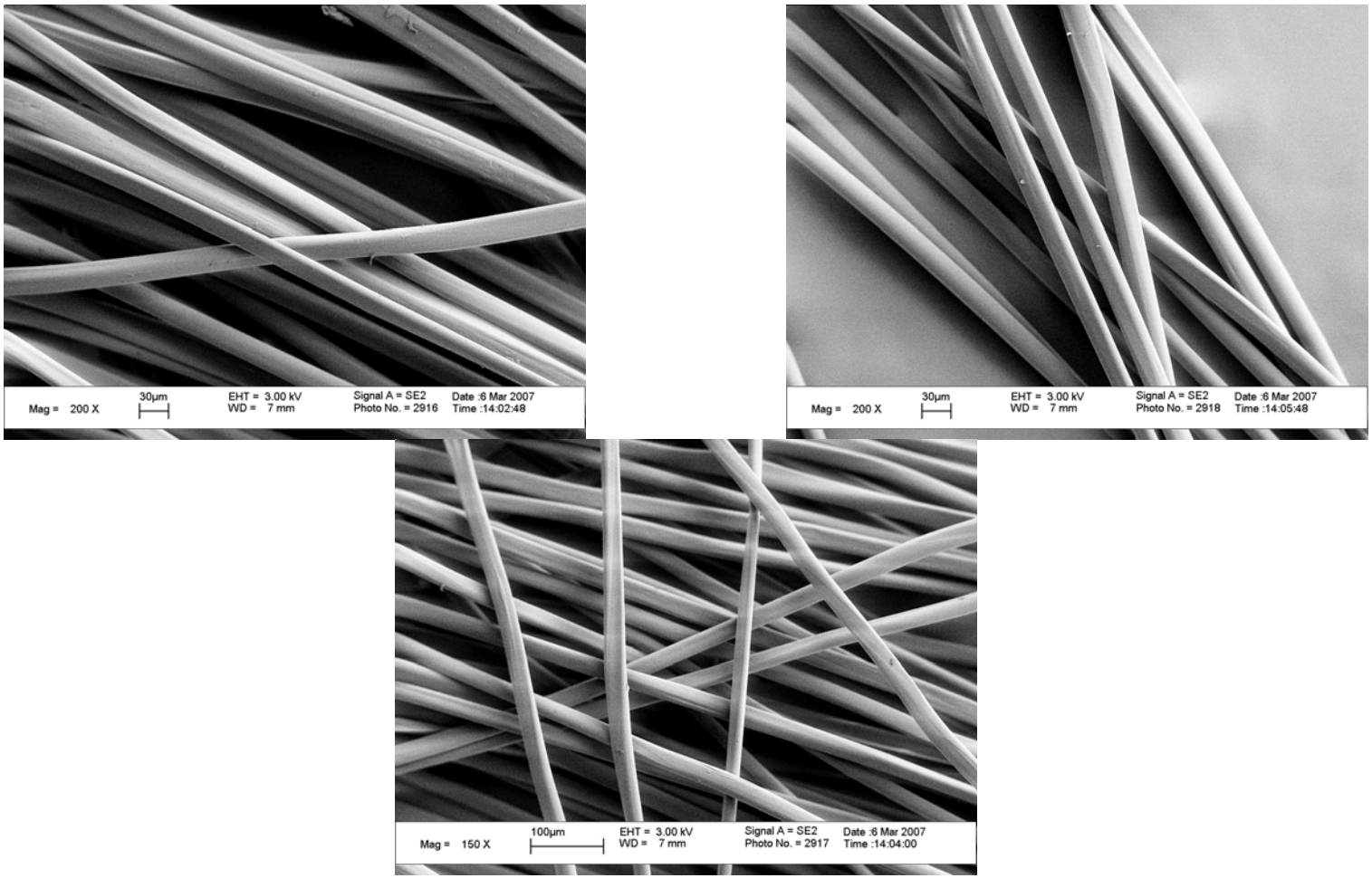

Figure C7: Session #2 - Run#7, 10%, T = 94.1°C, $\dot{\varepsilon}$ = 1.25 s^{-1}, v_t = 88 m/min, D_r = 41.9

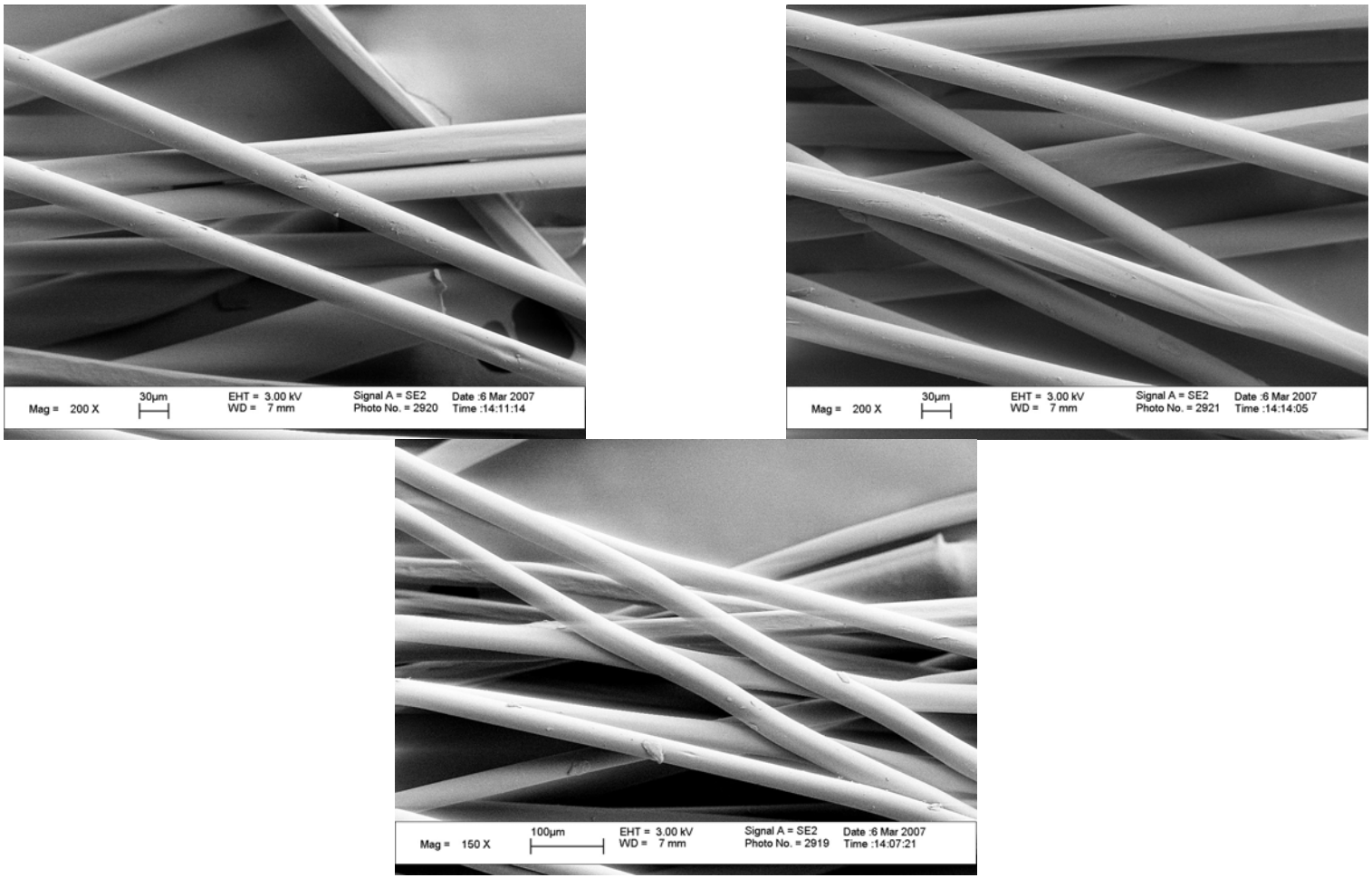

Figure C8: Session #2 - Run#8, 10%, T = 94.1°C, $\dot{\varepsilon}$ = 1.75 s^{-1}, v_t = 56 m/min, D_r = 19.0

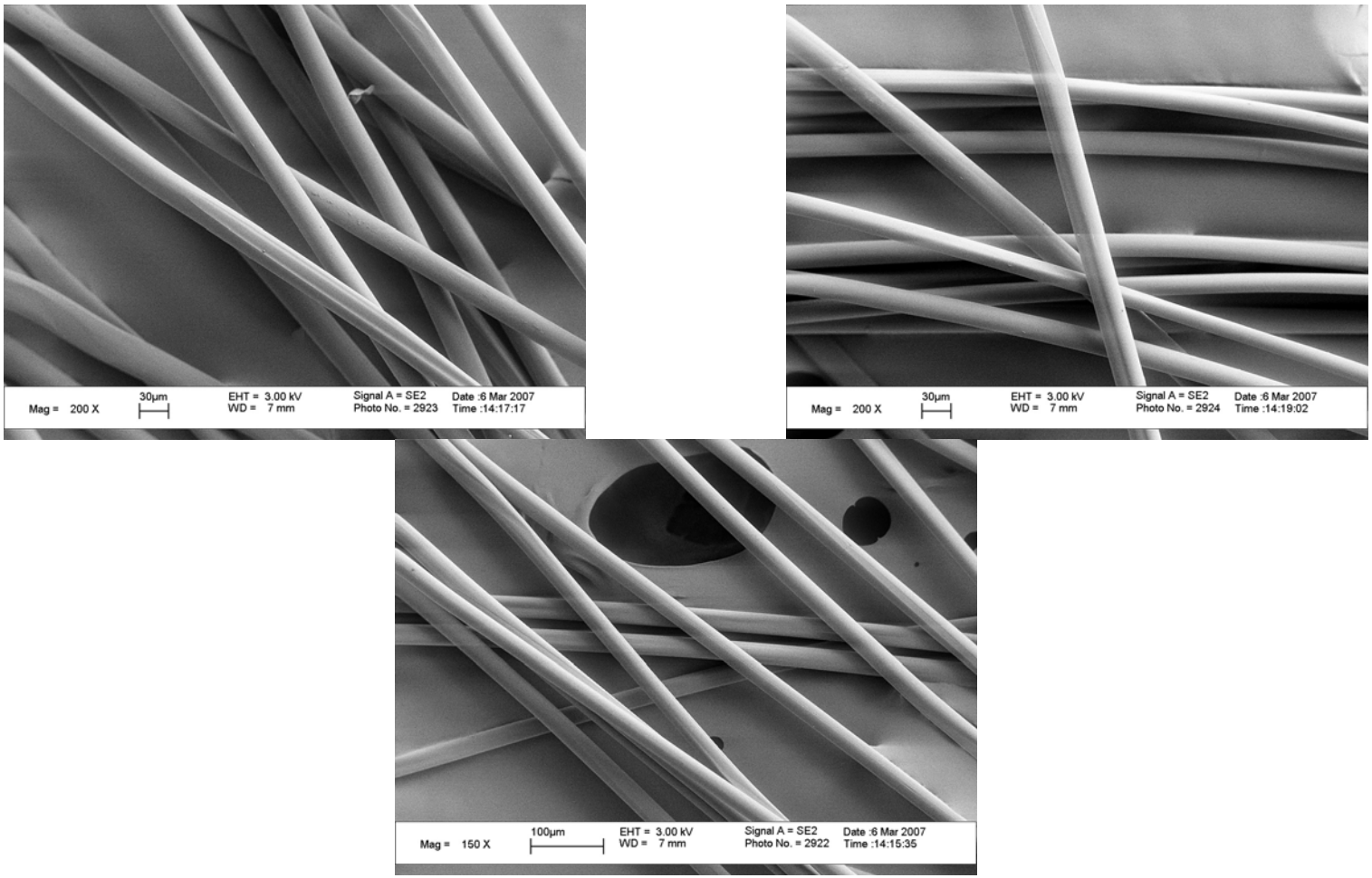

Figure C9: Session #2 - Run#9, 10%, T = 94.1°C, $\dot{\varepsilon}$ = 1.75 s^{-1}, v_t = 88 m/min, D_r = 29.9

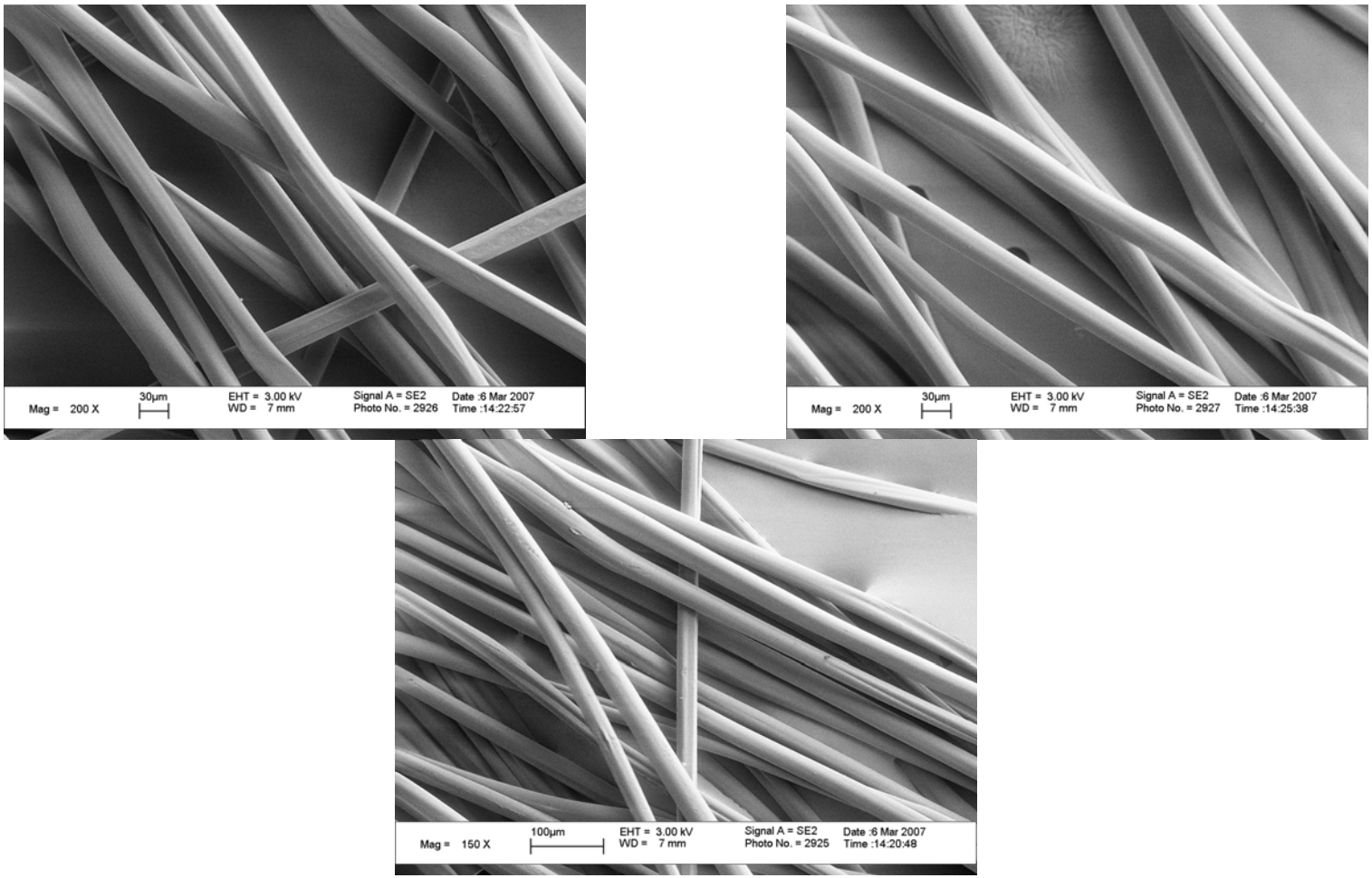

Figure C10: Session #3 - Run#10, 10%, T = 105.9°C, $\dot{\varepsilon}$ = 1.25 s^{-1}, v_t = 56 m/min, D_r = 26.7

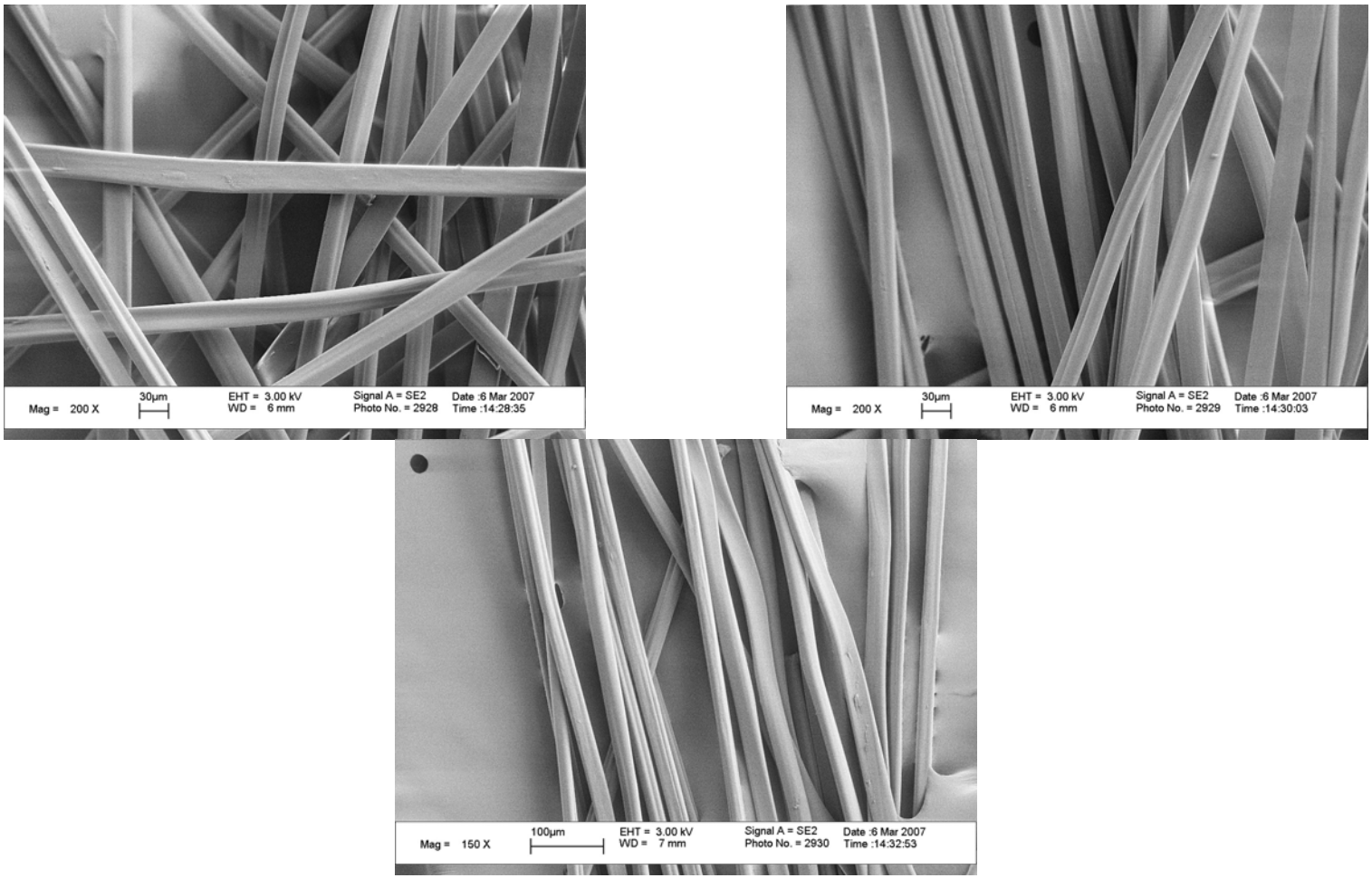

Figure C11: Session #3 - Run#11, 10%, T = 105.9°C, $\dot{\varepsilon}$ = 1.25 s^{-1}, v_t = 88 m/min, D_r = 41.9

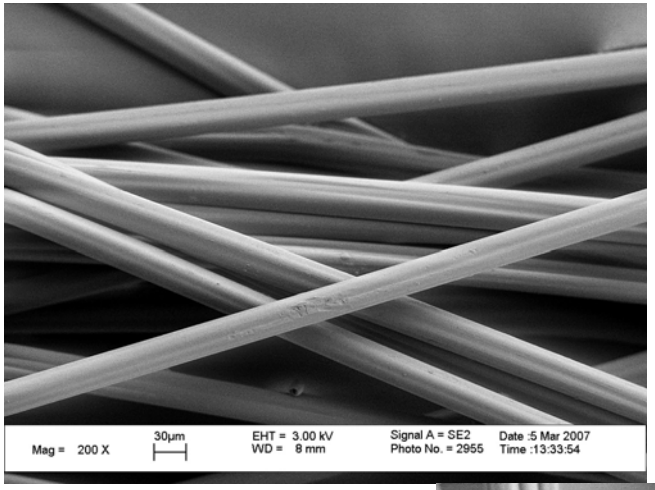

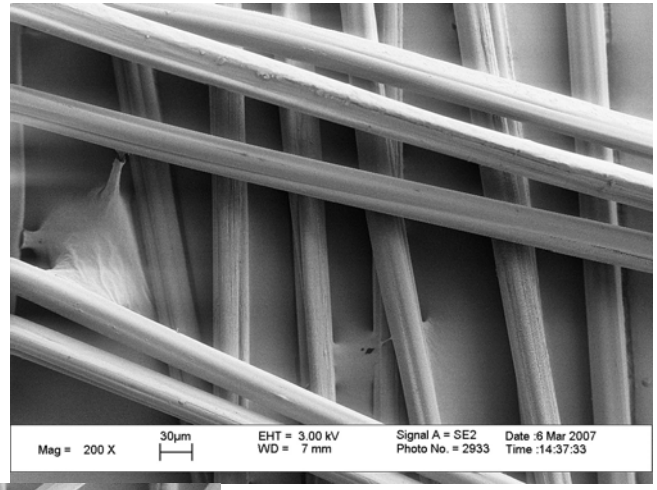

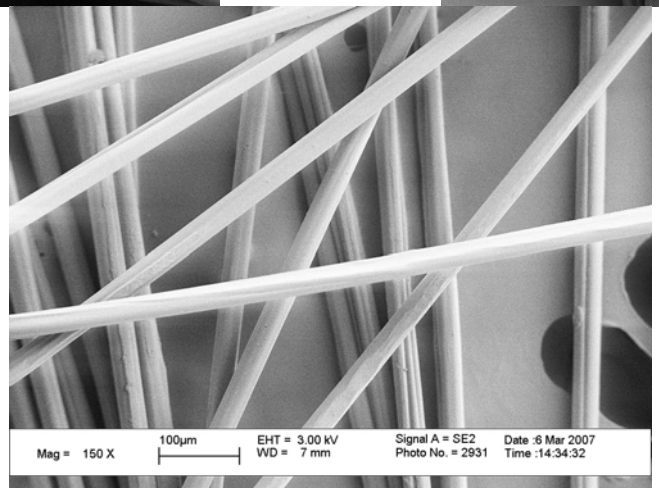

Figure C12: Session #3 - Run#12, 10%, T = 105.9°C, $\dot{\varepsilon}$ = 1.75 s^{-1}, v_t = 56 m/min, D_r = 19.0

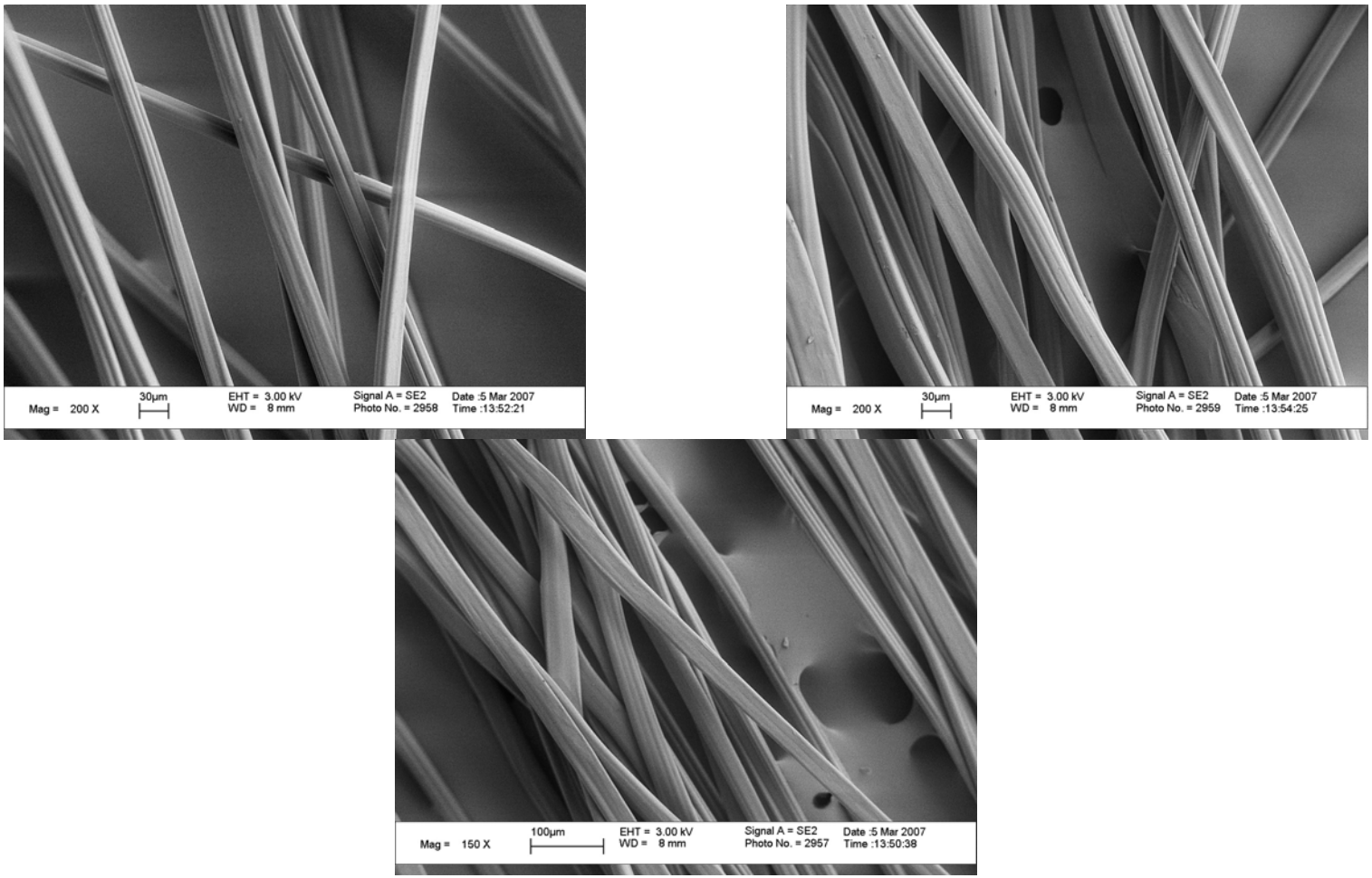

Figure C13: Session #3 - Run#13, 10%, T = 105.9°C, $\dot{\varepsilon}$ = 1.75 s^{-1}, v_t = 88 m/min, D_r = 29.9

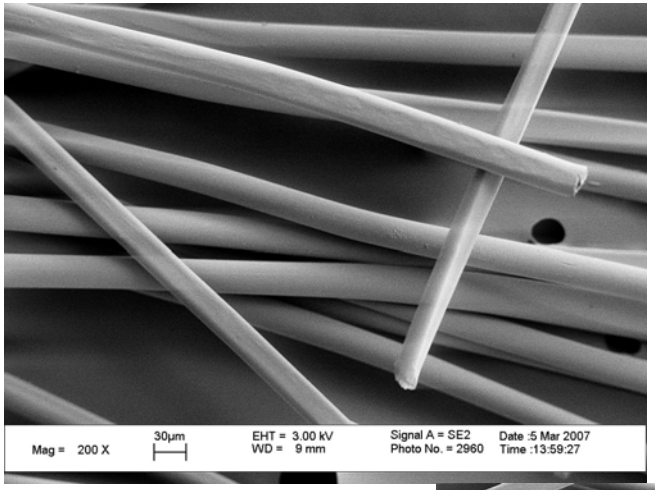

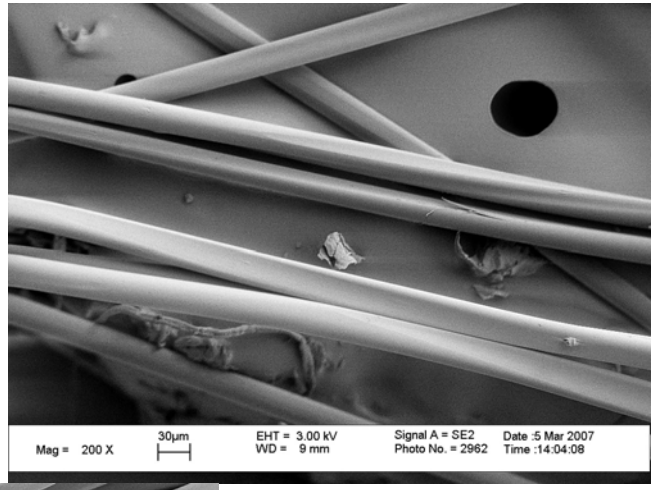

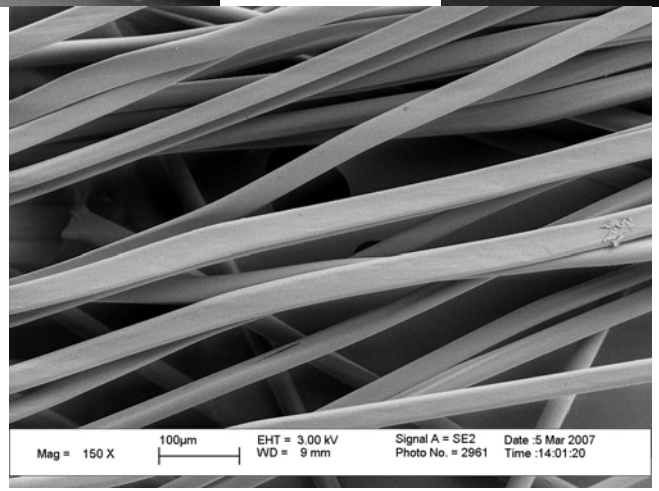

Figure C14: Session #4&5 - Run#14, 10%, T = 90°C, $\dot{\varepsilon}$ = 1.5 s^{-1}, v_t = 71 m/min, D_r = 28.2

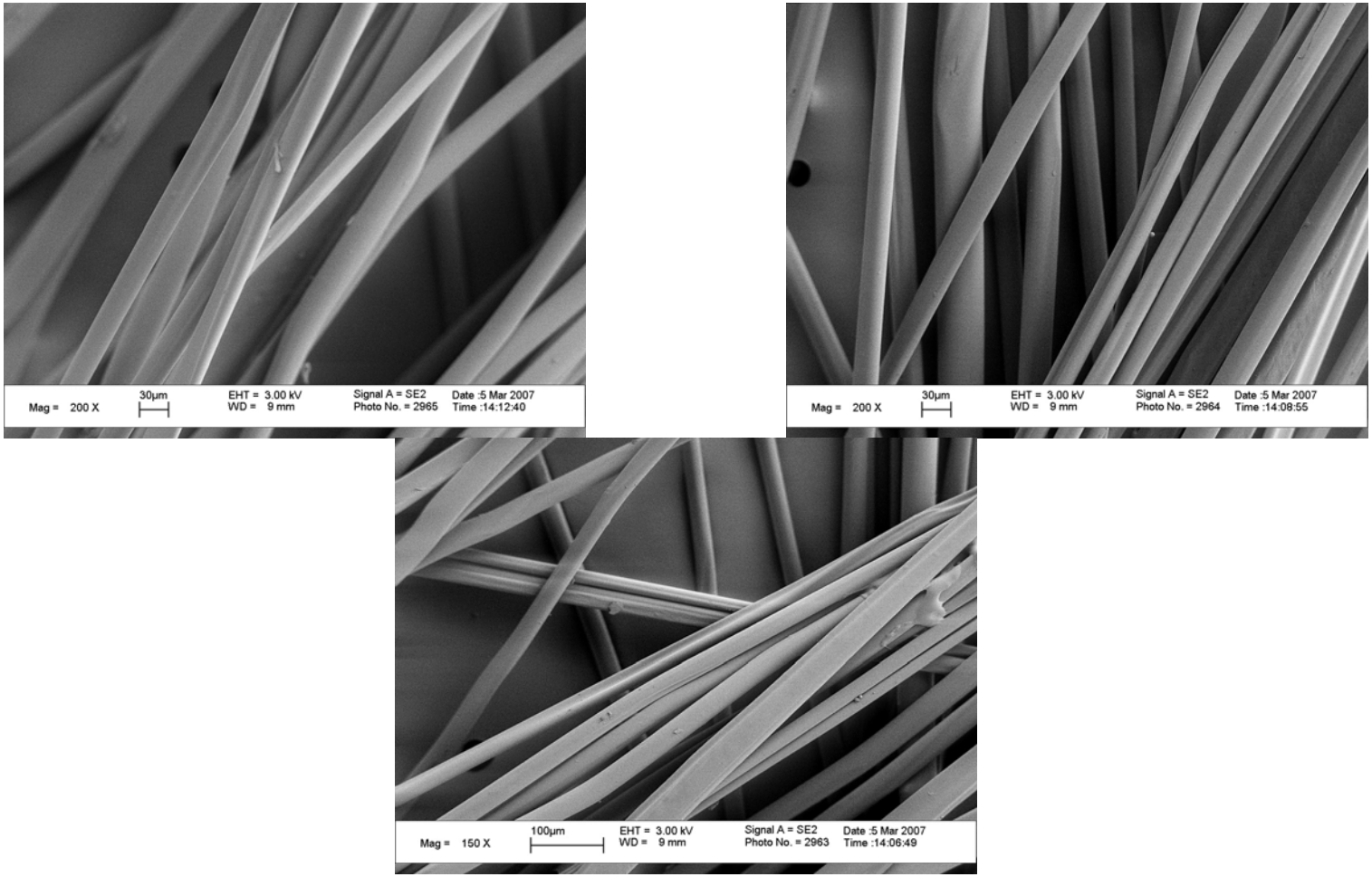

Figure C15: Session #4&5 - Run#15, 10%, T = 110°C, $\dot{\varepsilon}$ = 1.5 s^{-1}, v_t = 71 m/min, D_r = 28.2

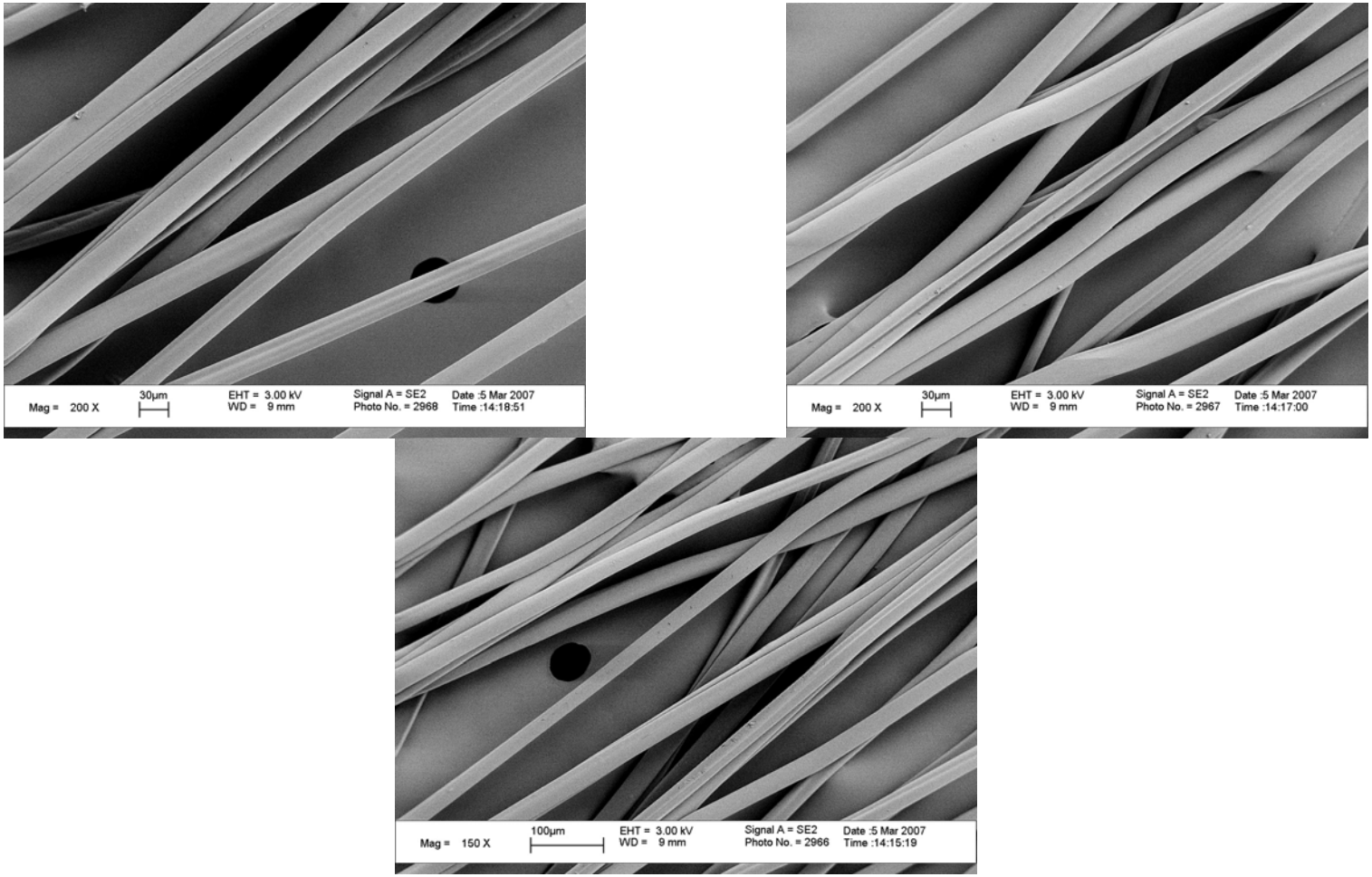

Figure C16: Session #6 - Run#16, 8%, T = 100°C, $\dot{\varepsilon}$ = 1.15 s^{-1}, v_t = 71 m/min, D_r = 36.7

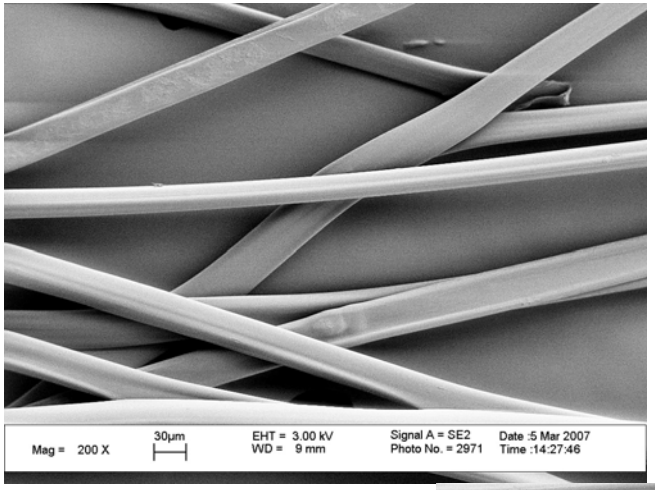

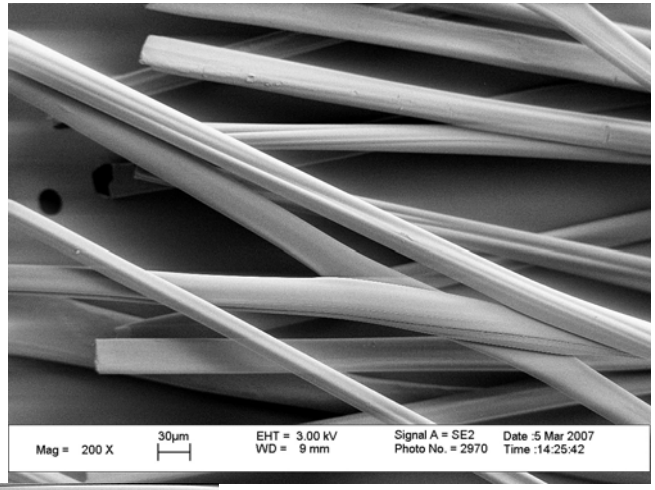

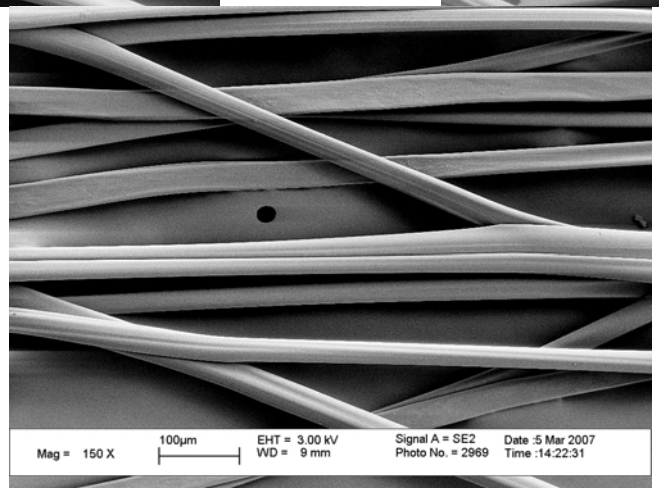

Figure C17: Session #6 - Run#17, 8%, T = 100°C, $\dot{\varepsilon}$ = 1.25 s^{-1}, v_t = 56 m/min, D_r = 26.7

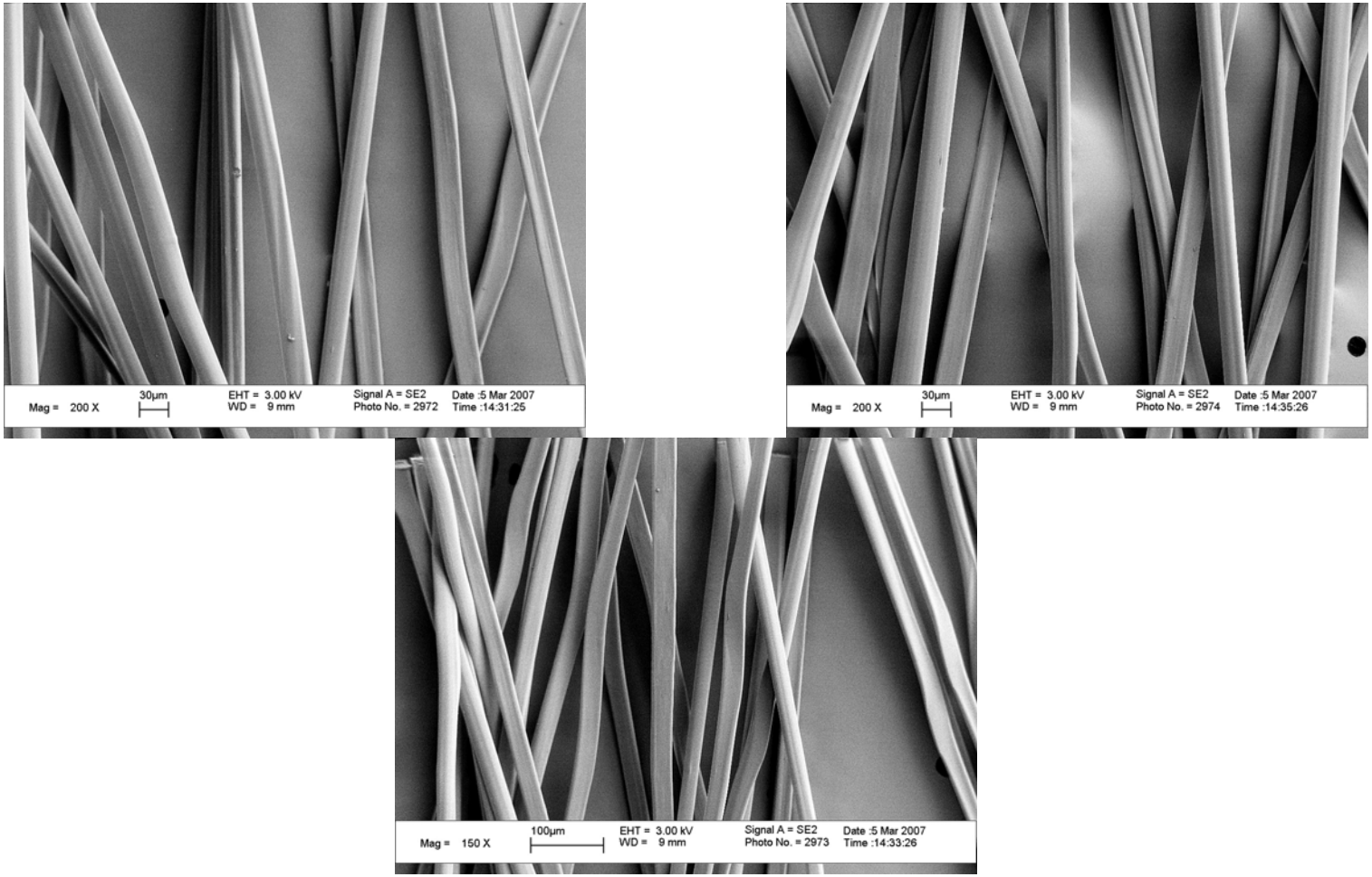

Figure C18: Session #6 - Run#18, 8%, T = 100°C, $\dot{\varepsilon}$ = 1.25 s^{-1}, v_t = 88 m/min, D_r = 41.9

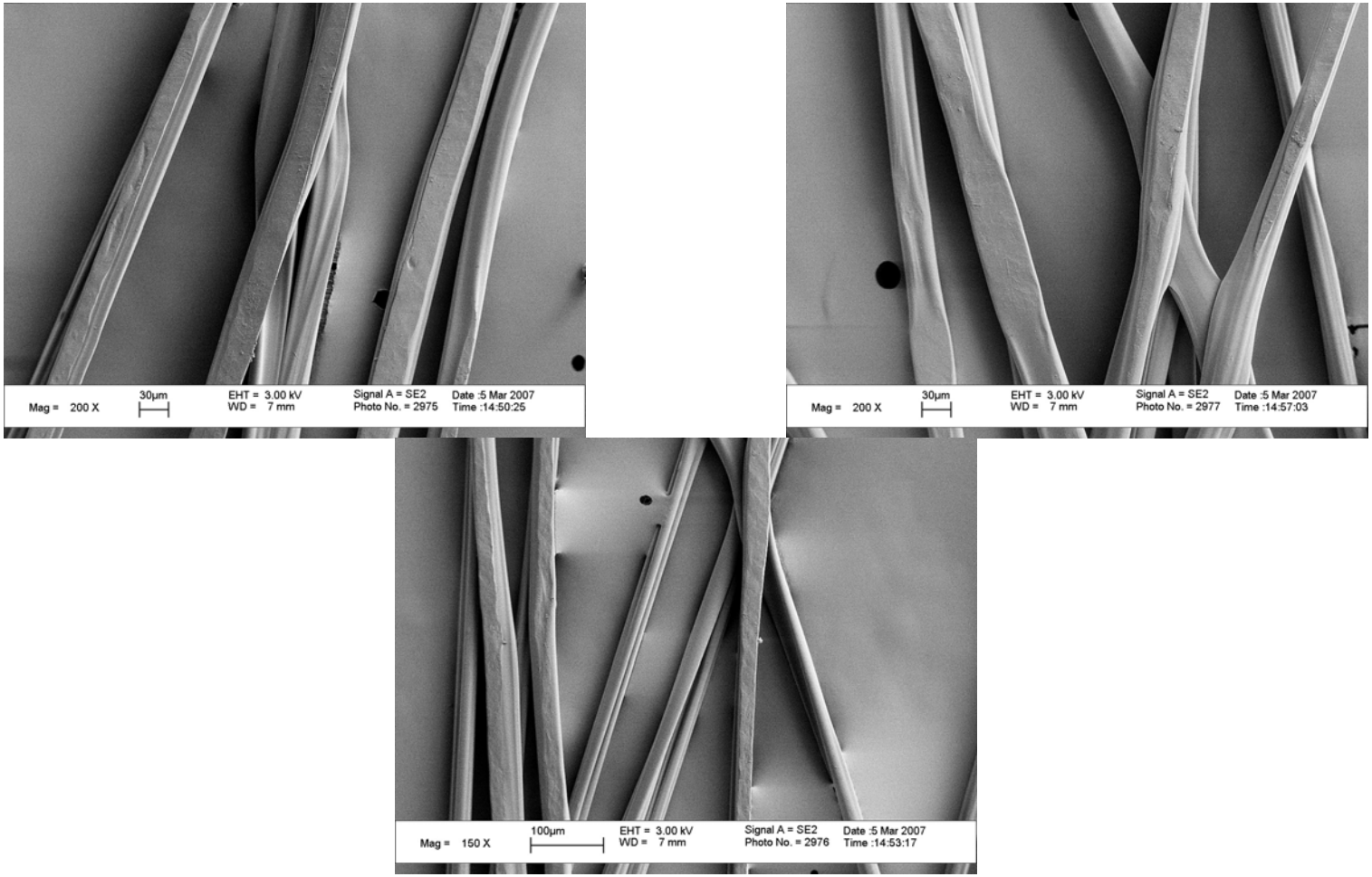

Figure C19: Session #6 - Run#19, 8%, T = 100°C, $\dot{\varepsilon}$ = 1.5 s^{-1}, v_t = 50 m/min, D_r = 19.8

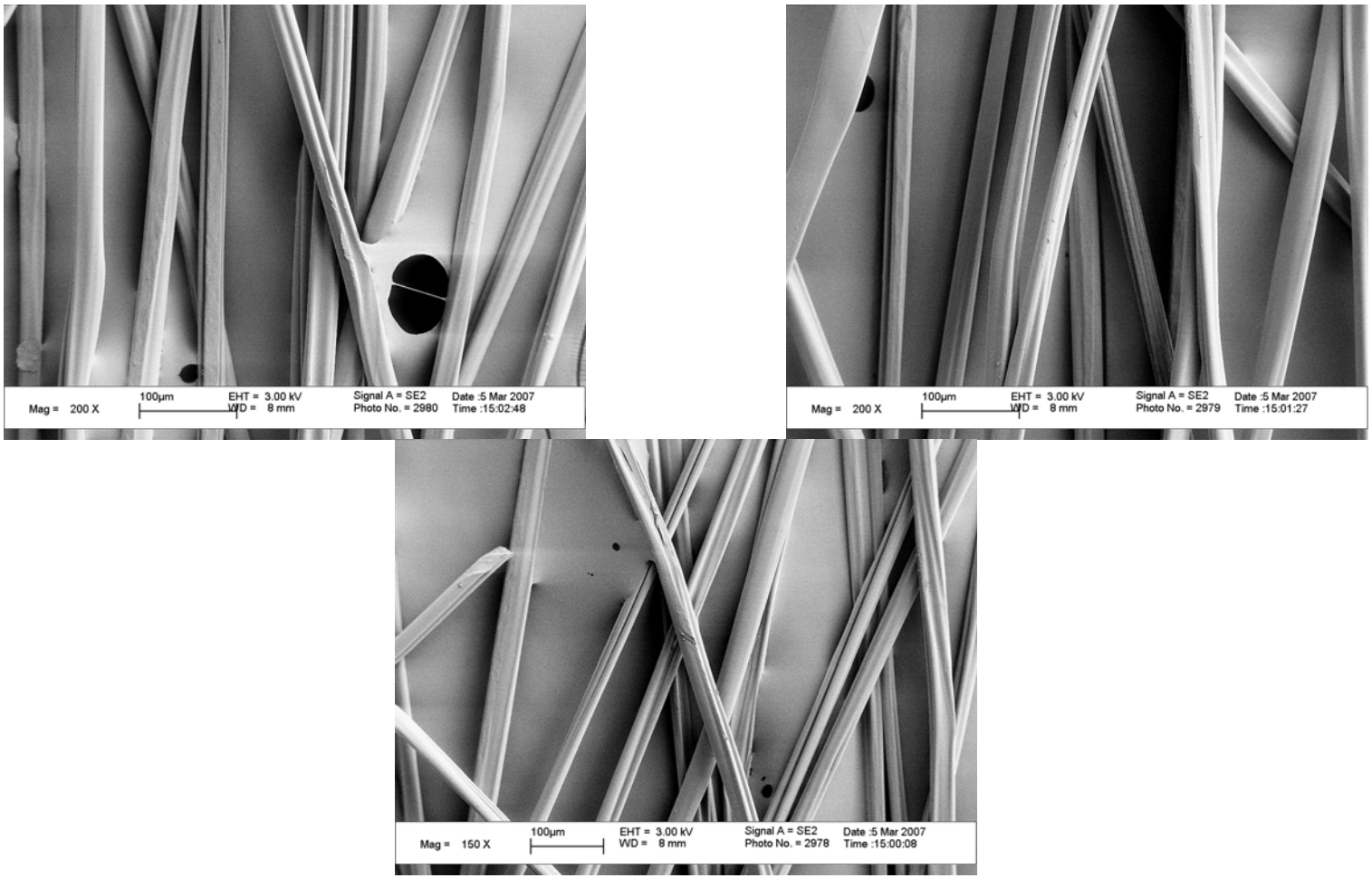

Figure C20: Session #6 - Run#20, 8%, T = 100^{o}C, $\dot{\varepsilon}$ = 1.5 s^{-1}, v_t = 71 m/min, D_r = 28.2

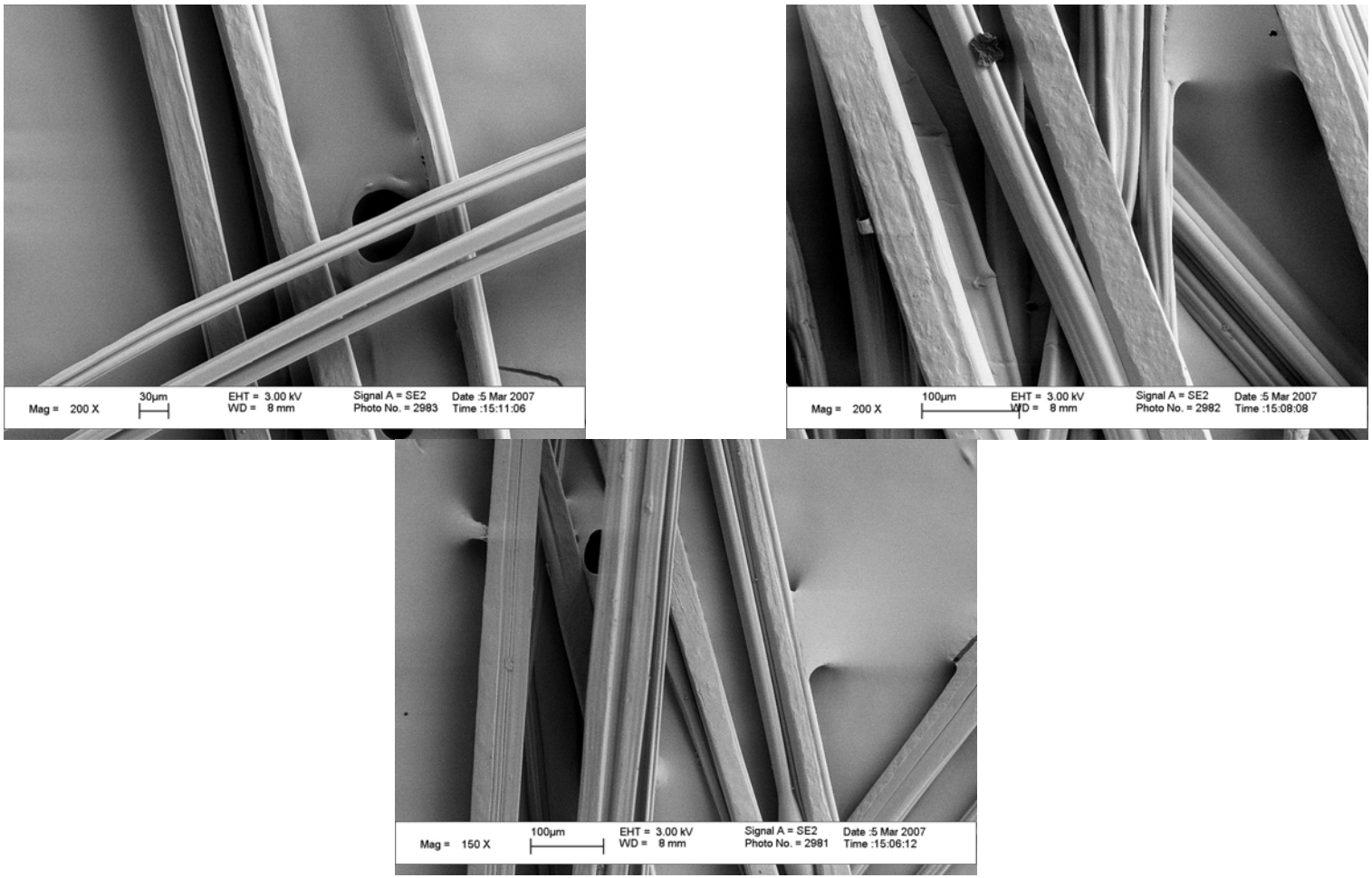

Figure C21: Session #6 - Run#21, 8%, T = 100°C, $\dot{\varepsilon}$ = 1.5 s^{-1}, v_t = 95 m/min, D_r = 37.7

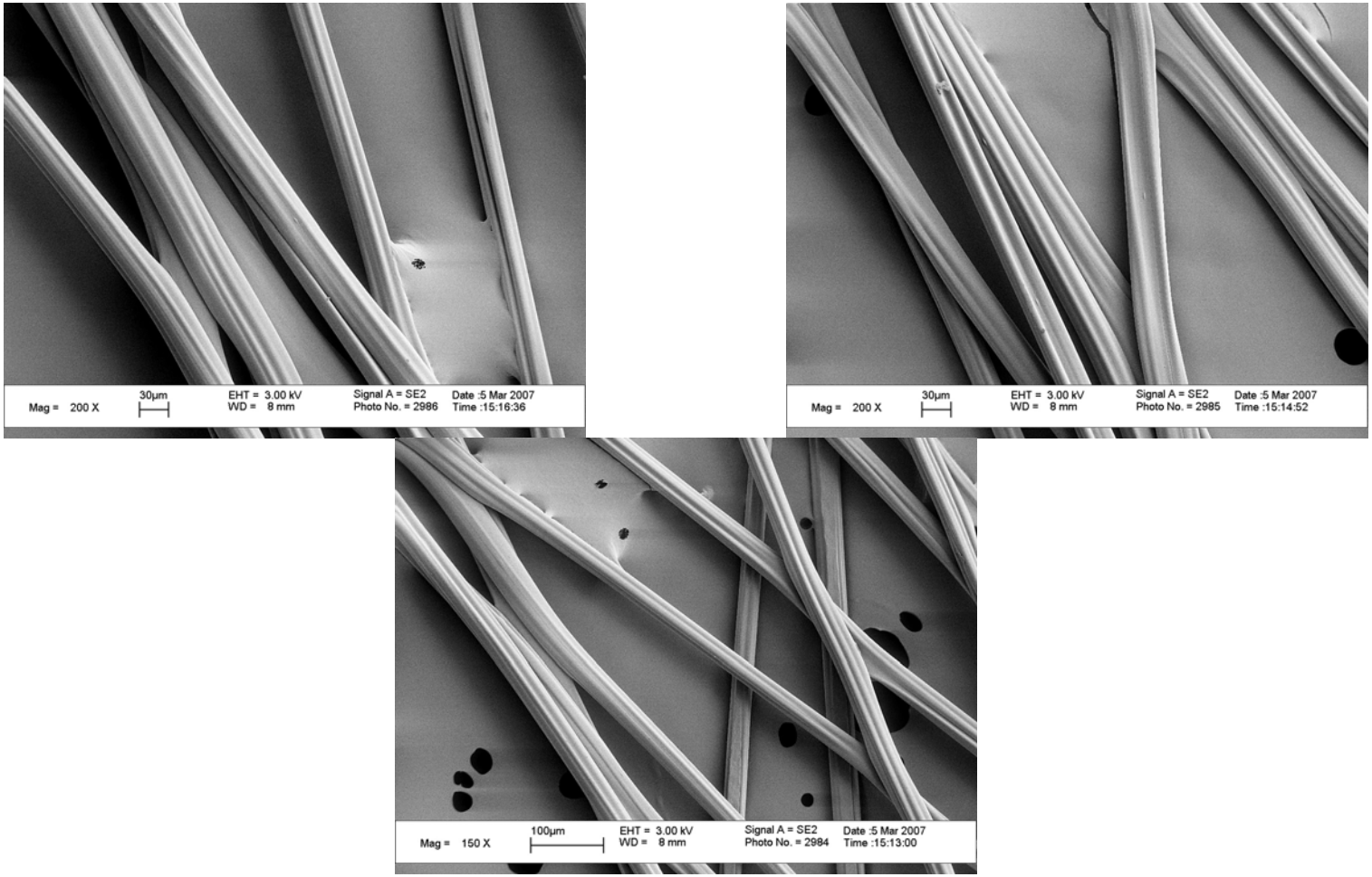

Figure C22: Session #6 - Run#22, 8%, T = 100°C, $\dot{\varepsilon}$ = 1.75 s^{-1}, v_t = 56 m/min, D_r = 19.0

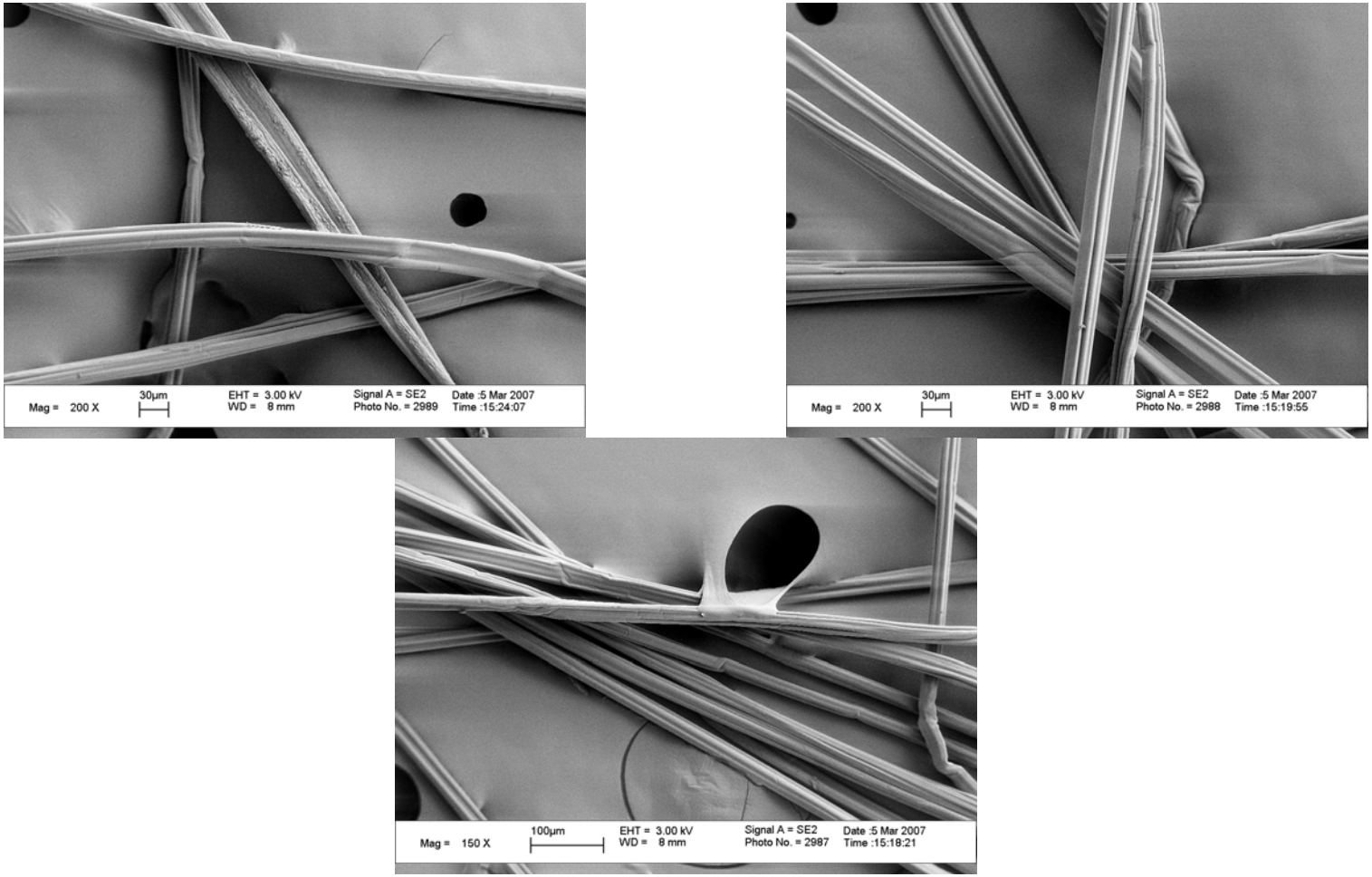

Figure C23: Session #6 - Run#23, 8%, T = 100°C, $\dot{\varepsilon}$ = 1.75 s^{-1}, v_t = 88 m/min, D_r = 29.9

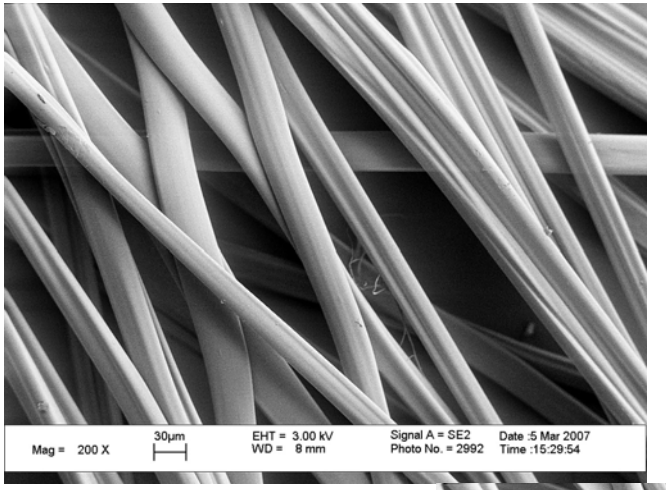

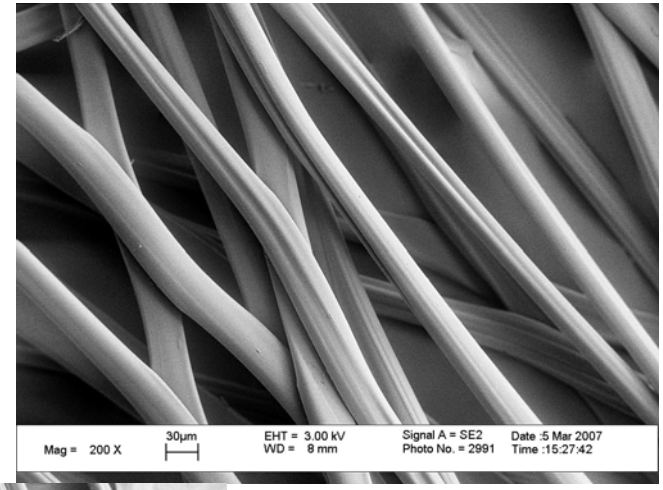

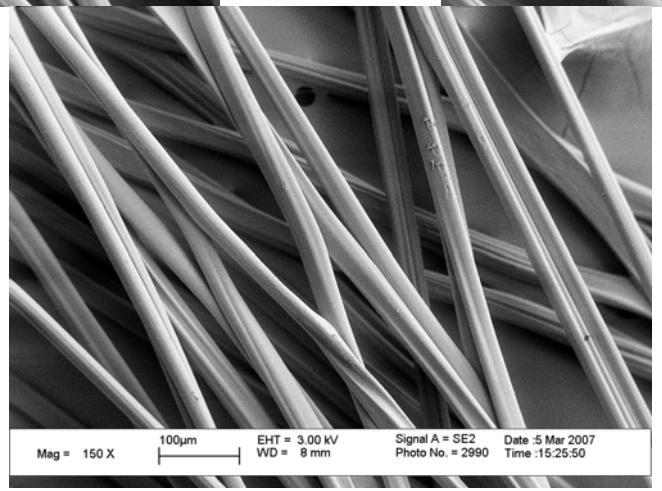

Figure C24: Session #6 - Run#24, 8%, T = 100°C, $\dot{\varepsilon}$ = 1.85 s^{-1}, v_t = 71 m/min, D_r = 22.8

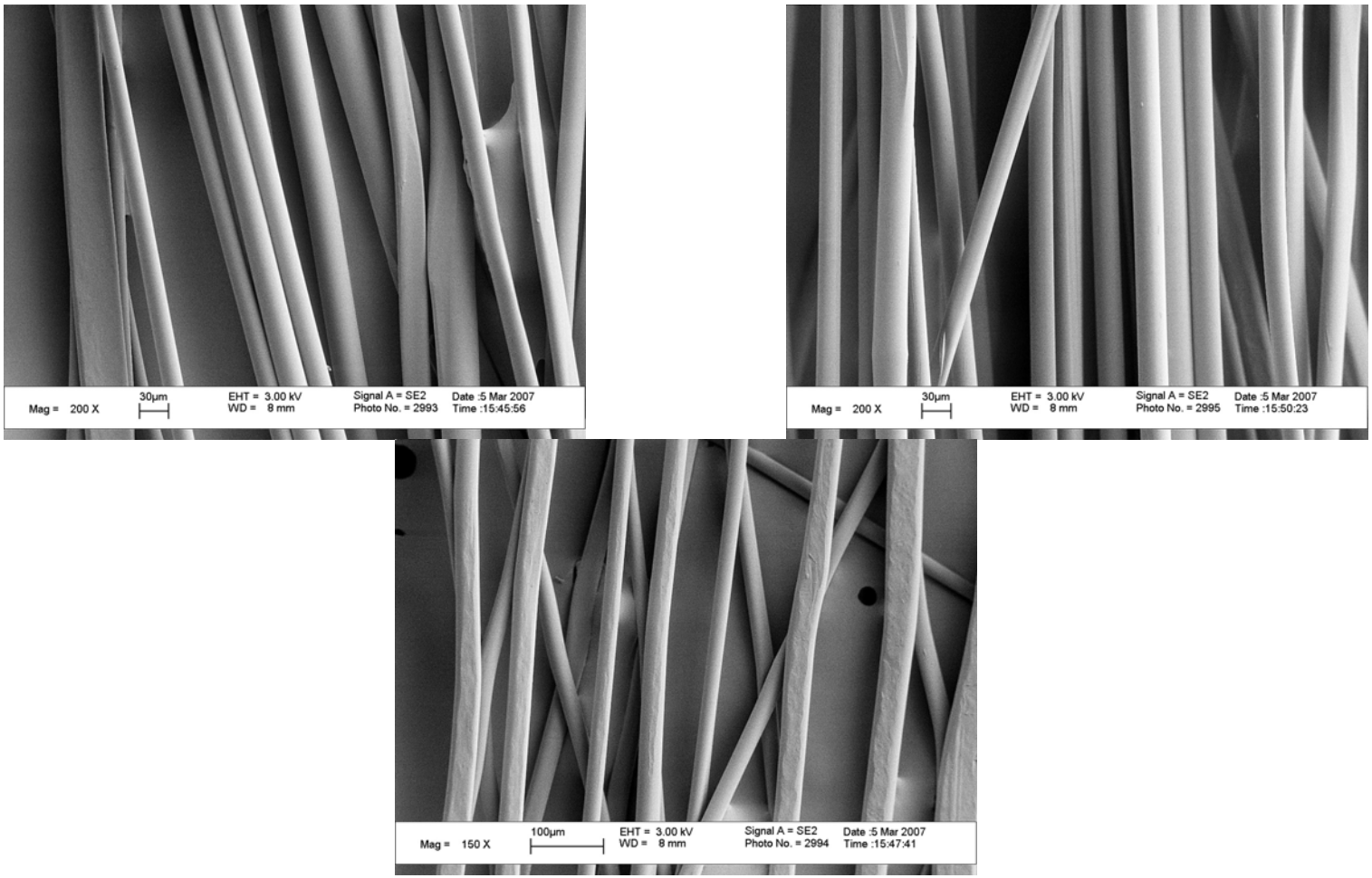

Figure C25: Session #7 - Run#25, 12%, T = 100°C, $\dot{\varepsilon}$ = 1.15 s^{-1}, v_t = 71 m/min, D_r = 36.7

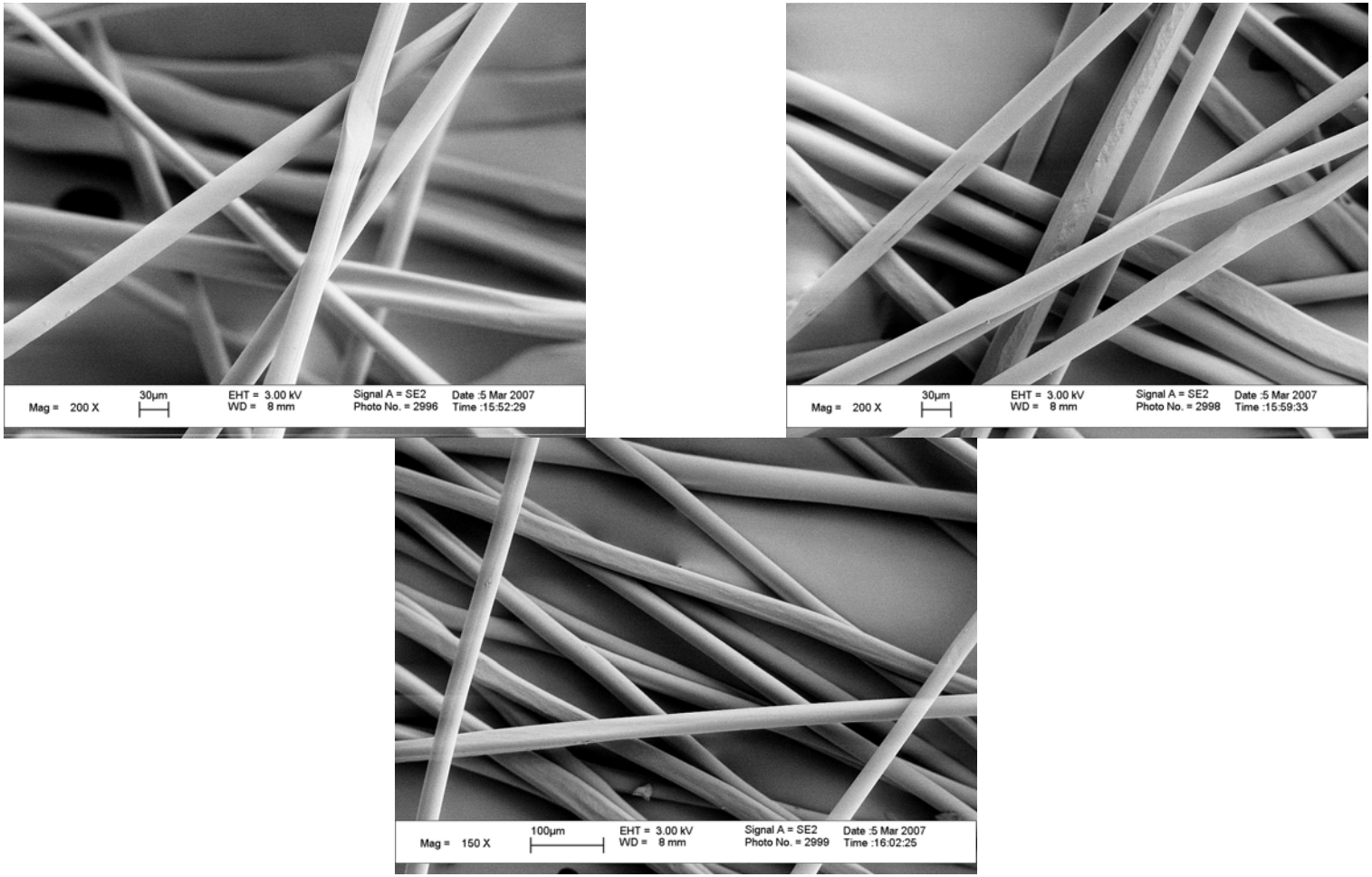

Figure C26: Session #7 - Run#26, 12%, T = 100°C, $\dot{\varepsilon}$ = 1.25 s^{-1}, v_t = 56 m/min, D_r = 26.7

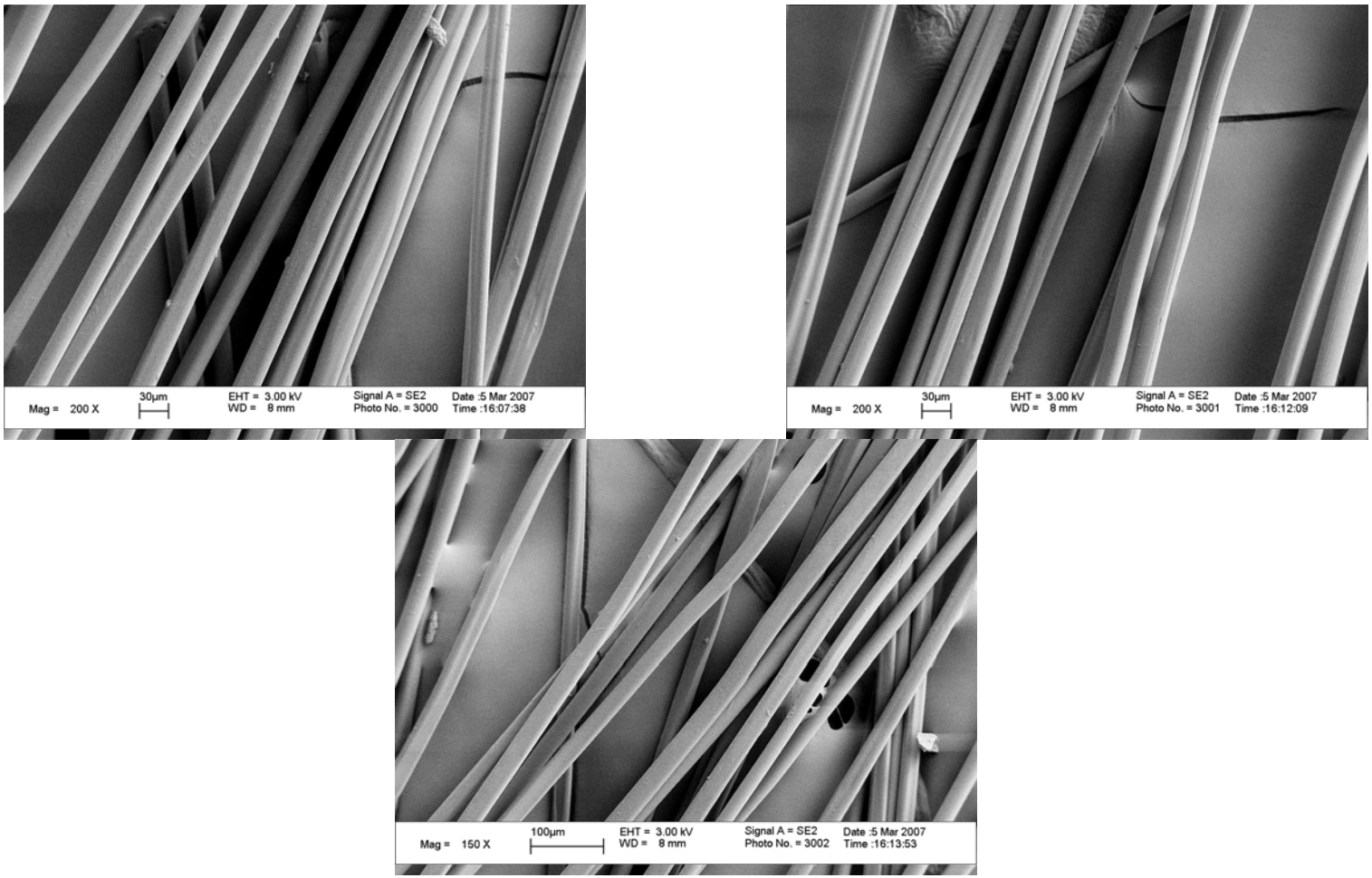

Figure C27: Session #7 - Run#27, 12%, T = 100°C, $\dot{\varepsilon}$ = 1.25 s^{-1}, v_t = 88 m/min, D_r = 41.9

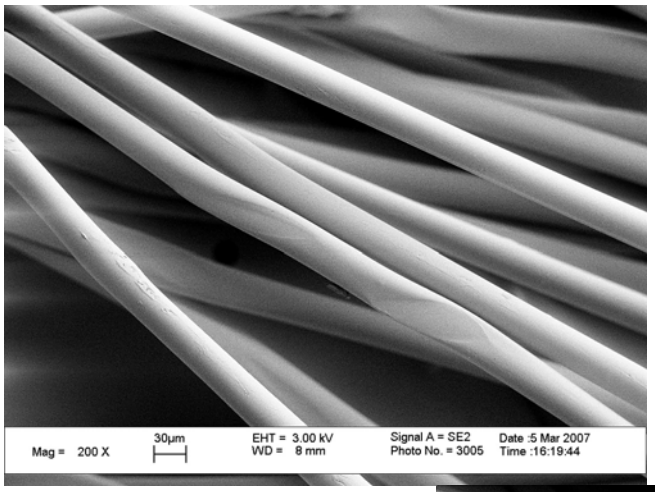

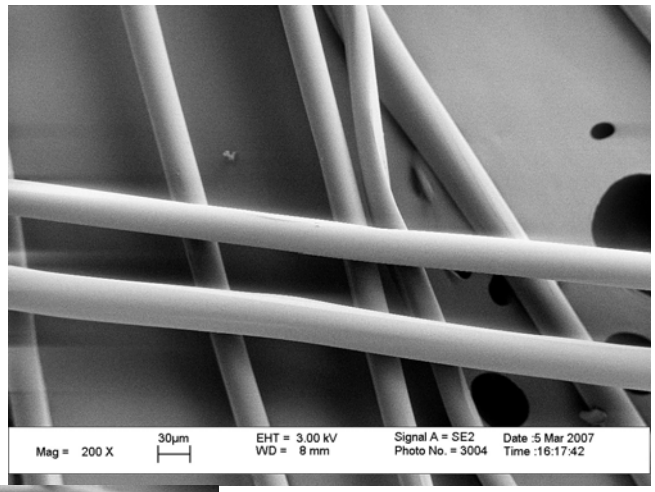

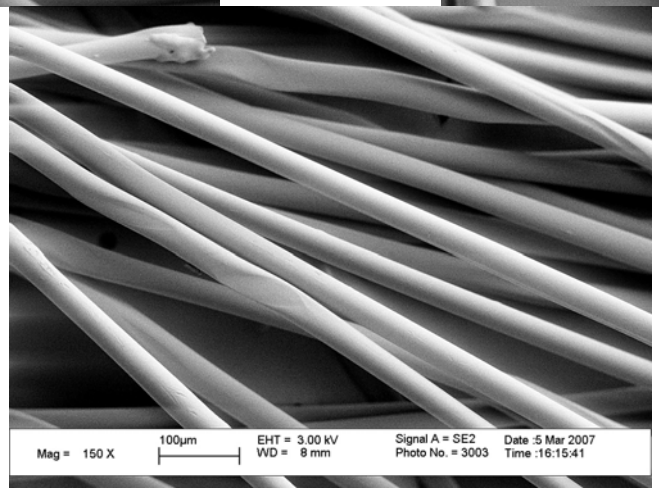

Figure C28: Session #7 - Run#28, 12%, T = 100°C, $\dot{\varepsilon}$ = 1.5 s^{-1}, v_t = 50 m/min, D_r = 19.8

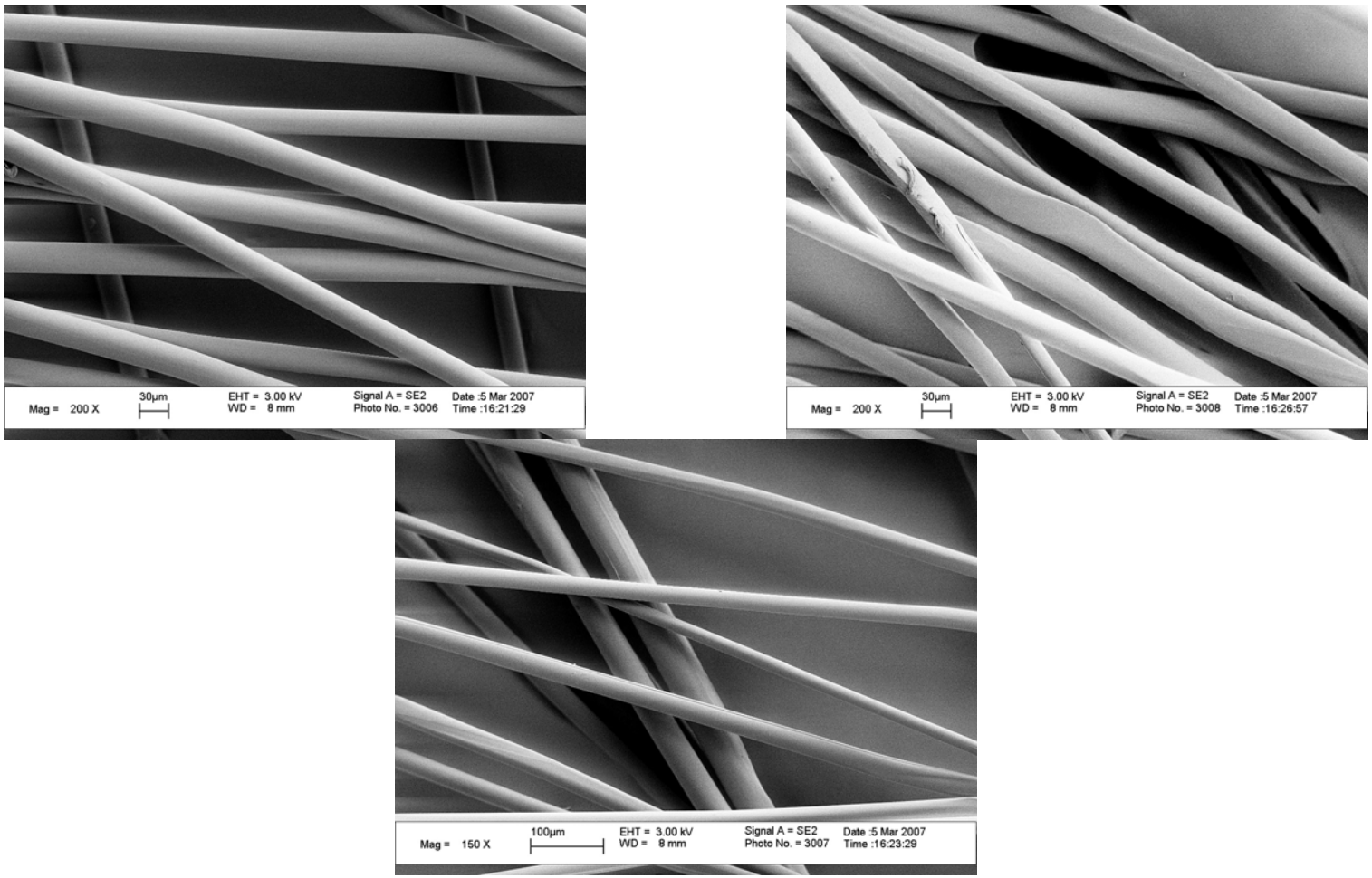

Figure C29: Session #7 - Run#29, 12%, T = 100°C, $\dot{\varepsilon}$ = 1.5 s^{-1}, v_t = 71 m/min, D_r = 28.2

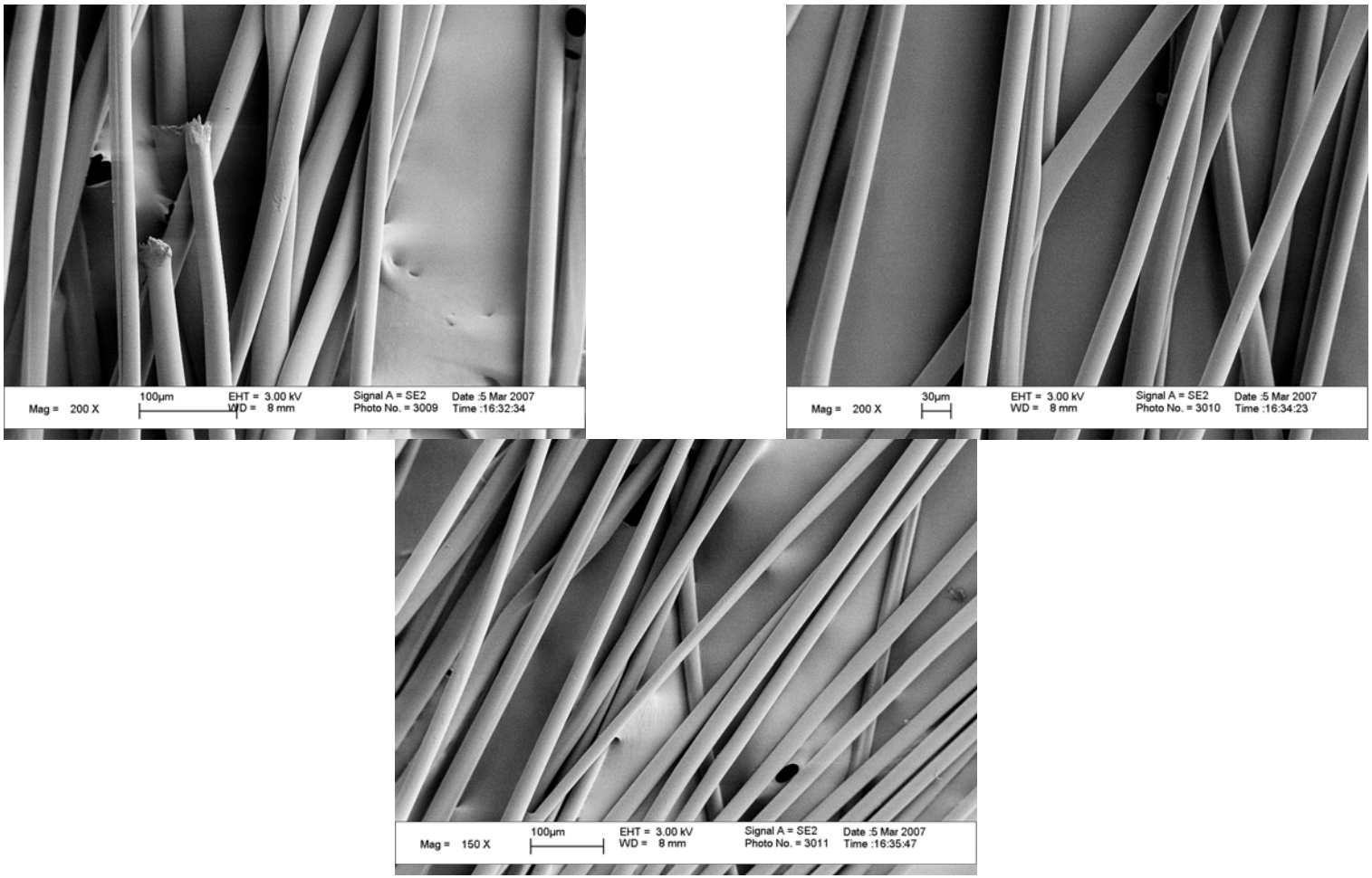

Figure C30: Session #7 - Run#30, 12%, T = 100°C, $\dot{\varepsilon}$ = 1.5 s^{-1}, v_t = 95 m/min, D_r = 37.7

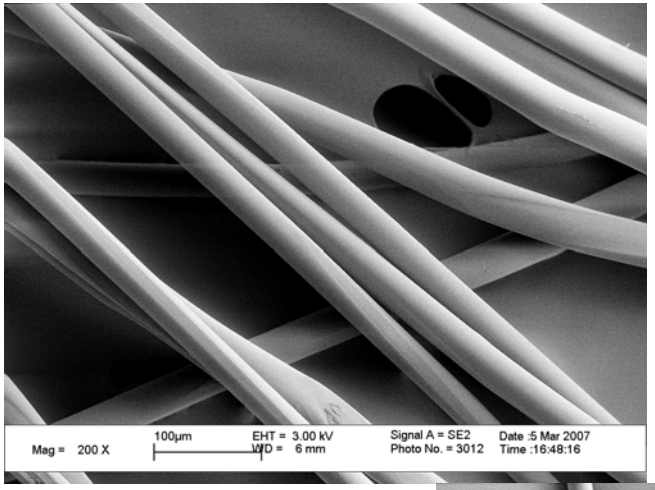

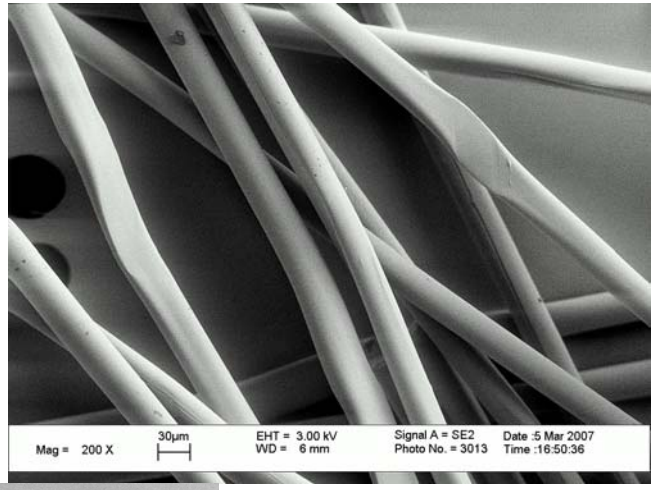

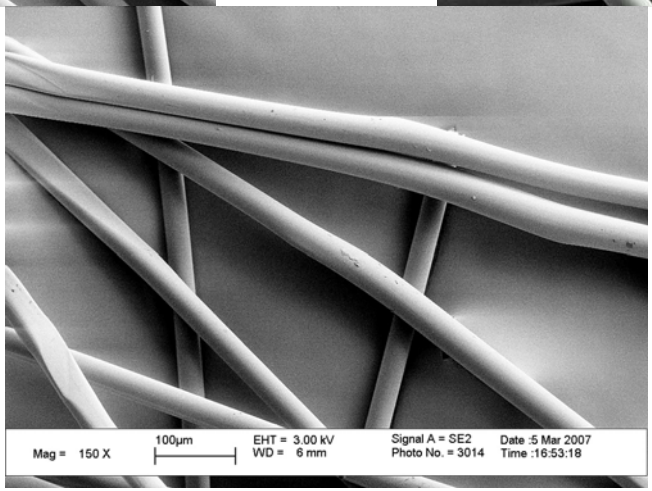

Figure C31: Session #7 - Run#31, 12%, T = 100°C, $\dot{\varepsilon}$ = 1.75 s^{-1}, v_t = 56 m/min, D_r = 19.0

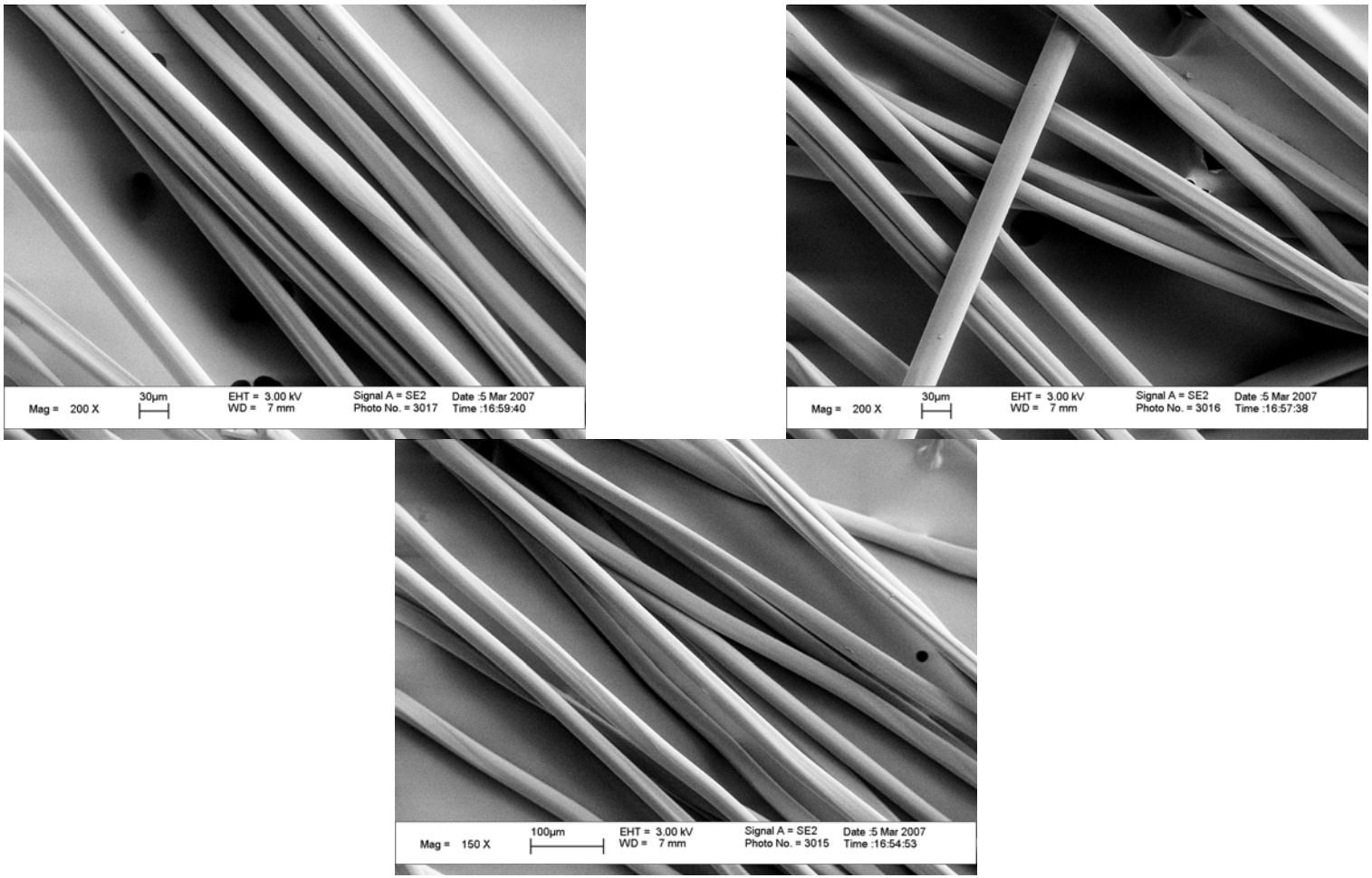

Figure C32: Session #7 - Run#32, 12%, T = 100°C, $\dot{\varepsilon}$ = 1.75 s^{-1}, v_t = 88 m/min, D_r = 29.9

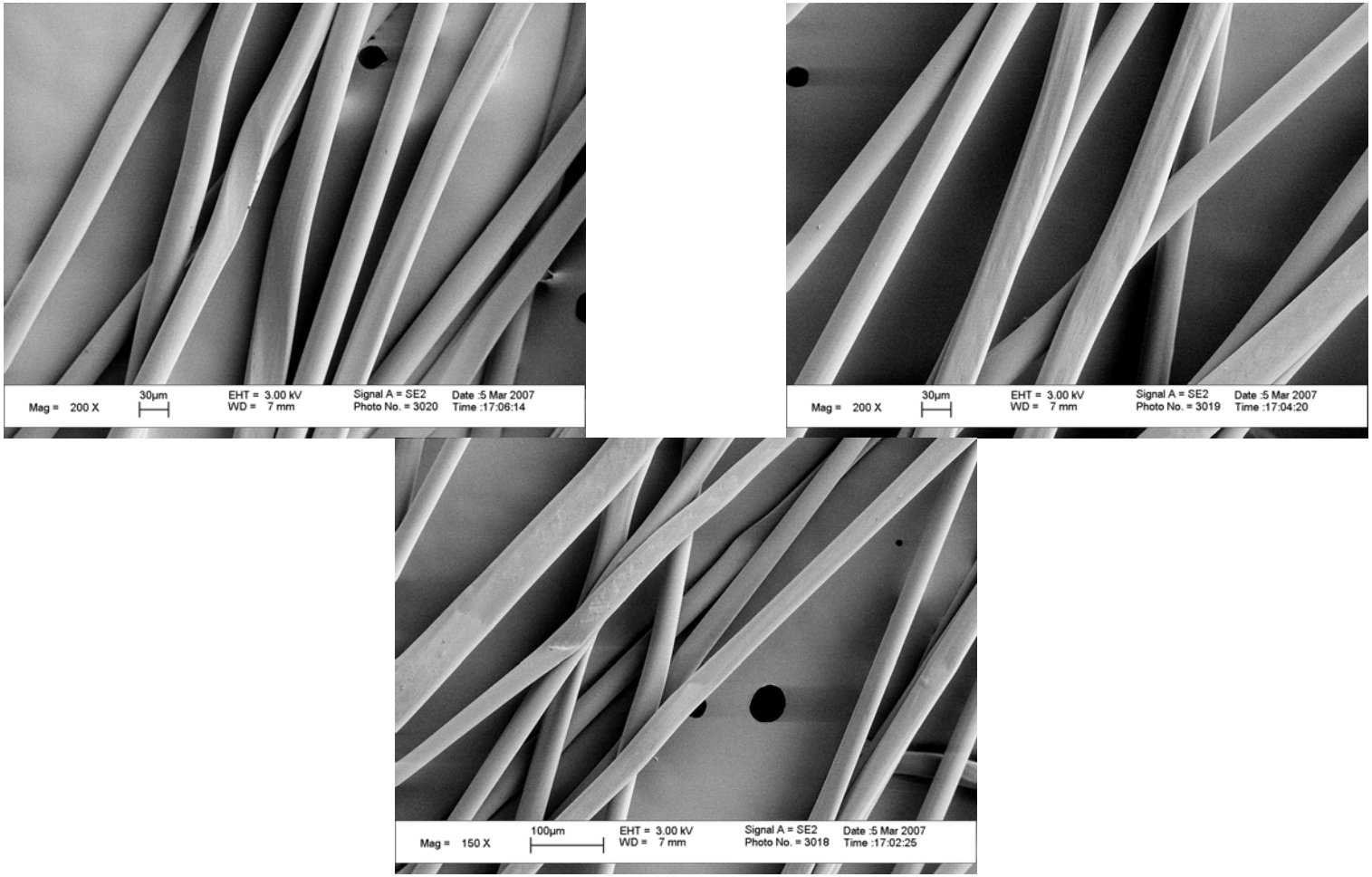

Figure C33: Session #7 - Run#33, 12%, T = 100°C, $\dot{\varepsilon}$ = 1.85 s^{-1}, v_t = 71 m/min, D_r = 22.8

APPENDIX D

X-ray Intensity Curves

Table 1D: Input Parameters for X'Pert WAXS

Diffractometer, Configuration and Settings		Scan Parameters	
Measurement program	Gonio 5-35	Scan Type	Measured scan
Measurement type	Absolute scan	Start Angle (°2Theta)	5.01
		End Angle (°2Theta)	34.99
Sample offset: 2Theta (°)	0.0	Step Size (°2Theta)	0.02
Sample offset: Omega (°)	0.0	Time per Step (s)	1.00
Sample offset: Phi (°)	0.0		
Sample offset: Psi (°)	0.0	Number of data points	1500
		Minimum (counts)	117.0
Scan Axis	Gonio	Minimum (counts/s)	117.0
Phi Angle (°)	100.0	Maximum (counts)	1072.0
Psi Angle (°)	0.0	Maximum (counts/s)	1072.0
Scan Mode	Continuous		
Control Unit	X'Pert PRO		
Goniometer	PW3050/65 (Theta/2Theta)		
Generator	PW3040 (mppc)		
Generator Tension (kV)	45.0		
Generator Current (mA)	40.0		
X-ray Tube	PW3373/00 Cu LFF		
Tube Focus	Line		
Take off angle (°)	6.0		
Used Radiation	K-Alpha		
K-Alpha1 Wavelength (Å)	1.54056		
K-Alpha2 Wavelength (Å)	1.54439		
K-Alpha2/K-Alpha1 ratio	0.5		
K-Beta Wavelength (Å)	1.39222		
Beam attenuator	None		
Beam attenuator activated	No		
Mirror	None		
Lens	None		
Incident beam anti-scatter slit	None		
Divergence slit	Slit Fixed 1°		
Divergence slit angle (°)	1.0		
Incident beam filter	None		
Incident beam mask	Inc. Mask Fixed 15 mm		
Incident beam mask width (mm)	15.0		
Incident beam monochromator	None		
Incident beam radius (mm)	320.0		
Incident beam soller slit	Soller 0.04 rad.		
Distance tube focus-incident beam mask (mm)	320.0		
Distance tube focus-divergence slit (mm)	100.0		
Sample Stage	MRD Cradle		
Oscillation	No		
Spinning	No		
Diffracted beam monochromater	PW3123/10 for Cu radiation		
Diffracted beam radius (mm)	320.0		
Diffracted beam anti-scatter slit	Slit Fixed 1°		
Diffracted beam anti-scatter slit (°)	1.0		
Receiving slit	Prog. Rec.Slit		
Receiving slit height (mm)	0.3		
Diffracted beam filter	None		
Diffracted beam mask	None		
Diffracted beam soller slit (°)	Soller 0.04 rad		
Detector	PW3011/20		
PHD lover lever (%)	35.0		
PHD upper level (%)	80.0		

Table 2D: Crystallinity Results

Run #	Conc.	Temp [T] (^oC)	Elong. Strain Rate [e] (s^{-1})	Take-up Velocity [v_t] (% of Total RPM)	Take-up Velocity [v_t] (m/min)	Take-up Velocity [v_t] (mm/s)	Exit Velocity [v_d] (mm/s)	Crystallinity (%)
1	10	100	1.08	35	71	1183	30.25	82.6
2	10	100	1.5	27	46	767	42.01	69.6
3	10	100	1.5	35	71	1183	42.01	74.6
4	10	100	1.5	43	98	1633	42.01	76.8
5	10	100	1.92	35	71	1183	53.77	70.4
6	10	94.1	1.25	30	56	933	35.01	76.4
7	10	94.1	1.25	40	88	1467	35.01	82.4
8	10	94.1	1.75	30	56	933	49.01	70.0
9	10	94.1	1.75	40	88	1467	49.01	77.6
10	10	105.9	1.25	30	56	933	35.01	72.8
11	10	105.9	1.25	40	88	1467	35.01	86.6
12	10	105.9	1.75	30	56	933	49.01	76.9
13	10	105.9	1.75	40	88	1467	49.01	76.6
14	10	90	1.5	35	71	1183	42.01	74.0
15	10	110	1.5	35	71	1183	42.01	82.6
16	8	100	1.15	35	71	1183	32.21	79.2
17	8	100	1.25	30	56	933	35.01	69.1
18	8	100	1.25	40	88	1467	35.01	78.4
19	8	100	1.5	28	50	833	42.01	64.9
20	8	100	1.5	35	71	1183	42.01	69.6
22	8	100	1.75	30	56	933	49.01	73.1
24	8	100	1.85	35	71	1183	51.81	74.0
25	12	100	1.15	35	71	1183	32.21	89.6
26	12	100	1.25	30	56	933	35.01	76.8
27	12	100	1.25	40	88	1467	35.01	81.7
28	12	100	1.5	28	50	833	42.01	73.9
29	12	100	1.5	35	71	1183	42.01	76.0
30	12	100	1.5	42	95	1583	42.01	74.1
31	12	100	1.75	30	56	933	49.01	75.0
32	12	100	1.75	40	88	1467	49.01	71.3
33	12	100	1.85	35	71	1183	51.81	75.9

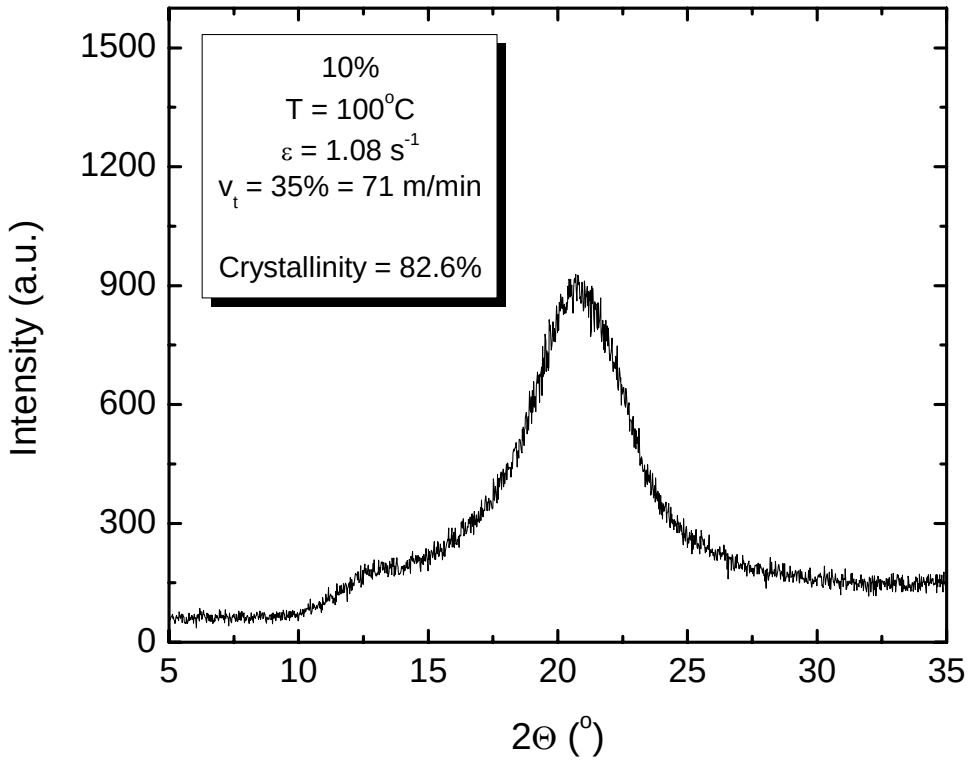

Figure D1: Session 1 - Run #1

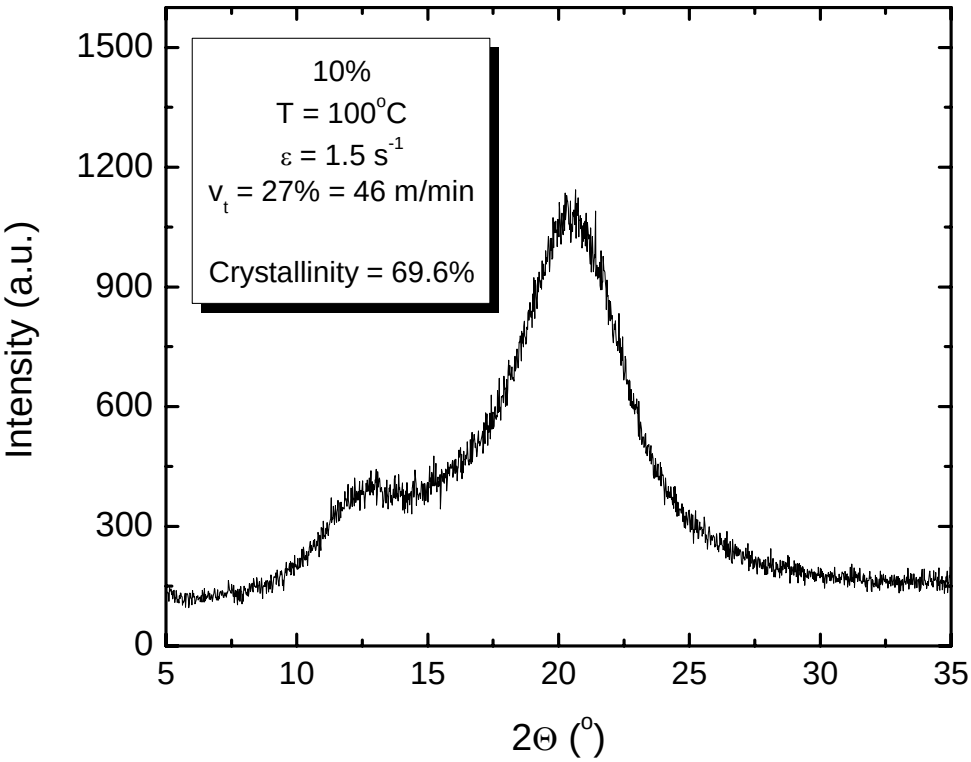

Figure D2: Session 1 - Run #2

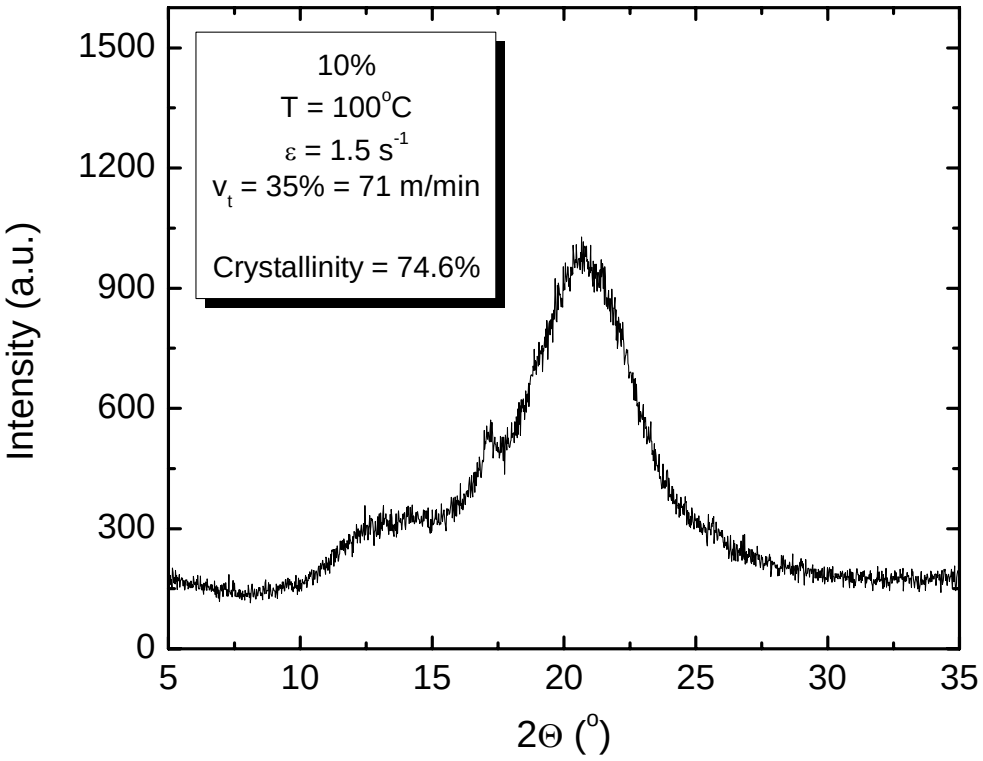

Figure D3: Session 1 - Run #3

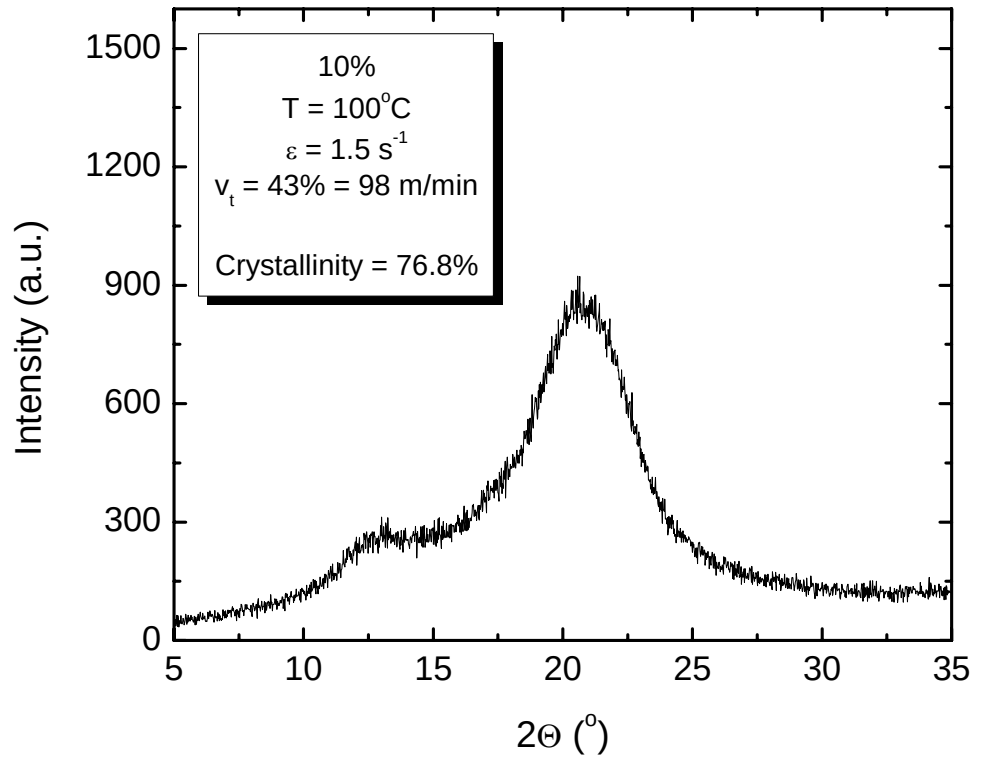

Figure D4: Session 1 - Run #4

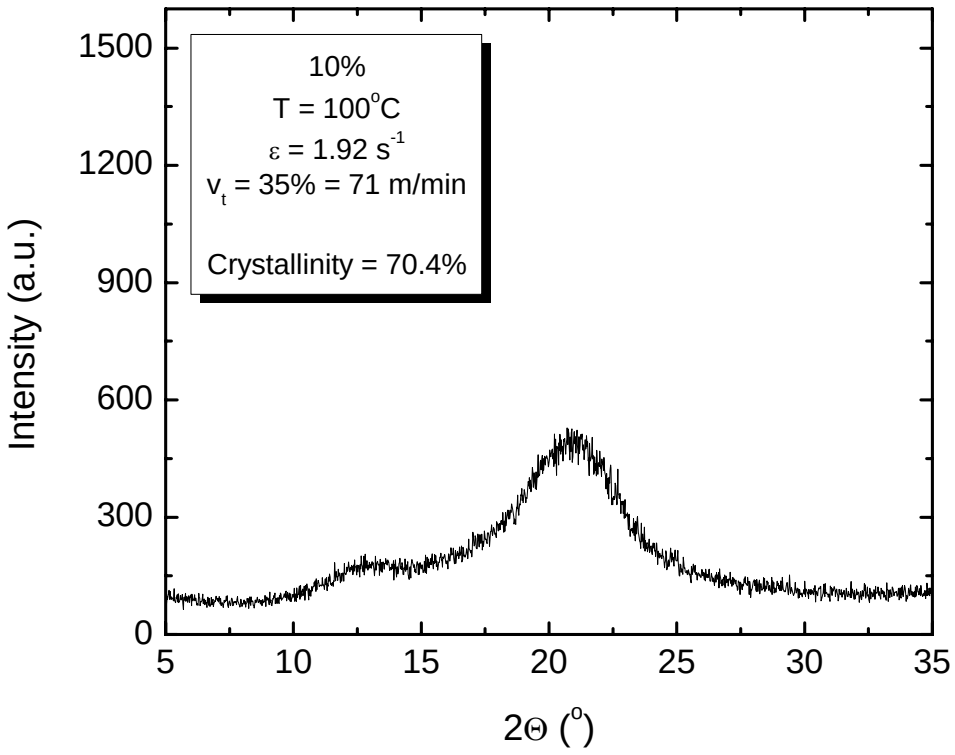

Figure D5: Session 1 - Run #5

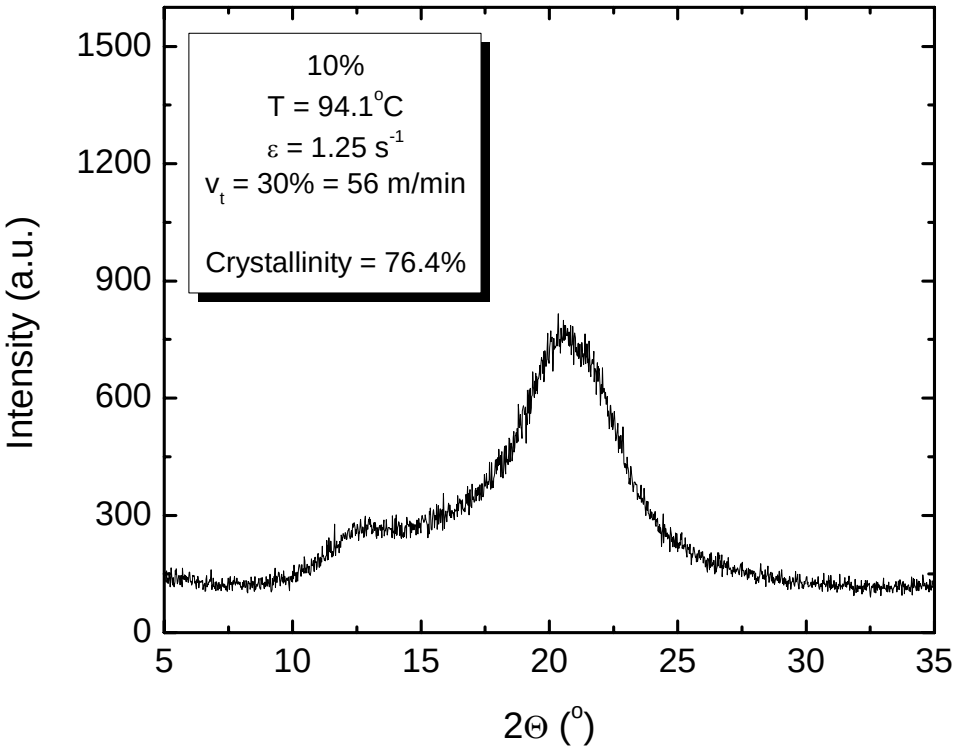

Figure D6: Session 2 - Run #6

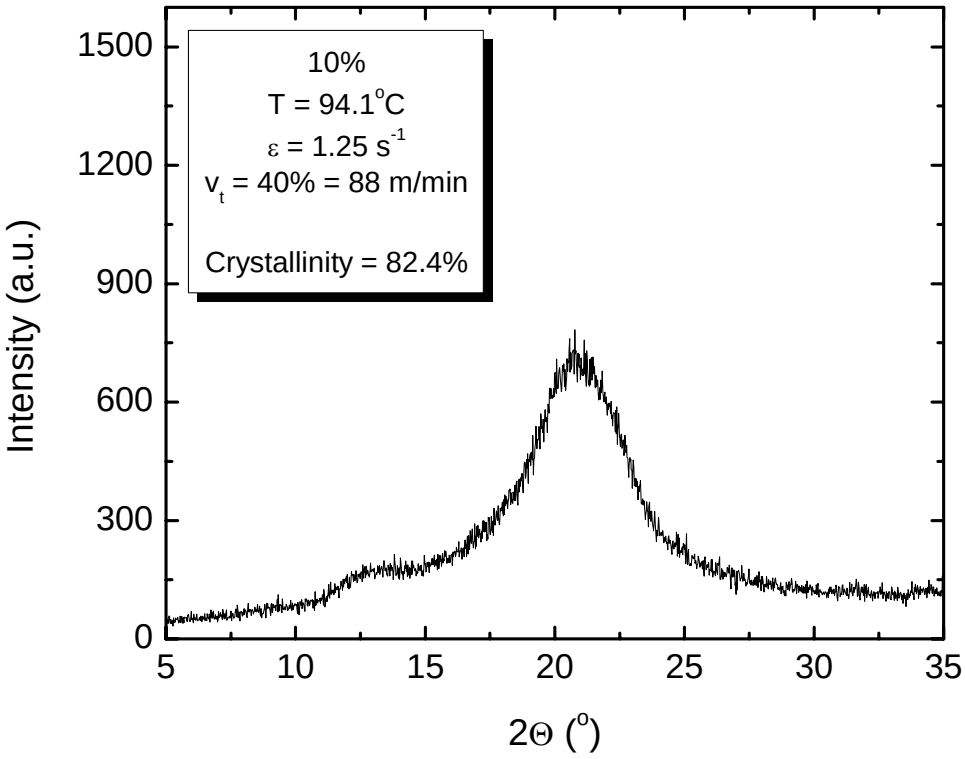

Figure D7: Session 2 - Run #7

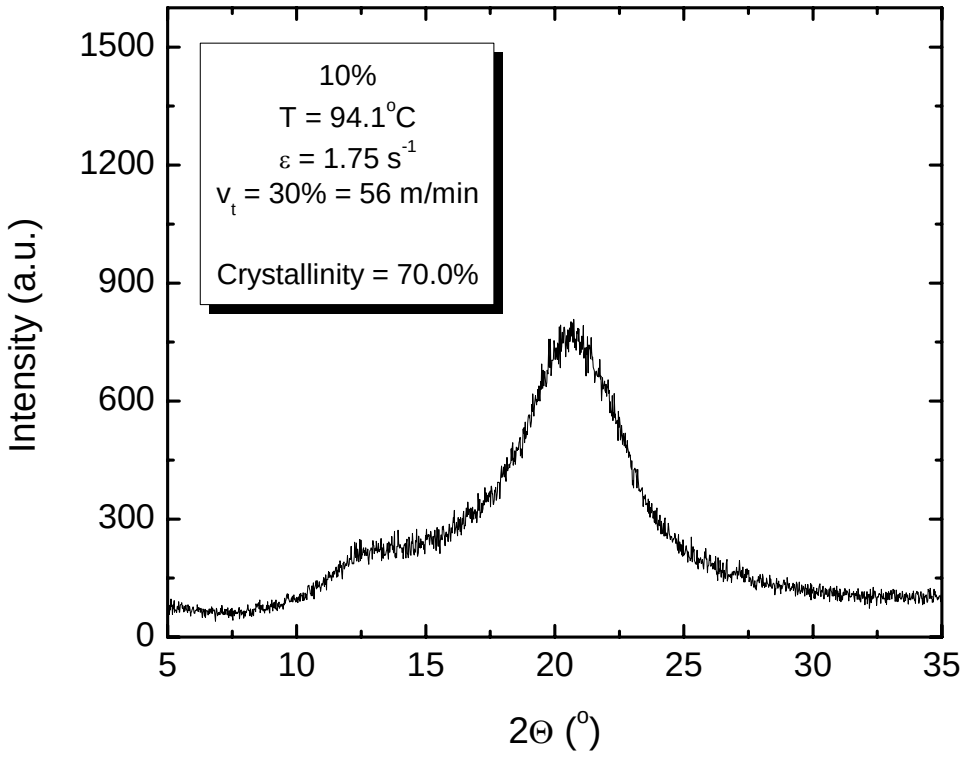

Figure D8: Session 2 - Run #8

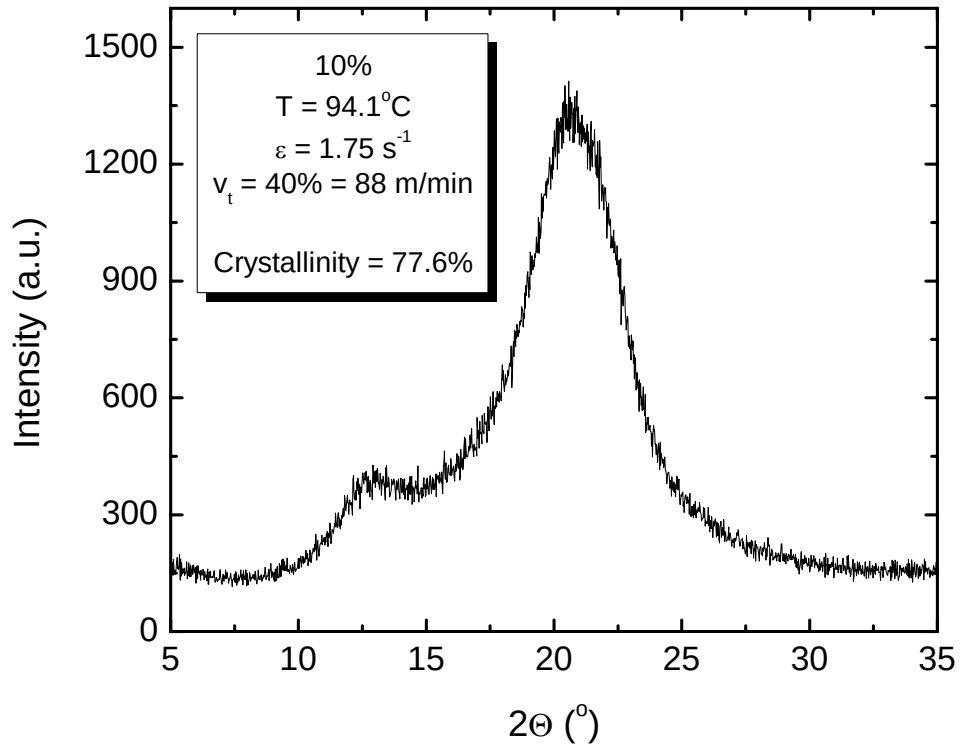

Figure D9: Session 2 - Run #9

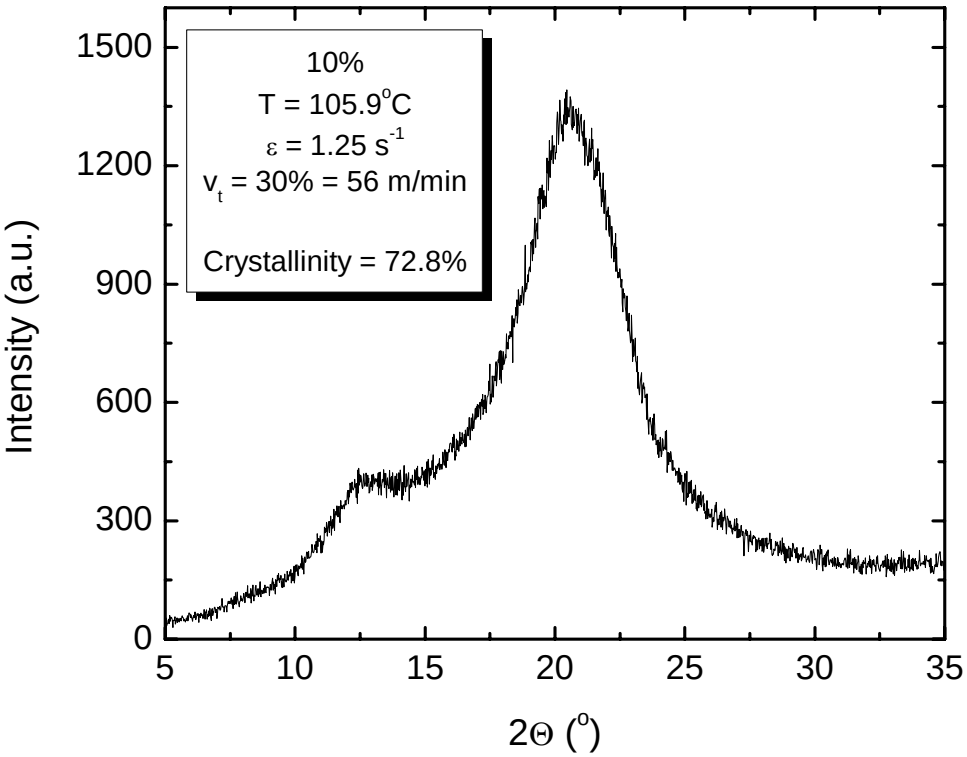

Figure D10: Session 3 - Run #10

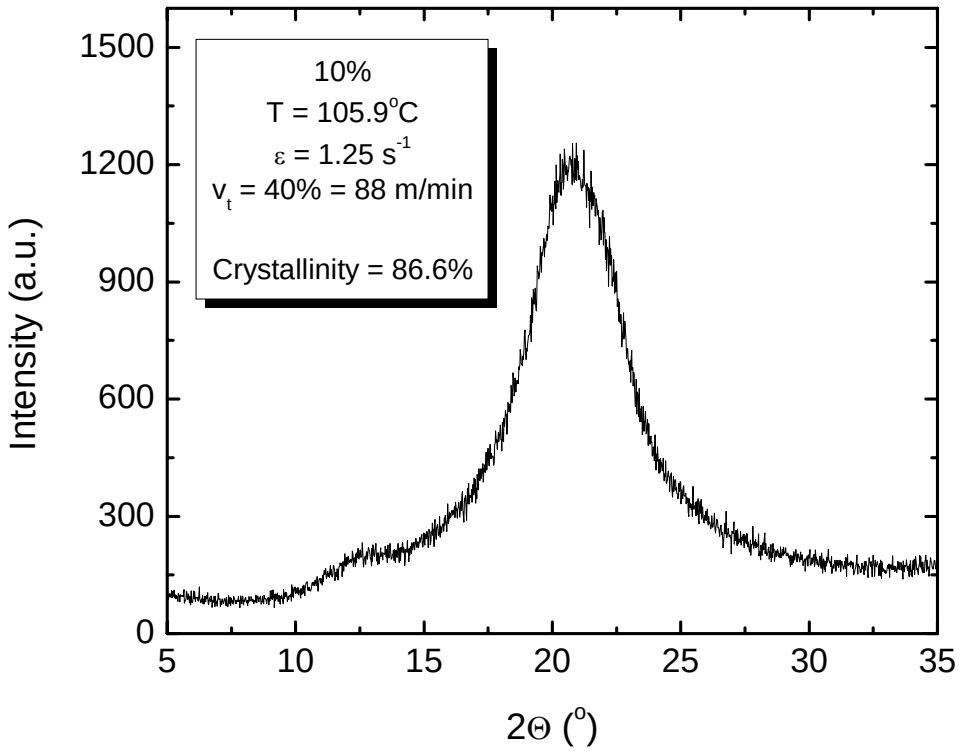

Figure D11: Session 3 - Run #11

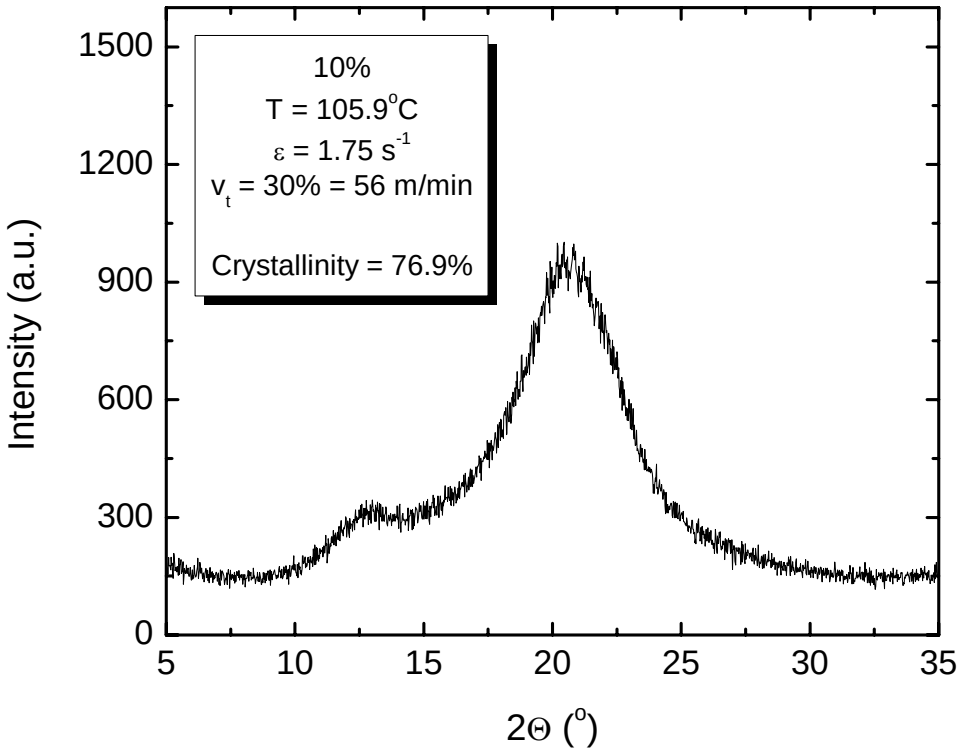

Figure D12: Session 3 - Run #12

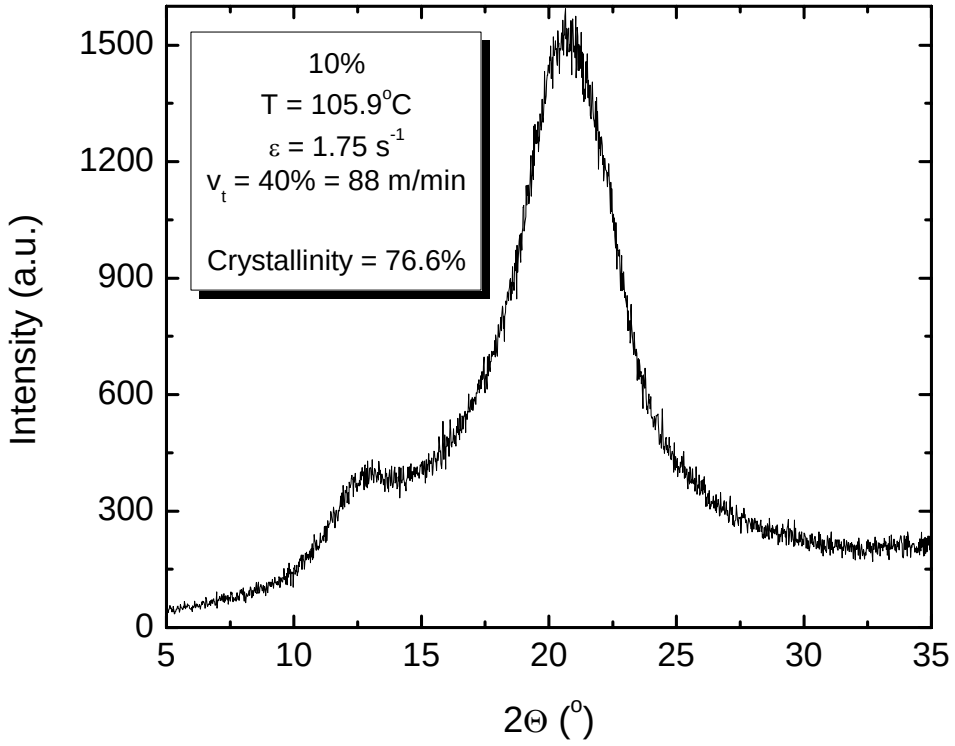

Figure D13: Session 3 - Run #13

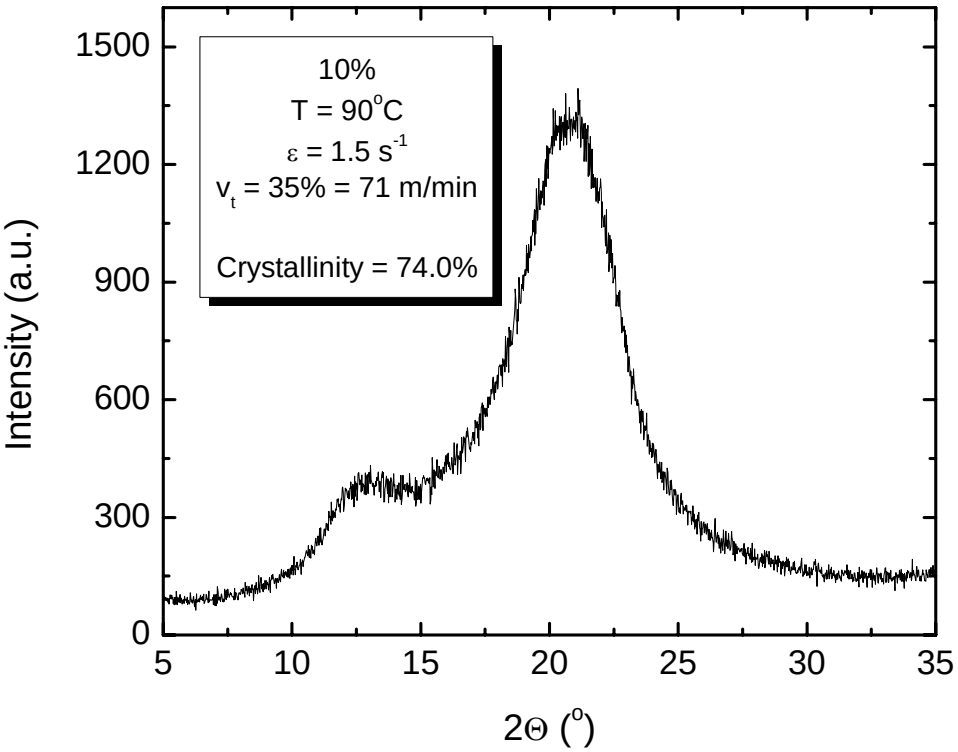

Figure D14: Session 4 - Run #14

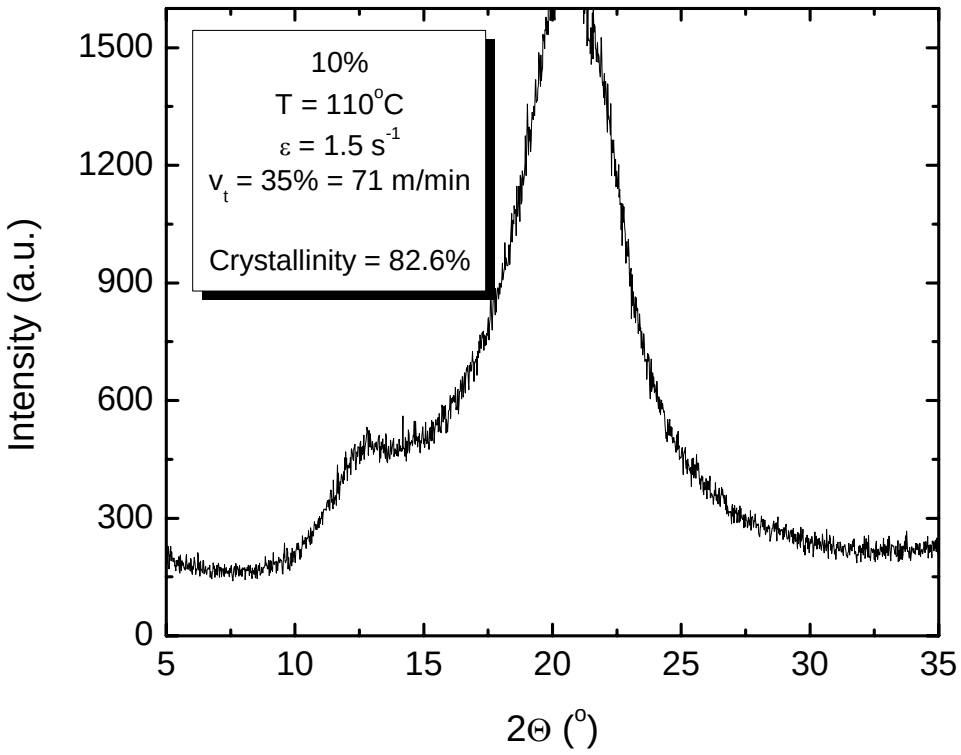

Figure D15: Session 5 - Run #15

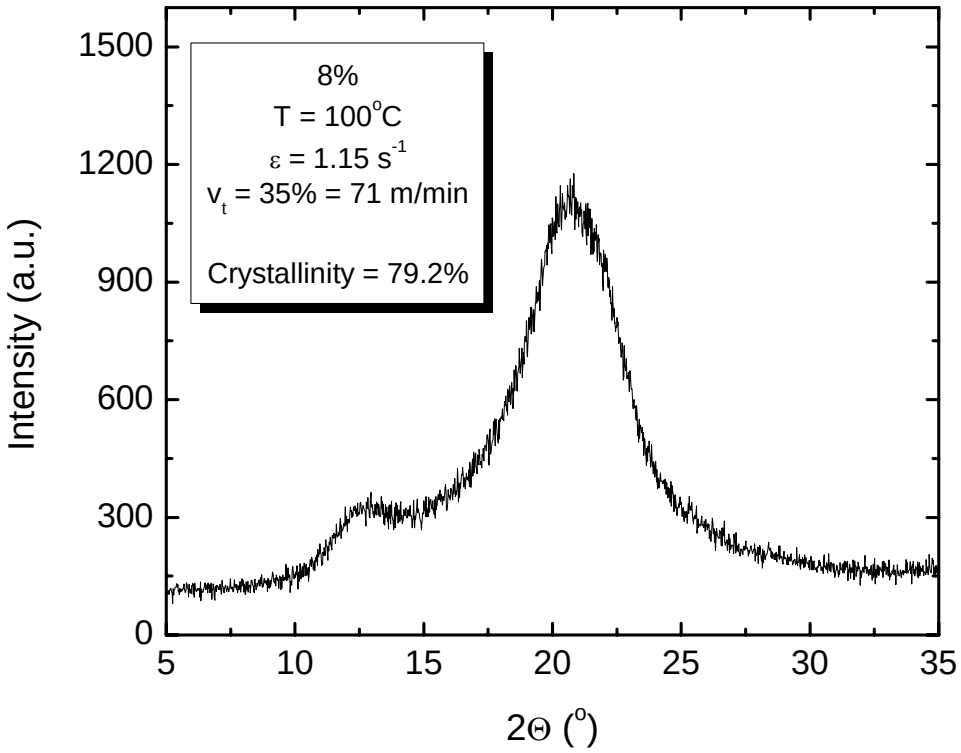

Figure D16: Session 6 - Run #16

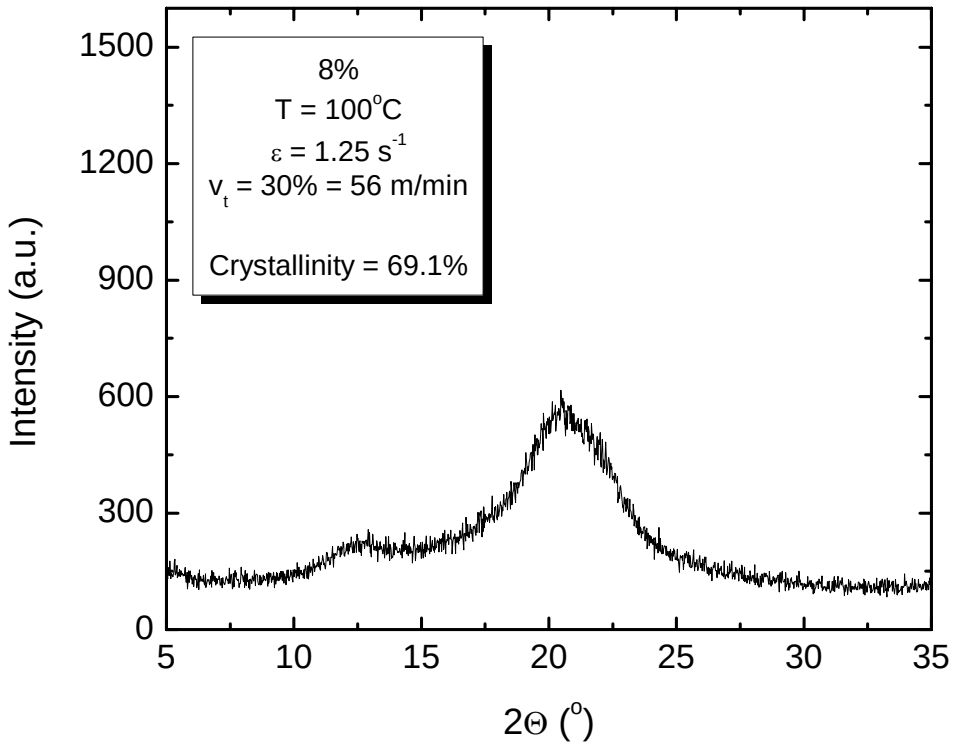

Figure D17: Session 6 - Run #17

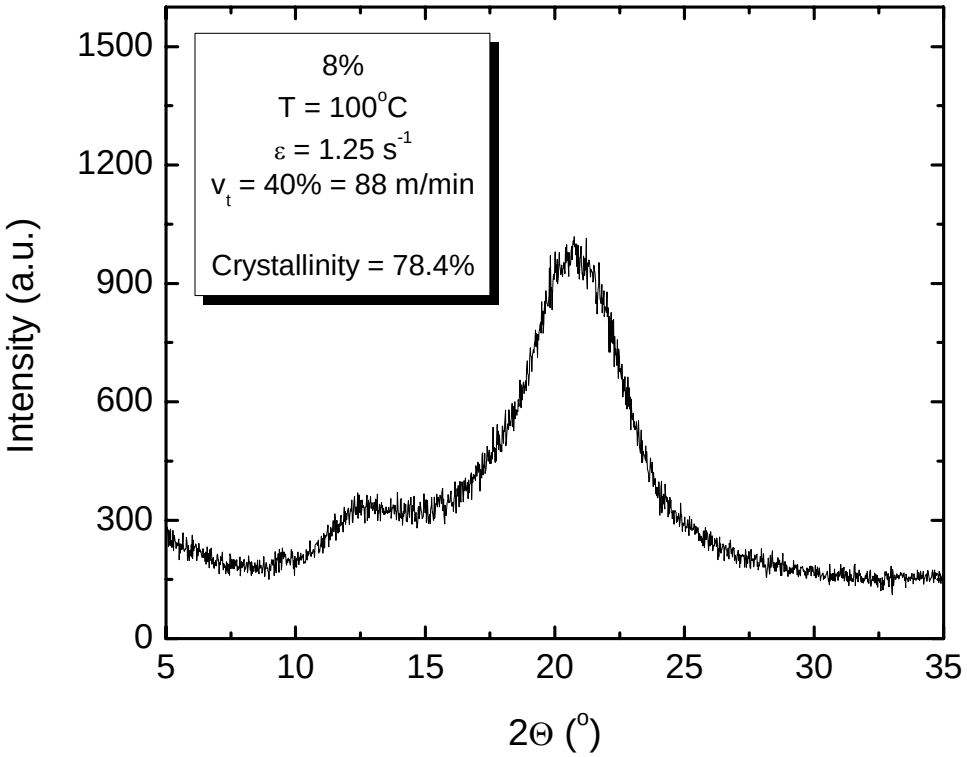

Figure D18: Session 6 - Run #18

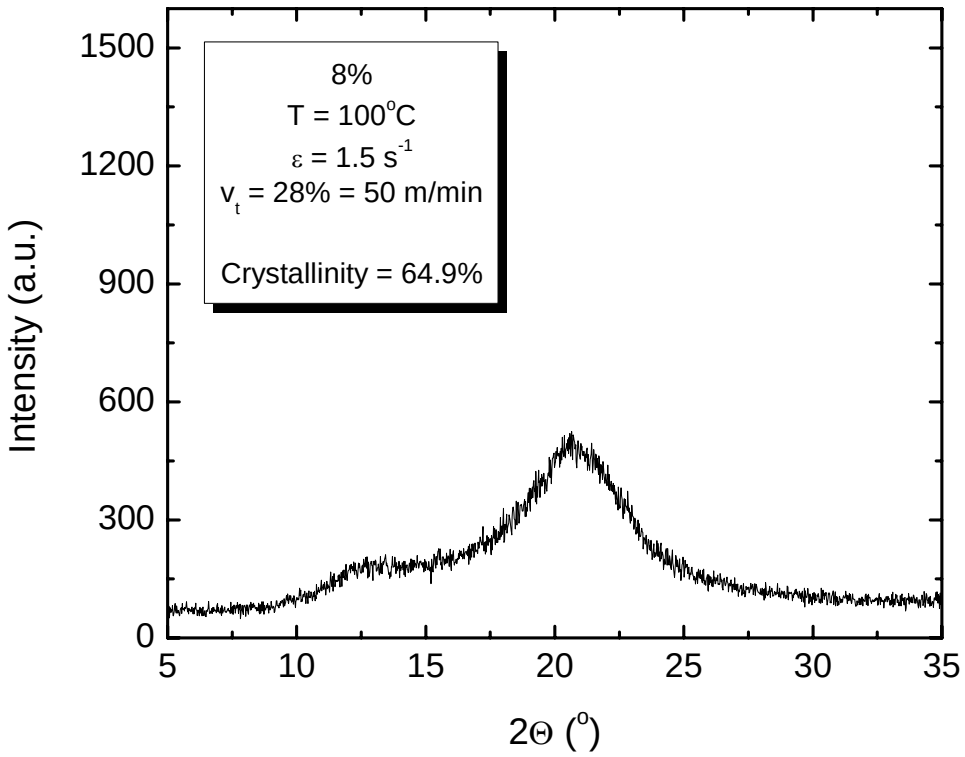

Figure D19: Session 6 - Run #19

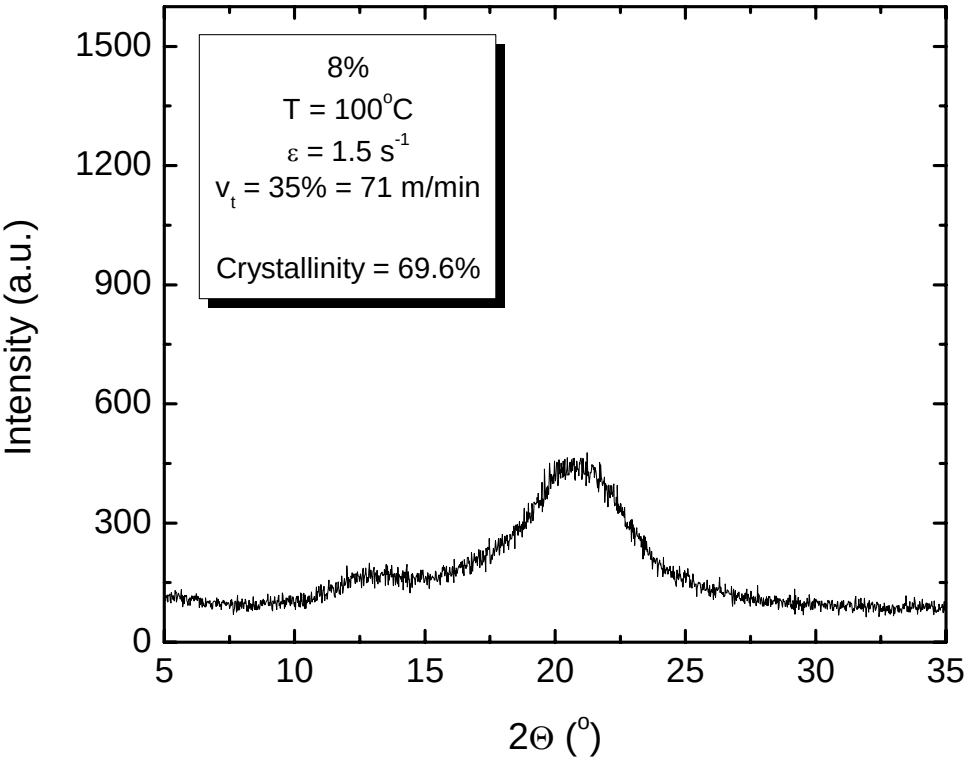

Figure D20: Session 6 - Run #20

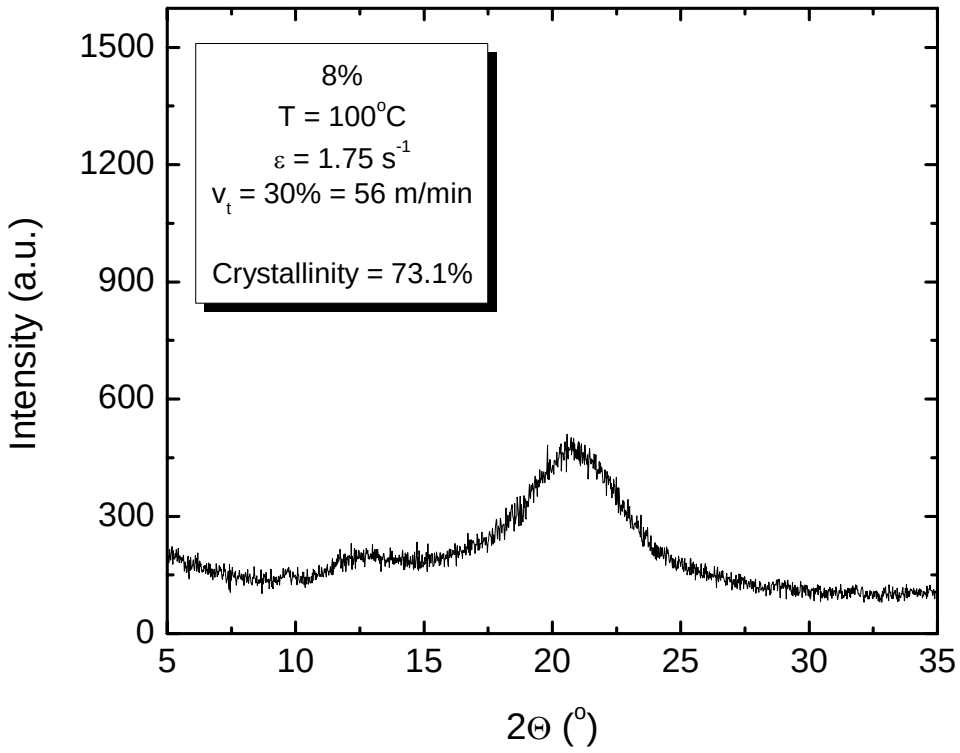

Figure D21: Session 6 - Run #22

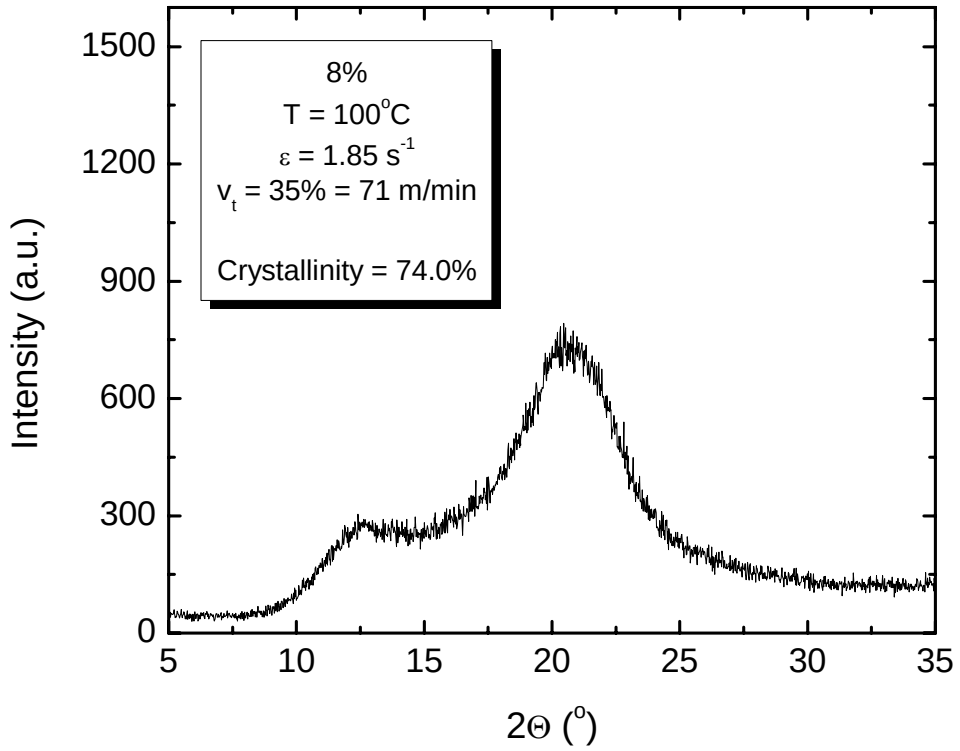

Figure D22: Session 6 - Run #24

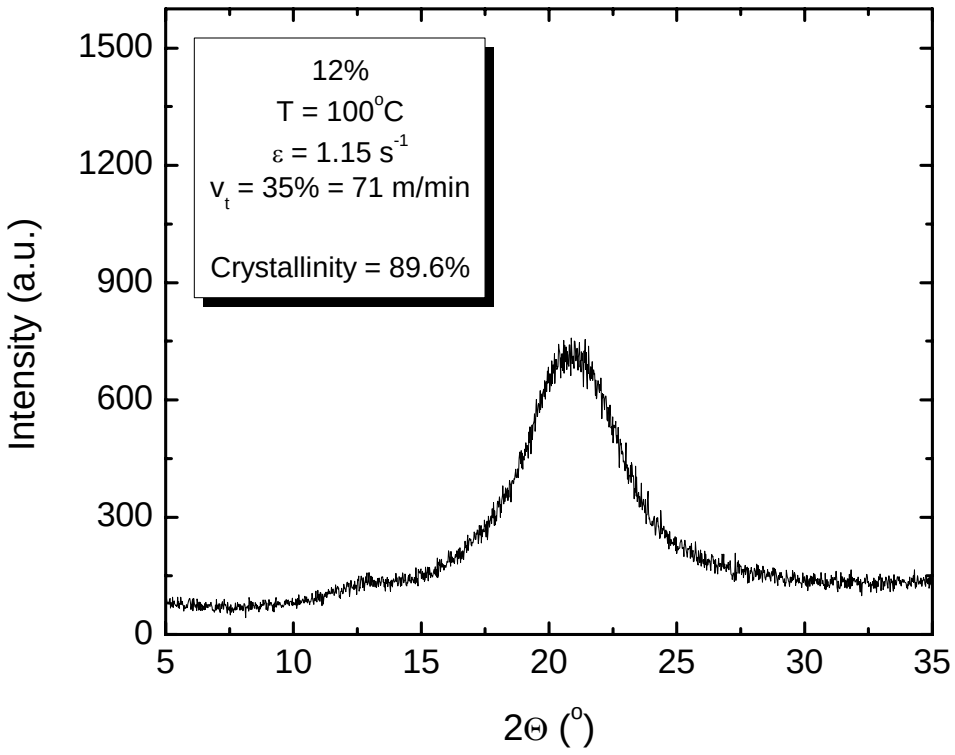

Figure D23: Session 7 - Run #25

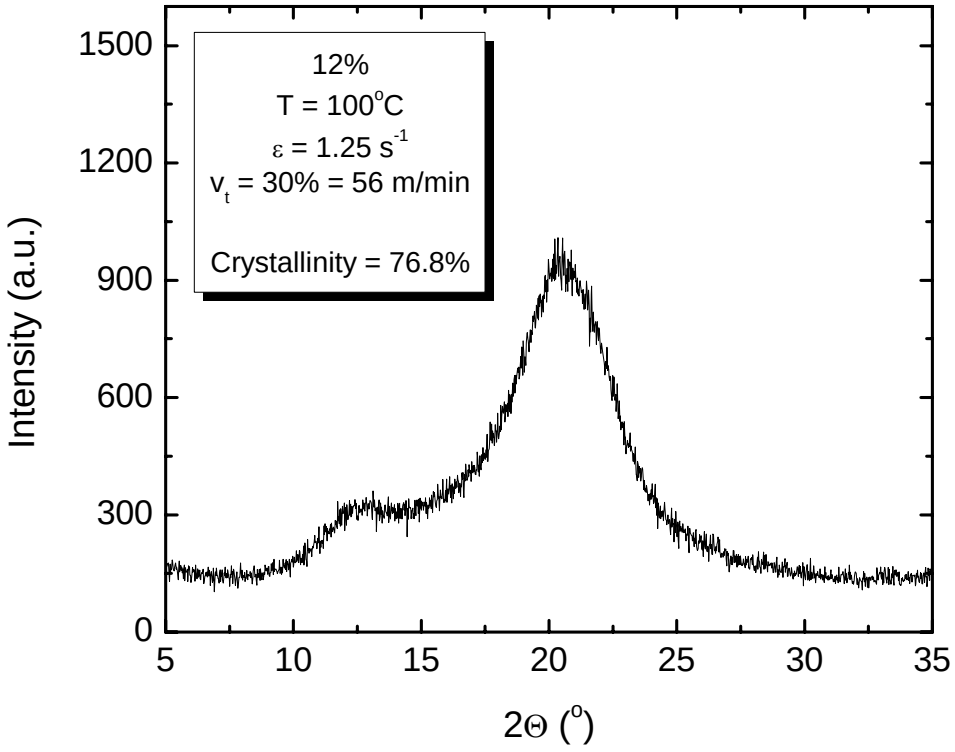

Figure D24: Session 7 - Run #26

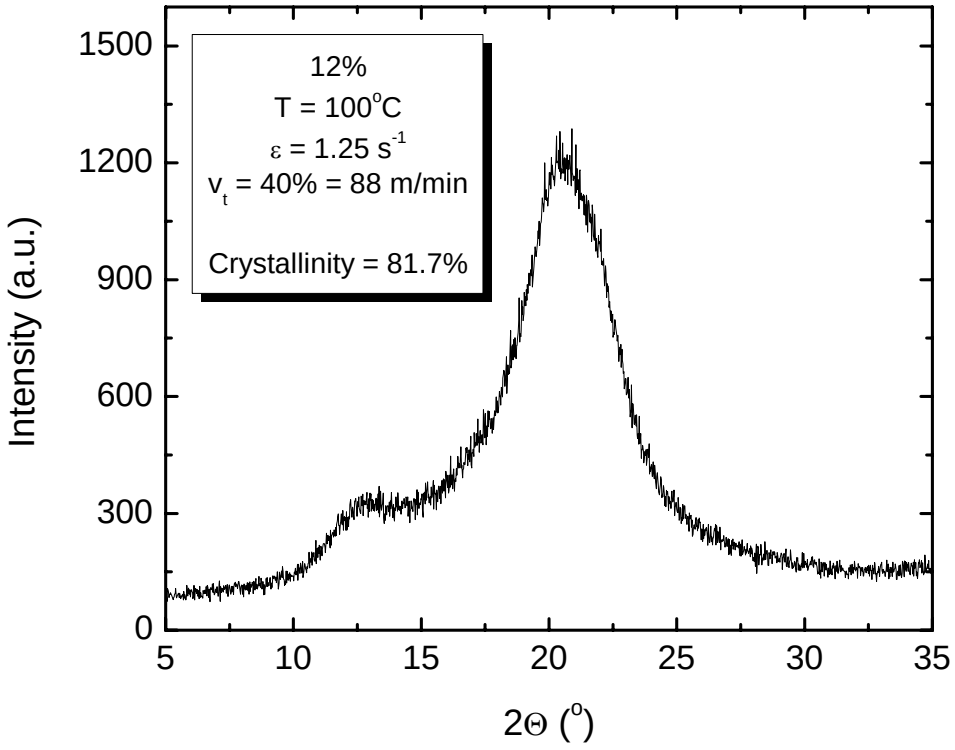

Figure D25: Session 7 - Run #27

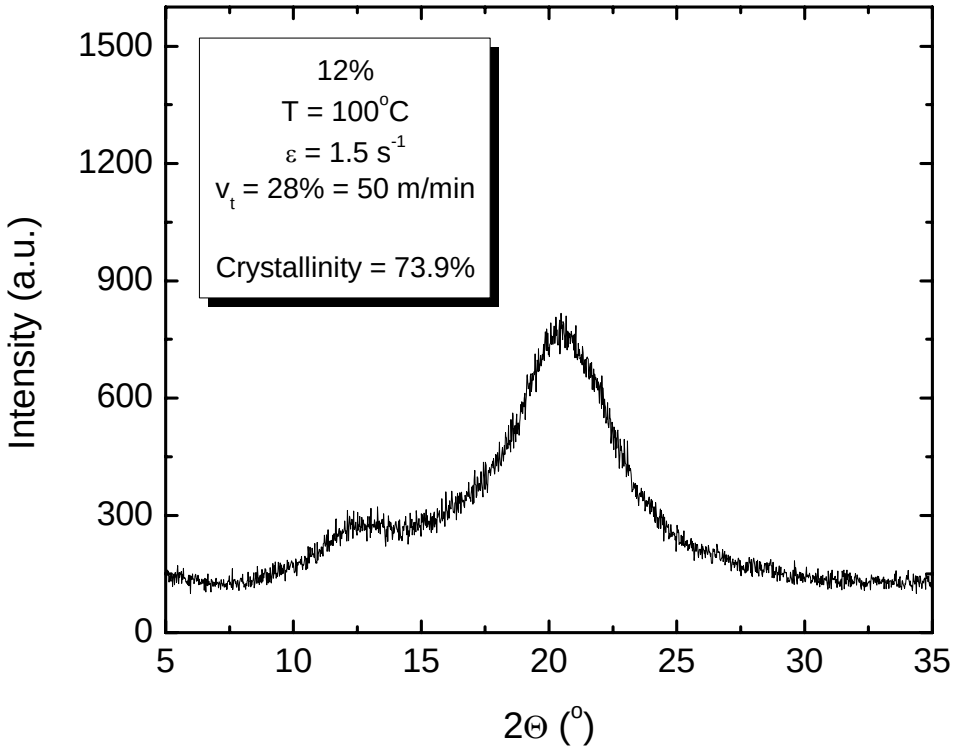

Figure D26: Session 7 - Run #28

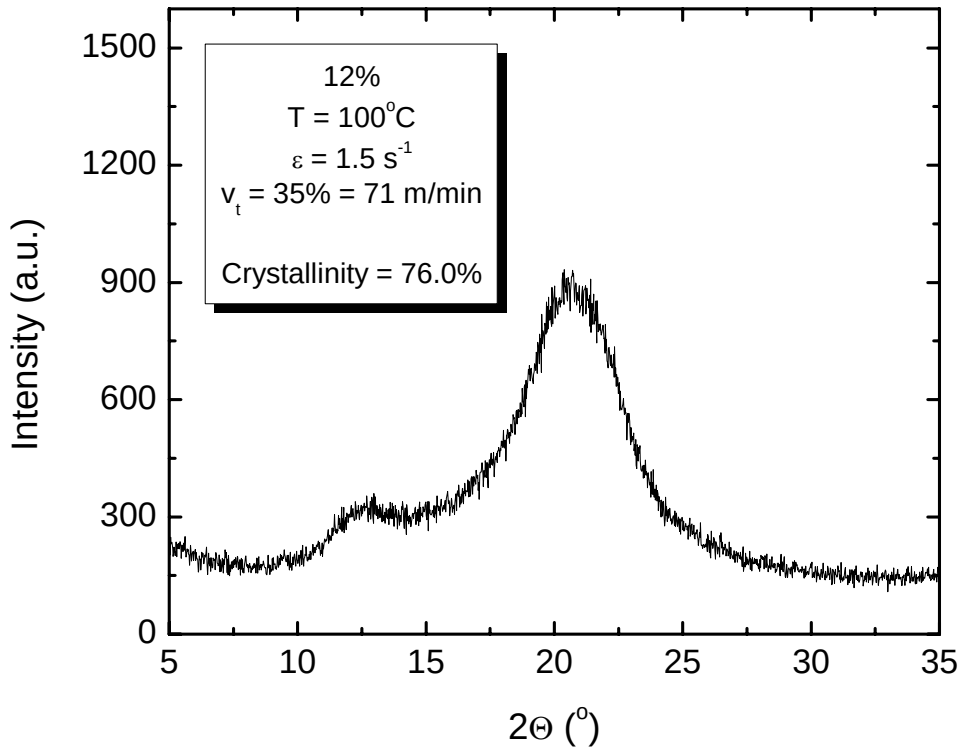

Figure D27: Session 7 - Run #29

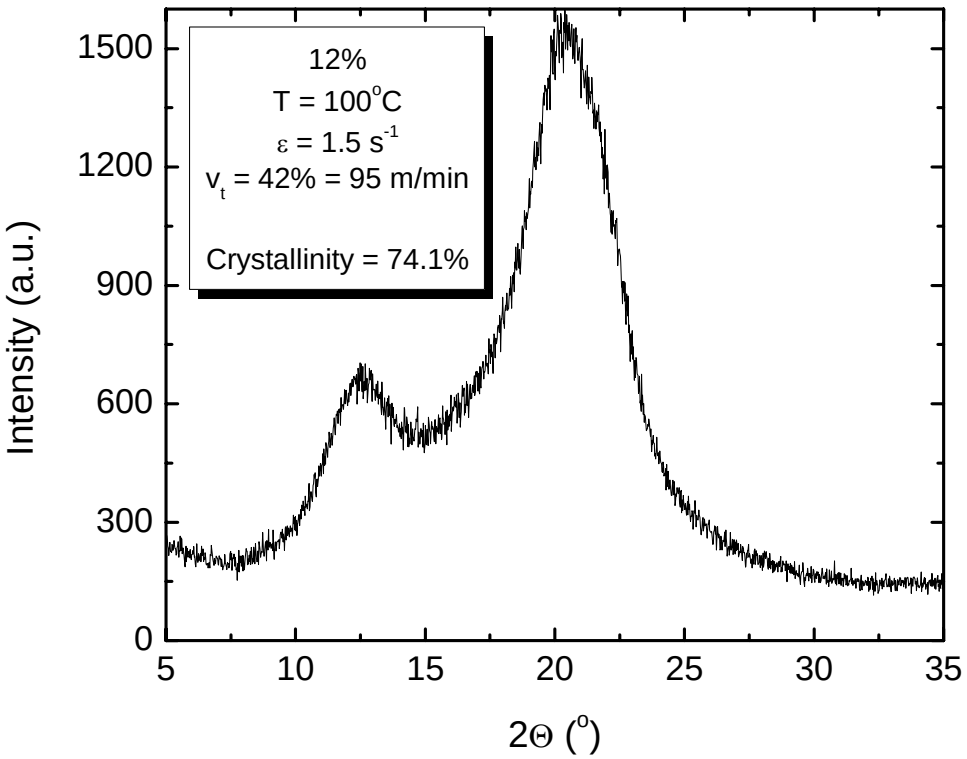

Figure D28: Session 7 - Run #30

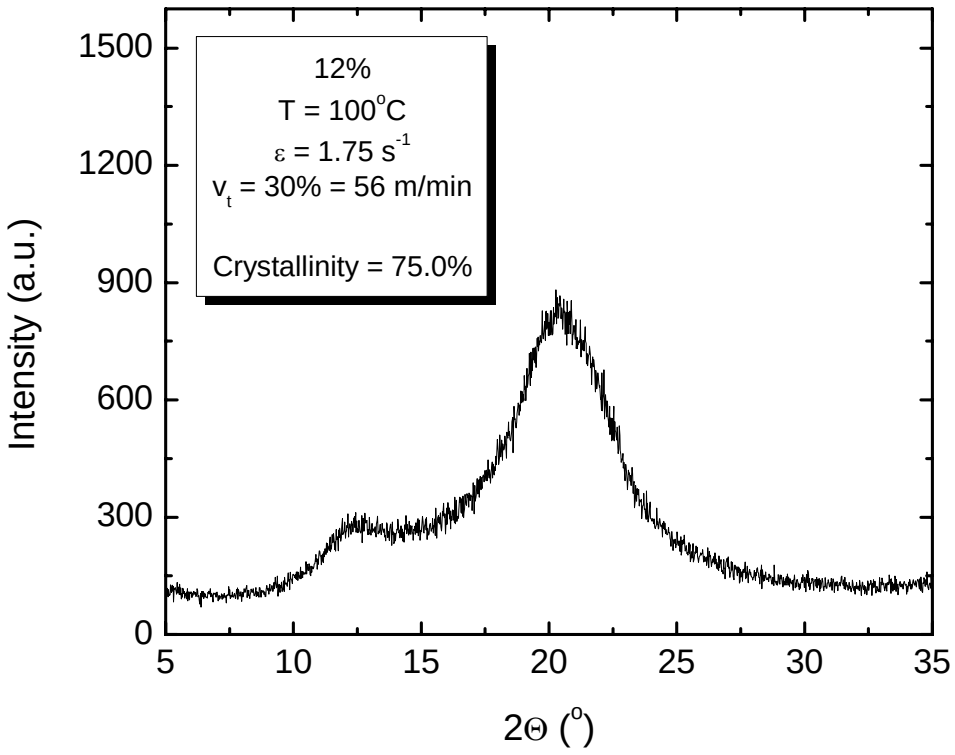

Figure D29: Session 7 - Run #31

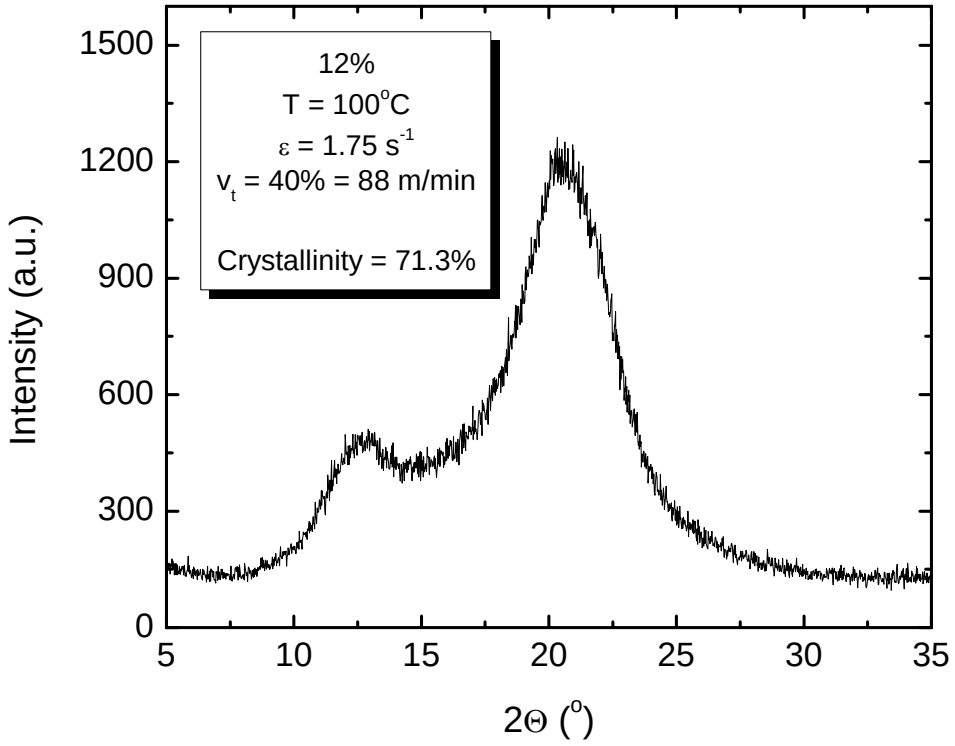

Figure D30: Session 7 - Run #32

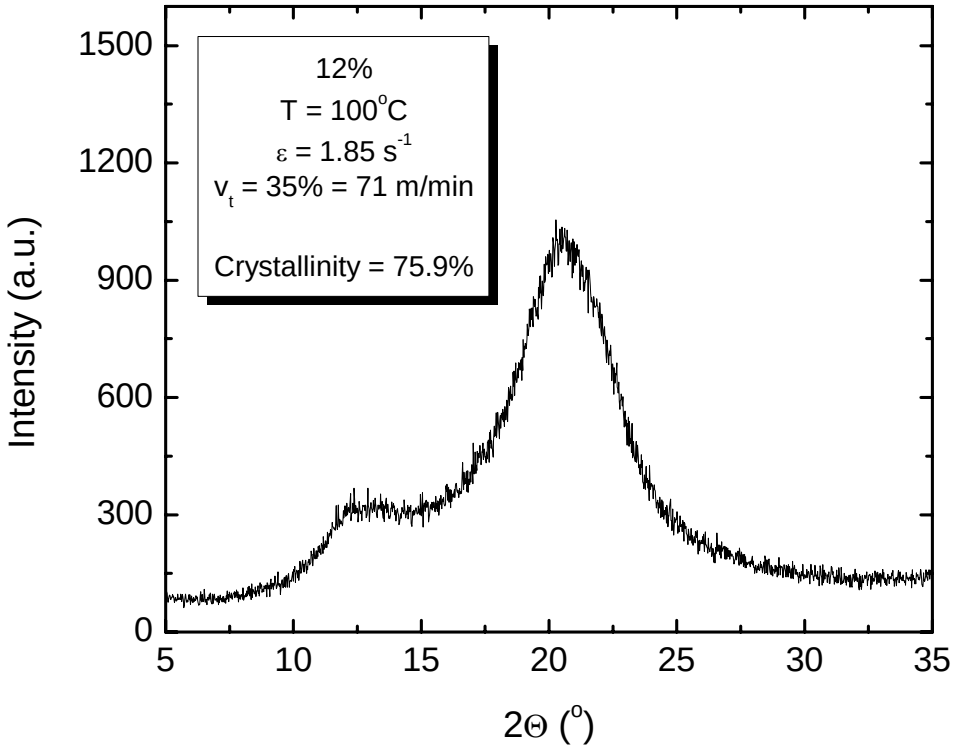

Figure D31: Session 7 - Run #33

APPENDIX E

Fiber Breakage – Displacement verses Load

Table 1E: Fiber Strength Results

Run #	Conc.	Temp [T] (^{o}C)	Elong. Strain Rate [e] (s^{-1})	Take-up Velocity [v_t] (% of Total RPM)	Take-up Velocity [v_t] (m/min)	Ave Displcment at Max. Pt. (mm)	Ave Load at Max Pt. (kgf)	Ave Linear Density (den)	Ave % Strain at Max. Pt. (%)	Ave Tenacity at Max. Pt. (g/den)
1	10	100	1.08	35	71	1.247	1.08E-02	5.07	8.2	2.134
2	10	100	1.5	27	46	2.763	2.16E-02	10.79	18.0	2.010
3	10	100	1.5	35	71	1.567	1.47E-02	7.47	10.1	1.978
4	10	100	1.5	43	98	1.014	1.12E-02	4.99	6.6	2.257
5	10	100	1.92	35	71	1.447	1.78E-02	9.08	9.4	1.967
6	10	94.1	1.25	30	56	1.705	1.91E-02	7.95	11.2	2.411
7	10	94.1	1.25	40	88	1.118	1.30E-02	4.92	7.4	2.648
8	10	94.1	1.75	30	56	2.287	2.56E-02	10.66	14.9	2.403
9	10	94.1	1.75	40	88	1.342	1.84E-02	7.27	8.8	2.536
10	10	105.9	1.25	30	56	1.797	1.16E-02	7.03	11.8	1.660
11	10	105.9	1.25	40	88	1.087	8.88E-03	5.00	7.1	1.780
12	10	105.9	1.75	30	56	2.115	1.68E-02	9.98	13.8	1.688
13	10	105.9	1.75	40	88	1.185	1.17E-02	6.38	7.8	1.836
14	10	90	1.5	35	71	1.492	2.14E-02	7.64	9.8	2.808
15	10	110	1.5	35	71	1.506	1.33E-02	6.97	9.8	1.912
16	8	100	1.15	35	71	1.188	8.38E-03	4.53	7.8	1.850
17	8	100	1.25	30	56	1.126	1.15E-02	5.66	7.4	2.037
18	8	100	1.25	40	88	0.964	8.50E-03	3.92	6.3	2.172
19	8	100	1.5	28	50	1.482	1.37E-02	8.16	9.7	1.677
20	8	100	1.5	35	71	1.098	1.01E-02	5.97	7.2	1.703
22	8	100	1.75	30	56	1.264	1.39E-02	7.50	8.3	1.847
24	8	100	1.85	35	71	0.929	1.13E-02	6.77	6.1	1.663
25	12	100	1.15	35	71	1.380	1.36E-02	5.80	9.1	2.351
26	12	100	1.25	30	56	1.744	1.56E-02	7.58	11.3	2.063
27	12	100	1.25	40	88	1.164	1.30E-02	5.77	7.6	2.272
28	12	100	1.5	28	50	1.873	2.11E-02	10.52	12.2	2.003
29	12	100	1.5	35	71	1.472	1.66E-02	8.32	9.6	1.996
30	12	100	1.5	42	95	1.047	1.32E-02	6.29	6.9	2.097
31	12	100	1.75	30	56	1.966	2.28E-02	11.41	12.8	2.000
32	12	100	1.75	40	88	1.130	1.42E-02	7.04	7.4	2.010
33	12	100	1.85	35	71	1.281	2.00E-02	9.97	8.4	2.013

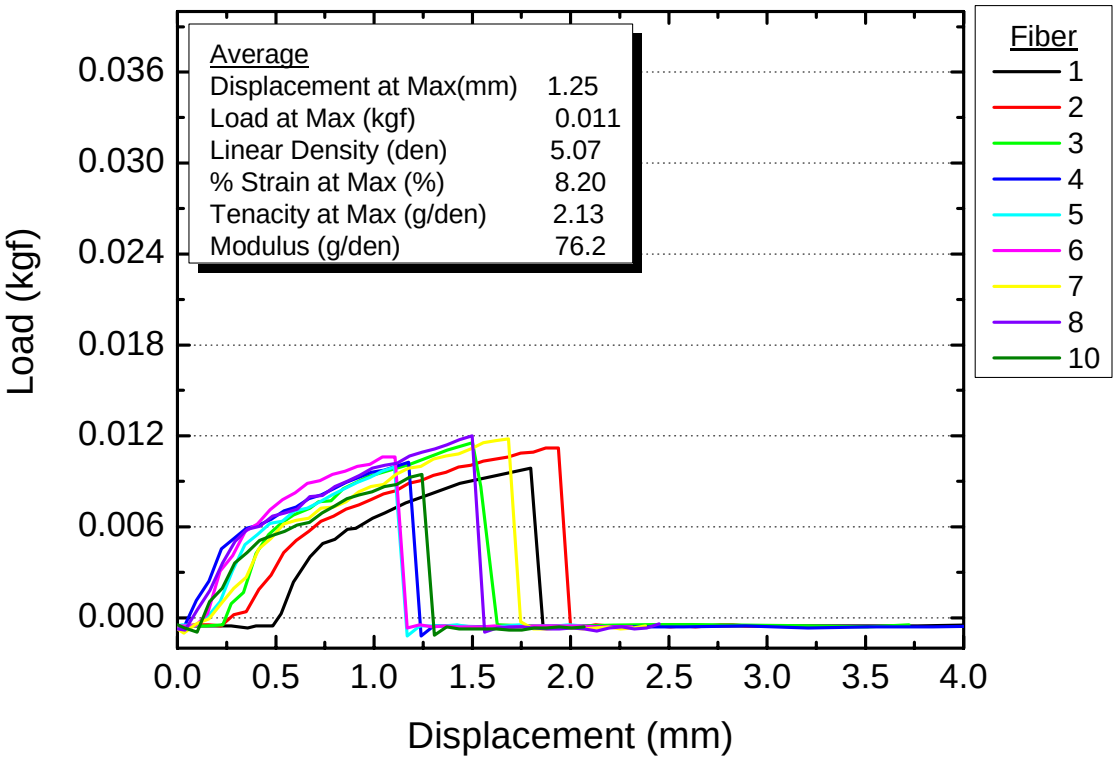

Figure E1: **Session 1 – Run #1**

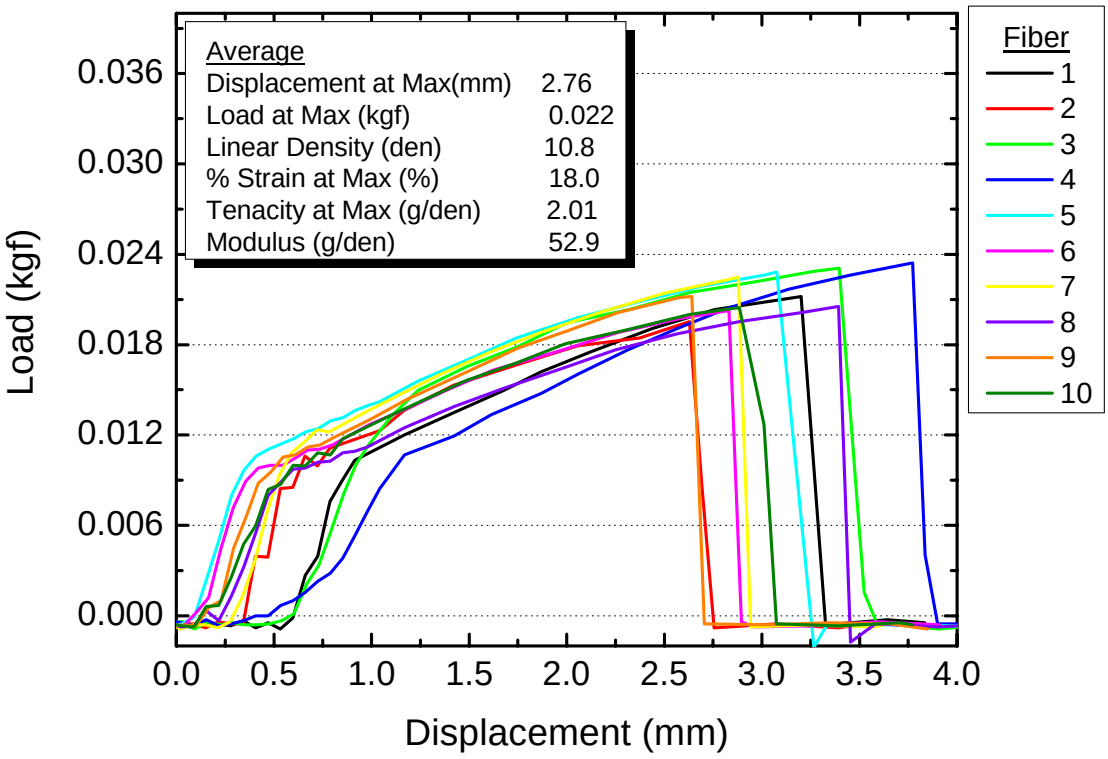

Figure E2: **Session 1 – Run #2**

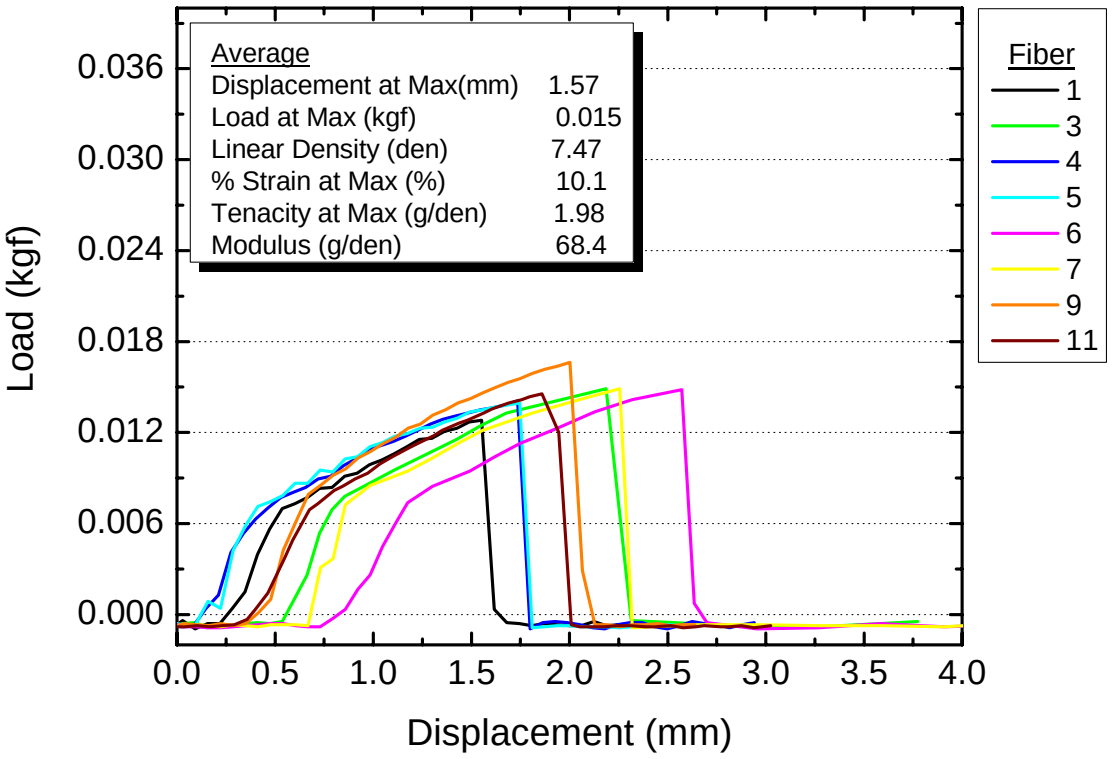

Figure E3: Session 1 – Run #3

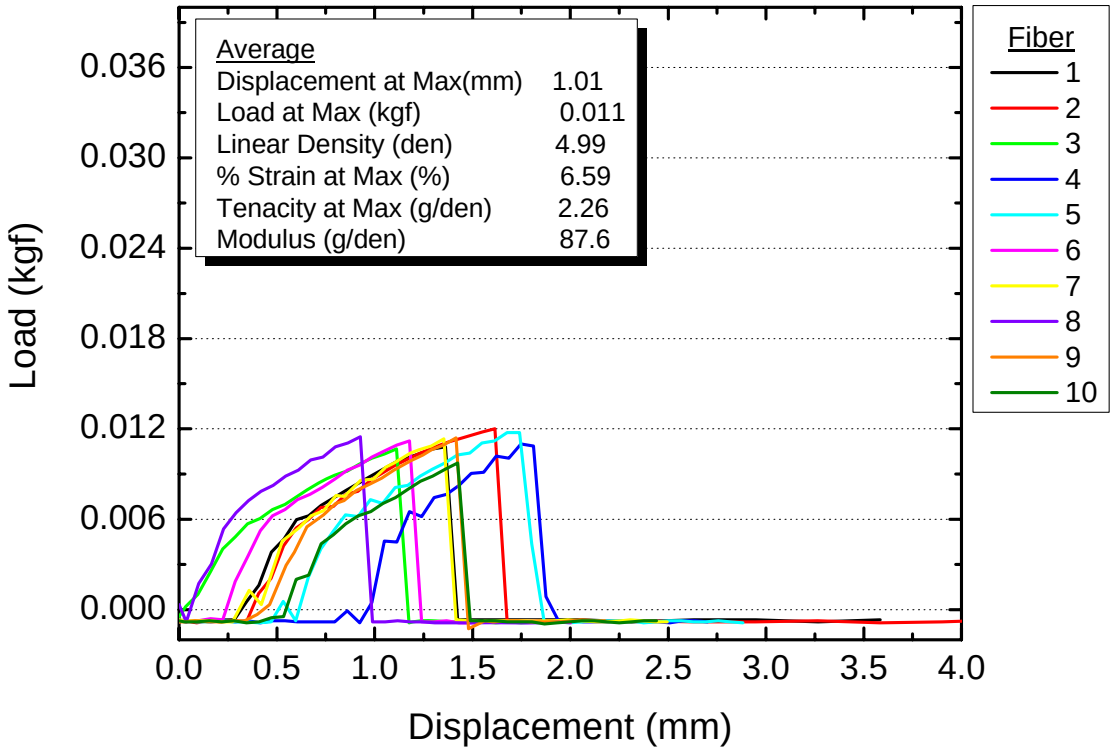

Figure E4: Session 1 – Run #4

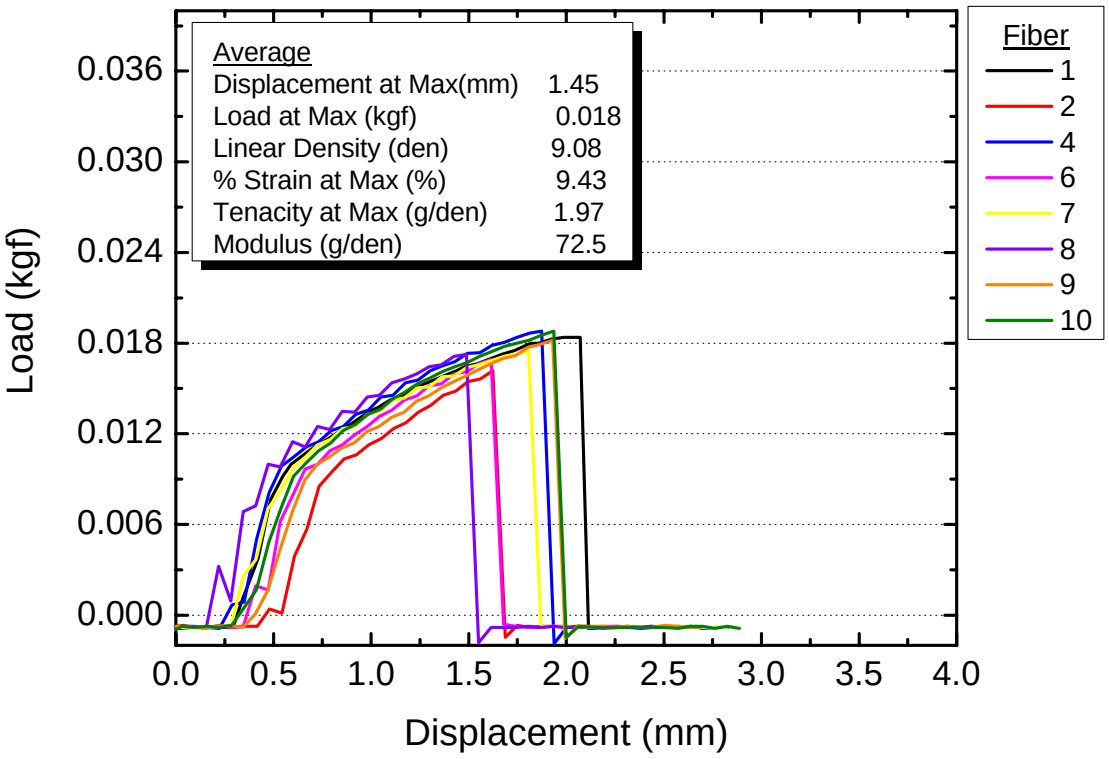

Figure E5: Session 1 – Run #5

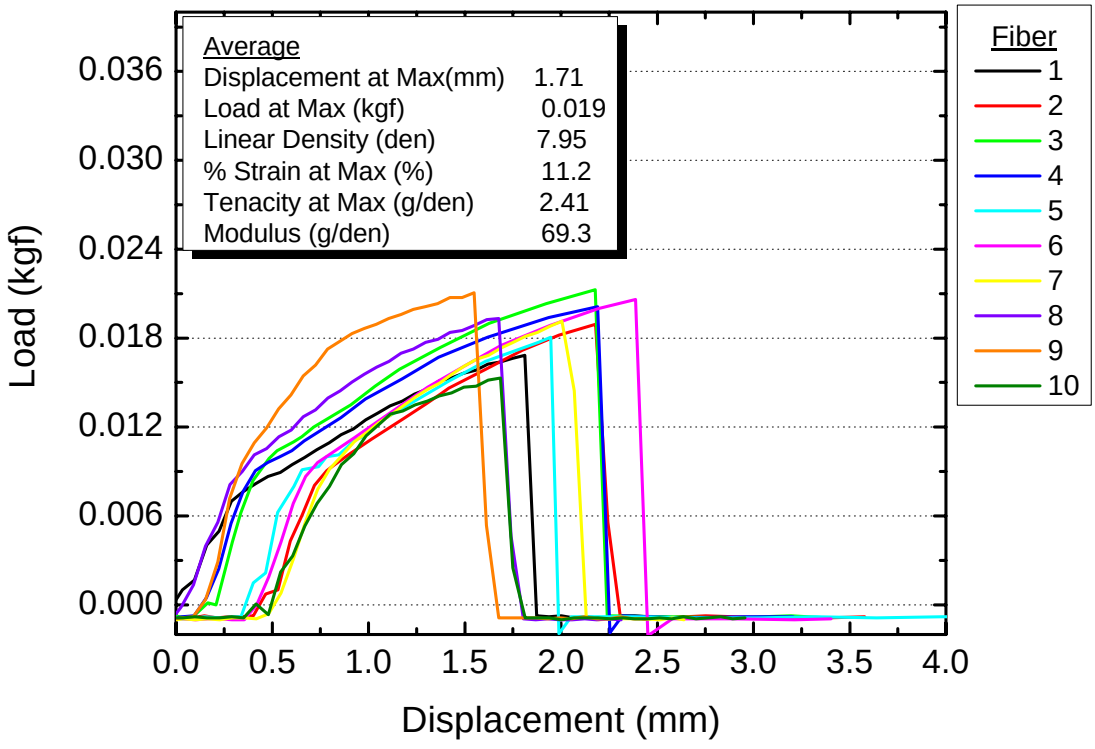

Figure E6: Session 2 – Run #6

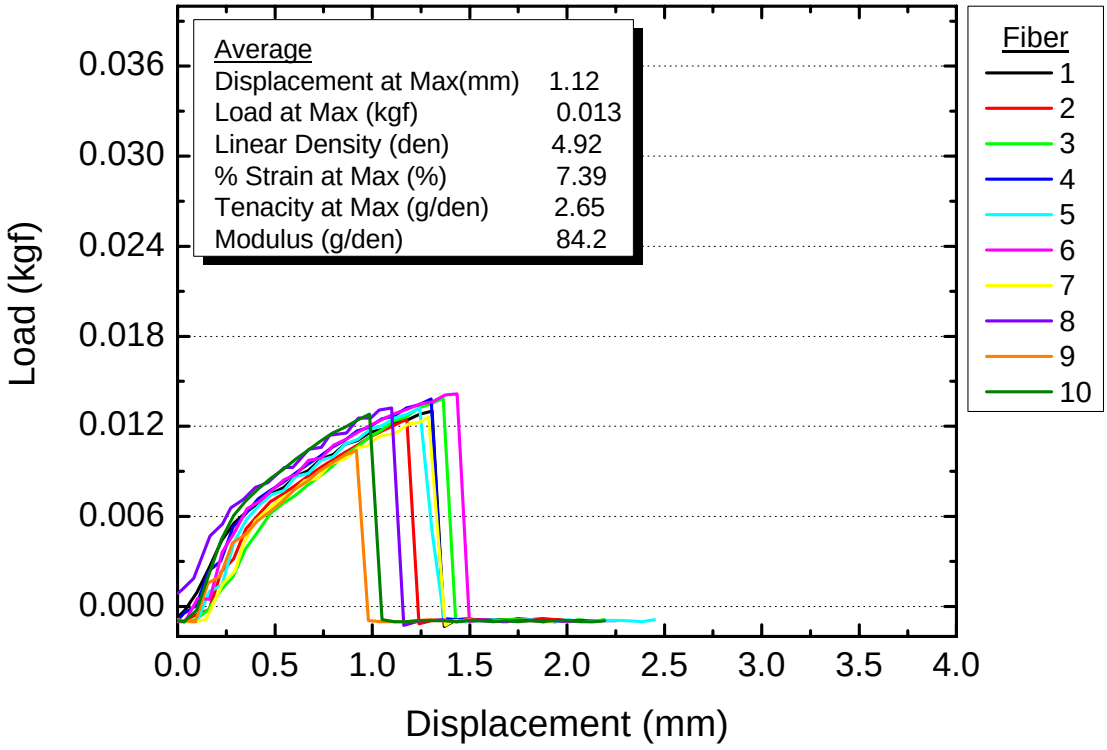

Figure E7: Session 2 – Run #7

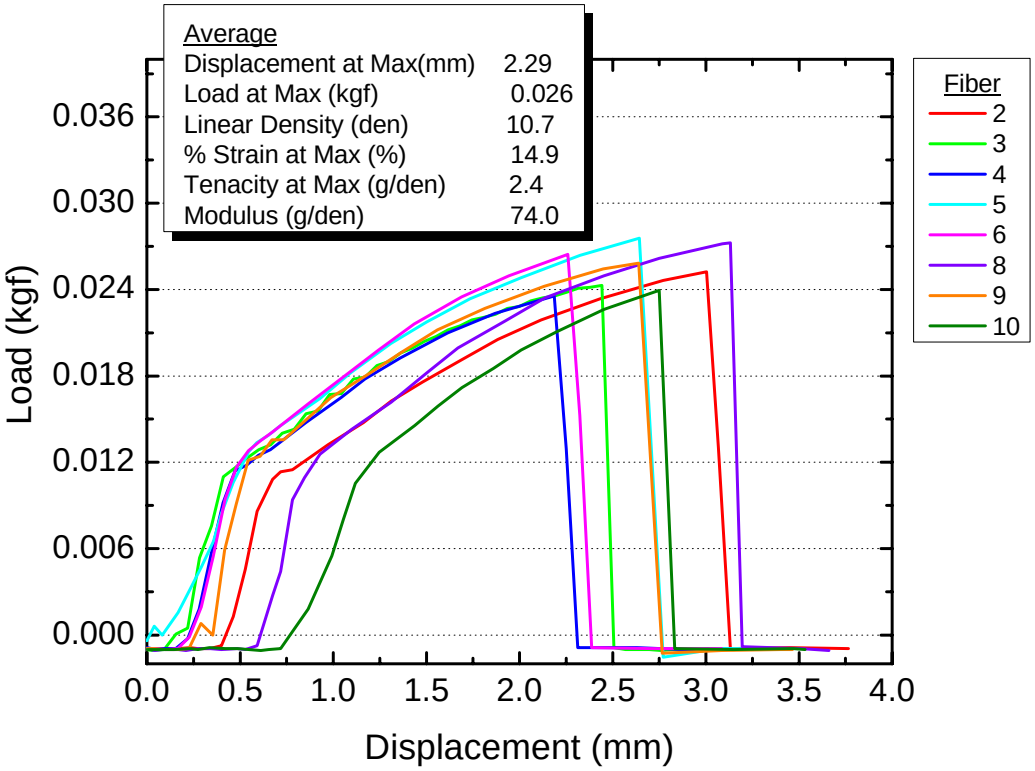

Figure E8: Session 2 – Run #8

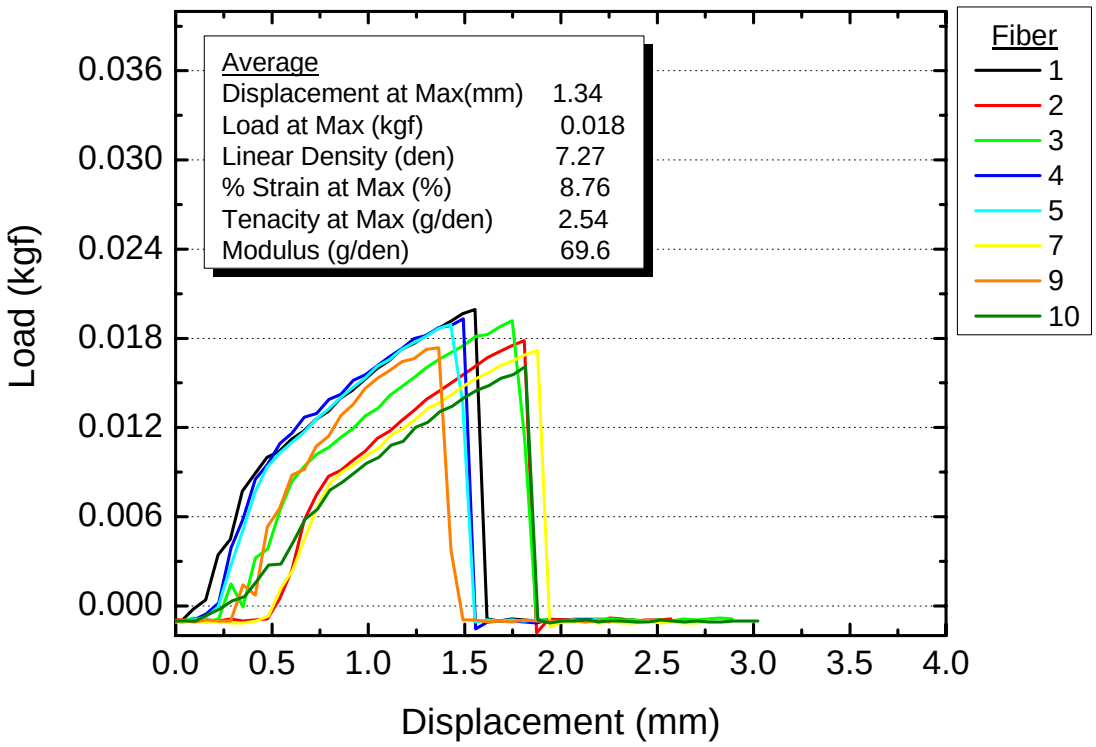

Figure E9: Session 2 – Run #9

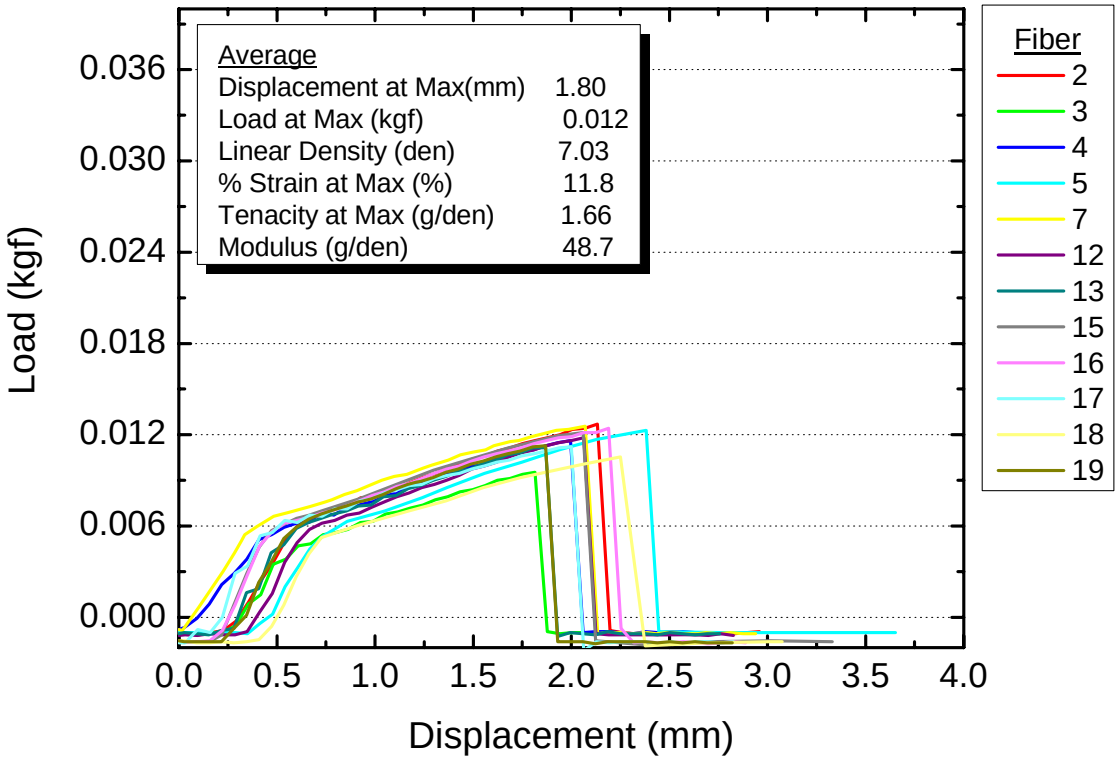

Figure E10: Session 3 – Run #10

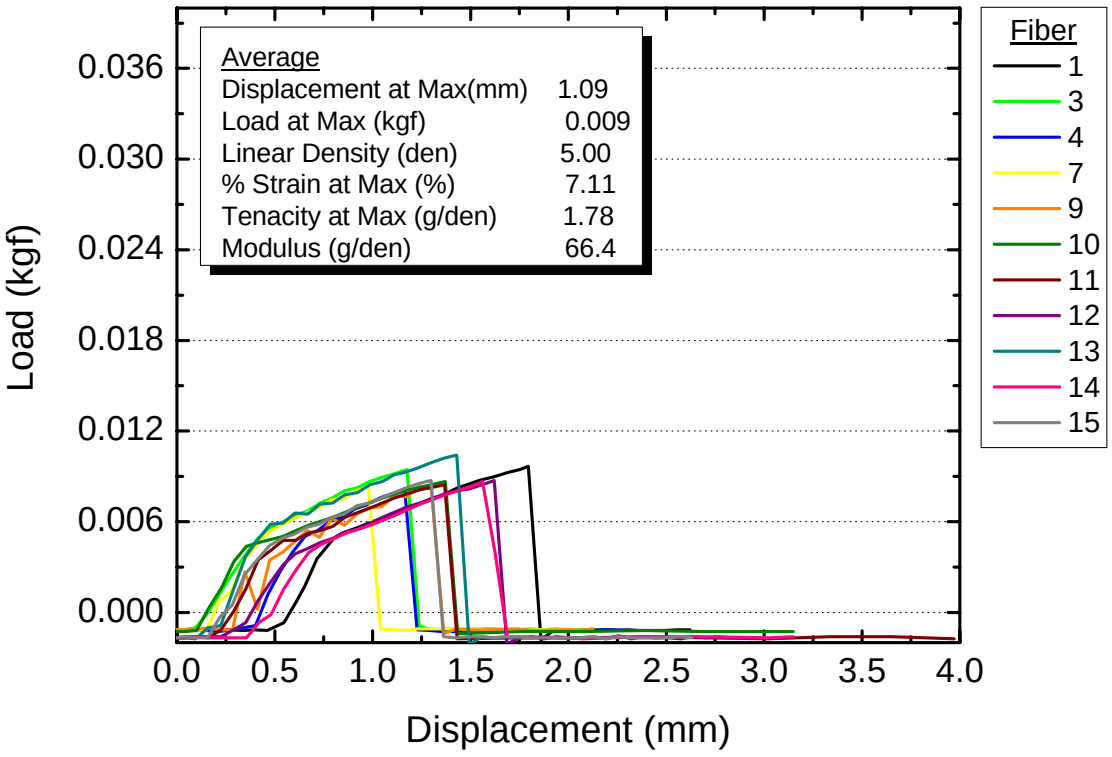

Figure E11: Session 3 – Run #11

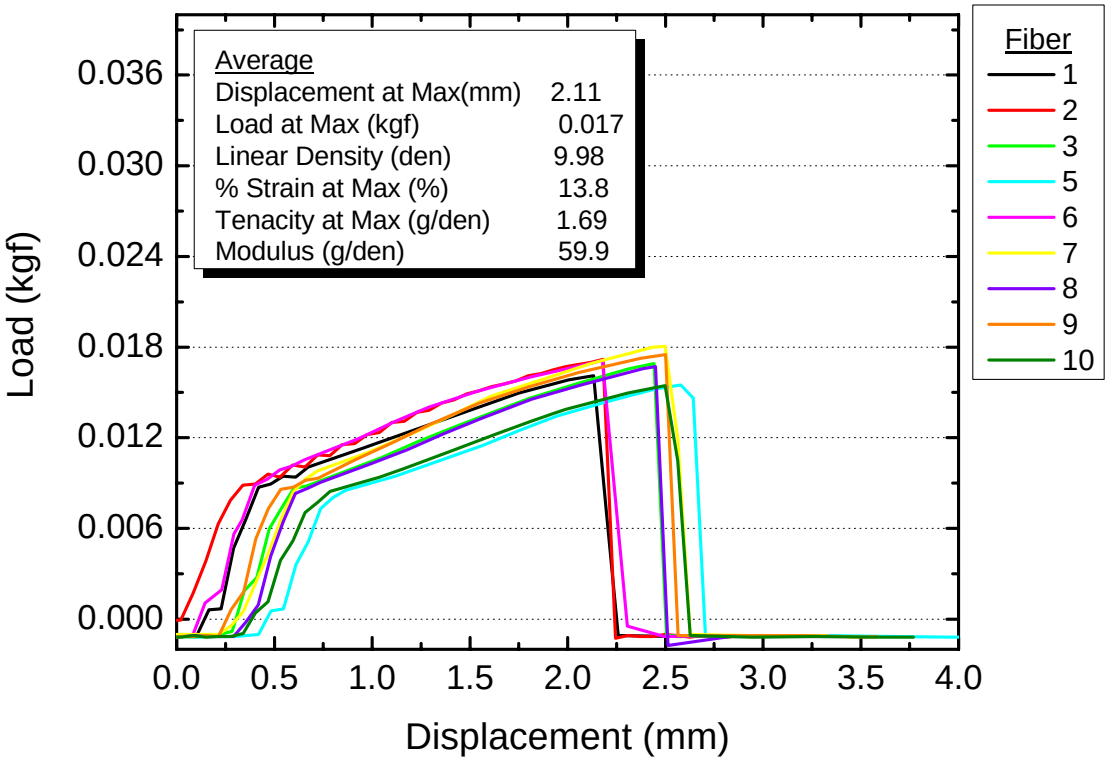

Figure E12: Session 3 – Run #12

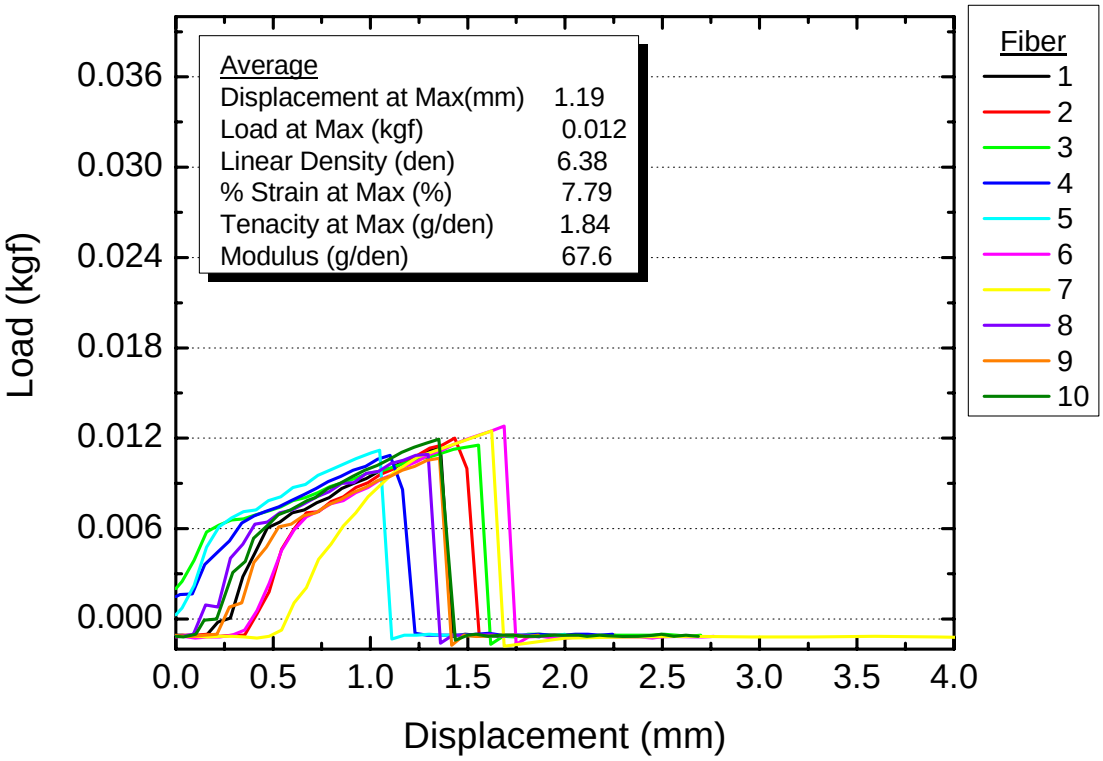

Figure E13: Session 3 – Run #13

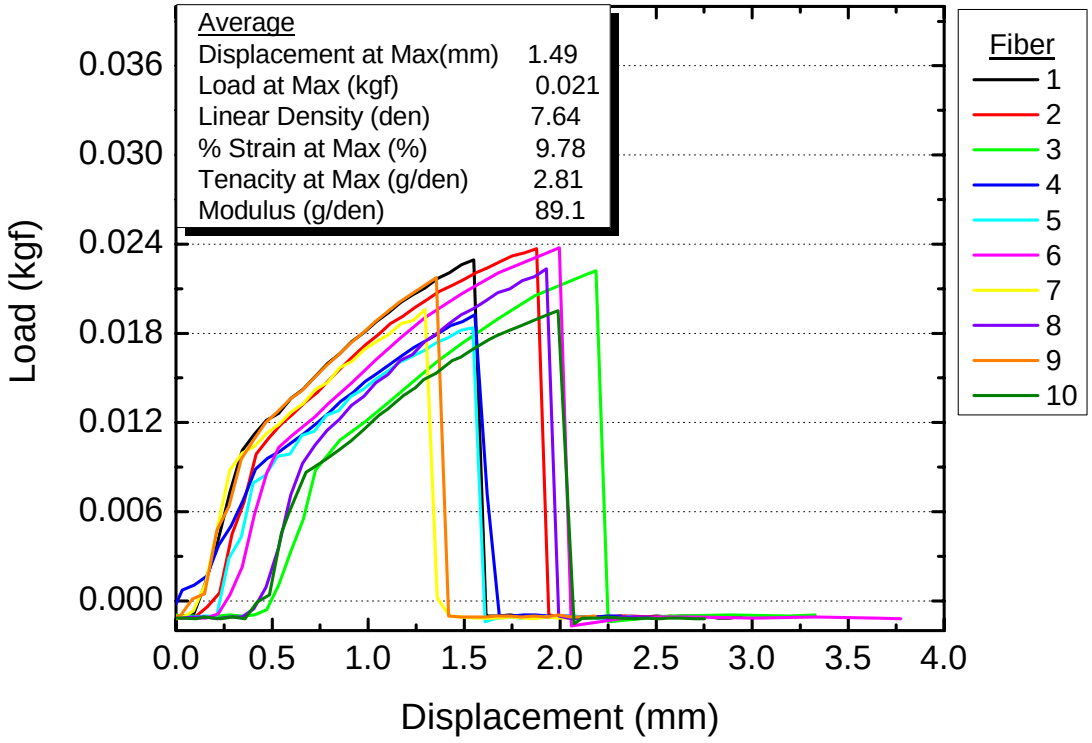

Figure E14: Session 4 – Run #14

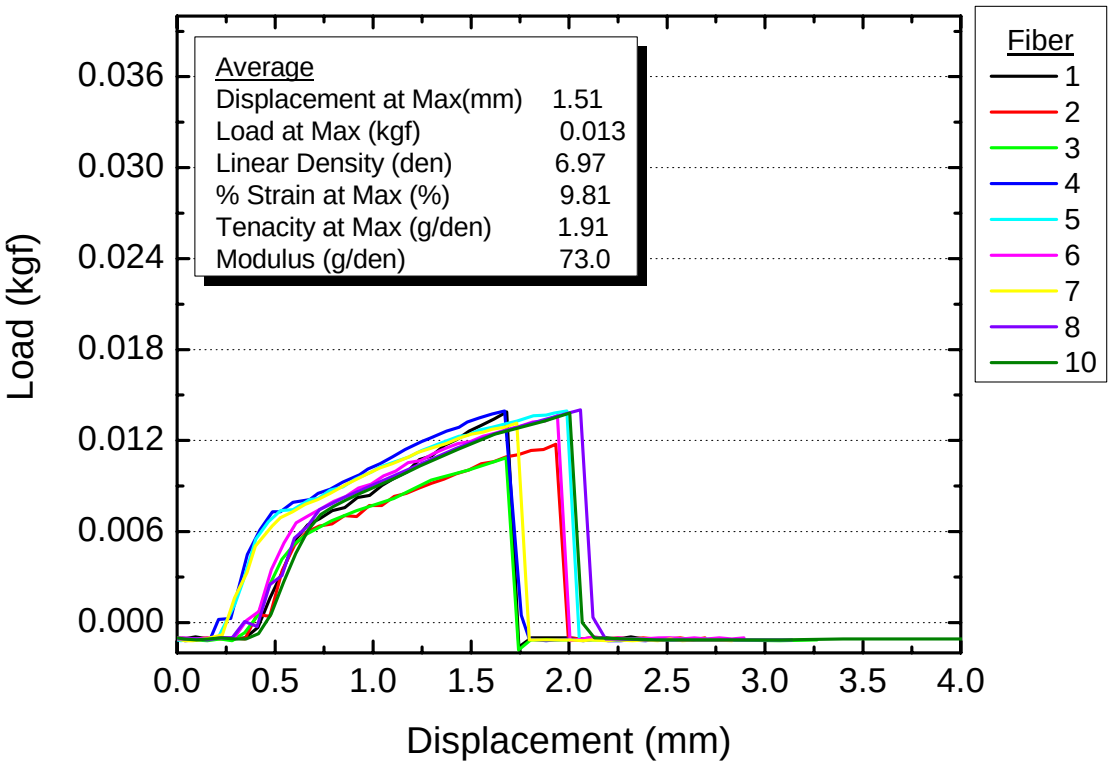

Figure E15: Session 5 – Run #15

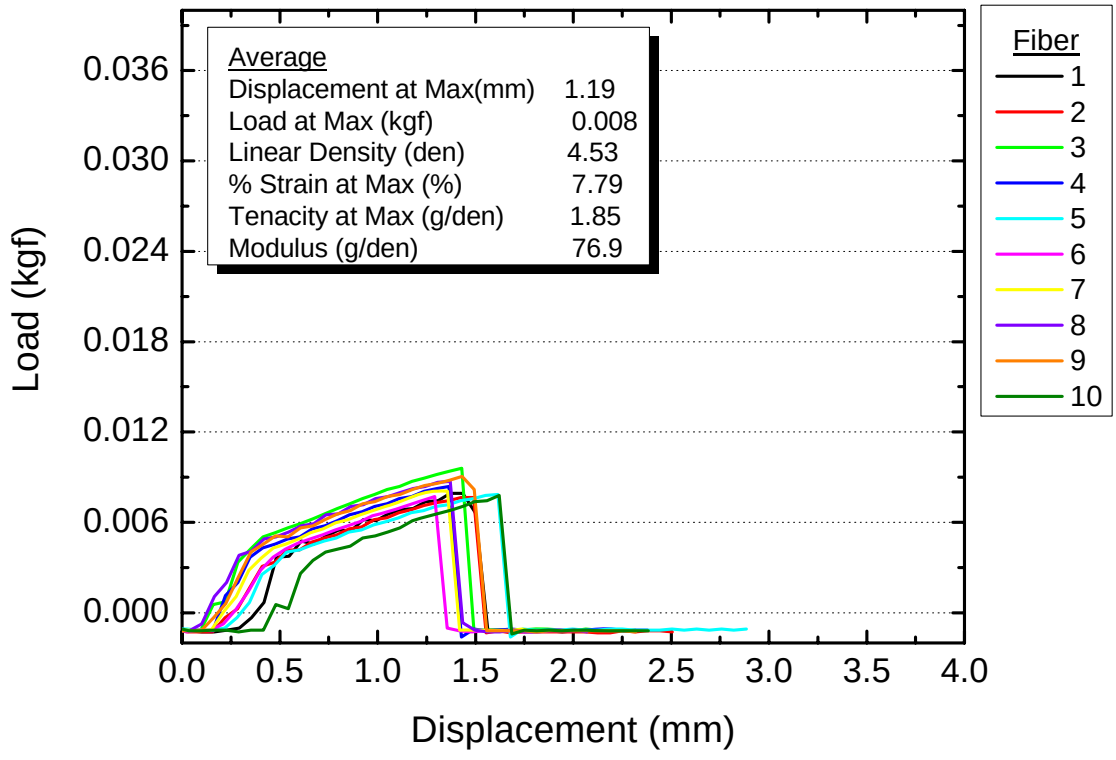

Figure E16: Session 6 – Run #16

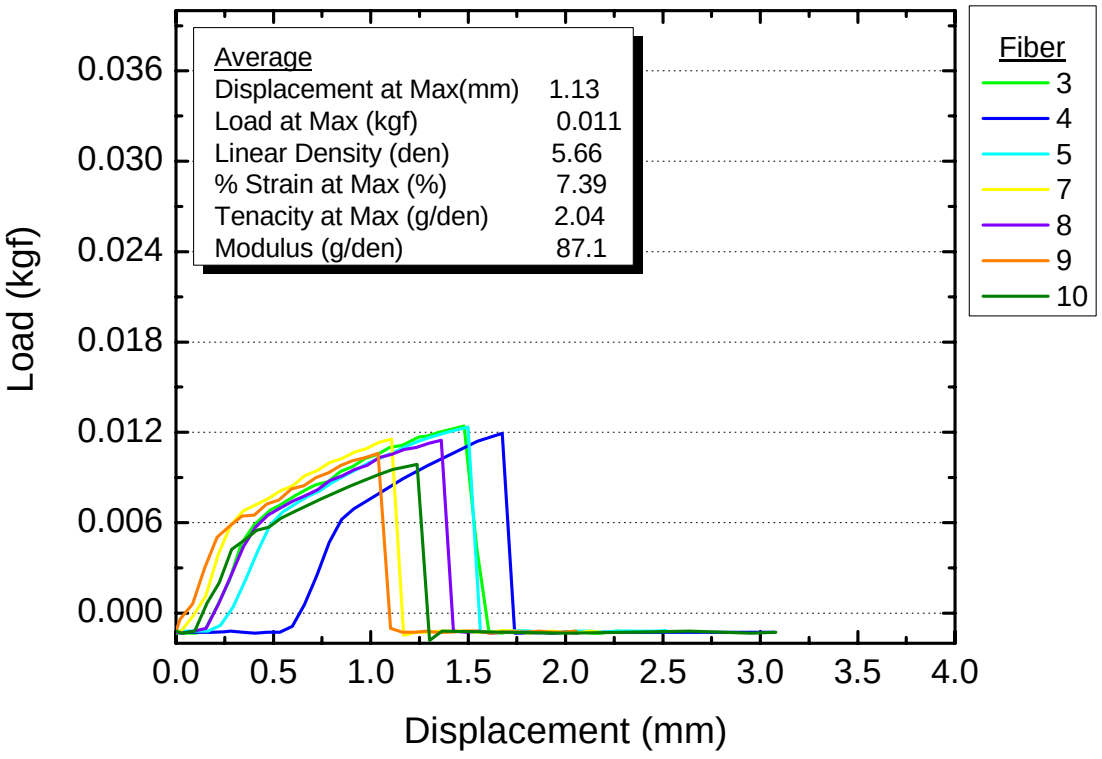

Figure E17: Session 6 – Run #17

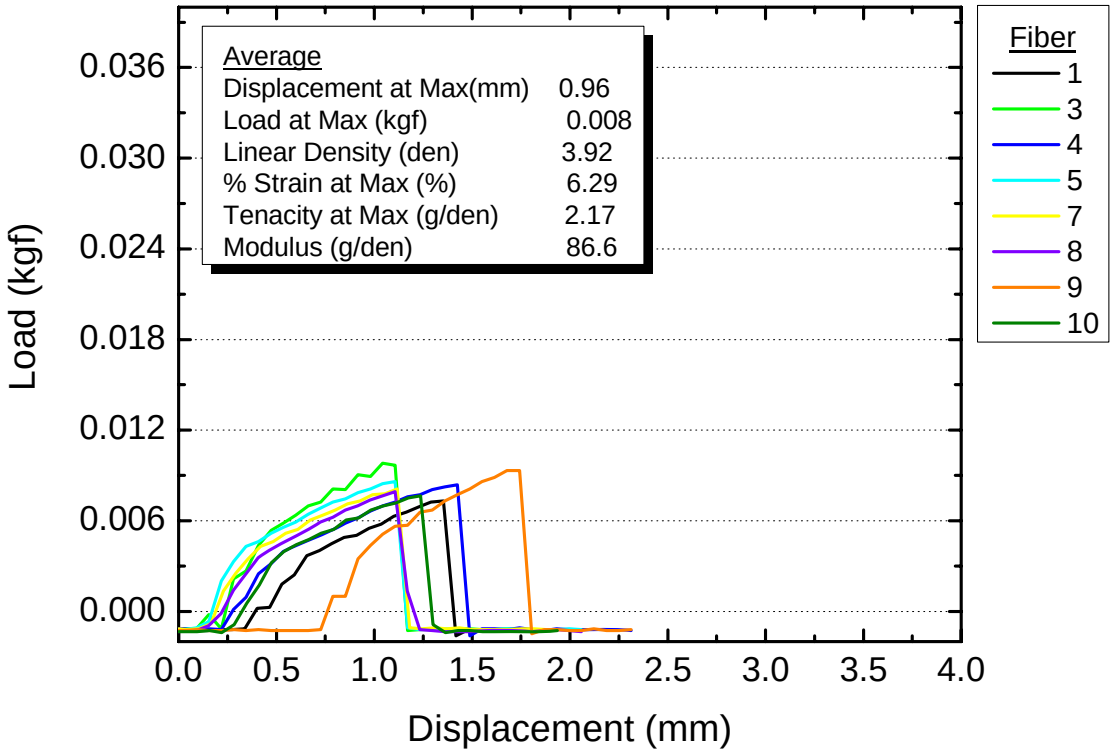

Figure E18: Session 6 – Run #18

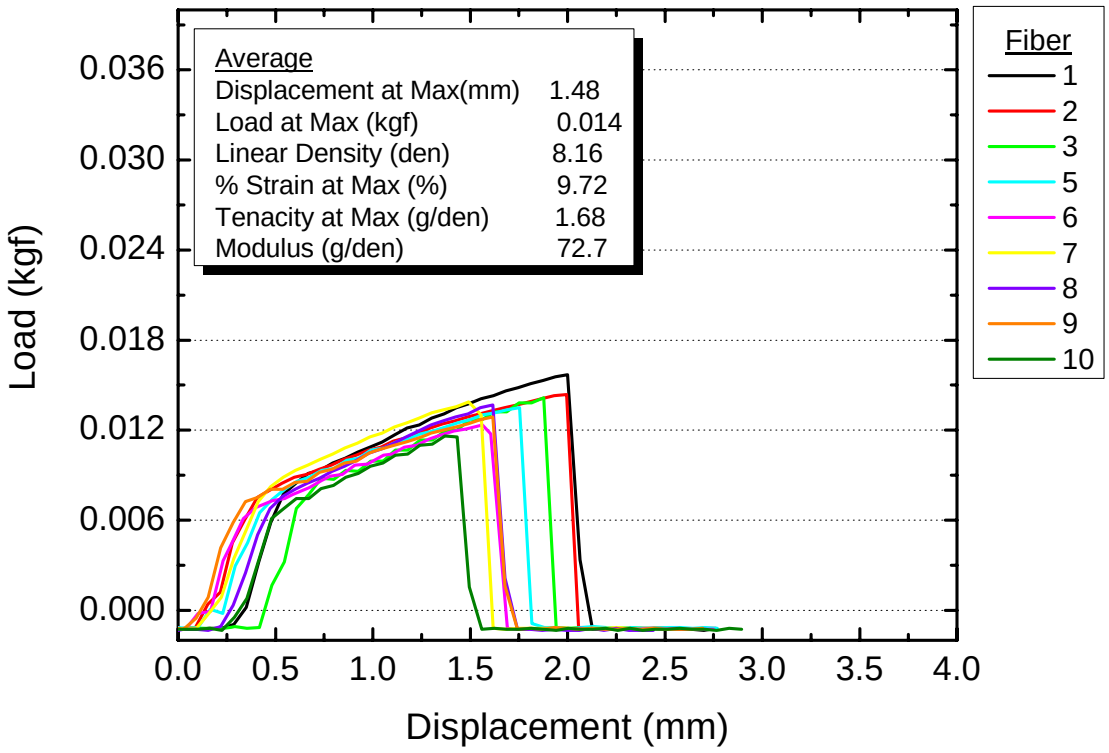

Figure E19: Session 6 – Run #19

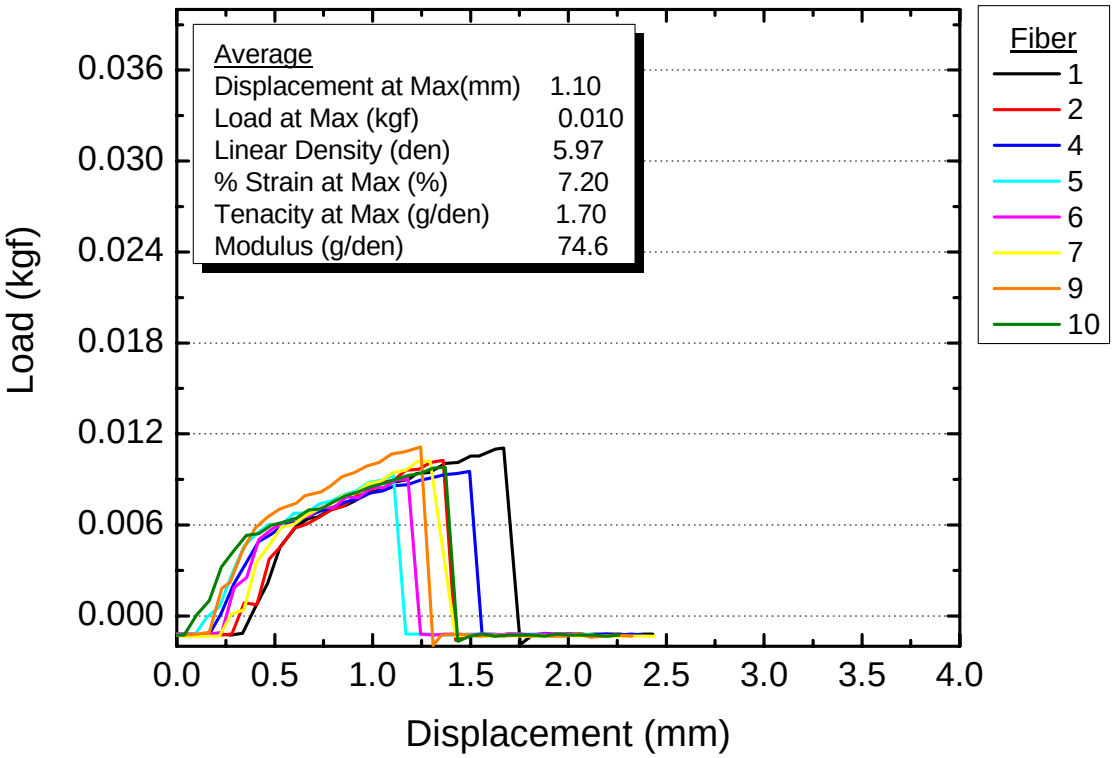

Figure E20: Session 6 – Run #20

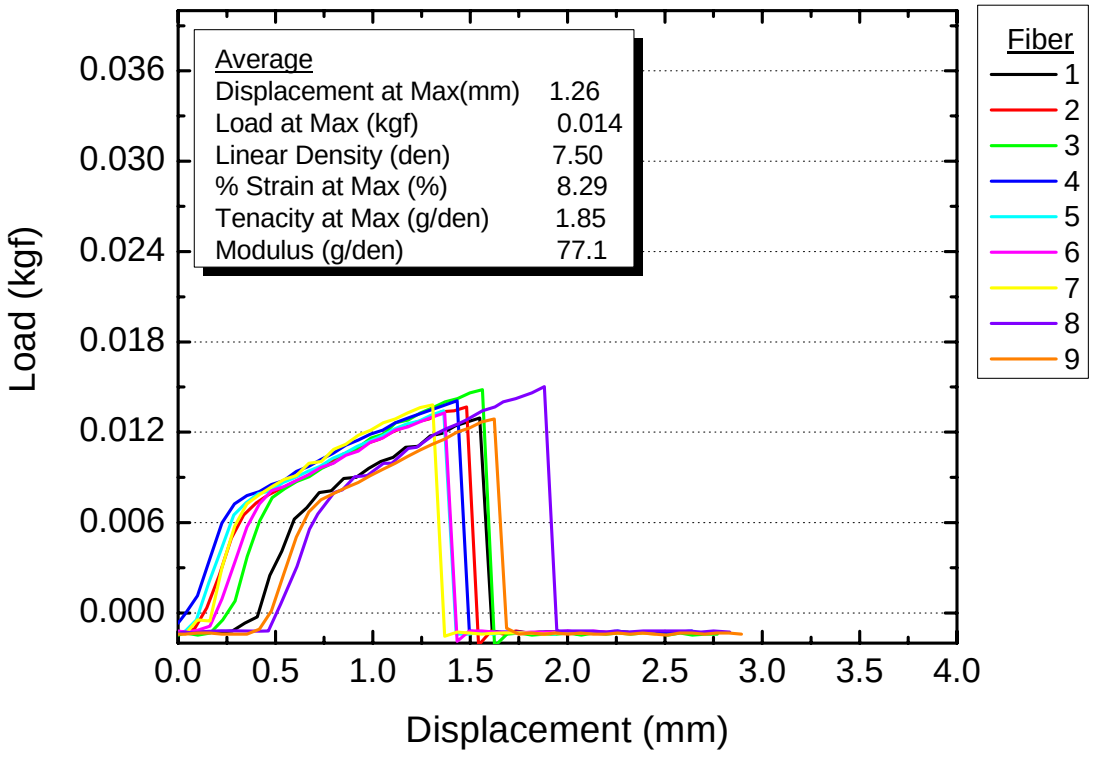

Figure E21: Session 6 – Run #22

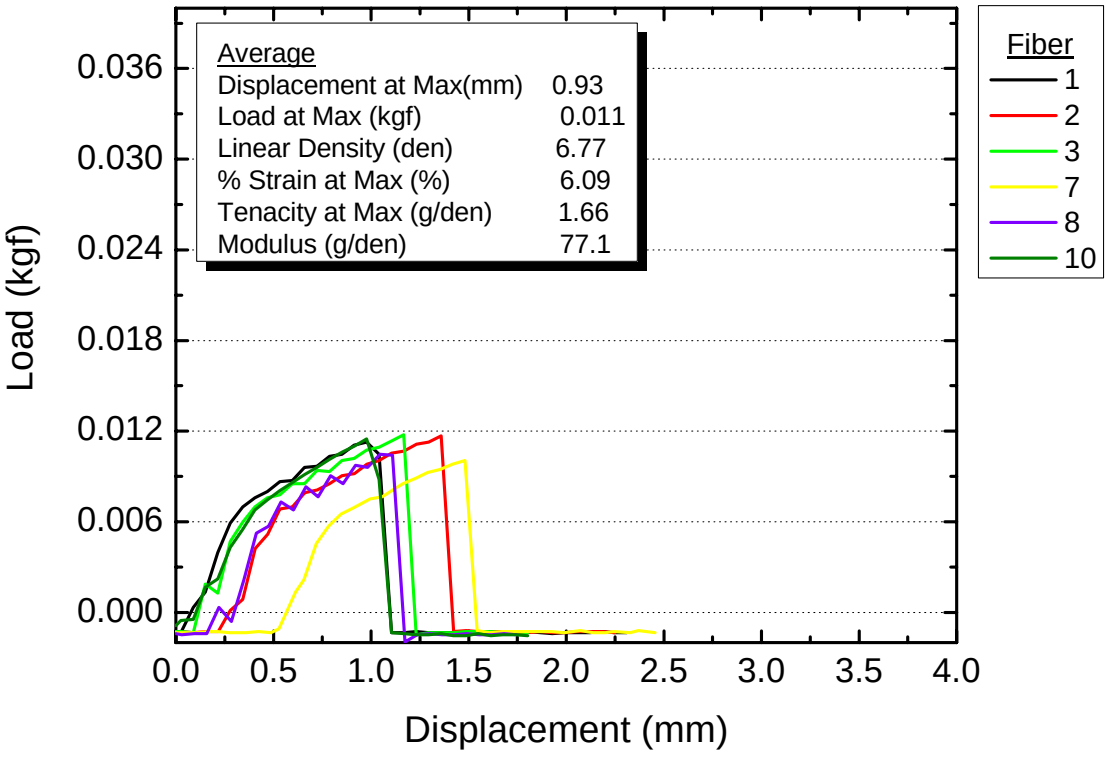

Figure E22: Session 6 – Run #24

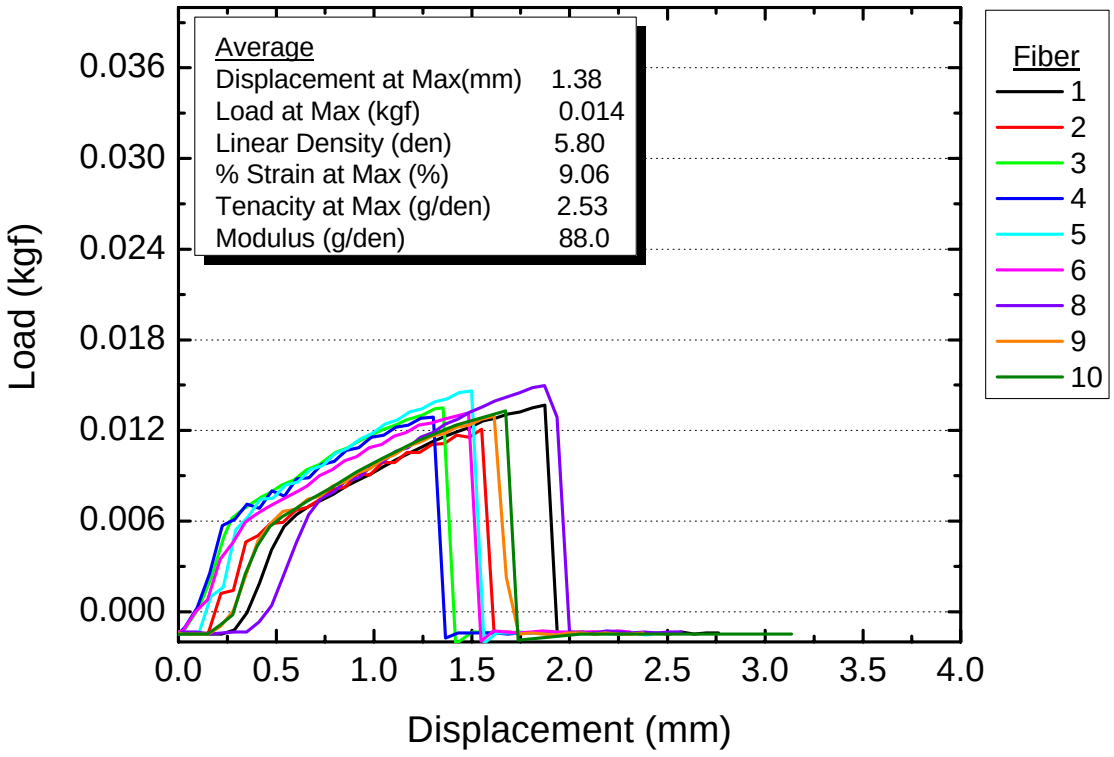

Figure E23: Session 7 – Run #25

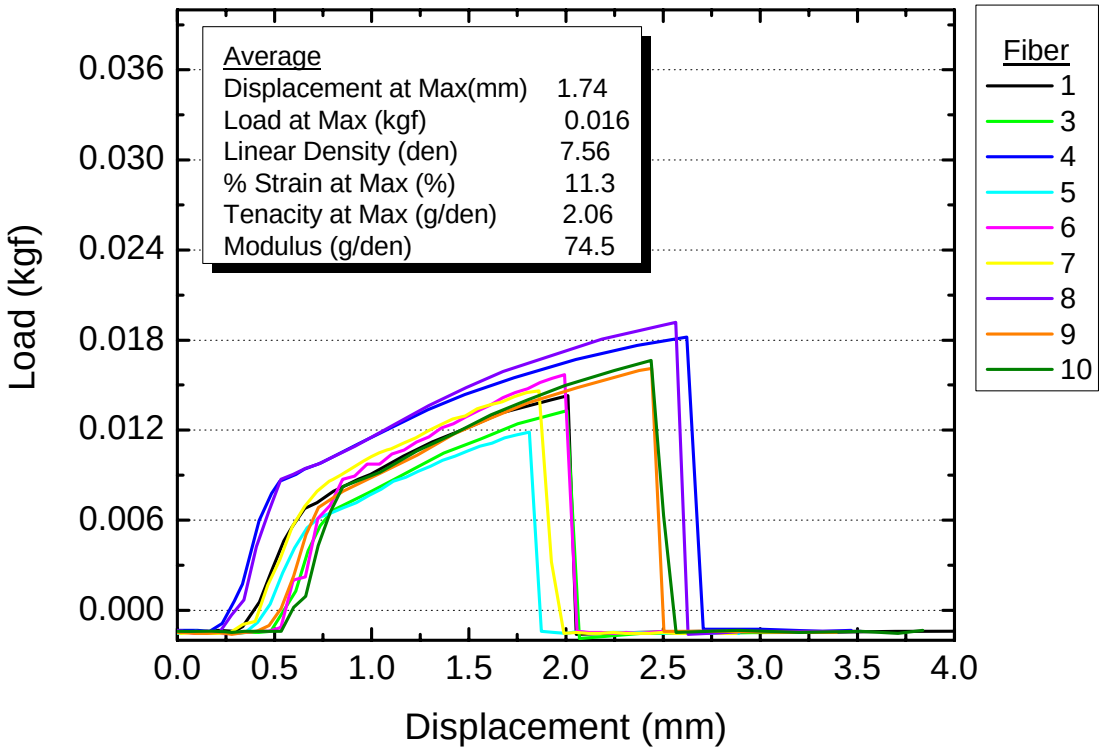

Figure E24: Session 7 – Run #26

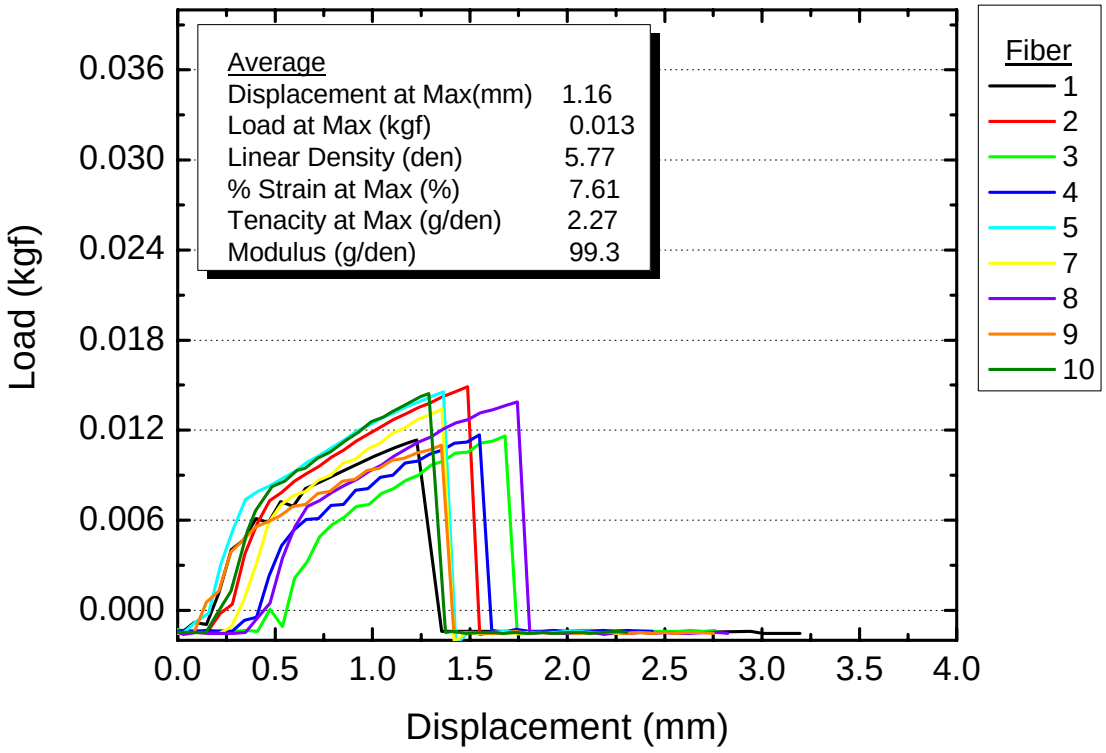

Figure E25: Session 7 – Run #27

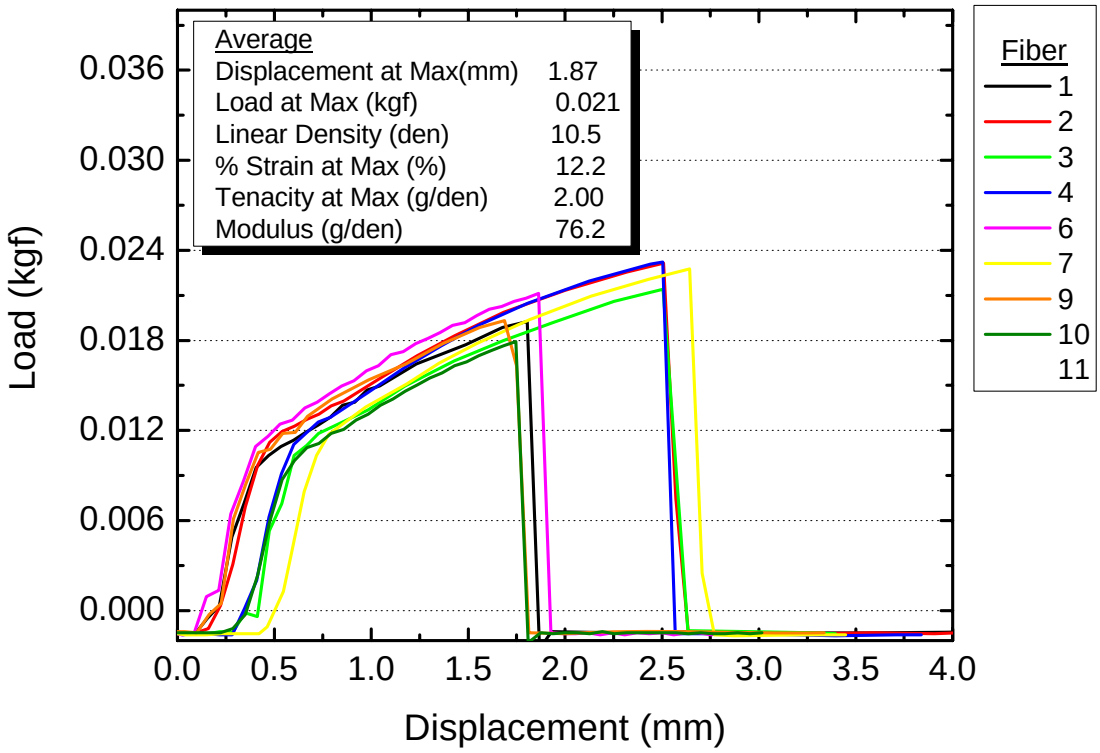

Figure E26: Session 7 – Run #28

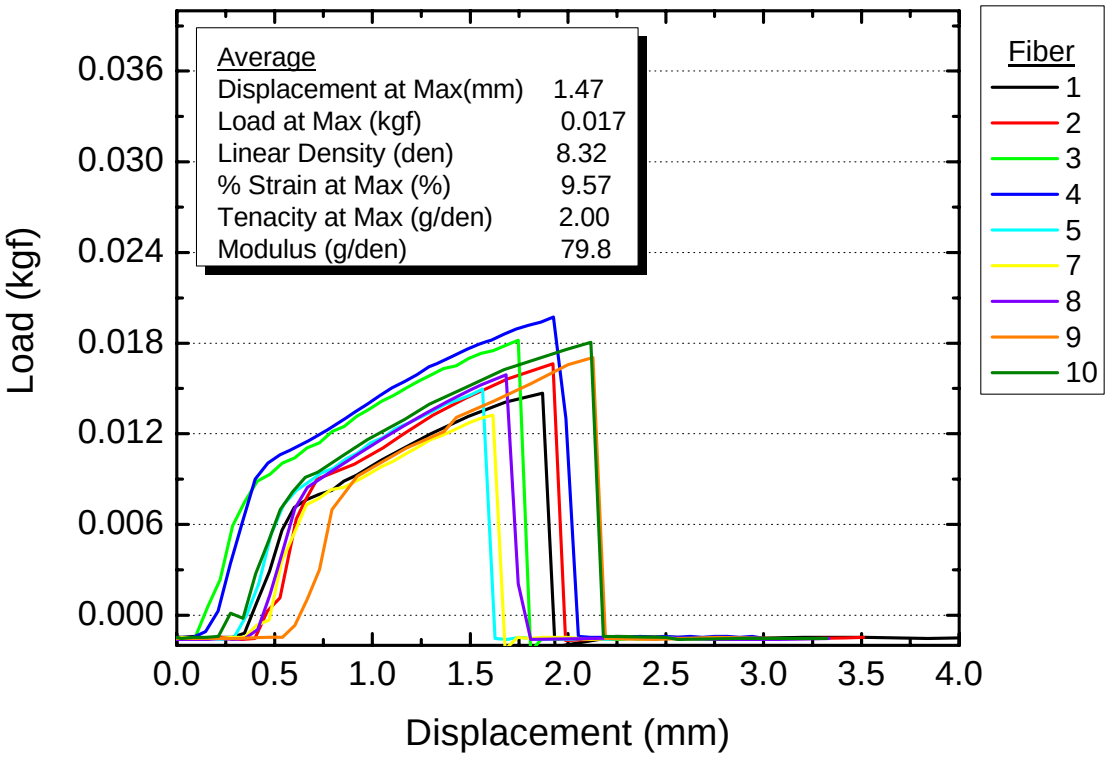

Figure E27: Session 7 – Run #29

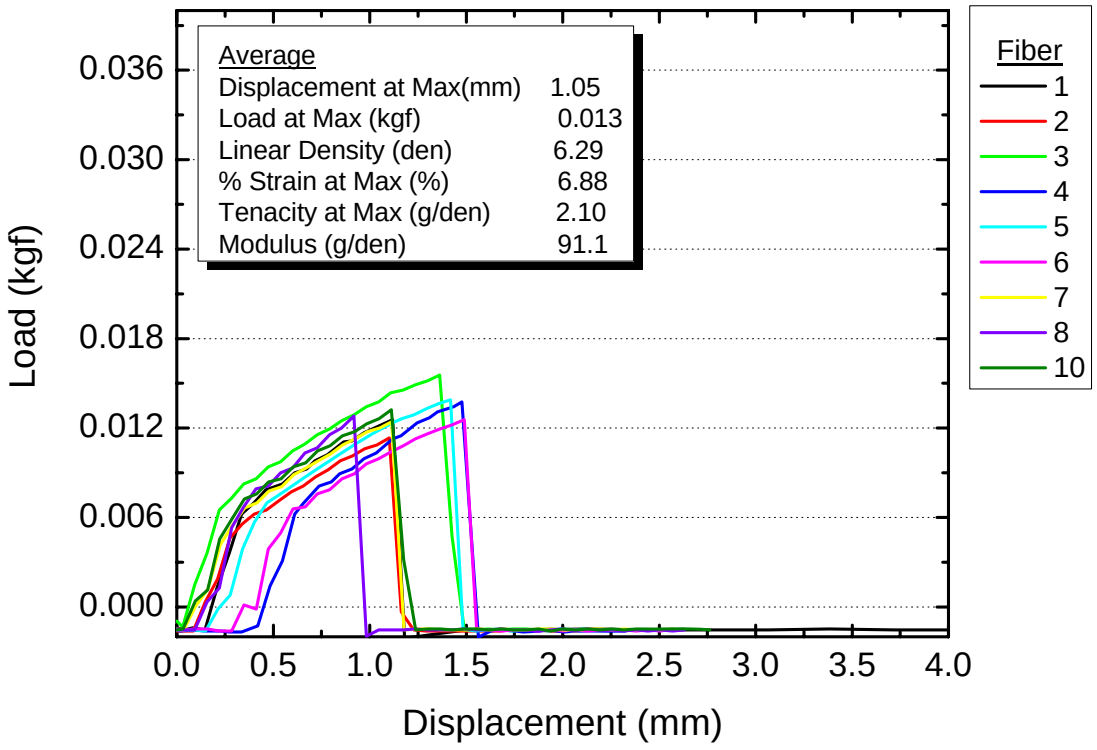

Figure E28: Session 7 – Run #30

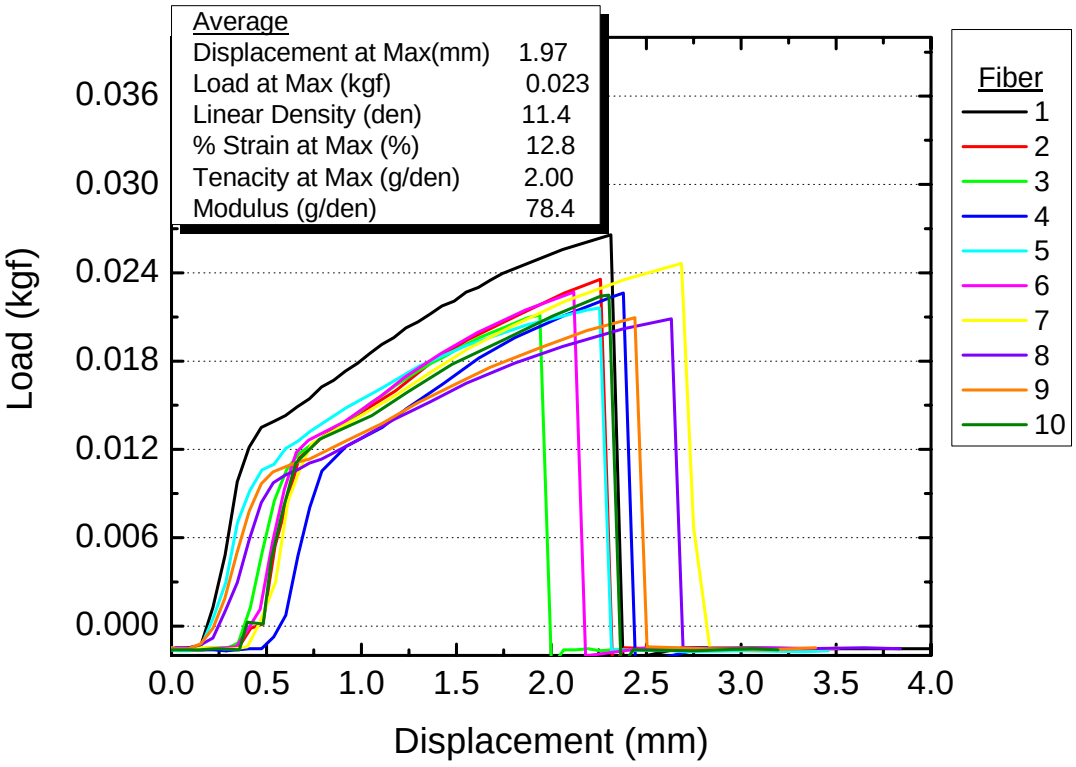

Figure E29: Session 7 – Run #31

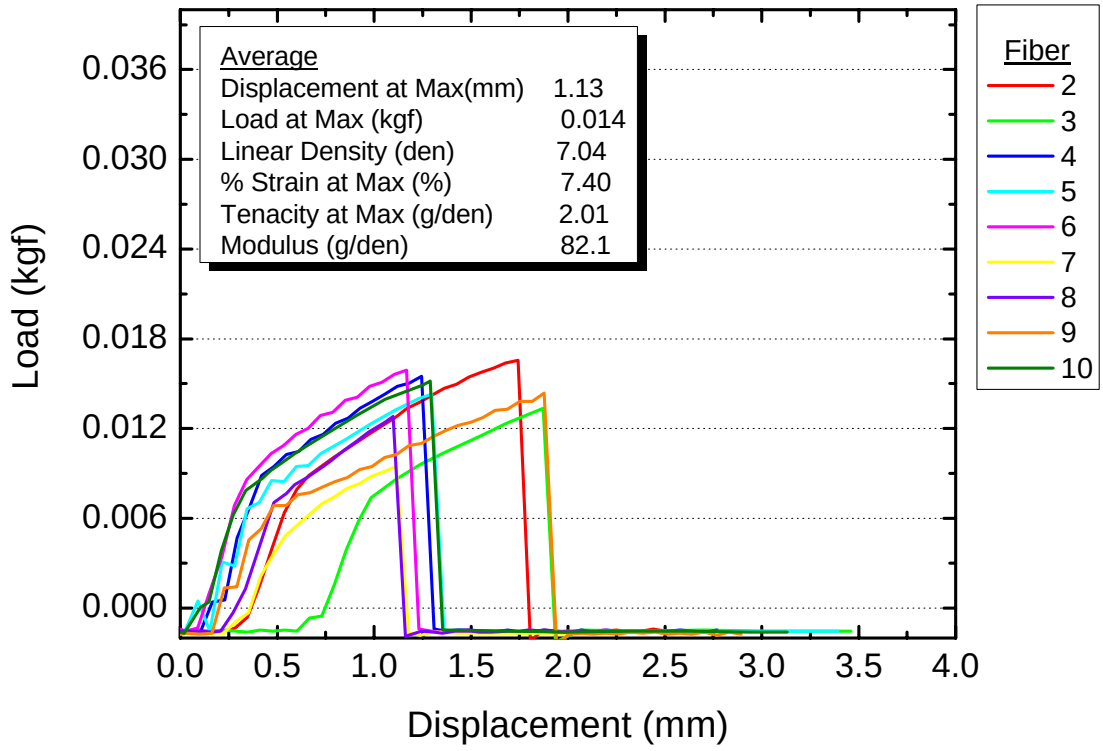

Figure E30: Session 7 – Run #32

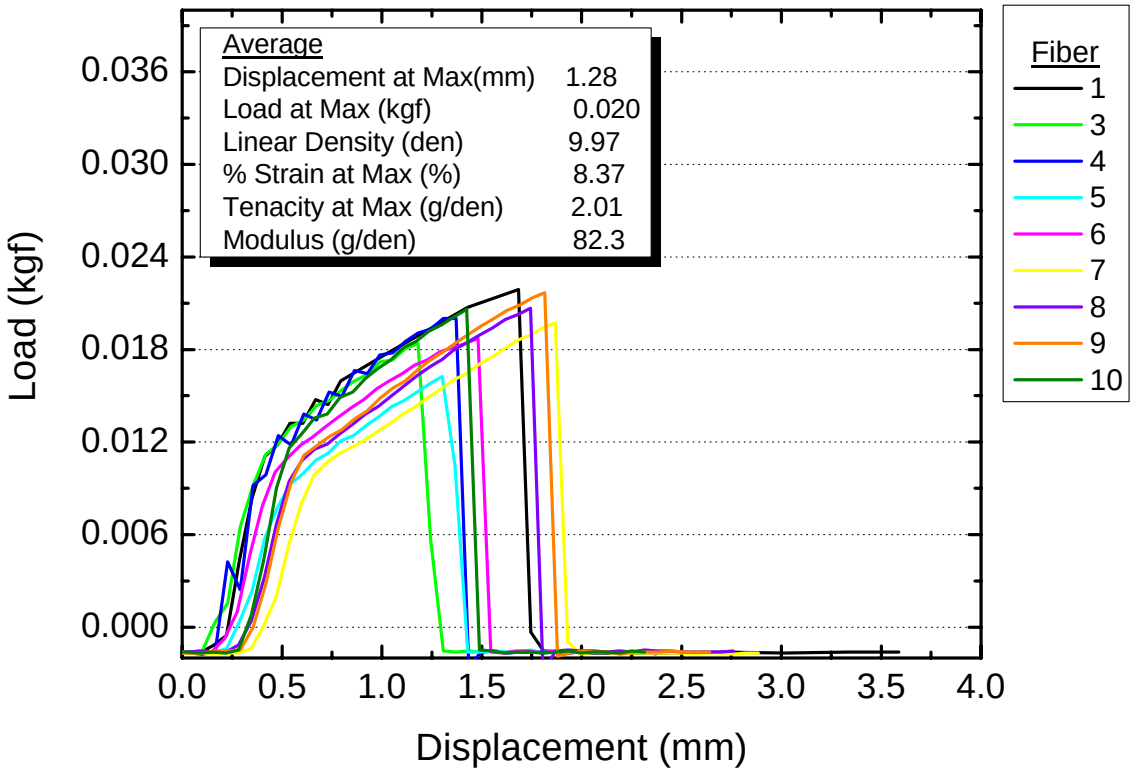

Figure E31: Session 7 – Run #33

APPENDIX F

Linear Density

Linear Density Regression Curves – Temperature Variation – Experiment 1

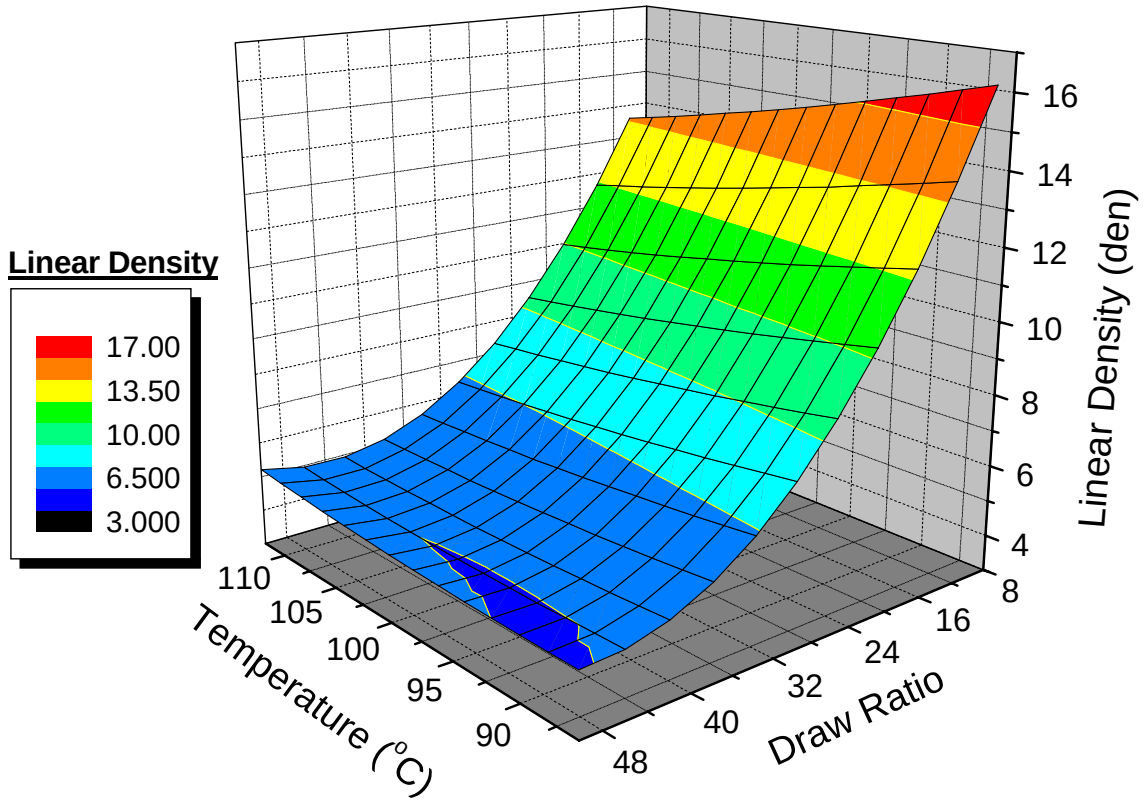

Figure F1: The effect of temperature and draw ratio on the linear density for a 10% solution.

Figure F1 represents the surface regression curve of the linear density as affected by the change in temperature and draw ratio. This graph illustrates that at low draw ratios, the linear density was higher. Also observed at higher draw ratios is a leveling off of the linear density thus indicating that the fiber will only reach a certain diameter. The goal of the fiber spinning is to have a fiber with a diameter in the range of 10 to 20 micrometers thus a lower linear density, therefore this figure indicates that lower temperatures and higher draw ratios would achieve this goal.

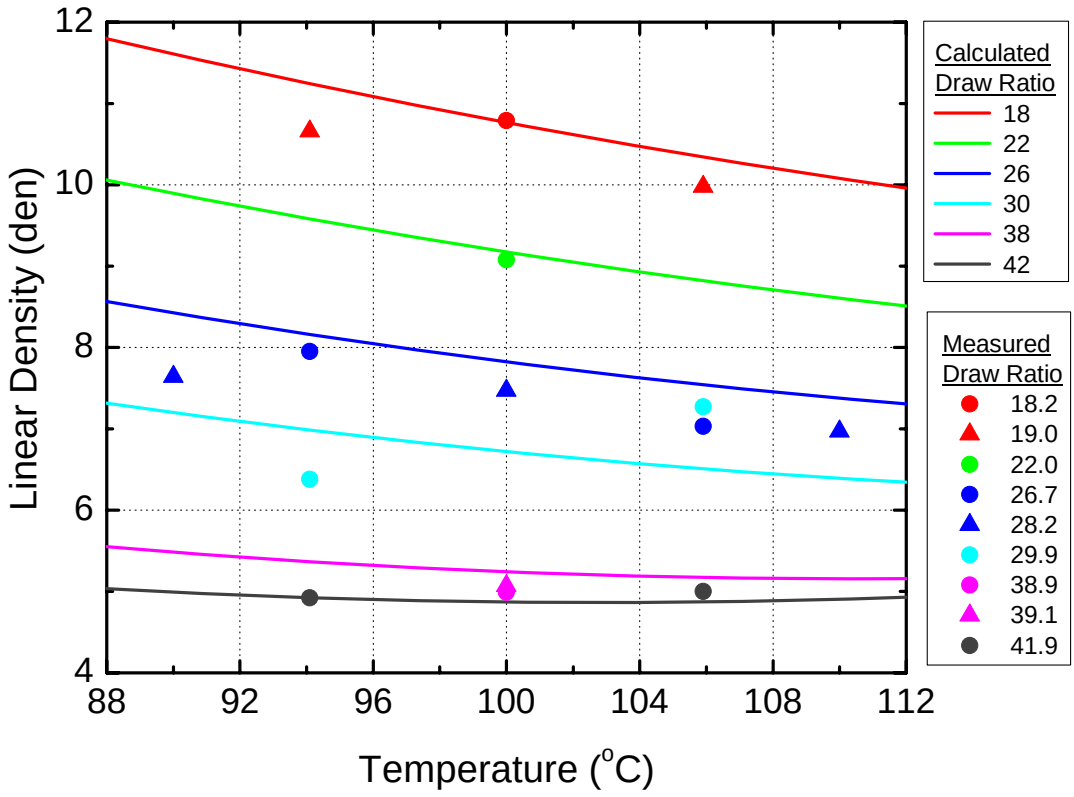

Figure F2: The effect of temperature on the linear density for a 10% solution at measured and calculated draw ratios.

Figure F2 represents the effect of temperature on the linear density where the lines are the calculated draw ratios based on the regression analysis and the points represent the measured draw ratios for the runs in Experiment 1. The graph indicates a decrease in the linear density of the fiber as the temperature increases. As the temperature continues to rise, the difference in the linear density of the fiber, at higher draw ratios, decreases suggesting that the fiber will maintain a certain level linear density. The points indicate that the measured draw ratios fit the calculated draw ratio curves where the closest measurement to calculation is for a draw ratio of 41.9.

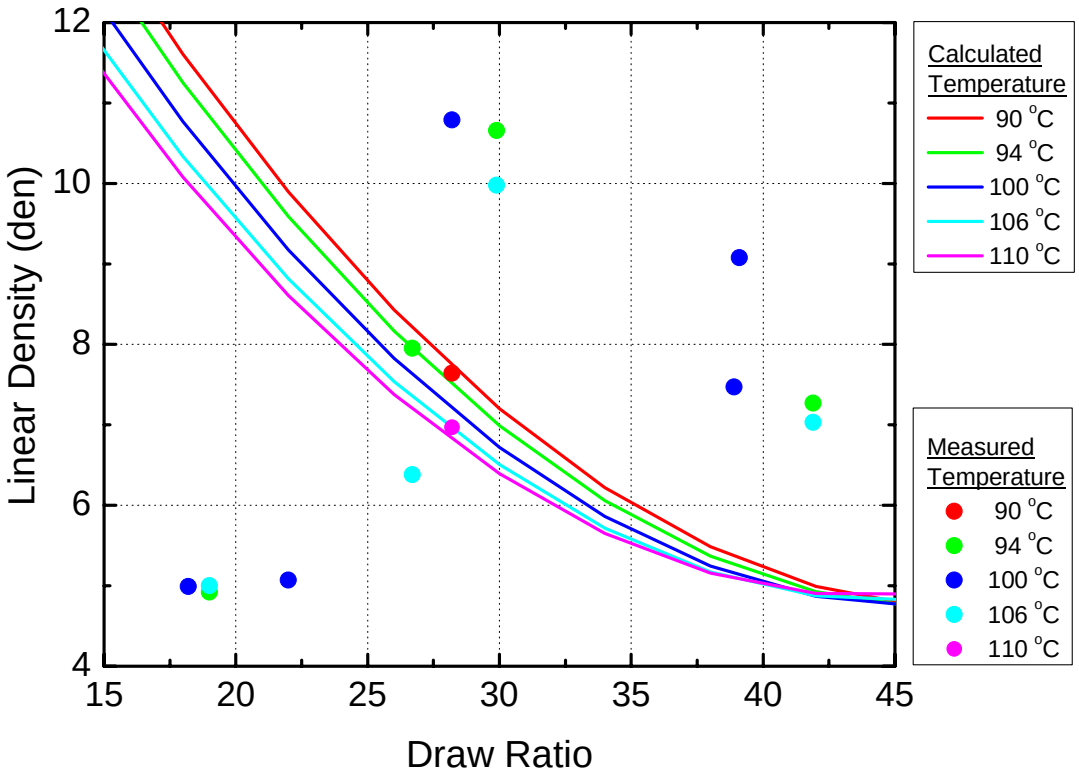

Figure F3: The effect of draw ratio on the linear density for a 10% solution at measured and calculated temperatures.

Figure F3 represents the effect of draw ratio on the linear density of the fiber. The regression lines on the graph indicate a decrease in the density as the draw ratio increases. The points indicate that the measured temperatures do not follow the calculated temperature curves closely with exception of the point at 90°C. Also observed in the graph is the minimal difference in the linear density at the higher draw ratios.

Based on these two figures the run with the lowest liner density was Run #7 with a linear density of 4.92 denier, run at a temperature of 94°C, a draw ratio of 41.9 and a concentration of 10%. The highest linear density was observed to be Run #2 with a linear density of 10.79 denier, run at a temperature of 100°C, a draw ratio of 18.2 and a concentration of 10%.

Linear Density Regression Curves – Concentration Variation – Experiment 2

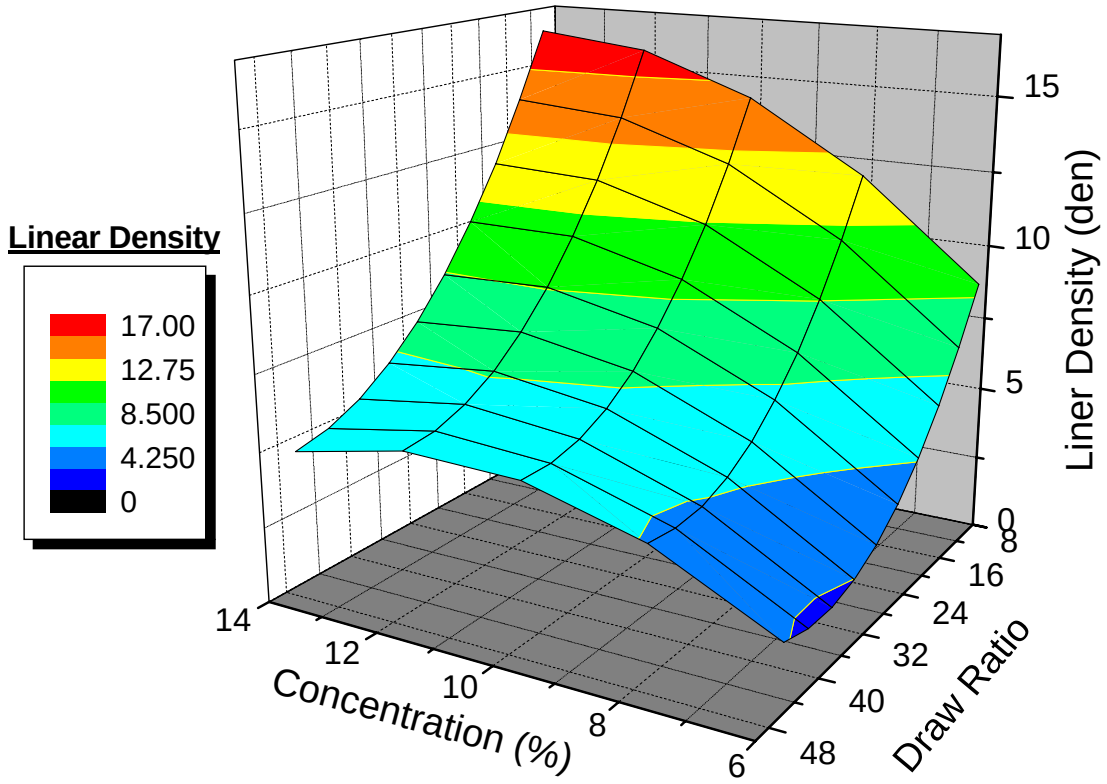

Figure F4: The effect of concentration and draw ratio on the linear density at 100°C.

Figure F4 represents the surface regression curve for effect solution concentration and draw ratio had on the linear density. This graph illustrates that the lowest linear density occurred at low concentrations and high draw ratios. This indicates that a low solution concentration at a high draw ratio would yield fibers with the smallest diameter. As previously stated, the goal of the fiber spinning is to have a fiber with the smallest diameter possible. Therefore, based on Figures F1 and F4, lower concentrations, higher draw ratios and lower temperatures would achieve this goal.

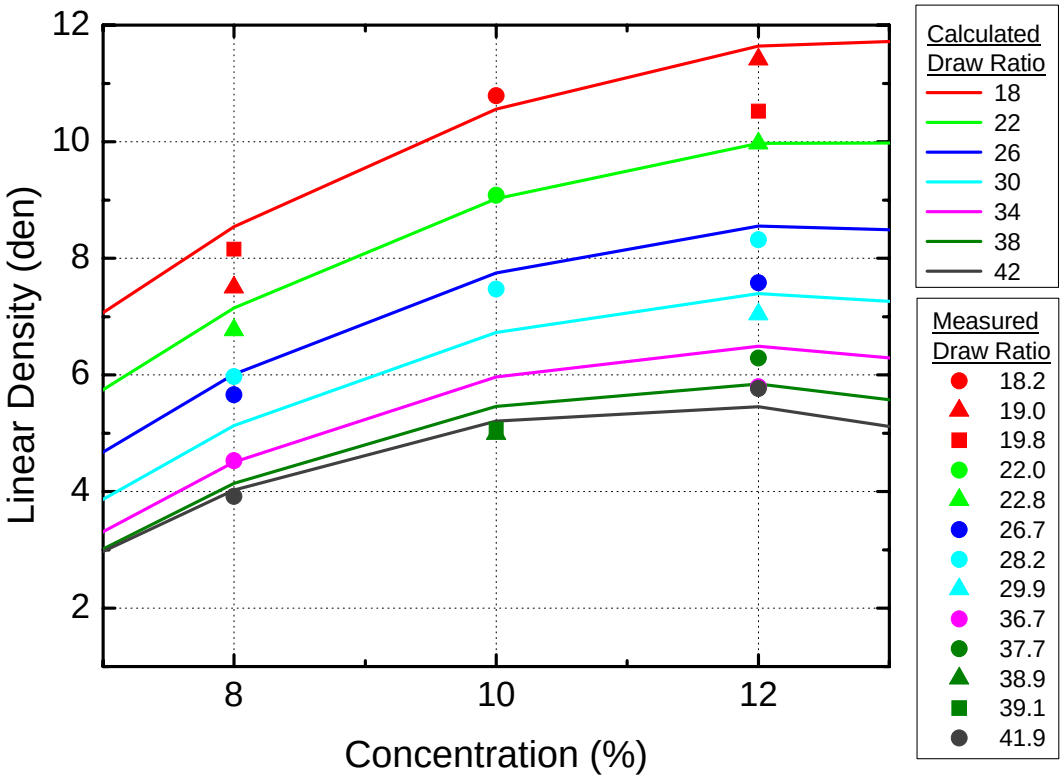

Figure F5: The effect of concentration on the linear density at 100°C for measured and calculated draw ratios.

Figure F5 represents the effect of concentration on the linear density where the lines are the calculated draw ratios based on the regression analysis and the points represent the actual data for the runs in Experiment 2. The graph indicates an increase in the linear density of the fiber as concentration increases. At the higher draw ratios, the linear density did not vary as widely in comparison to the lower draw ratios thus suggesting that the fibers could only reach a certain linear density before breaking. The points indicate that the measured draw ratios fit calculated draw ratio curves relatively well, where the closest measurements to calculation is for a draw ratio of 22.0 and 41.9.

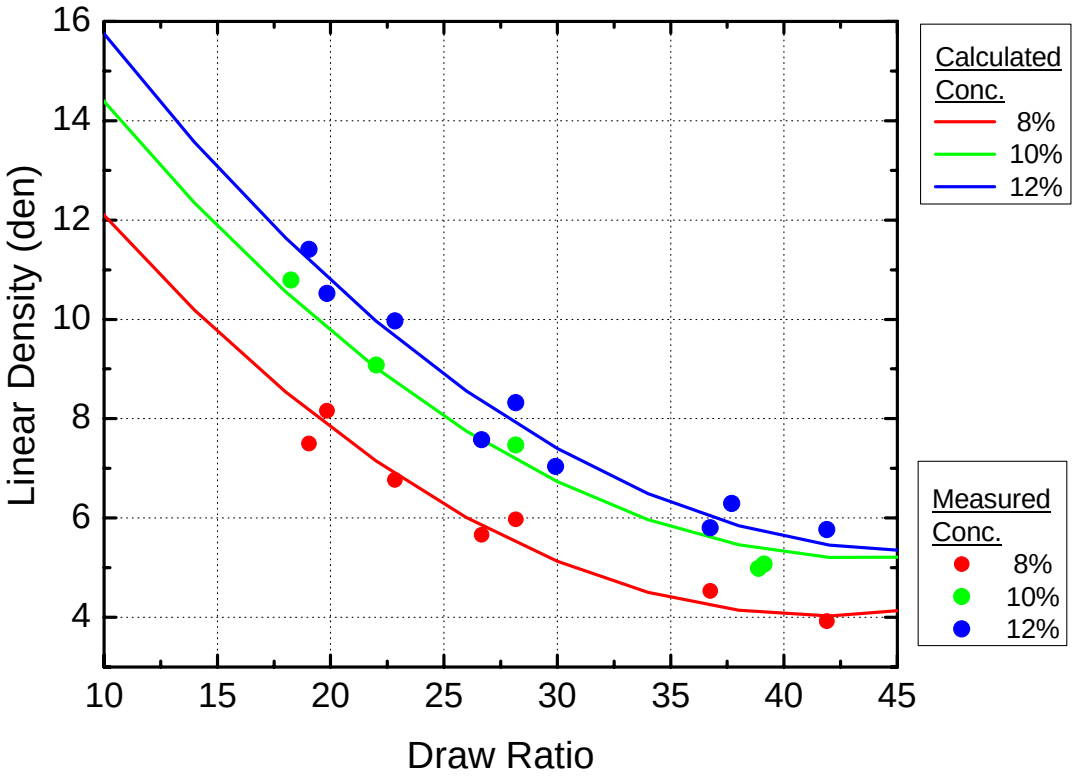

Figure F6: The effect of draw ratio on the linear density at 100°C for measured and calculated concentrations.

Figure F6 represents the effect of draw ratio on the linear density of the fiber. The graph shows a decrease in the linear density as the draw ratio increases. Also observed that the leveling off of the curve at the higher draw ratios, again suggesting that the fibers will only reach a certain linear density. The points indicate that the measured concentration points fit calculated concentration curves relatively well.

Based on these two figures, the run with the lowest linear density was Run #18 with a linear density of 3.92 denier, run at a temperature of 100°C, a draw ratio of 41.9 and a concentration of 8%. The highest linear density was observed to be Run #31 with a linear density of 11.41 denier, run at a temperature of 100°C, a draw ratio of 19.0 and a concentration of 12%

The ideal cellulose pre-cursor would have a low fiber linear density that is an indication of the diameter of the fiber. The analysis of the correlation results of the effect of temperature, concentration and crystallinity, shown in Figures F1 thought F6, indicate that a high draw ratio, low temperature and low concentration results in a fiber with a low linear density. Again these results are not normalized and it should be noted that there are several factors that affect the linear density, not just the parameters analyzed. One example would be possible voids in the fiber itself, it was assumed in the analysis of the linear density that the fibers had no voids. Voids in the fiber would affect the linear density; therefore, analyzing the effects on tenacity would give more useful results.

Based on the figures in this section, the draw ratio appeared to have the greatest effect on the linear density, more so than temperature or concentration. A high draw ratio will, in essence, pull the fiber during the spinning process thus reducing its diameter. A lower concentration also affected the linear density of the fiber. With less cellulose molecules present in the lower concentration solutions and when spun at a high draw ratio, it can be expected that the fiber linear density would be reduced. Again this was supported by results.

Therefore based on the results, the fiber linear density for all of the runs ranged from 3.92 to 11.4 denier, which was converted into a diameter range of 19.1 to 32.6 micrometers. Based on some studies, Lyocell fibers can range in linear density from 13 to 18 denier depending on the conditions of spinning (Peng et al., 2003 and Kreze et al., 2001). This indicates that the linear densities for the fibers spun from $[C_4mim]Cl$ solutions are lower but still comparable to the linear densities of Lyocell fibers.

APPENDIX G

Orientation Numbers

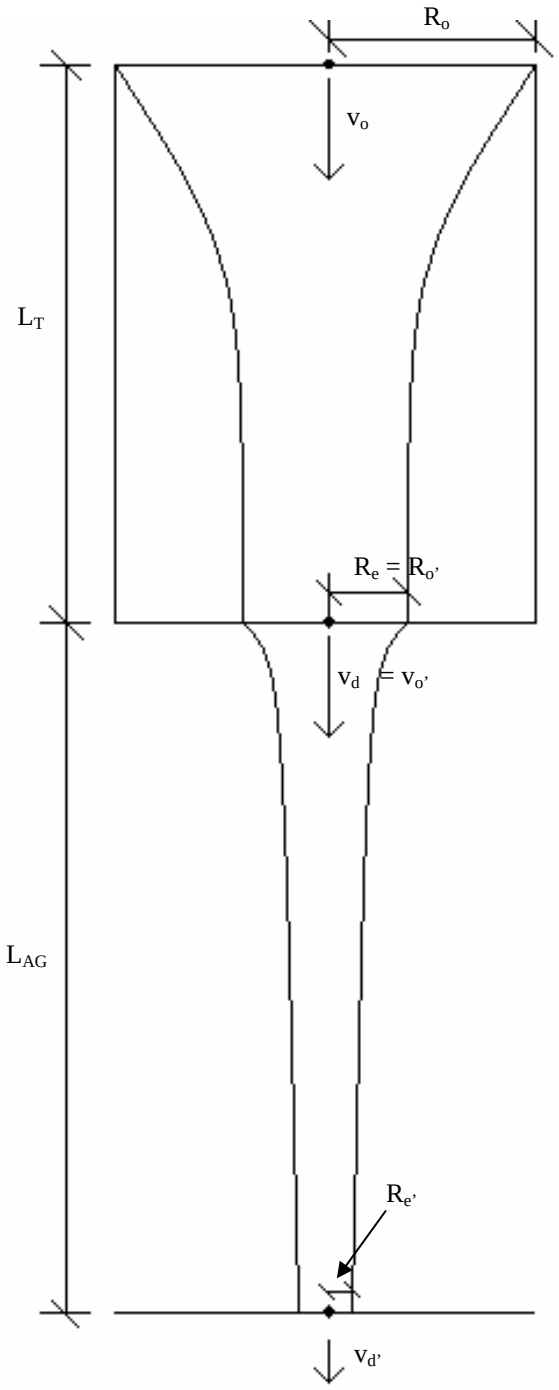

Not to Scale
(all units are in millimeters and seconds)

For the Die:

$\lambda = Given \quad L_T = 28mm \quad \dot{\varepsilon} = Given$

$$\varepsilon_H = \ln\left(\frac{R_o}{R_e}\right)^2 = \ln\left(\frac{10}{0.15}\right)^2 = 8.4$$

$$N_{OR(die)} = \lambda \varepsilon_H \dot{\varepsilon}$$

For the Air Gap:

$\lambda = Given \quad L_{AG} = 152.4mm$

$$\varepsilon_{H(AG)} = \ln\left(\frac{R_{o'}}{R_{e'}}\right)^2 \quad \text{where } R_{o'} = R_e$$

$$\text{so, } \varepsilon_H = \ln\left(\frac{R_e}{R_{e'}}\right)^2 = \ln\left(\frac{0.15}{R_{e'}}\right)^2$$

and $R_{e'} = Fiber\ Radius$

$$\dot{\varepsilon}_{(AG)} = \frac{v_{o'} L_{AG}}{(e^{\varepsilon_{h(AG)}} - 1)} \quad \text{where } v_{o'} = v_d$$

$$N_{OR(AG)} = \lambda \varepsilon_{H(AG)} \dot{\varepsilon}_{(AG)}$$

For the Total :

$\lambda = Given \quad L_{Tot} = 180.4mm$

$$\varepsilon_{H(Tot)} = \ln\left(\frac{R_o}{R_{e'}}\right)^2$$

$$\text{so, } \varepsilon_H = \ln\left(\frac{R_o}{R_{e'}}\right)^2 = \ln\left(\frac{10}{R_{e'}}\right)^2$$

and $R_{e'} = Fiber\ Radius$

$$\dot{\varepsilon}_{(Tot)} = \frac{v_o L_{Tot}}{(e^{\varepsilon_{h(Tot)}} - 1)}$$

$$N_{OR(Tot)} = \lambda \varepsilon_{H(Tot)} \dot{\varepsilon}_{(Tot)}$$

Figure G1: Schematic of hyperbolic die and air gap with N_{OR} calculations

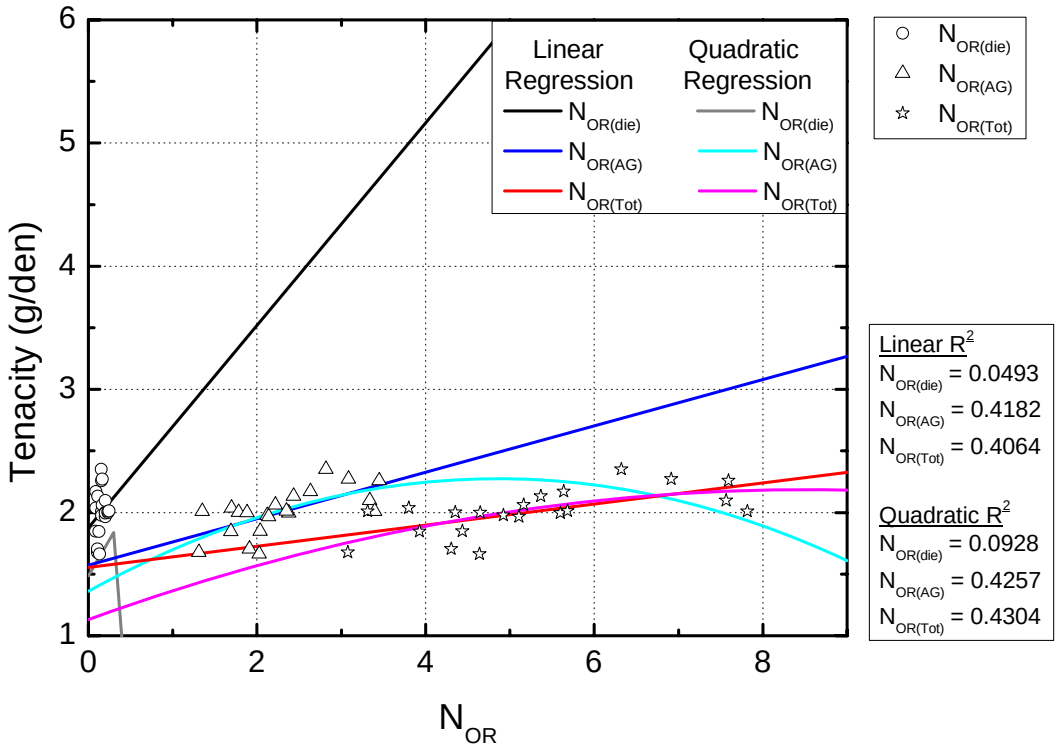

Figure G2: Tenacity verses all orientation numbers at a constant 100°C temperature for linear and quadratic regressions.

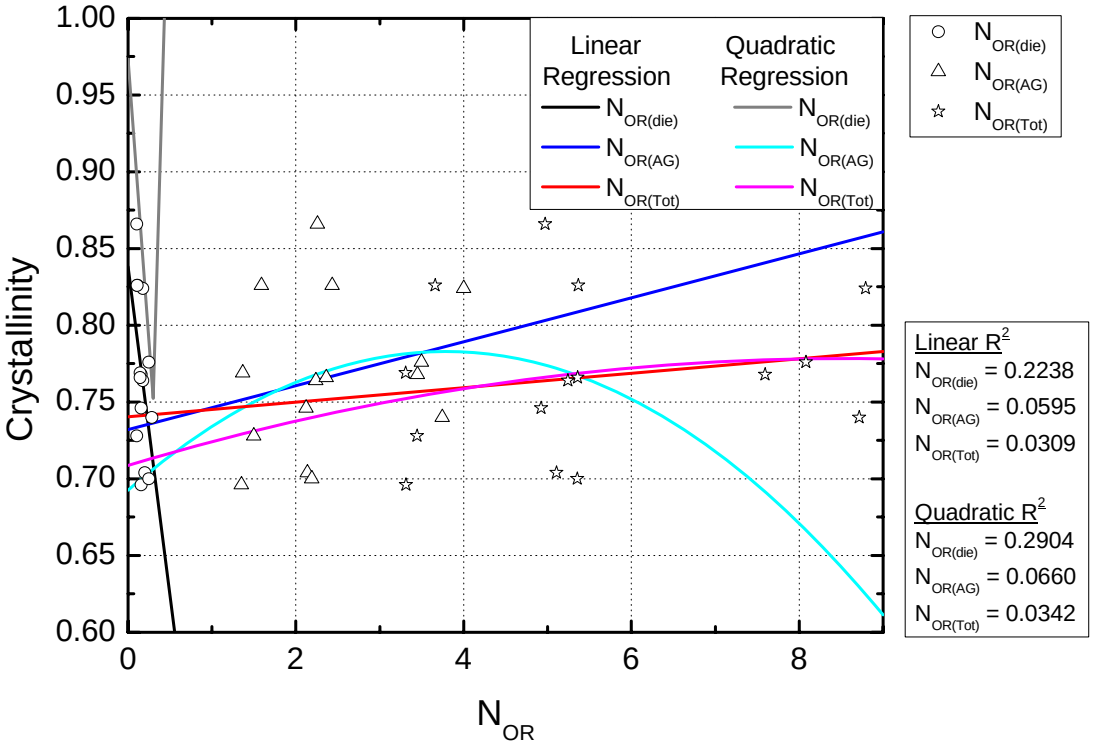

Figure G3: Crystallinity verses all orientation numbers at a constant 10% solution concentration for linear and quadratic regressions.

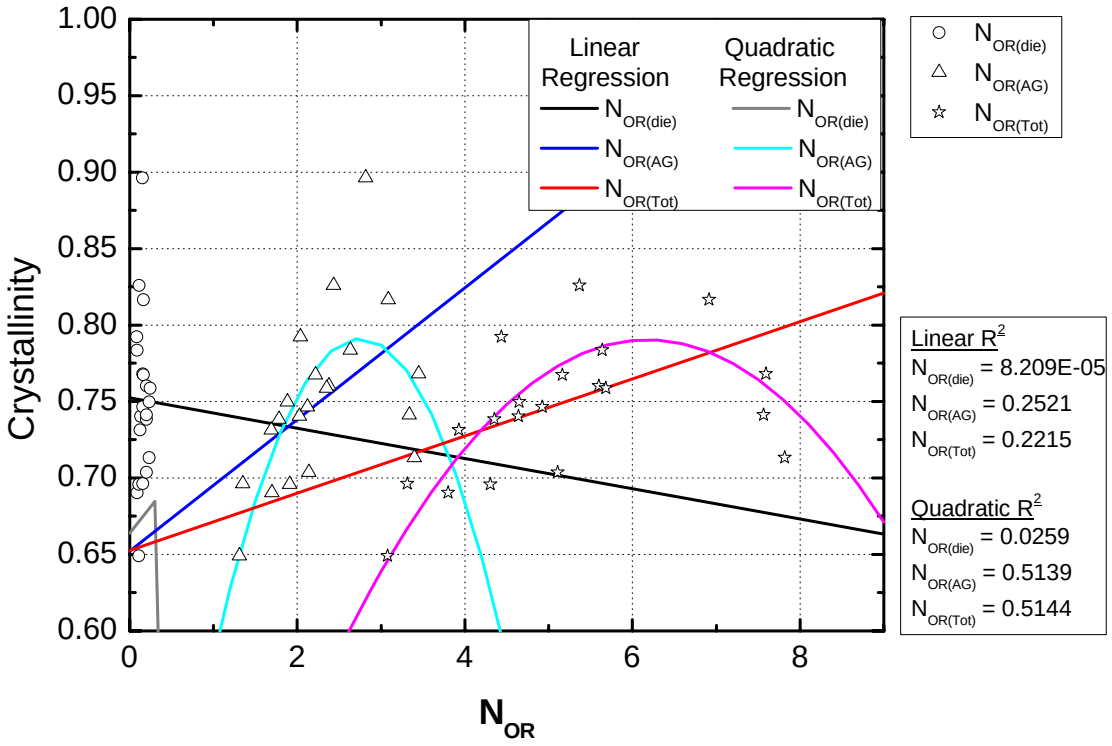

Figure G4: Crystallinity verses all orientation numbers at a constant 100°C temperature for linear and quadratic regressions.

Table 1G: Results of all N_{OR} calculations for all runs.

Run #	Conc.	Ave Linear Density (den)	Ave. Fiber Dia-meter (mm)	Elong. Strain Rate ε (s^{-1})	Take-up Velo-city v_t (mm/s)	Exit Velo-city v_d (mm/s)	Entr. Velo-city v_o (mm/s)	Relax-ation time λ (s)	Die Hencky Strain Rt. ε_H	N_{OR} (die)	Air Gap Hencky Strain Rt. $\varepsilon_{H(AG)}$	Elong. Strain Rate $\varepsilon_{(AG)}$ (s^{-1})	N_{OR} (AG)	Tot. Hencky Strain Rt. $\varepsilon_{H(Tot)}$	Elong. Strain Rate $\varepsilon_{(Tot)}$ (s^{-1})	N_{OR} (Tot)
1	10	5.07	0.0217	1.08	1183	30.25	0.0068	1.23E-02	8.4	0.112	5.3	37.6	2.43	13.6	31.94	5.369
2	10	10.79	0.0317	1.50	767	42.01	0.0094	1.23E-02	8.4	0.155	4.5	24.4	1.35	12.9	20.85	3.312
3	10	7.47	0.0264	1.50	1183	42.01	0.0094	1.23E-02	8.4	0.155	4.9	35.4	2.12	13.3	30.13	4.923
4	10	4.99	0.0215	1.50	1633	42.01	0.0094	1.23E-02	8.4	0.155	5.3	53.2	3.45	13.7	45.11	7.594
5	10	9.08	0.0291	1.92	1183	53.77	0.0121	1.23E-02	8.4	0.199	4.7	37.2	2.14	13.1	31.72	5.106
6	10	7.95	0.0272	1.25	933	35.01	0.0079	1.69E-02	8.4	0.177	4.8	27.7	2.24	13.2	23.57	5.244
7	10	4.92	0.0214	1.25	1467	35.01	0.0079	1.69E-02	8.4	0.177	5.3	44.9	4.00	13.7	38.13	8.793
8	10	10.66	0.0315	1.75	933	49.01	0.0110	1.69E-02	8.4	0.248	4.5	28.8	2.19	12.9	24.61	5.355
9	10	7.27	0.0260	1.75	1467	49.01	0.0110	1.69E-02	8.4	0.248	4.9	42.4	3.50	13.3	36.08	8.082
10	10	7.03	0.0256	1.25	933	35.01	0.0079	9.70E-03	8.4	0.102	4.9	31.3	1.50	13.3	26.65	3.446
11	10	5.00	0.0216	1.25	1467	35.01	0.0079	9.70E-03	8.4	0.102	5.3	44.2	2.26	13.7	37.50	4.972
12	10	9.98	0.0305	1.75	933	49.01	0.0110	9.70E-03	8.4	0.143	4.6	30.8	1.37	13.0	26.30	3.311
13	10	6.38	0.0244	1.75	1467	49.01	0.0110	9.70E-03	8.4	0.143	5.0	48.4	2.36	13.4	41.16	5.360
14	10	7.64	0.0267	1.50	1183	42.01	0.0094	2.23E-02	8.4	0.282	4.8	34.6	3.75	13.2	29.46	8.717
15	10	6.97	0.0255	1.50	1183	42.01	0.0094	8.50E-03	8.4	0.107	4.9	38.0	1.59	13.3	32.29	3.660
16	8	4.53	0.0205	1.15	1183	32.21	0.0072	8.47E-03	8.4	0.082	5.4	44.8	2.04	13.8	38.04	4.437
17	8	5.66	0.0230	1.25	933	35.01	0.0079	8.47E-03	8.4	0.089	5.1	39.0	1.70	13.5	33.13	3.802
18	8	3.92	0.0191	1.25	1467	35.01	0.0079	8.47E-03	8.4	0.089	5.5	56.4	2.63	13.9	47.83	5.638
19	8	8.16	0.0276	1.50	833	42.01	0.0094	8.47E-03	8.4	0.107	4.8	32.4	1.31	13.2	27.55	3.076
20	8	5.97	0.0236	1.50	1183	42.01	0.0094	8.47E-03	8.4	0.107	5.1	44.3	1.91	13.5	37.66	4.304
22	8	7.50	0.0264	1.75	933	49.01	0.0110	8.47E-03	8.4	0.125	4.9	41.1	1.69	13.3	34.97	3.930
24	8	6.77	0.0251	1.85	1183	51.81	0.0117	8.47E-03	8.4	0.132	5.0	48.2	2.03	13.4	40.98	4.640
25	12	5.80	0.0232	1.15	1183	32.21	0.0072	1.57E-02	8.4	0.152	5.1	35.0	2.82	13.5	29.72	6.324
26	12	7.58	0.0266	1.25	933	35.01	0.0079	1.57E-02	8.4	0.165	4.8	29.1	2.22	13.2	24.74	5.162
27	12	5.77	0.0232	1.25	1467	35.01	0.0079	1.57E-02	8.4	0.165	5.1	38.2	3.08	13.5	32.48	6.915
28	12	10.52	0.0313	1.50	833	42.01	0.0094	1.57E-02	8.4	0.198	4.5	25.1	1.78	12.9	21.39	4.351
29	12	8.32	0.0278	1.50	1183	42.01	0.0094	1.57E-02	8.4	0.198	4.8	31.7	2.38	13.2	27.03	5.599
30	12	6.29	0.0242	1.50	1583	42.01	0.0094	1.57E-02	8.4	0.198	5.0	42.1	3.34	13.4	35.77	7.566
31	12	11.41	0.0326	1.75	933	49.01	0.0110	1.57E-02	8.4	0.231	4.4	26.9	1.88	12.8	23.00	4.649
32	12	7.04	0.0256	1.75	1467	49.01	0.0110	1.57E-02	8.4	0.231	4.9	43.8	3.40	13.3	37.26	7.815
33	12	9.97	0.0305	1.85	1183	51.81	0.0117	1.57E-02	8.4	0.245	4.6	32.6	2.35	13.0	27.83	5.685

VITA

Rhea Sammons was born in Grand Rapids, Michigan on April 26, 1978. When she was 8 years old her family relocated to Tucson, Arizona where she completed grade school and junior high school. She graduated from Catalina Foothills High School in 1996. Rhea then proceeded to Purdue University to pursue a degree in Aerospace Engineering. However, after a semester in the aerospace department she decided that field of engineering was not her passion and found agricultural and biological engineering instead. She then graduated with a bachelor's degree in 2000 and a master's degree in 2002. After working for a few years Rhea returned to school to pursue a doctorate in Chemical Engineering at the University of Tennessee in Knoxville.

She is currently working on a post-doctorate at the Forest Products center on the University of Tennessee campus.